AN INVESTIGATION OF DYNAMIC-ANALYSIS METHODS FOR VARIABLE-GEOMETRY STRUCTURES

Fred Austin
and
Dino George

Grumman Aerospace Corporation
Bethpage, New York 11714

Report Number CSS-SSS-RP002

Prepared for the NASA Lyndon B. Johnson Space Center

Contract NAS9-15895

December 1980

FOREWORD

This work was performed under NASA JSC Contract NAS9-15895 entitled "Loads and Dynamics of Variable Geometry Structures." John Schliesing was the NASA Technical Monitor, and Fred Austin was the Grumman Program Manager.

The authors gratefully acknowledge the contributions of the following individuals: John Schliesing offered helpful advice and provided guidance throughout the program. Edward Magnani prepared the configuration review and provided data for the configurations that were selected for study. Morton Mantus offered useful advise and technical suggestions.

TABLE OF CONTENTS

TABLE OF CONTENTS (contd)

APPENDICES

APPENDICES (contd)

APPENDICES (contd)

LIST OF ILLUSTRATIONS

LIST OF ILLUSTRATIONS (contd)

LIST OF ILLUSTRATIONS (contd)

LIST OF ILLUSTRATIONS (contd)

LIST OF ILLUSTRATIONS (contd)

LIST OF ILLUSTRATIONS (contd)

LIST OF ILLUSTRATIONS (contd)

LIST OF TABLES

SUMMARY AND INTRODUCTION

The erection of large space structures requires construction, deployment, or a combination of these procedures. Some space structures also experience varying geometry as a result of on-board moving antennas or solar panels. The object of this contract is to develop practical methods for the dynamic analysis of structures with variable geometry. This includes exploring the applicability of standard fixed-geometry programs, such as NASTRAN, to the variable-geometry problem. To make detailed structural analyses feasible, methods are also required that are far more efficient than direct numerical integration of the equations of motion in pysical coordinates. This latter technique is extremely costly and time-consuming to formulate for each problem, and, in addition, is prohibitive for detailed idealizations in terms of computer time.

The study began with a literature survey of variable-geometry studies. Except for the Martin Marietta/NASA Goddard DISCOS program, and, to some extent, the Grumman SPACE12 program, existing variable-geometry structural programs are limited in their use to very specific problems with non-detailed structural idealizations. DISCOS can be used to study a structure composed of several flexible bodies that are hinged or somehow linked together. We attempted to use this program, and feel that it has significant potential but is not yet ready for widespread use. SPACE12 includes features such as internal mass motion (e.g., crew, elevator, or fluid movement within the vehicle); however, its variable-geometry modeling capability is limited to two flexible bodies that can have general prescribed motion relative to each other. Neither of these programs are well suited to problems involving growing structures such as the beam-fabrication problem studied under this contract.

It was also found that mechanism analysts have developed some interesting concepts to reduce the number of coordinates required for flexible mechanism problems. These concepts can, of course, be applied to variable-geometry space structures. One concept involves a coordinate-reduction scheme based on the deletion of coordinates, and is identical to the Guyan procedure often used for fixed-geometry structures. Other concepts employed vibration modes that vary with the geometry. As discussed later, a somewhat different variable-mode technique was developed under the present contract for application to space structures.

A review of selected space-structure configurations was conducted in order to define dynamic-analysis problems associated with variable geometry. This review was used as a basis to select a configuration that embodied many of these problems (see Appendix A). The selected configuration is illustrated in Fig. 1. Two seperate construction tasks are studied.

In the first task, "Beam Fabrication," a beam is fabricated by an Automatic Beam Builder (ABB) mounted in the orbiter. The 25 KW power module attached to the orbiter has very flexible solar panels; consequently, this configuration enables us to investigate the dynamics of a beam being constructed from a flexible base. Beam growth occurs in a pulse-like manner. As each bay is constructed within the ABB, the system's geometry does not change; however, after each bay is completed it is then expelled from the ABB. This recurring sequence of events gives rise to an approximately periodic axial load in the growing beam. The Remote Manipulator System (RMS) shown in the figure is stowed during this problem.

In the second task, "Beam Relocation," the completed beam is moved through a large angle (typically 90°) by rotating the RMS about the shoulder joint (Fig. 2). The power module with its solar panels is present, but is not shown in the figure.

The equations of motion were formulated in physical coordinates for both of these problems, and FORTAN computer programs were developed to generate solutions by numerically integrating the equations of motion. These solutions served as a standard of comparison to gauge the accuracy of approximate solution techniques that were developed and studied. Vibration was excited by either, or a combination of, three effects:

- acceleration of structural components as the geometry varied
- applied loads that are a function of time
- control-system loads

Control-system loads were generated by a simplified but closed-loop model of the orbiter vernier control system that was incorporated into each of the programs.

Good control was achieved in both the Beam-Fabrication and the Beam-Relocation problem. Unstable control-system coupling with the system flexibility did not occur. Also, it was found that variations in the stiffness of the beam due to the pulsating axial load during beam fabrication was not a significant effect.

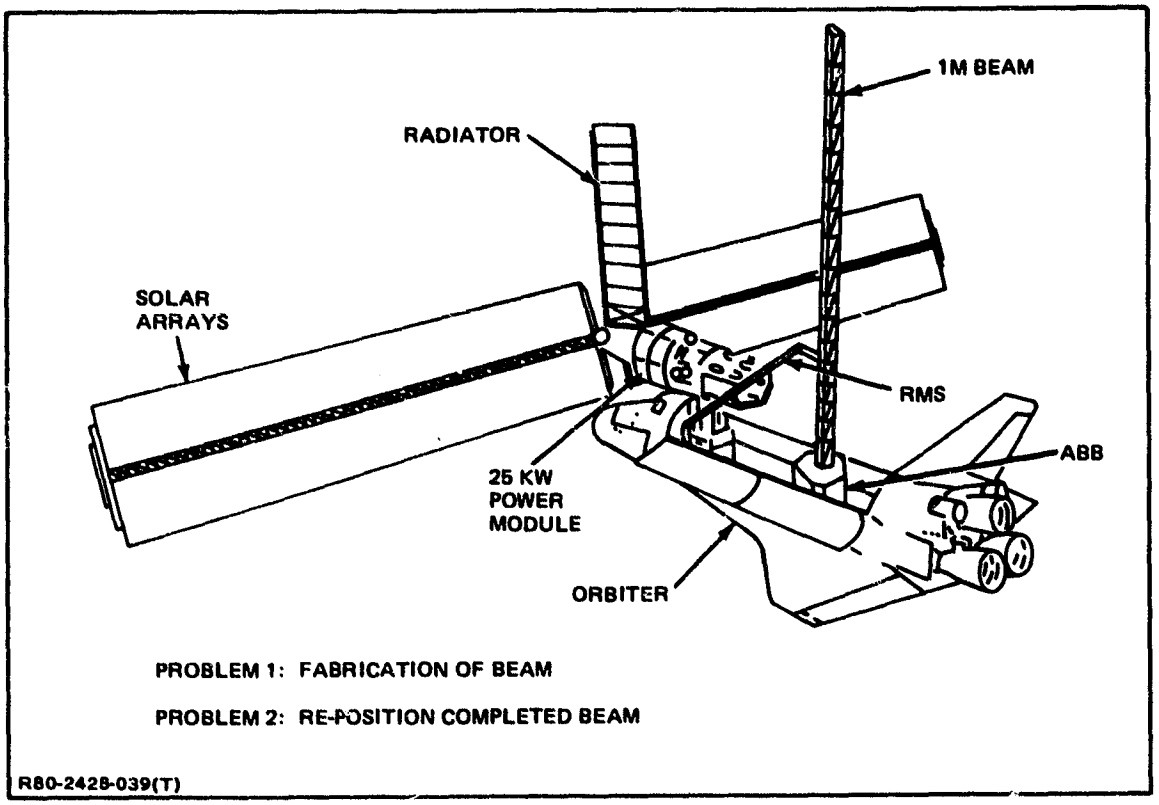

Fig. 1 Study Configuration

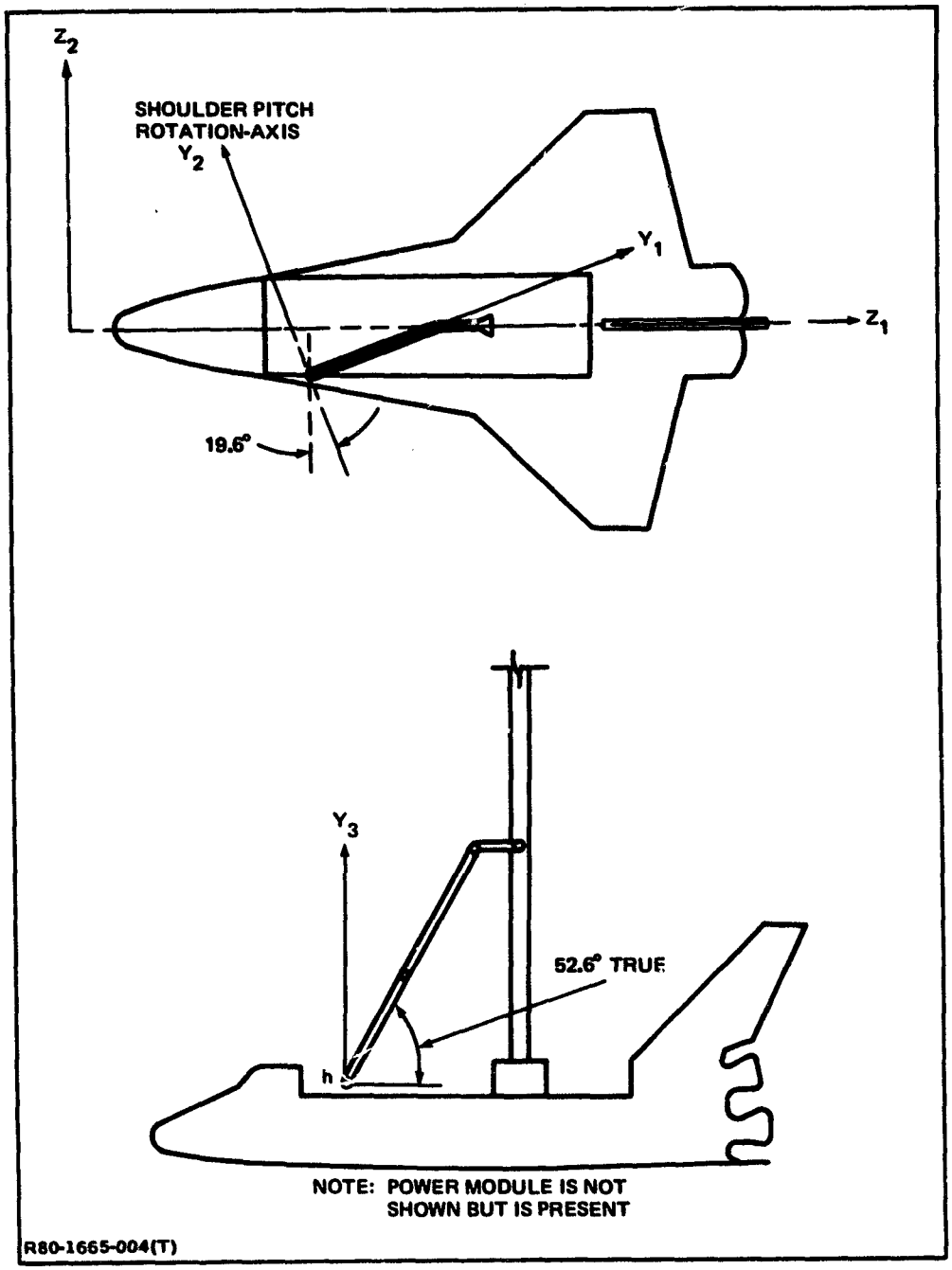

Fig. 2 Problem 2. Relocation of Beam Using RMS

An approximate method was developed for each problem to enable the analyst to investigate variable-geometry effects during a short time span by using standard fixed-geometry programs such as NASTRAN. This method is useful for investigating the dynamics during possible problem periods such as times when sudden changes in geometry occur. In this technique, called the Average-Geometry Technique*, the geometry is held fixed at its average value during the run. Variable-geometry effects are approximated by applying inertia loads that are based on rigid-body accelerations relative to the platform (orbiter plus power supply). In the Beam-Fabrication Problem acceptable approximate results were obtained provided the geometry variations were limited to 3% or less; however in the Beam-Relocation Problem, the RMS shoulder joint was moved as much as 40 deg., and a reasonably good approximate solution was obtained. The limitation of the method appears to be largely a function of the rate-of-change of the vibration frequency with the structural geometry.

A method employing modes of vibration that vary with the structural geometry was investigated for the Beam-Fabrication Problem. In this method, called the Variable-Mode-Technique, modes were computed at specific intervals. Between these intervals, the modes, modal masses, and modal stiffnesses are obtained by linear interpolation. Good accuracy was achieved for the problems investigated, and, in typical cases, the computer time was 85% lower than the time used to generate the corresponding physical-coordinate time-history solutions. Also, the use of modes has the potential to greatly simplify the analysis since many of the constraints are accounted for in the mode shapes.

---

*The method is called the Average-Length Technique in Section 2, which deals with the Beam-Fabrication Problem, and the Average-Angle Technique in Section 3, which deals with the Beam-Relocation Problem.

RECOMMENDED STUDIES

To ensure that the Average-Geometry Technique can be used as a reliable procedure to approximate the dynamic behavior of variable-geometry problems, it is necessary to determine whether the accuracy of the method is influenced by the mass of the construction platform (orbiter plus power supply for the problems considered in this report). It is possible that the success of this method is dependent on having a massive platform compared with the mass of the construction project (e.g., the beam being fabricated or being relocated by the RMS). This question was not explored during the current study.

The Variable-Mode Technique shows great promise of providing the capability for solving detailed structural problems with large geometry changes. It would be desirable to generalize this procedure so that the analyst could perform investigations without writing and programming the equations of motion for every specific problem. Before this is done, the technique should be explored further for geometry changes that are sufficiently large so that new nodes emerge from the construction base. In addition, a method is needed for automatically tracking the modes as they vary with the structural geometry to ensure that modal interpolation is performed among like modes. Since the method neglects the time rate-of-change of the modes with geometry, the limitations of the method for rapid geometry changes should be explored. If limitations for practical problems are discovered, correction terms should be developed for incorporation into the equations of motion. Finally a set of general equations should be developed which constitute the foundation for employing the Variable-Mode Procedure in a general-purpose program that would be applicable to any arbitrary structural configuration. It is envisioned that the program would be coupled with a general finite-element program such as NASTRAN to exploit existing structural-modeling capability.

NOTATION

$[\Gamma(\ )]$ cross-product matrix: i.e. given a vector $\{x\}$ with components x_1, x_2, and x_3

$$[\Gamma(x)] = \begin{bmatrix} 0 & -x_3 & x_2 \\ x_3 & 0 & -x_1 \\ -x_2 & x_1 & 0 \end{bmatrix}$$

$[1_k]$ identify matrix of order k

$\underset{\sim}{x}$ the tilde under a symbol represents a matrix or vector when it is a partition of a larger matrix. It is also used to denote a coordinate system; e.g. $\underset{\sim}{Z}$ is a coordinate system with axes Z_1, Z_2, and Z_3.

1 - LITERATURE SURVEY

1.1 Variable-Geometry Space Structures

DISCOS - The DISCOS (Dynamic Interaction Simulation of Controls and Structure) program described in Ref. 1 provides considerable capability for treating a very large class of variable-geometry problems; namely structures that an be idealized by a number of flexible bodies (See Fig. 1.1). Each body cannot grow in size. Consequently, DISCOS would not be suitable for the beam-builder problem treated herein; however, almost any type of constraint between linked bodies can be specified (e.g., pivots or a mechanism between bodies can be treated). The beam relocation problem studied herein would therefore be a good candidate for DISCOS. Additional capability includes built-in models for on-board inertia wheels and gravity-gradient loads. Other control effects and environmental loads may be treated; however, the user must write FORTRAN subroutines containing math models of these effects. Also, there is a provision for automatic linearization of the equations to enable control-system stability studies.

The method employed in the development of DISCOS is to assemble the equations of motion for each body and to account for the constraints between bodies by employing Lagrange multipliers. The vibration modes of each body are used to reduce the size of the problem. While the Lagrange-multiplier procedure provides great generality it also suffers from some inefficiency since the equations are not reduced by the number of constraints between bodies. In fact, while all of the accelerations are computed, requiring inversion of the mass matrices of each body, they are not all integrated since some of the velocities are more accurately obtained from the constraint equations. If this were not done, as time progresses, the solution of the constraint equations would be satisfied less and less accurately.

We have used the program at Grumman to solve simple problems and we have found that the solutions generated for these problems were correct. Unfortunately, we have found the documentation of both the theory and the program to be unsatisfactory. The considerable effort required to learn DISCOS could be significantly reduced by improved documentation. Also, we feel that the output of the program is incomplete and inadequately labeled. In summary, DISCOS

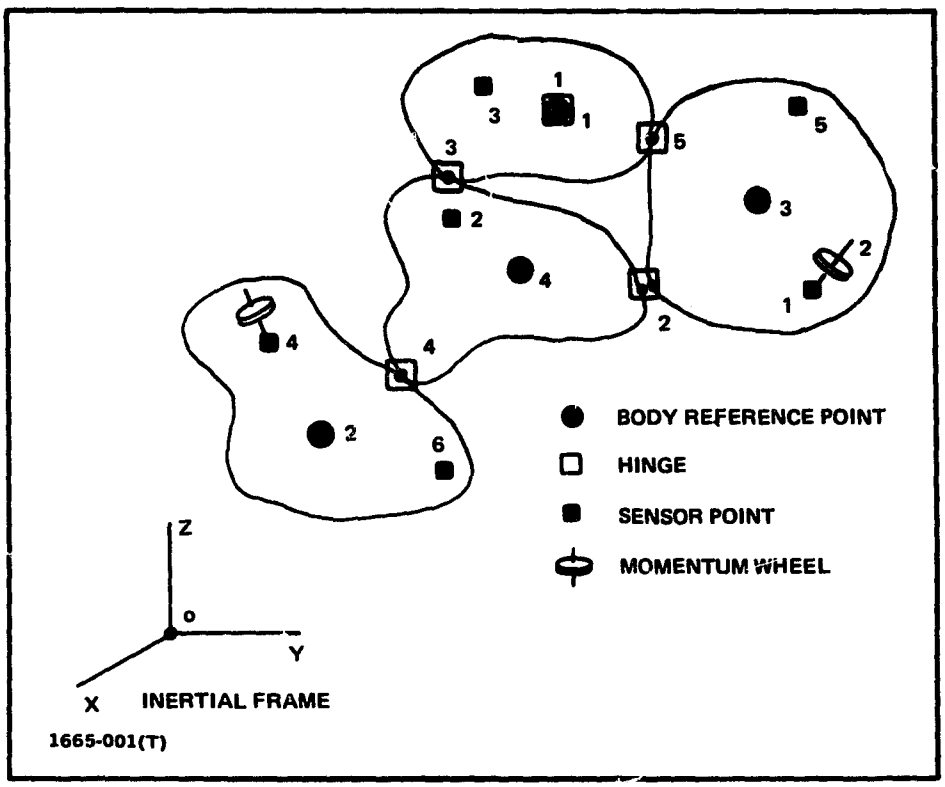

Fig. 1.1 General Idealization for the DISCOS Program

promises to provide great capability for variable-geometry structural analysis; however, we feel that the program and the documentation must be improved before it becomes a widespread tool.

SPACE10 - The SPACE10 computer program (Refs. 2 and 3) can be used to study the deployment of a class of two-body spacecraft. Each body can be represented by up to 100 physical mass points, each with six degrees of freedom. Modal analysis techniques are employed to reduce the order of the problem, and numerical-integration is used to obtain time-history solutions. Capability is provided for specific on-board control systems including attitude control using jet thrusters, system spin-speed control (both rotating and nonrotating satellites can be studied), and spacecraft nutation and precession control using a CMG. On-board disturbances include crew or other mass motion as well as fluids being pumped through pipes. Figure 1.2 shows a structure that could be analyzed with SPACE10. Subroutine interfaces have been provided to incorporate user-supplied control concepts and environmental loads. Additional control concepts and environmental loads on specific configurations were incorporated into a later version of the program, SPACE12. These loads include gravity-gradient, aerodynamic, and solar-radiation pressure effects.

Studies on Specific Configurations - DilPare studied the constant-velocity deployment of a long slender antenna from a uniformly accelerating infinite mass, representing a booster rocket (Ref. 4). The antenna was idealized as a six-node lumped-mass beam, and the equations of motion were numerically integrated. The nonlinear geometrical effects associated with large deflections were included; however, the effects of the variation of the linear and angular motion of the space vehicle resulting from the reaction of the beam on the vehicle were not addressed.

Wrenn, et al. studied the deployment of a flexible-rib antenna (Ref. 5). The ribs are the primary structural members that support flexible mesh in an umbrella-like fashion. In the retracted position, the ribs are wrapped around a central hub. Deployment is initiated by releasing restraints enabling the ribs to release their stored spring energy and unfurl. The study was confined to the case of planar motion, and all ribs were assumed to unfurl in phase. The order of the problem was greatly reduced by these simplifying assumptions.

Hedgepeth investigated the deployment of a 1500 m diameter Wire-Wheel antenna (Ref. 6). The depolyment is powered by the centrifugal force induced by spinning the system. Again, simplifying assumptions were made including equal

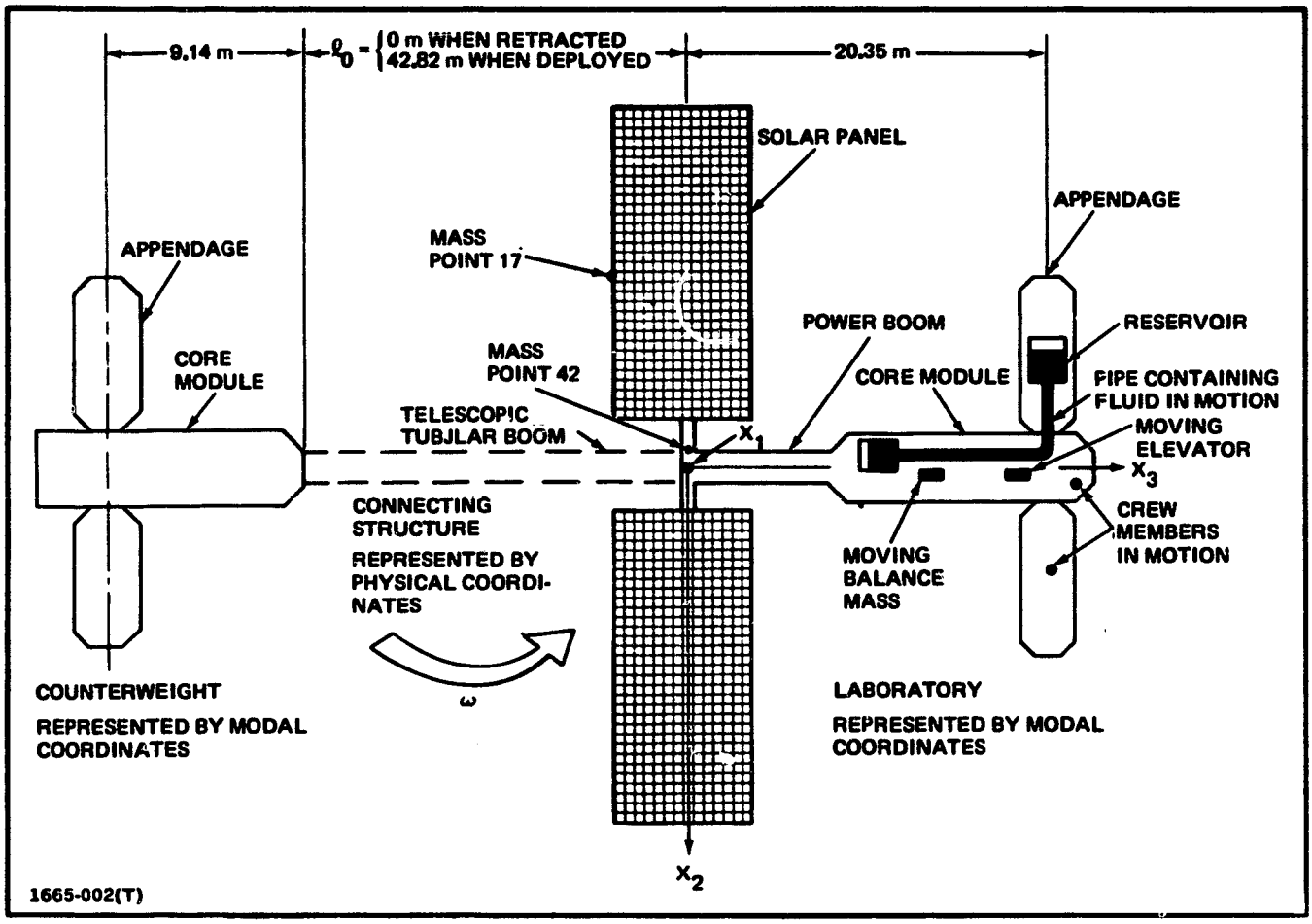

Fig. 1.2 Example of a Satellite that Can be Studied Using the SPACE 10 Program

motion of all meridial members enabling the structure to be reduced to a three degree-of-freedom system. The resulting equations were solved by numerical integration.

Bainum studied the dynamics of a rigid spinning spacecraft during the deployment of four flexible booms (Ref. 7). The booms were massless except for the tip mass. First, the complete equatons of motion of this 14 degree-of-freedom system were developed. Then the geometry was fixed at various intermediate positions of deployment, and the stability of motion was determined; thus all variable-geometry effects were not evaluated.

Lang used an analog computer to simulate the dynamics of two rigid masses deploying from a spinning rigid satellite (Ref. 8). He also studied the momentum and energy equations. Two techniques of deployment were investigated, each employing the centrifugal forces to actuate the deployment.

Developing the Equations of Motion - Various investigators have suggested methods for developing the equations of motion. These methods include: (1) Lagrange's equations with generalized coordinates, (2) Lagrange's equations with a mix of generalized and quasi coordinates, (3) variations of each of the last two methods by adding redundant coordinates (handled by Lagrange multipliers), (4) various Newton-Euler approaches, and (5) hybrid-coordinate approaches. Williams, et al. have prepared a comprehensive review of the methods used which includes a description of each technique (Ref. 9).

1.2 Structural-Analysis of Mechanisms

In addition to variable-geometry space structures, dynamic structural analysis methods have been developed for studying mechanisms such as four-bar linkages. Since the mechanism is a variable-geometry structure, many of the concepts developed for mechanism analysis are also applicable to space structures. A literature survey on the structural analysis of mechanisms is presented in Ref. 10. The papers discussed in more detail below, describe methods that are applicable to variable-geometry space structures.

Reference 10 also describes a method in which the finite-element technique is used to generate the mass and stiffness matrices for fixed snapshots of the structure at specific intervals as the geometry varies. These matrices remain fixed between intervals. The variable effects are introduced by applying reverse-acceleration forces obtained from a rigid-body analysis of the mechanism. This

reverse-acceleration technique is common to all of the mechanism-related methods discussed in this section. Modal analysis may be used to reduce the coordinates for each snapshot problem. On the other hand, the modes must be recomputed for each snapshot; therefore, there is an efficiency tradeoff to be made between modal- and physical-coordinate analysis. The paper does not provide numerical examples of these methods.

Reference 11 describes a method of variable-mode analysis for reducing the size of the system of equations of motion. Modes of vibration are computed at specific intervals and are extended between intervals by assuming linearity, using the derivatives of the mode shapes and eigenvalues ($1/\omega_i^2$'s) with respect to a geometric variable, the input crank-angle of a four-bar linkage. For two examples, both four-bar linkages, reasonably accurate eigenvalues could be obtained by this method for intervals of up to 14 deg. of variation in the input crank-angle. Time histories were generated by this variable-mode approach for both four-bar linkage configurations and for a six-bar mechanism that looks like two four-bar linkages in series. The equations of motion were not also solved in physical coordinates; therefore no comments can be provided regarding the overall accuracy of the method.

Another approach to reducing the size of the problem is described in Ref. 12. In this approach a number of physical coordinates are selected for elimination. Their values are assumed to be equal to the static deflections induced by the deflections of the retained coordinates at each increment of mechanism position. The method is based upon the Guyan procedure described in Ref. 13 for fixed-geometry elastic structures.

2 - BEAM FABRICATION

2.1 Idealization

The idealization for the beam-fabrication problem is shown in Figs. 2.1 and 2.2. The beam manufactured by the ABB is idealized with axially inextensible beam segments separated by nodes that are a distance "ℓ" apart. These nodes are numbered 1, 2, ..., n, where n is a variable that increases as the beam is constructed. The rotatory inertia of these nodes is neglected. The ABB is idealized as a rigid point with variable mass which decreases as each beam node is expelled during beam construction. The orbiter and power supply, nodes 100 and 200, respectively, are rigid bodies, with rotatory inertia, that are rigidly connected to each other. The solar panels are represented as beams. Each of the nodes P_1, P_2, ..., P_6 has a mass and pitch rotatory inertia. Its rotatory inertia in bending is neglected. Each of these nodes has two elastic degrees-of-freedom, fore-and-aft bending and pitch rotation. For the other degrees-of-freedom, the nodes are constrained to move as if the panels were rigidly attached to the power supply.

The portion of the structure with nonvarying geometry (the orbiter, ABB, power supply, and solar panels) will be referred to as the platform, and the ABB-constructed beam will be referred to as the beam.

2.2 Stiffness Matrix

The details involved in forming the stiffness matrix are presented in Appendix B. The main concepts are discussed in this section.

The stiffness matrix for the beam is re-formed each time the beam changes in length by assembling the stiffness matrices of beam members in accordance with the displacement method used in finite-element analysis (Ref. 14). All rotational coordinates, except those at the root of the beam, are deleted from the resulting matrix by employing the Guyan reduction procedure. By using this procedure, the coordinates which are to be deleted are set equal to their static values; i.e., the values which they would have if their associated mass properties (moments of inertia in the case of rotations) were zero.

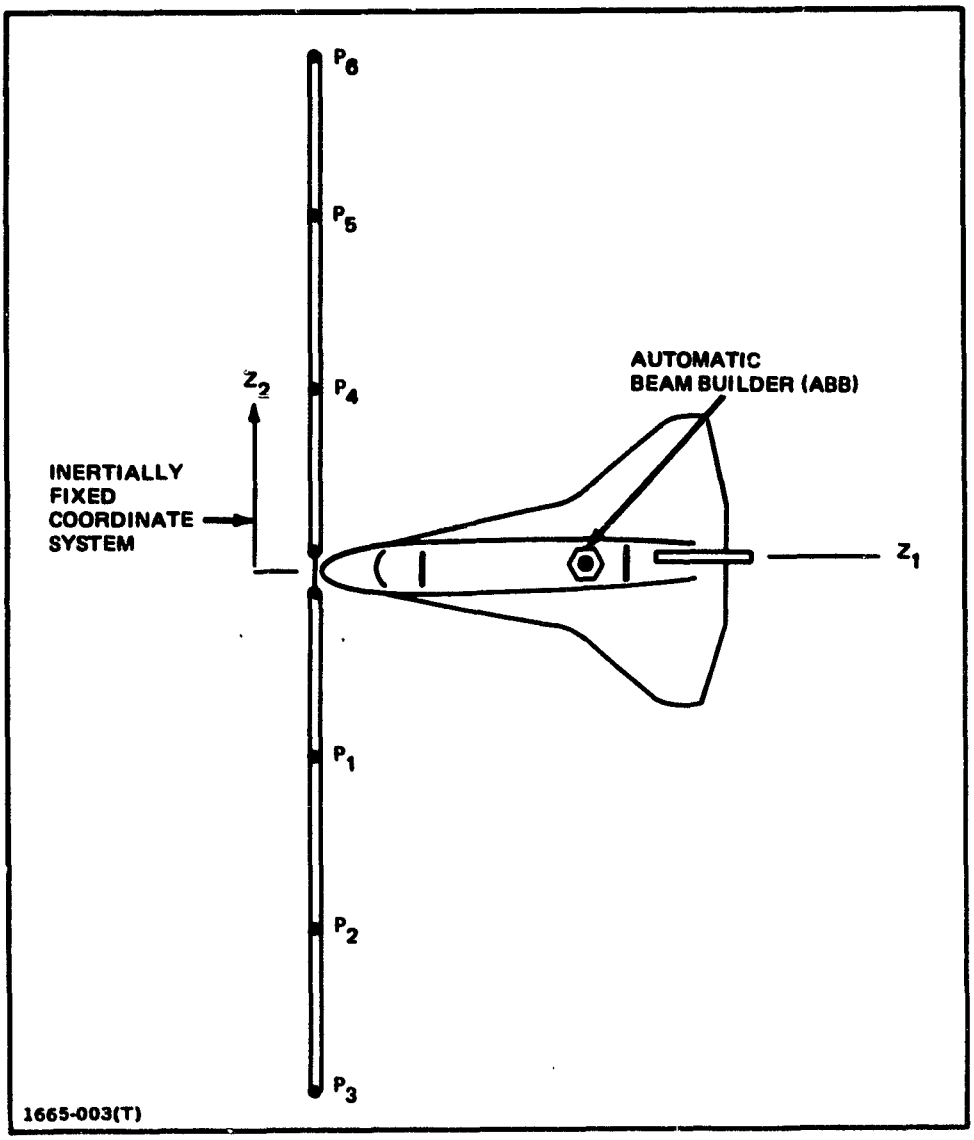

Fig. 2.1 Idealization for Beam-Fabrication Problem – Plan View

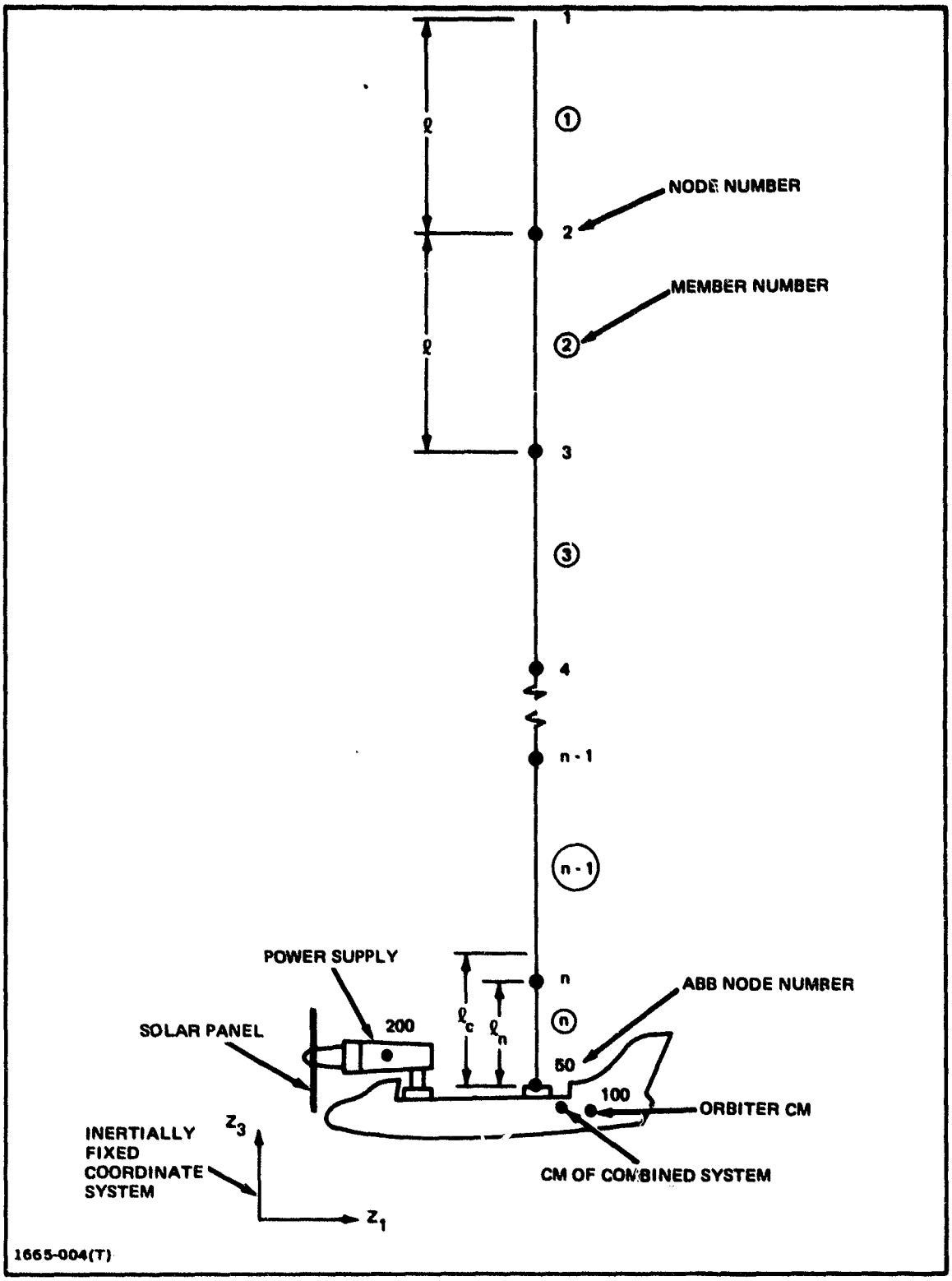

Fig. 2.2 Idealization for Beam Fabrication Problem – Elevation View

Member n of Fig. 2.2 requires special attention. When ℓ_n is small, this member is very stiff and therefore gives rise to a very high vibration frequency. In fact, when node n first emerges, and ℓ_n is differential in size, this frequency is infinite. In order to solve the problem by direct numerical integration, this high-frequency component was deleted from the formulation. Whenever ℓ_n is less than a given length ℓ_c, that is input data to the program, the coordinates of node n were deleted by assuming that their values are set equal to their static values. The mass of node n is redistributed, in a consistent way, by multiplying the mass as well as the stiffness matrix by the transpose of the matrix that reduces the coordinates. The reduction was first accomplished by using the Guyan procedure; however, numerical inaccuracies still resulted when ℓ_n was small. This problem was traced to the fact that ℓ_n appears in the denominator of the stiffness terms of member n, and in some terms ℓ_n^2 and ℓ_n^3 appear in the denominator. When ℓ_n is near zero, extremely large stiffness terms arise. These high stiffness terms would be added to the lower stiffness terms of the adjacent beam segment causing several digits of the smaller terms to be lost. As a result, when the high stiffnesses are then removed by the Guyan procedure, the resulting stiffness matrix is very inaccurate whenever a new node emerges from the ABB.

For this reason a geometrical procedure was selected to eliminate the coordinates of node n whenever $\ell_n < \ell_c$. The stiffness matrix for the beam is formulated with node n deleted; i.e., the length of member n-1 is assumed to extend from node n-1 to the ABB, node 50. The curve of the deflected beam between these nodes is a cubic, consequently, given the deflection and slopes at nodes n-1 and 50, the cubic coefficients and therefore the deflection of node n can be computed. When only one node is exposed, the beam is assumed to be undeformed whenever $\ell_1 < \ell_c$. In either case, this information will later be used to reduce the mass matrix and applied load vector. Since the actual curve between nodes is also a cubic, this procedure provides the same results as the Guyan procedure*; however, it is more accurate when ℓ_n is small.

After a bay of the beam is completed, the bay is pushed out of the ABB. The resulting acceleration and deceleration of the beam gives rise to axial loads.

---

*This was numerically verified for cases where ℓ_n was not very small.

In order to evaluate this beam-column effect, its influence on the stiffness matrix is accounted for. The axial load in each beam member is obtained by summing the acceleration and applied loads on all nodes above the member. Since this requires recomputing the stiffness matrix at each time point, even when the beam is not growing, it is a costly procedure; consequently an input-data option has been provided in the program to neglect the beam-column effect when the user feels that it is not significant.

The stiffness matrix for the platform (orbiter assembly and solar panels) is a fixed quantity. It was obtained by using NASTRAN and is input data to the program. The total stiffness matrix for the structure is obtained by assembling the beam stiffness matrix and the platform stiffness matrix using the displacement method of finite-element analysis.

The resulting structural stiffness matrix was compared with a matrix generated by NASTRAN for a system containing a fixed-length beam, and the results agreed. However, because of numerical round-off, the rigid-body properties of the resulting stiffness matrix were slightly inaccurate; i.e., when the structure was given a rigid-body displacement, it very slowly drifted in space. The behavior was characteristic of very small positive or negative spring ties between the structure and ground. The drifting led to inaccurate total deflections in long computer runs. This effect was rectified by making small adjustments to some of the terms in the stiffness matrix so that

$$[K][U_R] = [0] \tag{2-1}$$

where $[U_R]$ is the six-column matrix containing the six rigid-body modes. When the beam-column effect is included, only the platform stiffness matrix is adjusted since $[K]\{u_R\}$ will be equal to a required applied load and will therefore not be zero when $\{u_R\}$ is a rigid-body rotation (see Fig. 2.3).

Another precaution that was taken in the program to improve the accuracy of the stiffness matrix was to perform key operations in double precision.

2.3 Kinematics of Beam Emission

As indicated in Fig. 2.4, the beam is composed of a series of bays. After each bay is fabricated within the ABB, it is emitted by expelling it, first at constant acceleration until it reaches cruise velocity, then it cruises at constant

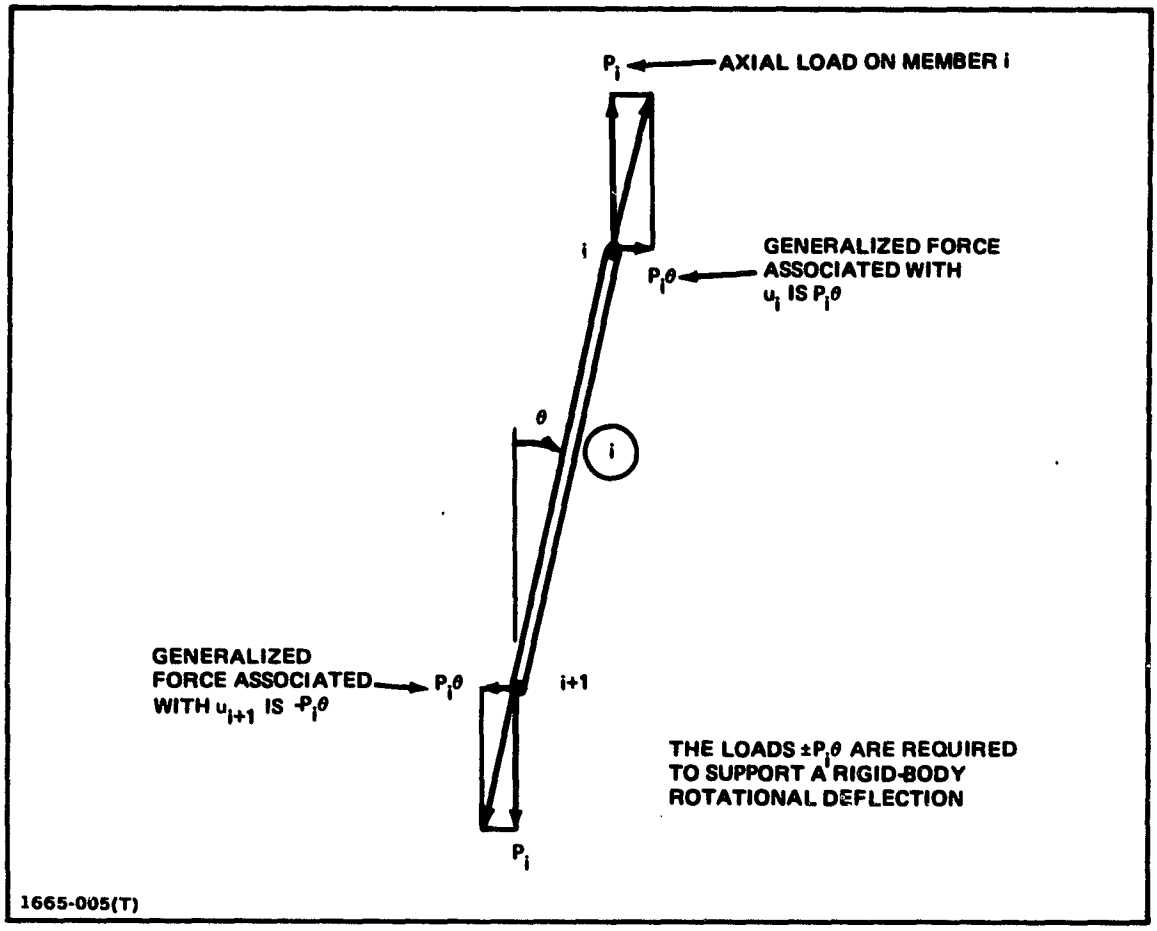

Fig. 2.3 Demonstration that External Loads are Required to Maintain a Rigid-Body Rotation when the Beam-Column Effect is Included in the Stiffness Matrix

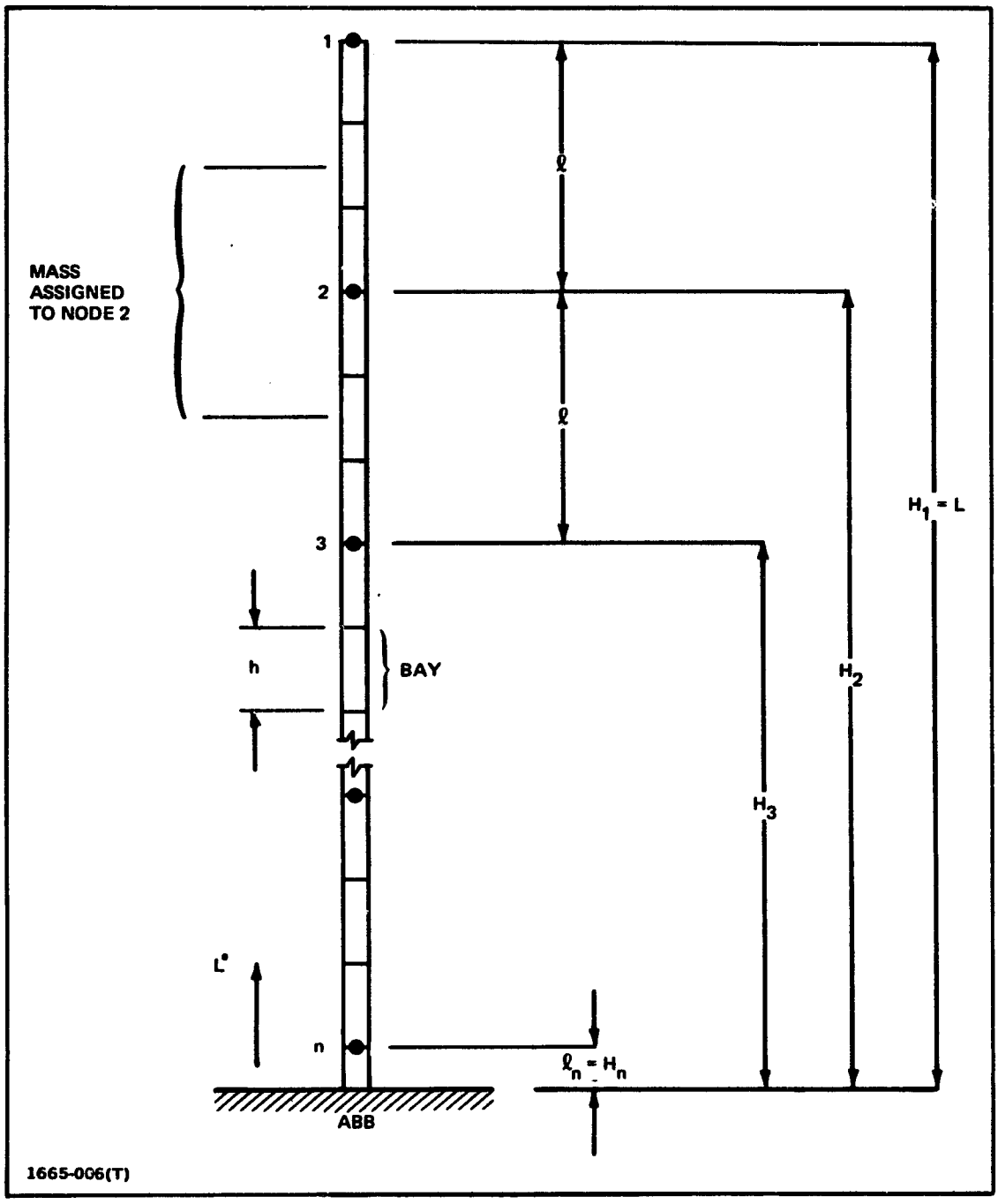

Fig. 2.4 Detailed Idealization of Beam

velocity, and finally it decelerates at constant deceleration until it comes to a stop. Then there is a pause as the next bay is fabricated, and, after that, the process is repeated. The resulting beam motion is shown in Fig. 2.5. The equations used to characterize this motion are presented in Appendix C.

2.4 Treatment of Constraints

The method of treating constraints is described in this section and is justified in Appendix D. Although F = ma and T = Iα are used to derive the equations of motion, it is assumed that the equations of motion are in the Lagrangian form (i.e., arranged so that the mass matrix is symmmetric). As an example of the constraint procedure, it is assumed that the equations of motion are

$$[M]\{\ddot{x}\} = \{g\} \tag{2-2}$$

and that the constraints are expressed by the following linear equation with a constant coefficient matrix [T]:

$$\{x\} = [T]\{y\} \tag{2-3}$$

{y} will contain fewer coordinates than {x}; therefore forces of constraint will usually arise if {x} is constrained, so that it must be equal to a linear combination of the columns of [T]. However, if (2-3) is substituted into (2-2) and the result is multiplied through by $[T]^T$, the forces of constraint will no longer be present in the right-hand vector; i.e., the equation

$$[T]^T[M][T]\{\ddot{y}\} = [T]^T\{g\} \tag{2-4}$$

does not contain any contribution of the forces of constraint. Thus, multiplication of the equations of motion by $[T]^T$ not only systematically reduces the number of equations while retaining the symmetry of the reduced mass matrix, it also eliminates the forces of constraint from the problem.

Equation (2-3) may be a geometrical relation among coordinates arising from rigidity within the structure. Another possibility is a Guyan tranformation which is a systematic way of determining [T] so that selected coordinates are omitted (see Section B4 of Appendix B). In this case multiplication of the equations by $[T]^T$ redistributes the mass of the omitted coordinates to the retained coordinates. Equation (2-3) may also represent a modal transformation where the columns of

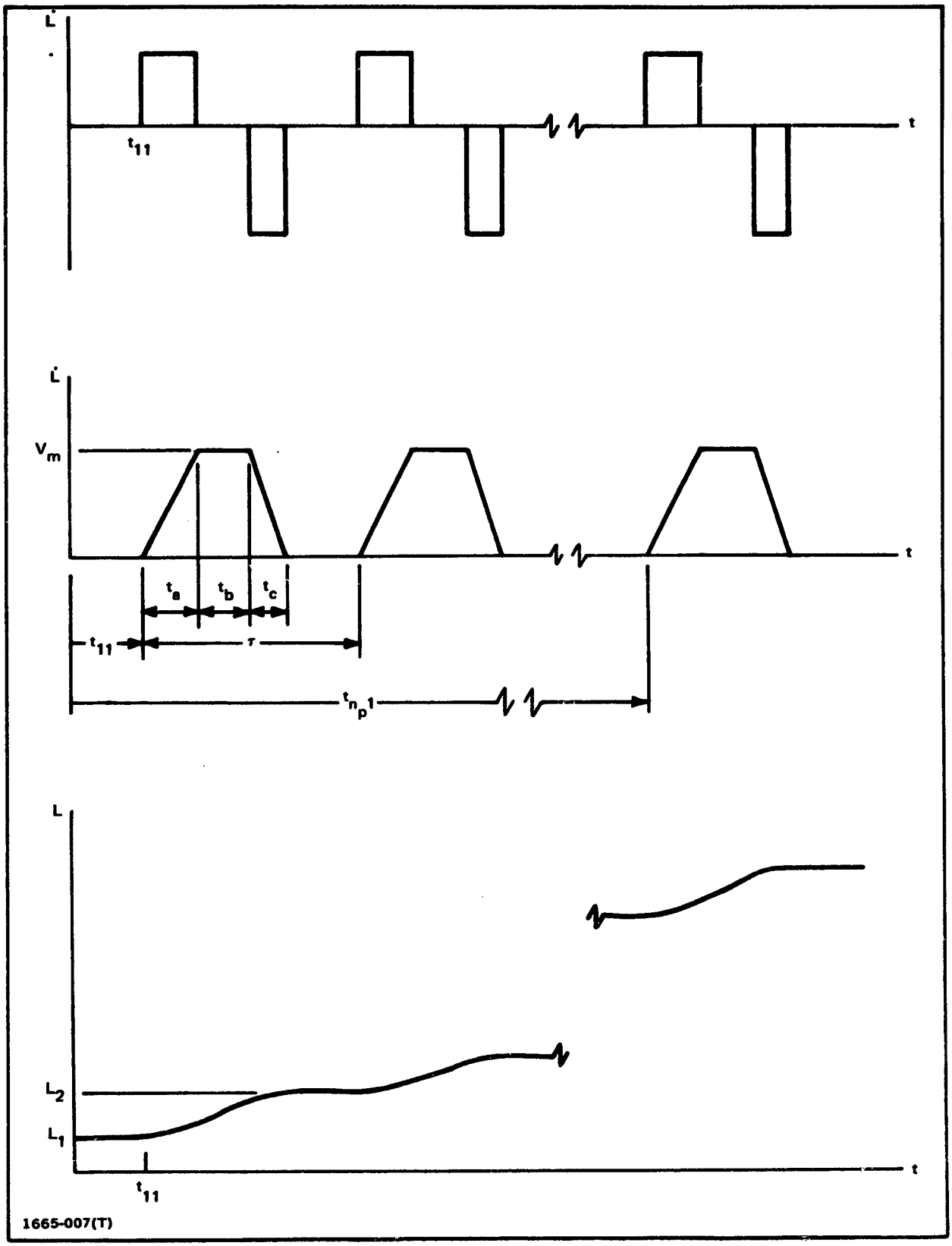

Fig. 2.5 Beam Length, Velocity, and Acceleration (Fabrication Rates) as a Function of Time

[T] are the mode shapes and {y} contains the modal displacements. When the deformation vector is constrained so that its value is a linear combination of a few modes, forces of constraint arise, and the constraint theory is applicable. In this sense, the modal transformation may be viewed as a constraint transformation.

Appendix D also treats more complex constraints such as time-varying constraints and nonlinear constraints. However, the procedure to be used is the same. The constraint equation is substituted into the equations of motion, and the result is premultiplied by the transpose of the constraint matrix.

2.5 Equations of Motion

2.5.1 Equations Before Applying Constraints

The following equations of motion are written before applying the constraints.

1. Newton's law in all three directions for each node on the beam. The rotatory inertia of these points is neglected; therefore no torque equations are written.

2. Newton's law in all three directions for Node 50, the portion of the ABB which contains the masses that eventually will turn up on the nodes of the manufactured beam. The beam masses are located between bays as indicated in Fig. 2.4. The bays are expelled from the ABB at a stop-start pulsing rate (Fig. 2.5); therefore each node begins from rest and is then accelerated away from the ABB. Accordingly, the mass of the ABB decreases incrementally as each node leaves it. The constant portion of the ABB may be lumped together with the orbiter so that its rotatory-inertia properties can be included.

3. Newton's law and Euler's equations are written in all three coordinate directions for the orbiter, node 100.

4. Newton's law and Euler's equations are written in all three coordinate directions for the power supply, node 200.

5. For each node on the solar panels, Newton's law is written in all three coordinate directions. Only the pitching inertia of the solar-panel node is considered to be significant; therefore, Euler's equation is written for rotation about the 2, or pitch, axis only.

Accordingly, the equations of motion are

$$[M_{GG}]\{\ddot{Z}_G\} = \{F_G\} \tag{2-5}$$

where the subscript G denotes the original, or grid, set of coordinates, and

$$[M_{GG}] = \begin{bmatrix} m_1 I_3 & & & & & & & & & & & & \\ & m_2 I_3 & & & & & & & & & & & \\ & & \ddots & & & & & & & & & & \\ & & & m_n I_3 & & & & & & & & & \\ & & & & m_{50} I_3 & & & & & & & & \\ & & & & & m_{100} I_3 & & & & & & & \\ & & & & & & I_{100} & & & & & & \\ & & & & & & & m_{200} I_3 & & & & & \\ & & & & & & & & I_{200} & & & & \\ & & & & & & & & & m_{p_1} I_3 & & & \\ & & & & & & & & & & I_{p_1} & & \\ & & & & & & & & & & & m_{p_2} I_3 & \\ & & & & & & & & & & & & I_{p_2} \\ & & & & & & & & & & & & & \ddots & & \\ & & & & & & & & & & & & & & m_{p_6} I_3 & \\ & & & & & & & & & & & & & & & I_{p_6} \end{bmatrix} \tag{2-6}$$

$$\{Z_G\} = \begin{Bmatrix} \underset{\sim}{r}_1 \\ \underset{\sim}{r}_2 \\ \vdots \\ \underset{\sim}{r}_n \\ \underset{\sim}{u}_{50} \\ \underset{\sim}{u}_{100} \\ \underset{\sim}{\theta}_{100} \\ \underset{\sim}{u}_{200} \\ \underset{\sim}{\theta}_{200} \\ \underset{\sim}{u}_{P_1} \\ \theta_{P_1} \\ \underset{\sim}{u}_{P_2} \\ \theta_{P_2} \\ \vdots \\ \underset{\sim}{u}_{P_6} \\ \theta_{P_6} \end{Bmatrix}, \qquad \{F_G\} = \begin{Bmatrix} \underset{\sim}{F}_1 \\ \underset{\sim}{F}_2 \\ \vdots \\ \underset{\sim}{F}_n \\ \underset{\sim}{F}_{50} \\ \underset{\sim}{F}_{100} \\ \underset{\sim}{T}_{100} \\ \underset{\sim}{F}_{200} \\ \underset{\sim}{T}_{200} \\ \underset{\sim}{F}_{P_1} \\ t_{P_1} \\ \underset{\sim}{F}_{P_2} \\ t_{P_2} \\ \vdots \\ \underset{\sim}{F}_{P_6} \\ t_{P_6} \end{Bmatrix} \tag{2-7}$$

where m_k is the mass of node k and $[I_k]$ (or $\underset{\sim}{I}_k$ - the tilde is used alternatively to denote a matrix or vector) is its mass moment-of-inertia matrix, $[1_3]$ is the 3 by 3 identity matrix, I_{p_j} is the pitch moment of inertia of node P_j, and the terms in the displacement vector are defined in Fig. 2.6. The notation is used that $\{r_i\}$ contains the components of $\vec{r}_i$ in the $\underset{\sim}{Z}$ coordinate system. Also,

$$\{u_k\} = \begin{Bmatrix} u_{k1} \\ u_{k2} \\ u_{k3} \end{Bmatrix} \tag{2-8}$$

$$\{\theta_k\} = \begin{Bmatrix} \theta_{k1} \\ \theta_{k2} \\ \theta_{k3} \end{Bmatrix} \tag{2-9}$$

and $\theta_{P_j} = \theta_{P_j 2}$, the pitching, or axis-2, rotation of node P_j. $\{\ddot{r}_i\}$ is used to represent the acceleration of node i on the beam instead of the second derivative of the elastic deflection because $\{\ddot{r}_i\}$ contains the component of acceleration due to growth of the beam. The load vector $\{F_G\}$ contains the forces and torques that correspond to the coordinates. The forces are

$$\{F_i\} = \begin{Bmatrix} F_{i1} \\ F_{i2} \\ F_{i3} \end{Bmatrix}; \quad i = 1, 2, \ldots, n; 50; 100; 200; P_1, P_2, \ldots, P_6 \tag{2-10}$$

and the torques are

$$\{T_i\} = \begin{Bmatrix} T_{i1} \\ T_{i2} \\ T_{i3} \end{Bmatrix}; \quad i = 100, 200 \tag{2-11}$$

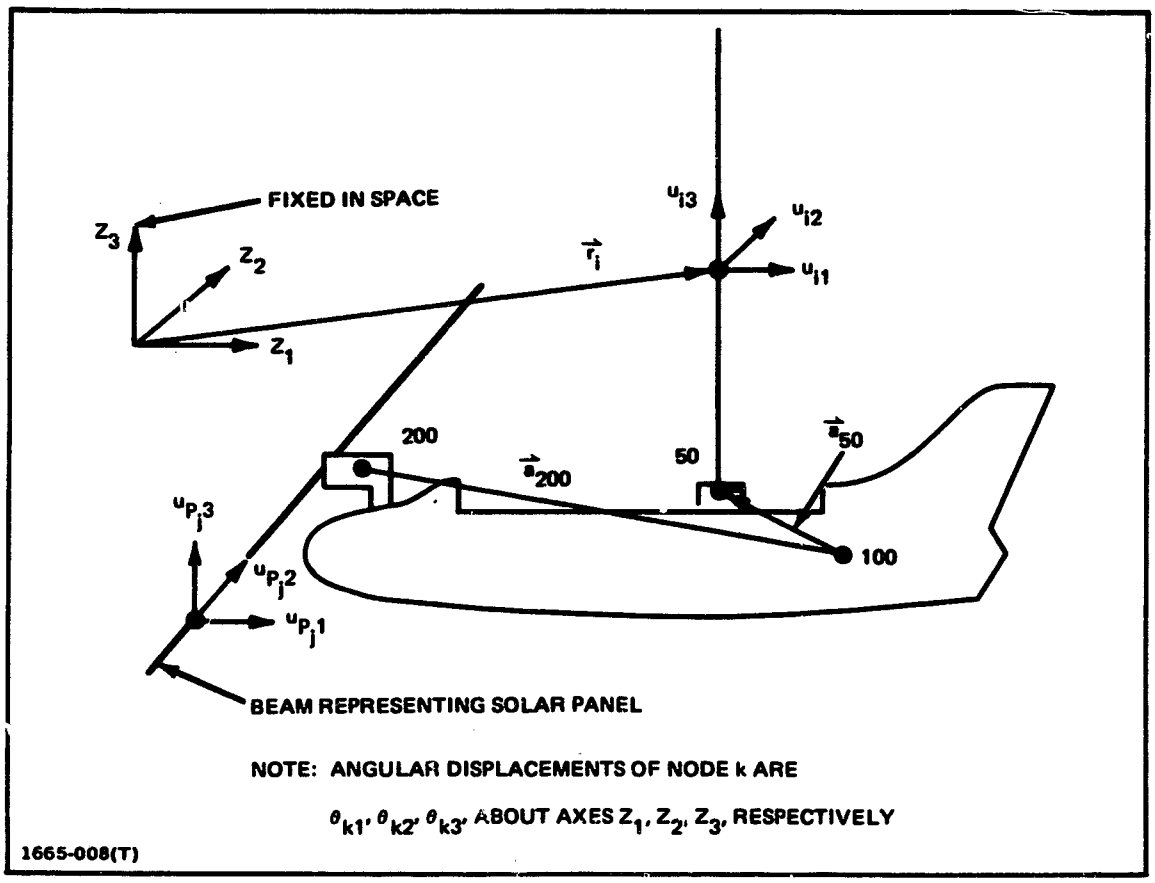

Fig. 2.6 Notation for Expressing Displacements

and $t_{P_j} = T_{P_j 2}$, the torque on node P_j in the pitch direction (j=1, 2, ..., 6).

2.5.2 Reduction to Independent Coordinates

The detailed relations used in reducing the equations of motion to independent coordinates are developed in Appendix E. The basic concepts are summarized in this section. Using geometry, the acceleration vector is expressed as a function of the derivatives of the independent coordinates $\{Z_F\}$ as follows:

$$\{\ddot{Z}_G\} = [U]\{\ddot{Z}_F\} + \{v_G\} \tag{2-12}$$

where the subscript F denotes the flexible coordinate set, and [U] is a function of the geometry (defined by (E9)), $\{Z_F\}$ contains the independent coordinates (defined by (E10)) and $\{v_G\}$ is a function (defined by (E10)) of $\ddot{L}$, the prescribed acceleration of the beam emanating from the ABB. In accordance with the method of treating constraints described in Appendix D, (2-12) is substituted into (2-5) and the result is multiplied through by $[U]^T$. The resulting equations are

$$[M_{FF}]\{\ddot{Z}_F\} = \{f_F\} - \{g_F\} \tag{2-13}$$

where the subscript F denotes the flexible set of coordinates. The matrices in (2-13) are defined as

$$[M_{FF}] = [U]^T[M_{GG}][U] \tag{2-14}$$

$$\{f_F\} = [U]^T\{F_G\} \tag{2-15}$$

$$\{g_F\} = [U]^T[M_{GG}]\{v_G\} \tag{2-16}$$

Equations (2-14) - (2-16) must be evaluated every numerical-integration time-point. In order to increase the computational speed, the matrix multiplications indicated in these equations were performed algebraically, and the resulting expressions, (E24), (E39), and (E43), were programmed.

As discussed in Section 2.2, when node n is close to the ABB (i.e., when $\ell_n < \ell_c$), the deformation coordinates of node n are eliminated. This is accomplished via the transformation

$$\{Z_F\} = [\bar{G}]\{\bar{Z}_F\} \; ; \qquad \ell_n < \ell_c \tag{2-17}$$

where $\{\bar{Z}_F\}$ is identical to $\{Z_F\}$ except that the deformation coordinates of node n are deleted. The equations of motion for the case where $\ell_n < \ell_c$ are obtained by substituting (2-17) into (2-13) and multiplying the result by $[\bar{G}]^T$.

2.5.3 Final Form of Equations of Motion

The reduced equations of motion are given by (E49). If stiffness and damping terms are incorporated, the matrix equation becomes

$$[M]\{\ddot{z}\} + [C]\{\dot{z}\} + [K]\{z\} = \{f\} - \{g\} \tag{2-18}$$

where the stiffness matrix [K] is obtained by the method described in Section 2.2. Since the problem is solved in physical coordinates, modal damping cannot be used. To incorporate some damping, in this work the damping matrix is assumed to be proportional to the stiffness matrix; i.e.,

$$[C] = \alpha[K] \tag{2-19}$$

where α is a constant that is input data. One reason for determining [C] in accordance with (2-19) is that, since [K] is a matrix for a free structure, rigid-body motions will not give rise to damping forces. It is shown, in Appendix F, that the higher-frequency contributions to the response are more highly damped than the lower-frequency contributions for the case of stiffness-proportional damping. The ratio of the damping coefficient to the critical value of each contribution to the response is proportional to the frequency of that contribution.

2.5.4 Solution of Equations of Motion

Equation (2-18) is solved for $\{\ddot{z}\}$ and the vectors $\{\ddot{z}\}$ and $\{\dot{z}\}$ are numerically integrated to obtain $\{\dot{z}\}$ and $\{z\}$ at the next time interval. A fixed-interval Runge-Kutta numerical-integration routine was used for this purpose.

When $\ell_n > \ell_c$, all of the flexible displacements and velocities are known (see E51 and E10). However when the distance between Node n and the ABB is less than ℓ_c ($\ell_n < \ell_c$), the coordinates of node n $\{q_n\}$ and $\{\dot{q}_n\}$ are not among the integrated variables since they were eliminated by the reduction procedure discussed in Section 2.5.2. In this case the motion of node n is

computed as a function of the integrated variables by using (G1) - (G3) of Appendix G.

As the beam expands, whenever the lowest node, node n, reaches the elevation ℓ_c (see Fig. 2.2), the elements of $\{q_n\}$ become independent coordinates, and the number of equations increase by two. This change is accomplished in the program by re-starting the integration procedure. Equations (G1) and (G2) are used to obtain the initial conditions for the coordinates of node n.

Appendix G also contains the equations for supplementary results that are printed and plotted by the computer program. These results include the displacements of nodes relative to axes fixed in the orbiter ((G4) and (G5)), and the motion of beam nodes before they emerge from the ABB (which is set equal to the motion of the ABB -(see (G6) and (G7)). In addition, equations are provided for the torque at the root of the beam (see (G8)). Finally, an equation is given for the axial load in the beam (Eq. (G9)). This load is used in (B10) which, in turn, is used in the stiffness matrix coefficients, (B2) - (B9) when the option to incorporate its influence on [K] is selected by the program user. Otherwise, the axial load is set to zero in the stiffness matrix.

Several checks were made on the equations of motion and the computer program. These include

- Re-derivation using a different approach
- Comparison of subroutine outputs with hand calculations
- Symmetry checks when symmetric mass and loads data were used and the initial conditions were symmetric
- A comparison of the results when the geometry was not permitted to vary with results of the same problem solved by direct numerical integration (Rigid Format 9) in NASTRAN.
- The solution of the equations, including the variable-geometry effects, was checked at one time point by performing these operations in NASTRAN. Variable geometry effects at this time point were incorporated as input data using DMI cards, and the equations were gen-

erated to obtain the acceleration vector by altering Rigid-Format 9 with DMAP instructions.

All checks were successfully completed.

2.6 Control System

A control system was incorporated into the program in order to enable studies into the influence of controls on the structural dynamics of variable-geometry systems. The control system model is a simple approximation to the orbiter vernier attitude-control system. As in the actual control system, thruster levels are 25 lbs, and the thrusters are located and directed in accordance with the specifications on the orbiter (Ref. 15). However, the thruster firing logic has been simplified. Specific thrusters have been selected to induce specific rotations about each axis; e.g., if an upward pitch motion is desired, the two forward thrusters would always fire. To simplify the model, if the same thruster is needed for two corrections at the same time, say positive pitch and positive roll, the program will apply the loads corresponding to the two corrections simultaneously. Consequently, the load for that thruster is doubled. In a real control system, the loads would be applied sequentially; however, the total impulse would be very nearly the same as for the model. Another assumption is that certain thrusters have been assigned to fire for shorter times than others during a maneuver; however, the model has been simplified by applying reduced loads corresponding to these thrusters, so that all thrusters fire for the same length of time during the maneuver. The reduced load compensates for the increased firing time so that the total impulse is correct.

Thrusters are switched on and off in accordance with the attitude misalignment of the orbiter relative to a desired pointing direction and the rate-of-change of this quantity. The control law is illustrated in Fig. 2.7 for the jth axis, where j=1,2,3 for roll, pitch, and yaw, respectively. The coordinates are the attitude error e_j, and its rate $\dot{e}_j$. The term e_j is equal to the shuttle angle about axis j, $\theta_{100,j}$, minus the commanded value of this angle. In this study, the commanded values were set to zero; therefore, $e_j = \theta_{100,j}$. In regions 1 and 2 of Fig. 2.7, a positive torque is applied, in regions 3 and 4 a negative torque is applied, and in regions 5 and 6, the dead band, a zero torque is applied. The regions are separated by parabolic switching curves (A,B,C, and D) which have predetermined curvatures that are based on the rigid-body angular accelerations that are induced by the thrusters.

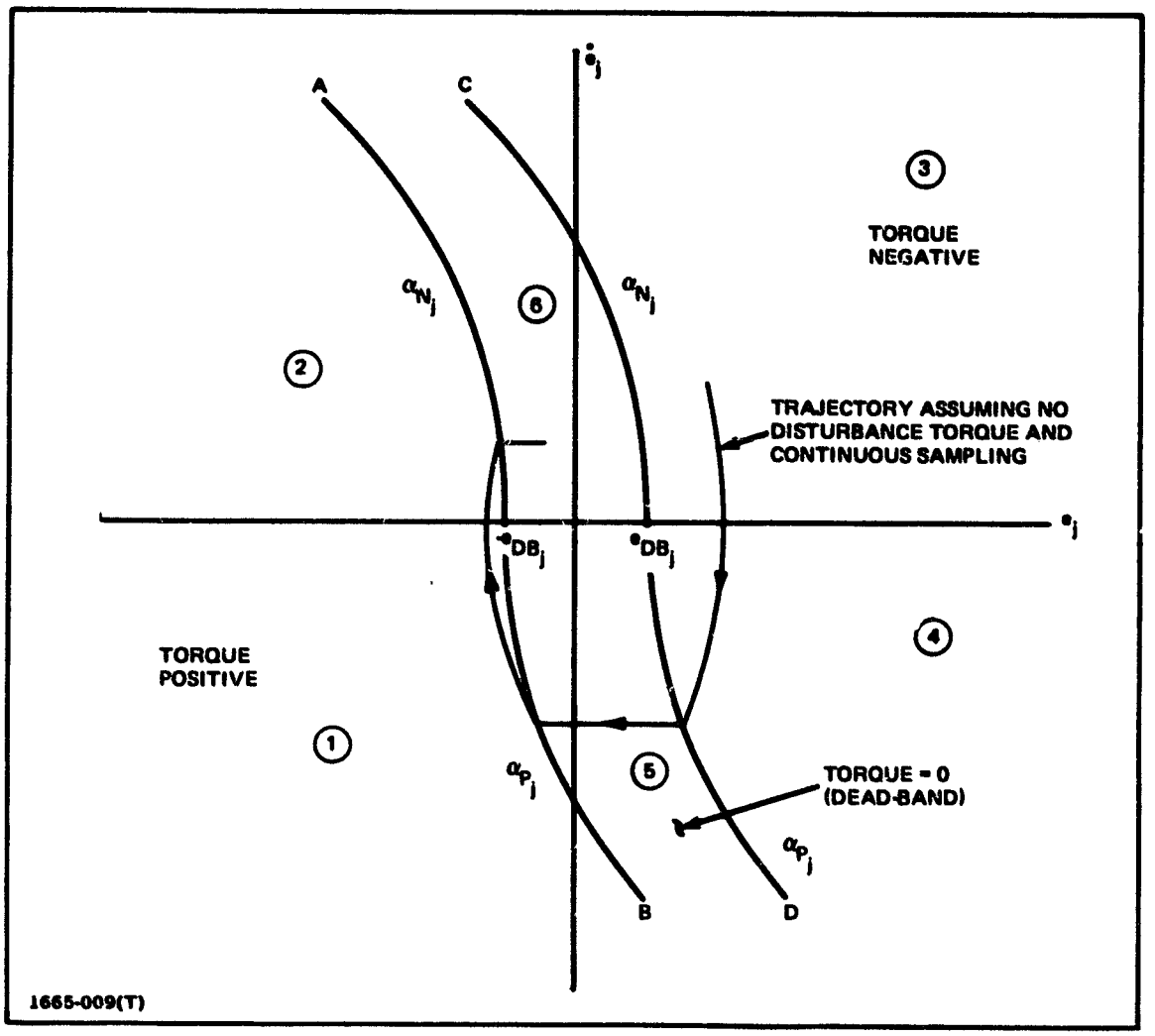

Fig. 2.7 Assumed Control Law

If there are no disturbance torques, the trajectory of the motion in the error phase plane is as shown in Fig. 2.7; the trajectories are a sequence of parabolic curves during thrusting and horizontal lines corresponding to constant angular-velocity cruises across the dead-band region. As indicated, the trajectory spirals into the origin. Actually, the trajectory will reach a limit-cycle for small errors and error rates because the thruster-firing decisions are not made continuously, but at specific intervals, every τ seconds. Thus, the sample time τ is the minimum time that a thruster can be on or off.

The same control system is employed for the beam relocation problem. Control-system details are presented in Appendix H.

2.7 Modes That Vary with Geometry

For many variable-geometry structures problems, direct numerical integration would not be practical because of the number of coordinates required to represent the structure. This is especially true of the more complex systems discussed in Appendix A. Consequently, a method was explored to reduce the coordinates by employing modes of vibration that vary with the geometry.

2.7.1 General Procedure

It is assumed that the number of modes used in the solution is r. Ideally, at each instant in time, the modes would satisfy the following equation:

$$\omega_i^2 [M]\{\varphi_i\} = [K]\{\varphi_i\} \; ; \; i = 1, 2, \ldots, r \qquad (2\text{-}20)$$

where the mass and stiffness matrices are those of (2-18). These matrices vary with the structural geometry. The modes are normalized so that the modal mass is unity for each mode; i.e.,

$$\{\varphi_i\}^T [M]\{\varphi_i\} = 1 \qquad i = 1, 2, \ldots, r \qquad (2\text{-}21)$$

The following transformation to modal coordinates is employed:

$$\{y\} = [\varphi]\{\xi\} \qquad (2\text{-}22)$$

where the columns of $[\phi]$ are the mode shapes $\{\phi_i\}$, From (2-22),

$$\{\dot{y}\} = [\varphi]\{\dot{\xi}\} + [\dot{\varphi}]\{\xi\}$$

$$\{\ddot{y}\} = [\varphi]\{\ddot{\xi}\} + 2[\dot{\varphi}]\{\dot{\xi}\} + [\ddot{\varphi}]\{\xi\} \qquad (2\text{-}23)$$

In the current procedure it is assumed that the structure varies sufficiently slowly so that the boxed terms can be neglected. Equations (2-22) and (2-23) are substituted into (2-18) with [C] given by (2-19). The result is premultiplied by $[\phi]^T$ and orthognality is employed yielding

$$\ddot{\xi}_j = f_j' - \alpha \kappa_j \dot{\xi}_j - \kappa_j \xi_j \; ; \; j = 1, 2, \ldots, r \qquad (2\text{-}24)$$

where κ_j is the modal stiffness and is equal to ω_j^2, and

$$f_j' = \{\varphi_j\}^T(\{f\} - \{g\}) \qquad (2\text{-}25)$$

The terms $\alpha\kappa_j\dot{\xi}_j$ could be replaced by modal damping, if desired.

In practice, the $\{\phi_i\}$'s and κ_i 's are computed at intervals of configuration geometry. Between these intervals, the values of $\{\phi_i\}$ and κ_i are obtained by linear interpolation. Orthogonatity is assumed between intervals so that the form of the equations is still (2-24).

For the beam fabrication problem an eigenvalue routine was introduced into the program and modes were computed at predetermined beam lengths $\bar{L}_1$, $\bar{L}_2$, ... If at $\bar{L}_{i+1}$ a new node has emerged from the ABB, it is not present in the modal vectors at $\bar{L}_i$. For the purpose of interpolation, the modal displacement of this node is set equal to the modal displacement of the ABB (i.e. of node 50) as determined by (G6). In order to improve the accuracy of the interpolated modes in the region where new nodes emerge, the set of the $\bar{L}_i$'s should include those lengths that correspond to the emergence of new nodes.

The details concerned with the emergence of new nodes during the variable-mode analysis were not programmed. The results that will be discussed in Section 2.8.7 were obtained for time spans during which no new node emerged.

2.7.2 Initial Conditions

The initial conditions in modal coordinates are obtained by premultiplying (2-22) and (2-23) by $[\phi]^T[M]$ and using orthogonality and (2-21). The results are

$$\{\xi\} = [\phi]^T[M]\{z\} \tag{2-26}$$

$$\{\dot{\xi}\} = [\phi]^T[M]\{\dot{z}\} \tag{2-27}$$

It can be shown that this procedure provides a best-fit solution to the initial conditions in a least-square error sense where the error function is weighted by the mass matrix; i.e. $\{\xi\}$ as obtained by (2-26) minimizes the function

$$E = \{e\}^T[M]\{e\} \tag{2-28}$$

where

$$\{e\} = \{z\} - [\phi]\{\xi\} \tag{2-29}$$

2.7.3 Advantages of the Procedure

An important advantage that is gained by using modal analysis is that the variable-geometry derivation can be written with the rigidity constraints disregarded. If the modes are obtained with the use of a finite-element structural-analysis program such as NASTRAN, the constraints will already be embodied in the modes. Another advantage is that by eliminating the high-frequency modes, the high-frequency component of the solution is no longer present when a node is close to the ABB, i.e., when $\ell_n < \ell_c$. Consequently, the modal procedure avoids the need to eliminate the coordinates of node n when $\ell_n < \ell_c$. These advantages significantly simplify the derivation and formulation.

Finally, there is the potential of reducing computer time. The procedure not only reduces the size of the problem, it also uncouples the equations of motion. In addition, deletion of the high-frequency modes, enables the use of a larger numerical-integration step size. These factors must be traded against the time required to compute the modes; however, as indicated in Section 2.8.7, for the beam-fabrication problem a savings of 85% of the computer time was effected with no appreciable loss in accuracy.

2.7.4 Additional Considerations

It is necessary to track the modes as the structure varies so that the interpolation will always take place between similar modes. This cannot be done simply by ordering the modes in accordance with the order of their frequencies. For example, when the beam begins to emerge from the ABB, the mode with the fundamental fore-and-aft beam bending motion is the 19th mode of the structure. As the beam grows, the frequency of this mode drops and it eventually becomes the seventh, or lowest, flexible mode. Evidently, it is not acceptable to simply interpolate between the 19th mode before incrementing the geometry, and the 19th mode after incrementing the geometry. In the present study, the tracking took place manually; i.e., the computer run was done in two steps. First the modes were computed and examined at the desired increments of beam length. Then, the mode-tracking information was supplied to the program as input data to the second step. It appears possible to automate this procedure by comparing modes for the different structural increments, using either a root-mean-square error method, an inner product weighted by the mass matrix*, or some other procedure to provide a basis for comparison.

Since the sign of the mode is not uniquely determined by the normalization procedure (2-21), it is necessary to account for the fact that the mode computed by the eigenvalue routine may suddenly change sign as the structure is incremented. This actually occurred in the numerical problems addressed in this study.

Another problem that must be avoided is that when the frequencies of two modes cross, the mode shapes become coupled; e.g., a solar-panel mode could contain significant beam motion and a beam mode could contain significant solar-panel motion when their frequencies become equal as the geometry is varied. If these modes are used to derive interpolated modes, the numerical-integration results will be in error since the theory assumes that the modes vary gradually. This problem can be avoided simply by deleting the problem set of modes and incrementing the geometry slightly to obtain a replacement set of modes.

---

* If $\{\bar{\phi}_j\}$ is a mode with the geometry incremented, and $\{\phi_i\}$ is a mode prior to incrementing the geometry, then the product $\{\bar{\phi}_j\}^T[M]\{\phi_i\}$ would be formed for each mode $\{\phi_i\}$. Because of orthogonality, this product would be close to zero for all values of $\{\phi_i\}$ except the one that corresponds to $\{\bar{\phi}_j\}$.

A similar problem arises with the rigid-body modes. Since they are all of equal frequency (actually zero frequency), the eigenvalue routine may compute modes with very different amounts of coupling as the structure is varied. For example, a mode which is primarily aft translation may contain significant pitch-rotation after the structure is varied. This problem was resolved by computing the rigid-body modes from geometrical considerations, orthogonalizing them using the Gram-Schmidt procedure (Ref. 16)*, and then normalizing them in accordance with (2-21).

2.7.5 Comparison With Existing Procedure

As discussed in Section 1.2, Ref. 11 describes a method for using variable-modal analysis to solve flexible mechanism problems. The procedure of this report differs from that of Ref. 11 in that the modes are obtained by interpolation rather than through the use of the derivatives of the modes with respect to a geometric parameter. The interpolation procedure involves significantly less computation. On the other hand, the derivative procedure avoids the complexity of tracking the modes. Another significant difference is that in the current procedure the generalized stiffnesses and generalized masses** are also obtained by interpolation. Since it is unnecessary to perform matrix operations to compute these quantities and the left side of the equations of motion remains uncoupled, a further saving in computation time is achieved.

2.8 Numerical Results

Properties of the structure are presented in Appendix I. These include mass, stiffness, and geometry data. Kinematics data on beam fabrication is also provided.

---

* For the current application, the inner product and the norm used in the equations of the reference are defined as follows. The inner produce (x,y) of two vectors $\{x\}$ and $\{y\}$ is defined as $(x,y) = \{x\}^T [M] = \{y\}$ and the norm $||x||$ is defined by the relation $||x||^2 = \{x\}^T [M] \{x\}$.

** Actually, the modes are normalized to unit modal mass so that interpolation of generalized masses is not even necessary.

Several runs were made with and without the influence of the pulsating axial load on the stiffness matrix, and, except for the case discussed in Section 2.8.4, where the beam was expelled at an artificially rapid rate, this influence had no discernable effect on the response. Consequently, the other results that will be presented are for runs that did not include this effect. The inertia-load effects of the pulsing are, however, included in all of the runs.

2.8.1 Mode Shapes and Frequencies for Fixed-Geometry Structure

The mode shapes and frequencies of the free-free structure were computed by using NASTRAN for eleven different stages of beam construction with beams ranging from 0 to 199.5 m. Figures 2.8 to 2.15 show the first eight flexible beam modes for a configuration with a beam of 189 m. Fig. 2.16 shows the first flexible beam mode, fore and aft bending, for the free-free structure with three different beam lengths. The variation of the lower system frequencies with beam length is illustrated in Fig. 2.17. Since the orbiter is relatively massive, and the beam has symmetric cross-sectional properties; the frequencies of the fore and aft bending modes are nearly identical to the frequencies of the right and left bending modes.

The free-free system modes that primarily involve solar-panel motion are described in Table 2.1. Beam growth has almost no effect on these modes; e.g., the frequencies are the same, within four digits, for the case with the beam fully retracted as for the case where 199.5 meters of beam extends from the orbiter.

2.8.2. Fabrication of Seven Bays

In order to examine the vibration due to only variable geometry, several computer runs were made with no disturbances present other than beam growth. In one of these runs the dynamics of the structure was simulated by direct numerical integration during the fabrication of seven bays. The beam is initially 103.5 m long (69 bays) as indicated in Fig. 2.18 and grows to 114 m at the end of the run. Five nodes are present on the beam at t = 0; however after the first bay is fabricated the sixth beam node appears; thus, the study includes the

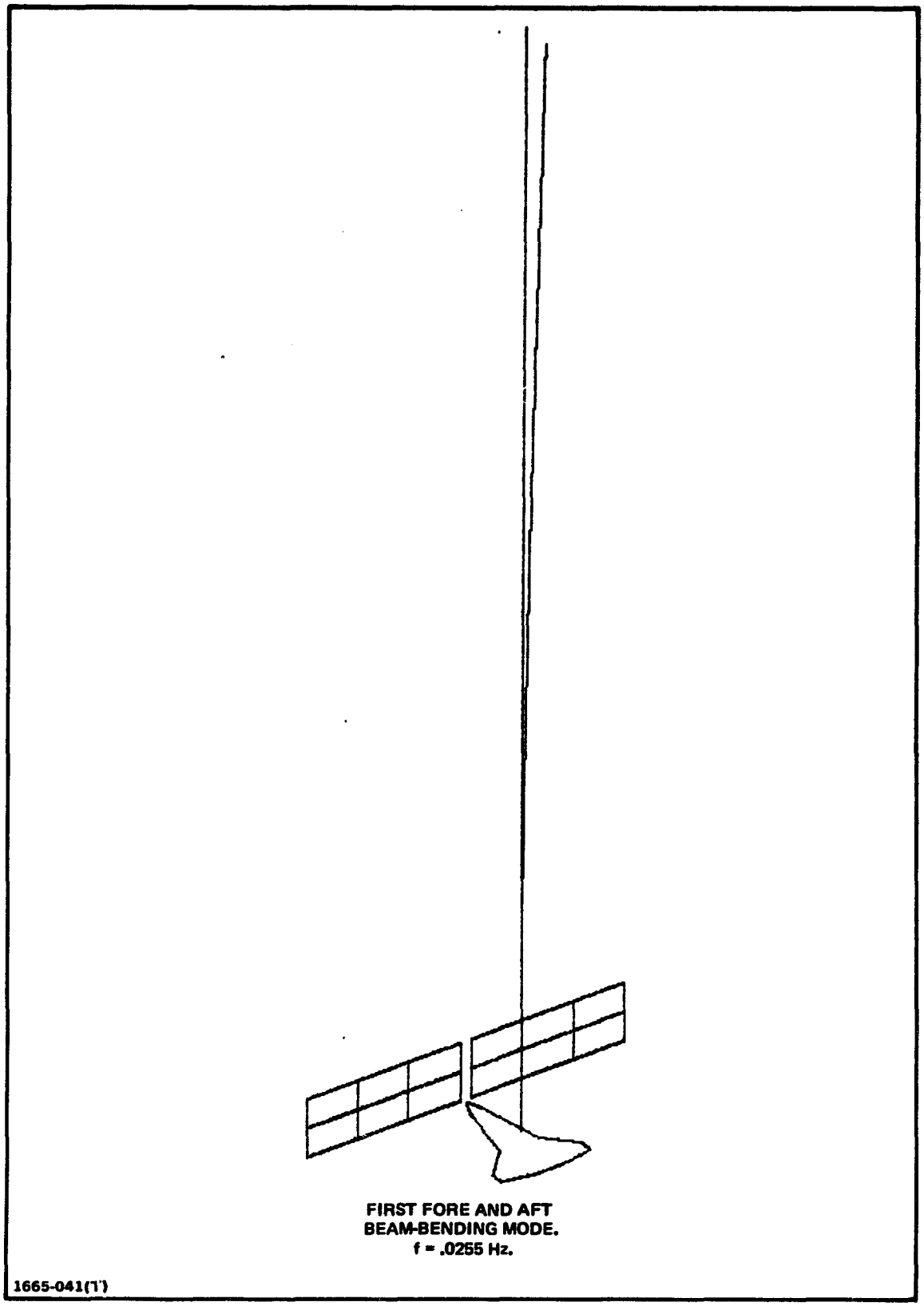

Fig. 2.8 First Flexible Mode for Beam-Fabrication Problem with 189 m Beam

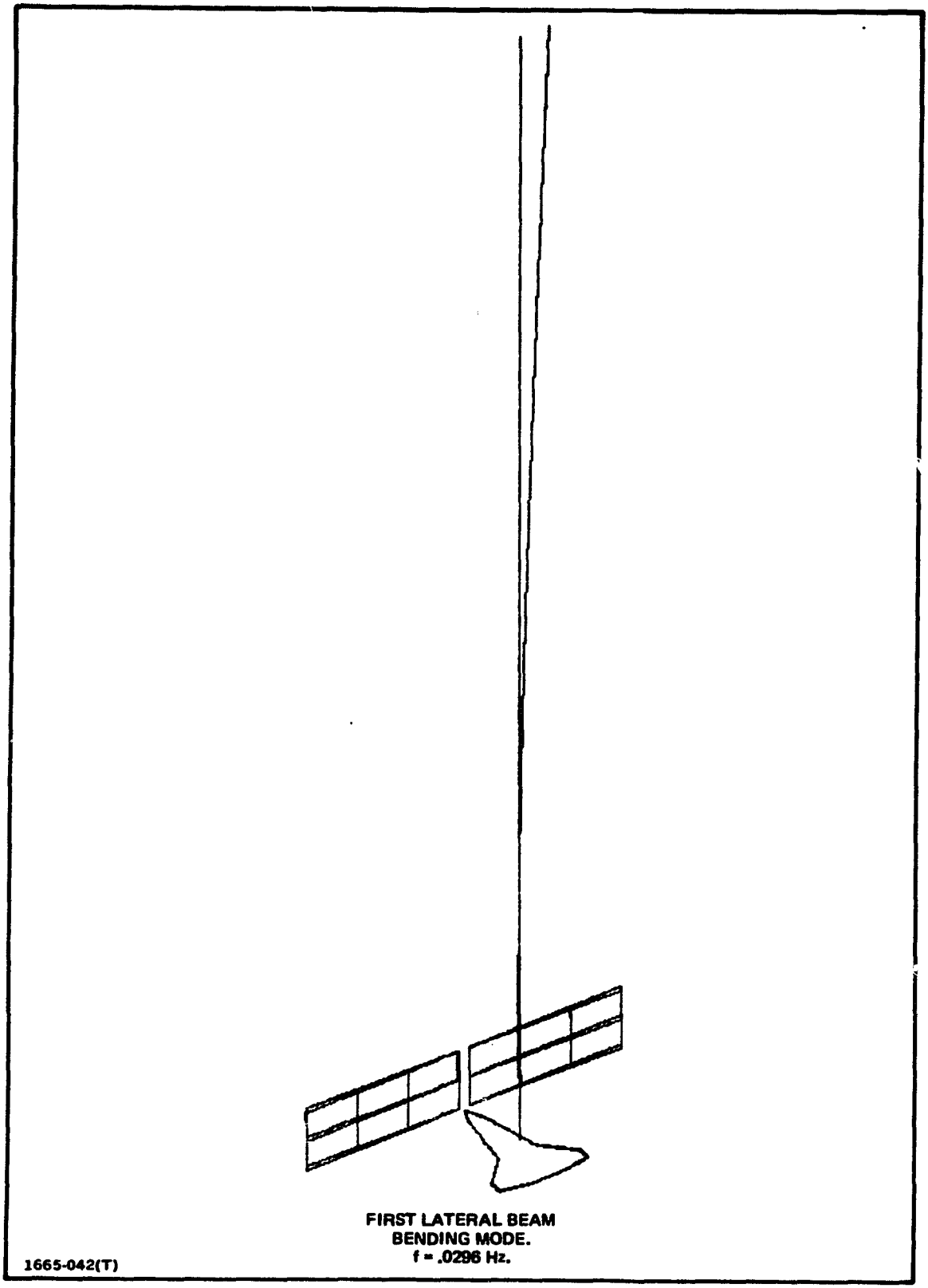

Fig. 2.9 Second Flexible Mode for Beam-Fabrication Problem with 189 m Beam

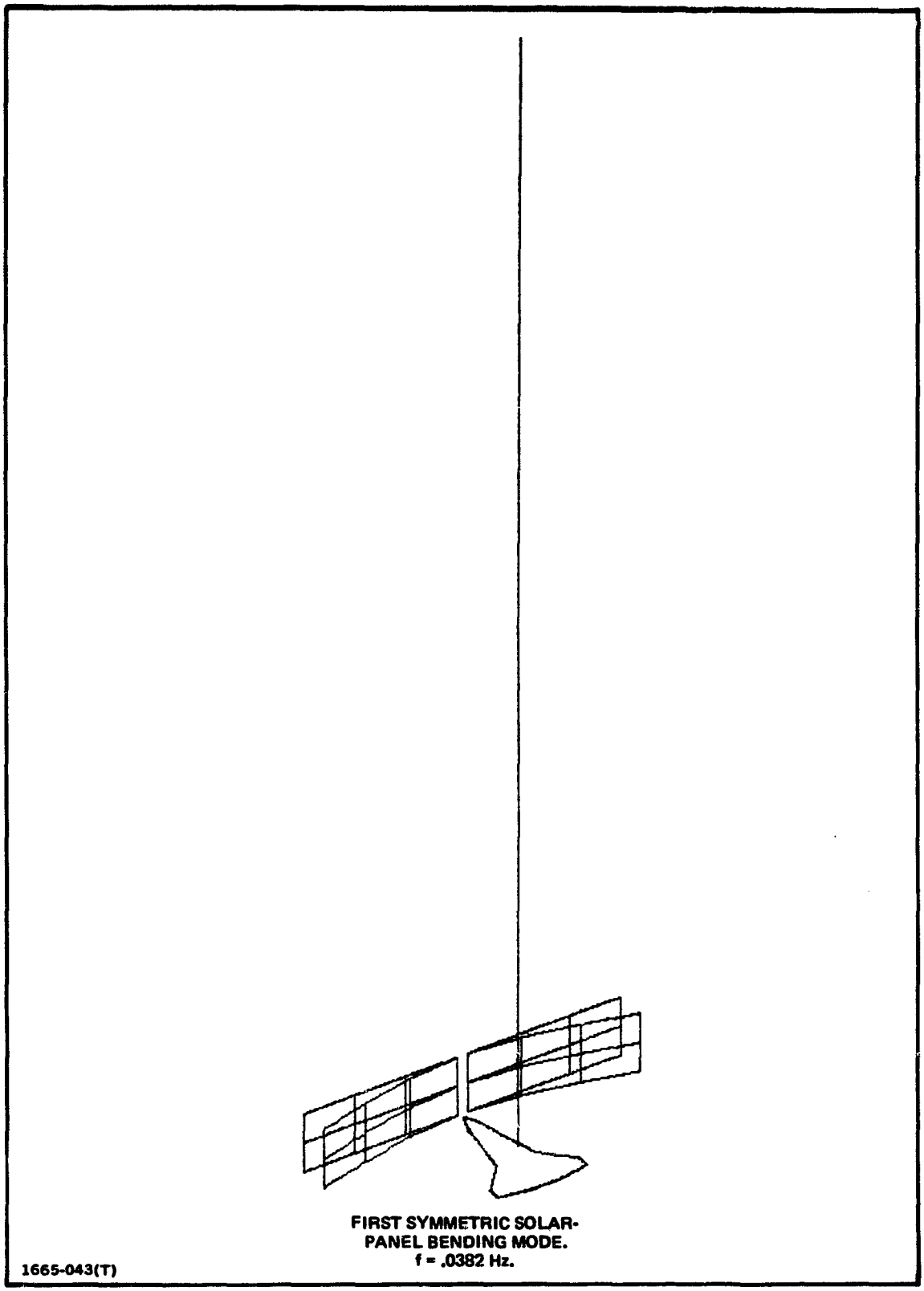

Fig. 2.10 Third Flexible Mode for Beam-Fabrication Problem with 189 m Beam

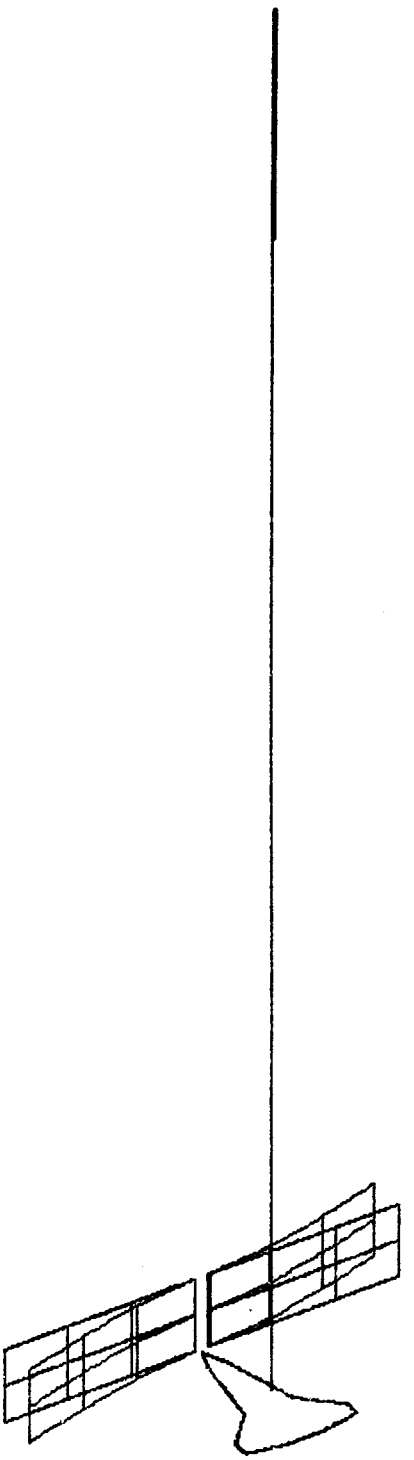

FIRST ANTISYMMETRIC SOLAR-
PANEL BENDING MODE.
f = .0389 Hz.

1665-044(T)

Fig. 2.11 Fourth Flexible Mode for Beam-Fabrication Problem with 189 m Beam

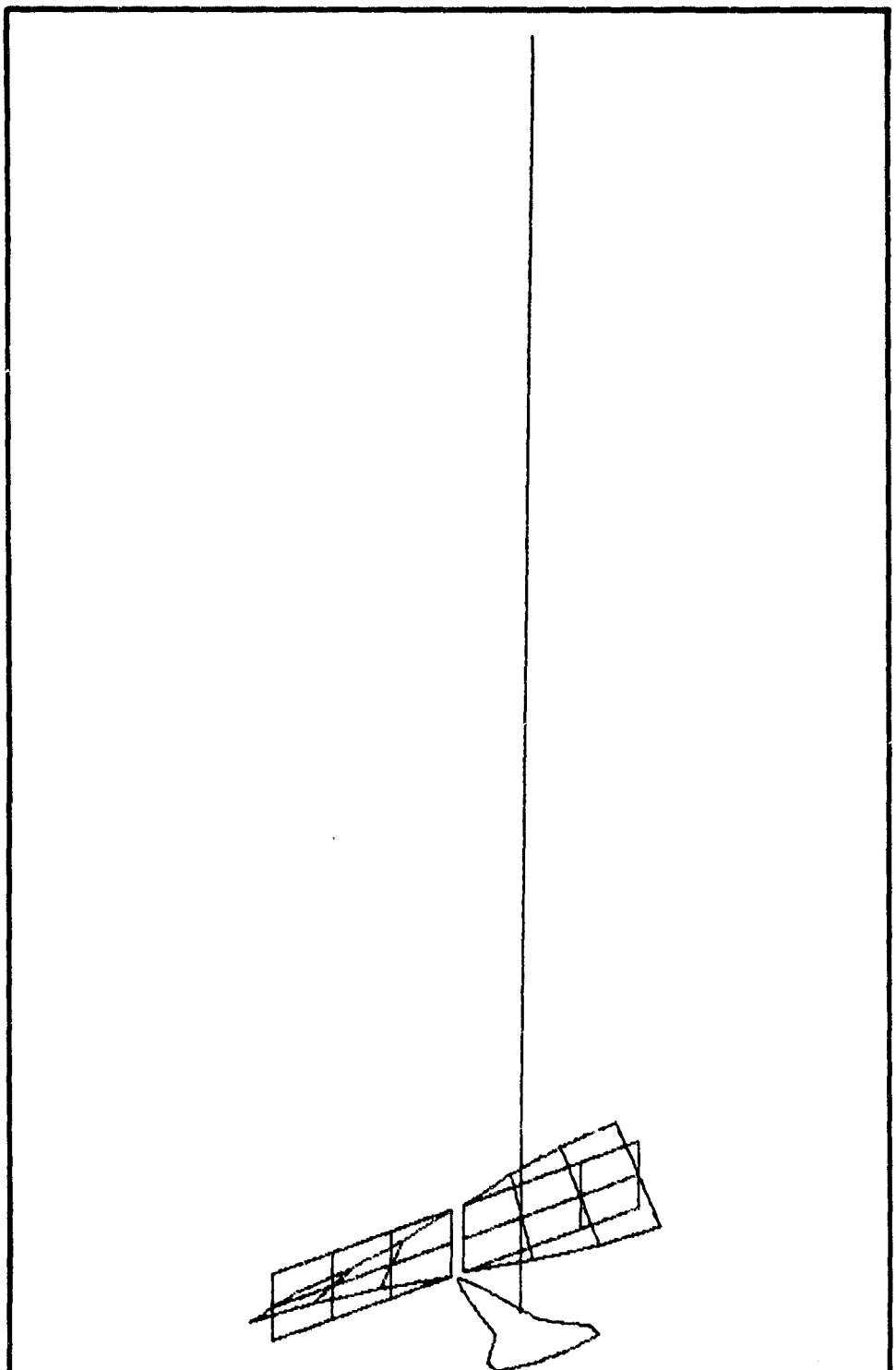

Fig. 2.12 Fifth Flexible Mode for Beam-Fabrication Problem with 189 m Beam

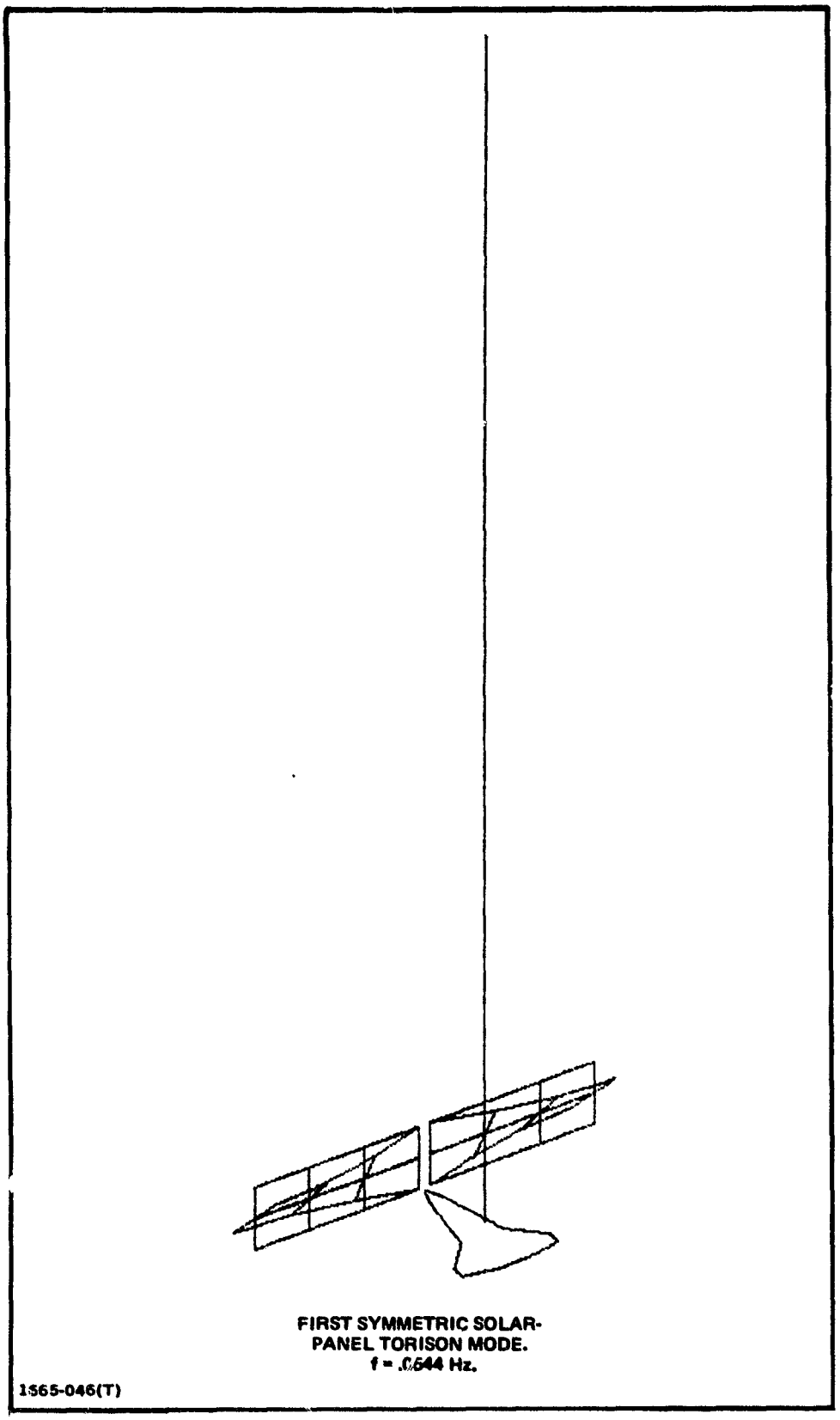

Fig. 2.13 Sixth Flexible Mode for Beam-Fabrication Problem with 189 m Beam

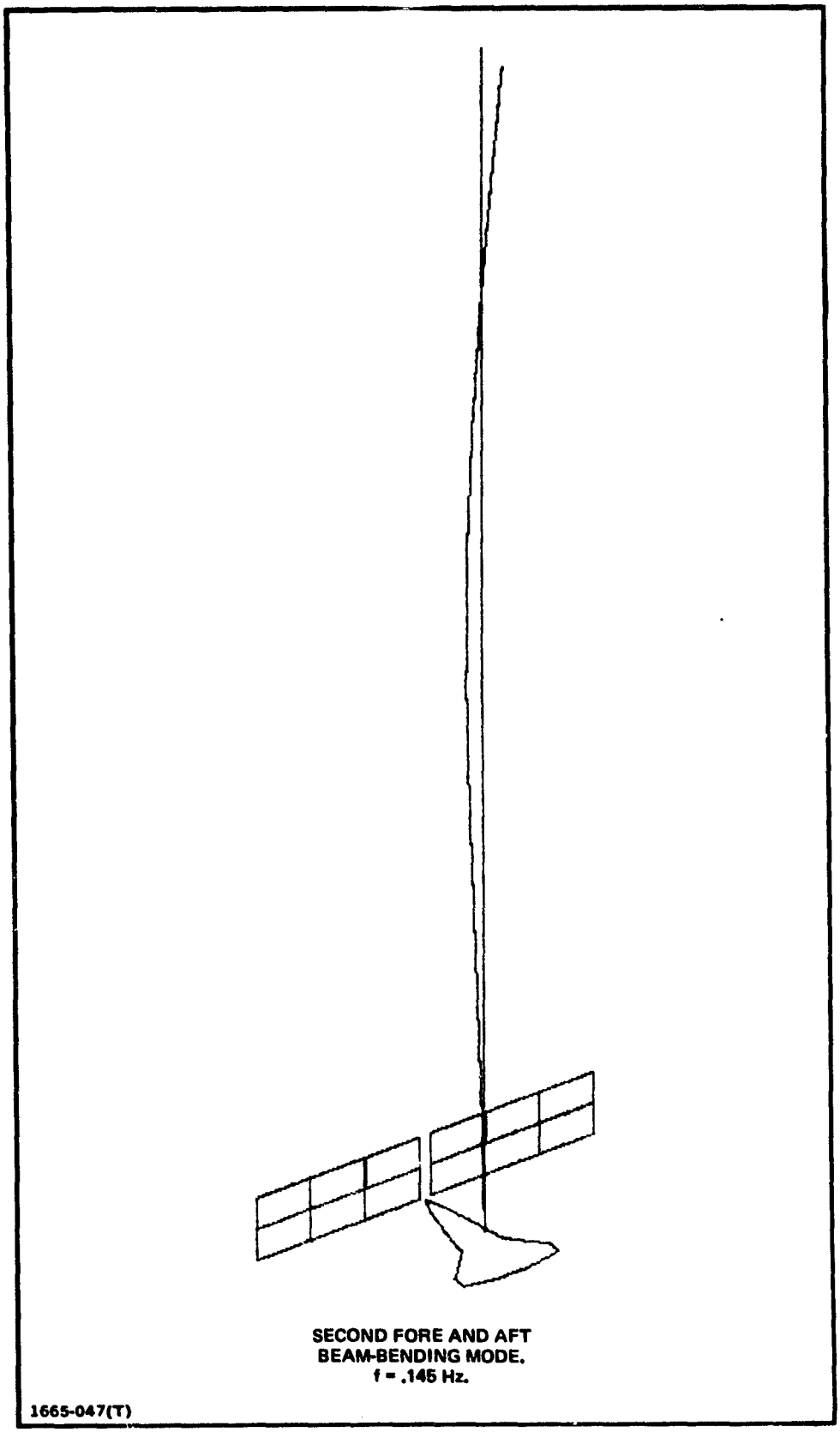

Fig. 2.14 Seventh Flexible Mode for Beam-Fabrication Problem with 189 m Beam

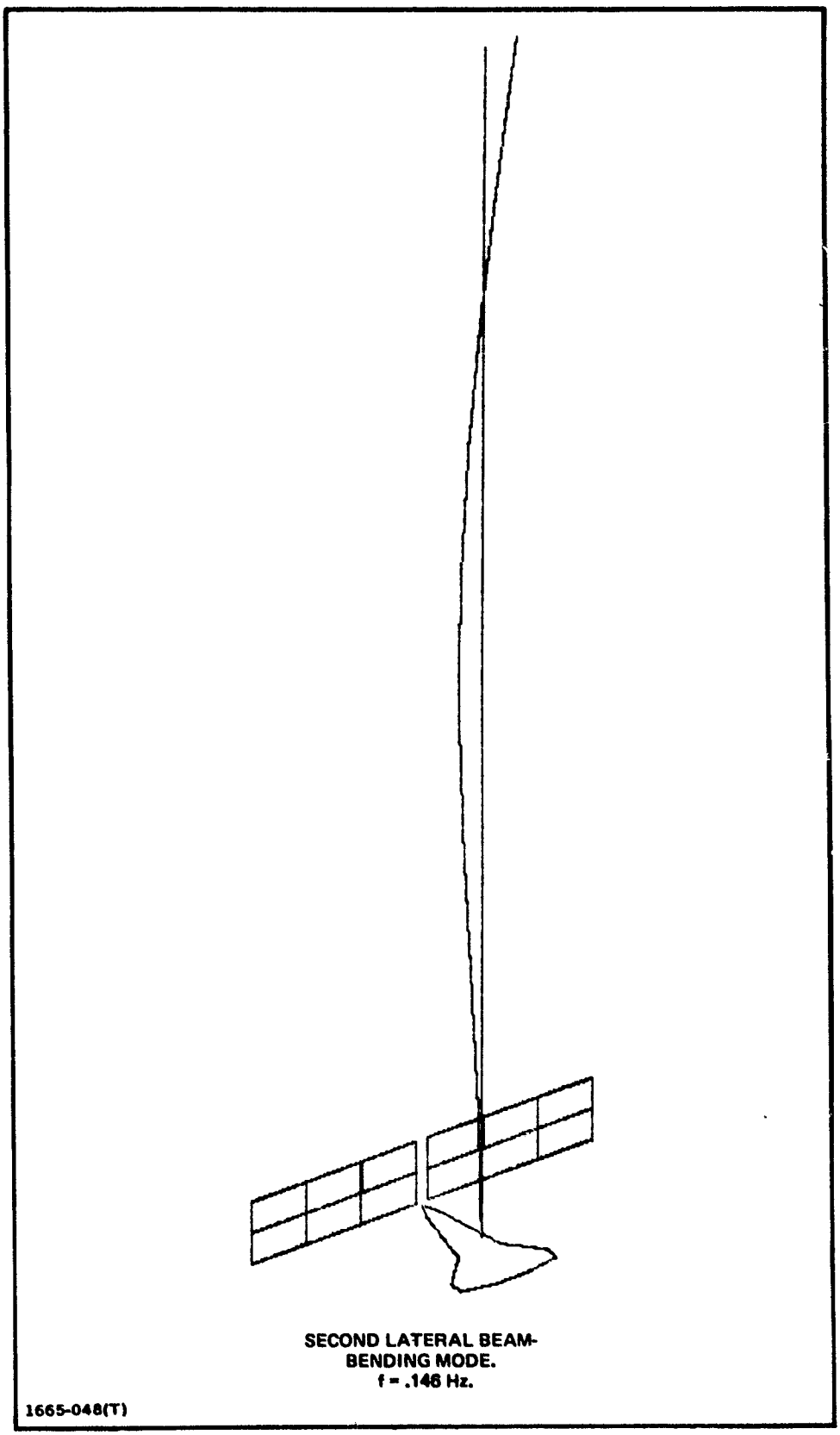

Fig. 2.15 Eighth Flexible Mode for Beam-Fabrication Problem with 189 m Beam

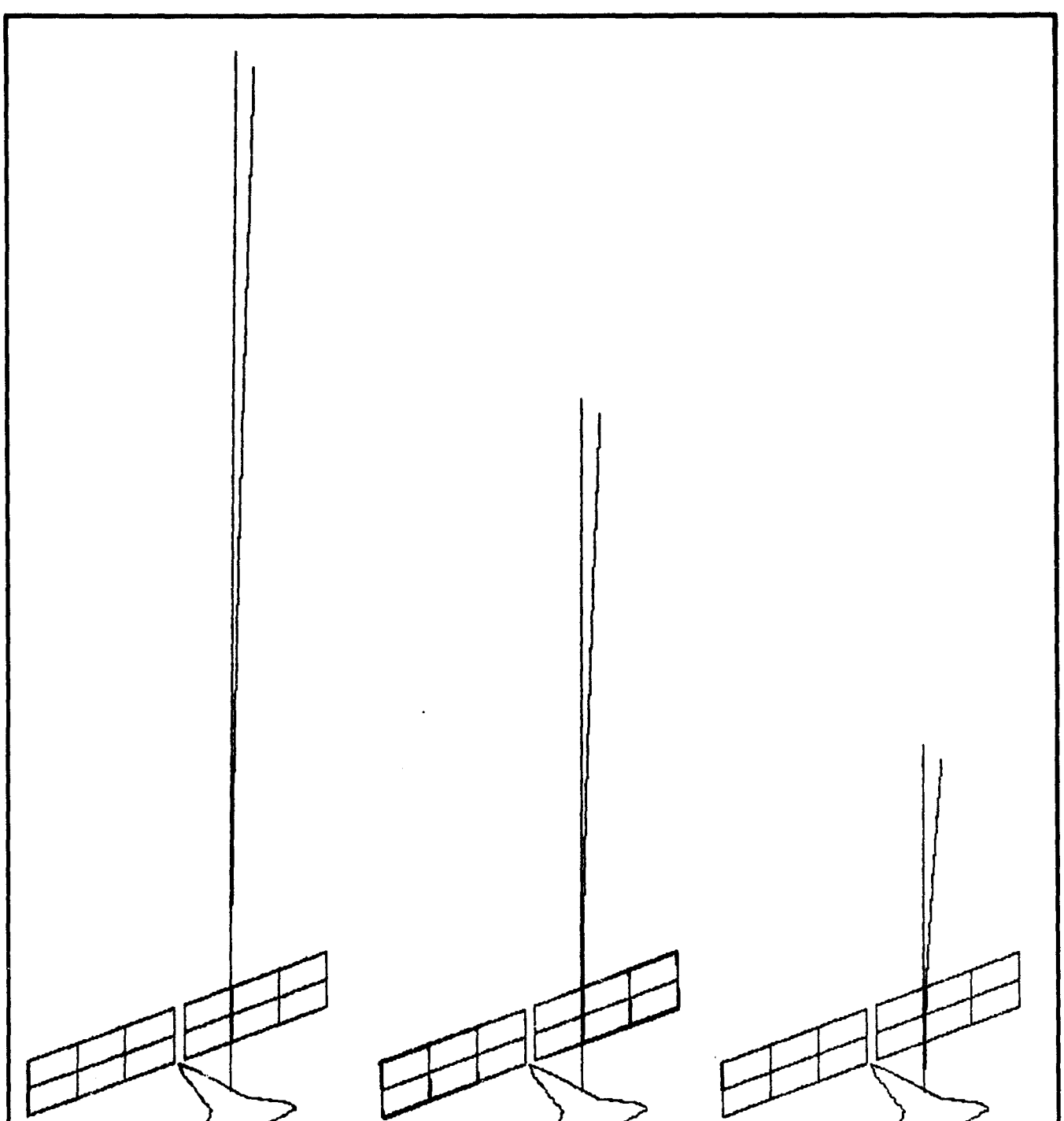

Fig. 2.16 Variation of First Beam Bending Mode Shape with Beam Length

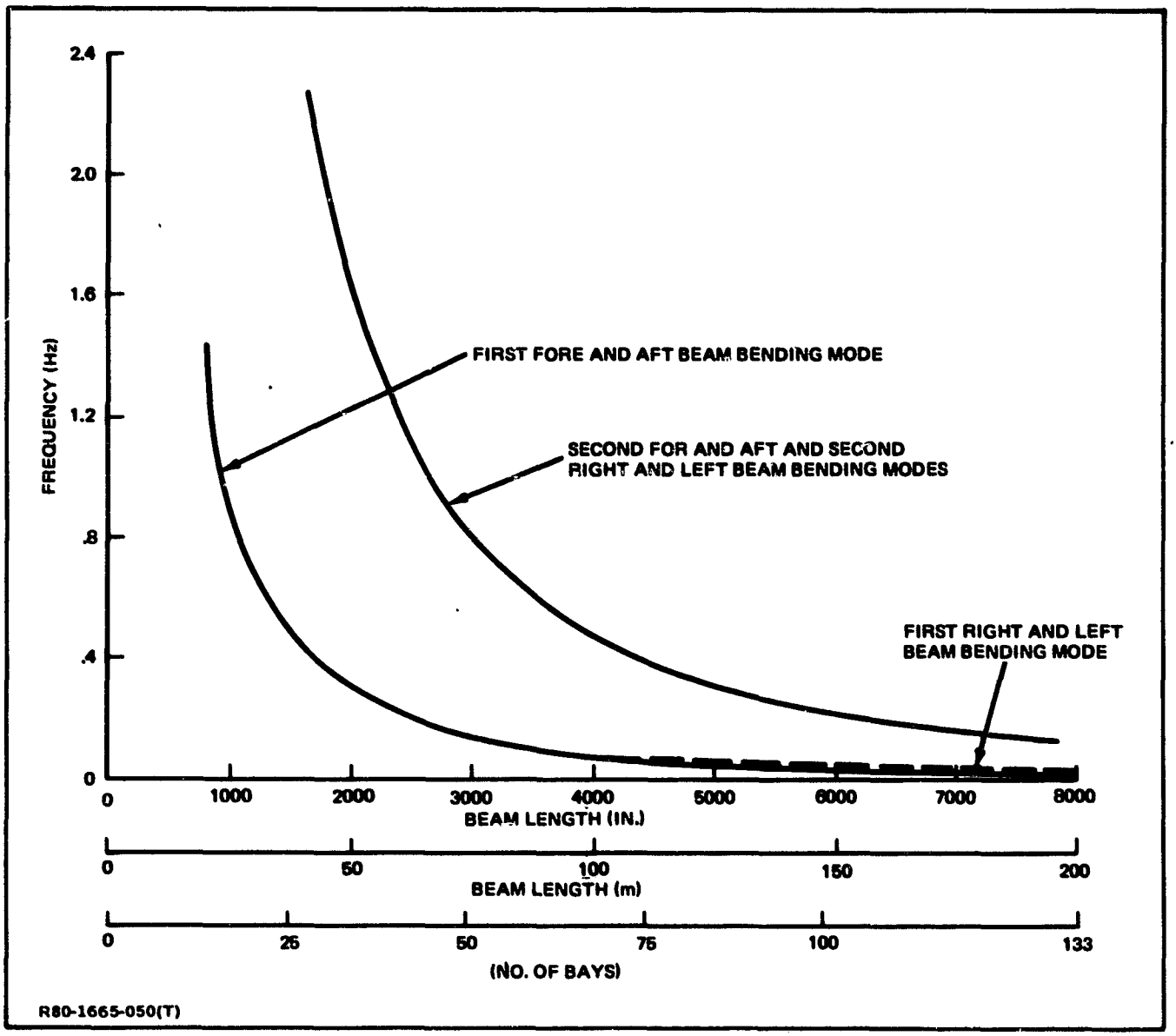

Fig. 2.17 Variation of Lower Vibration Frequencies with Beam Length for Free-Free System

TABLE 2.1 VIBRATION MODES THAT PRIMARILY INVOLVE SOLAR-PANEL BENDING

FREQUENCY (Hz)	DESCRIPTION OF SOLAR PANEL MOTION
.0382	FIRST SYMMETRIC BENDING MODE
.0389	FIRST ANTISYMMETRIC BENDING MODE
.0544	FIRST ANTISYMMETRIC TWISTING MODE
.0544	FIRST SYMMETRIC TWISTING MODE
.1485	SECOND ANTISYMMETRIC TWISTING MODE
.1485	SECOND SYMMETRIC TWISTING MODE
.2029	THIRD ANTISYMMETRIC TWISTING MODE
.2029	THIRD SYMMETRIC TWISTING MODE
.2149	SECOND ANTISYMMETRIC BENDING MODE
.2150	SECOND SYMMETRIC BENDING MODE
.5348	THIRD ANTISYMMETRIC BENDING MODE
.5349	THIRD SYMMETRIC BENDING MODE

R80-1665-138(T)

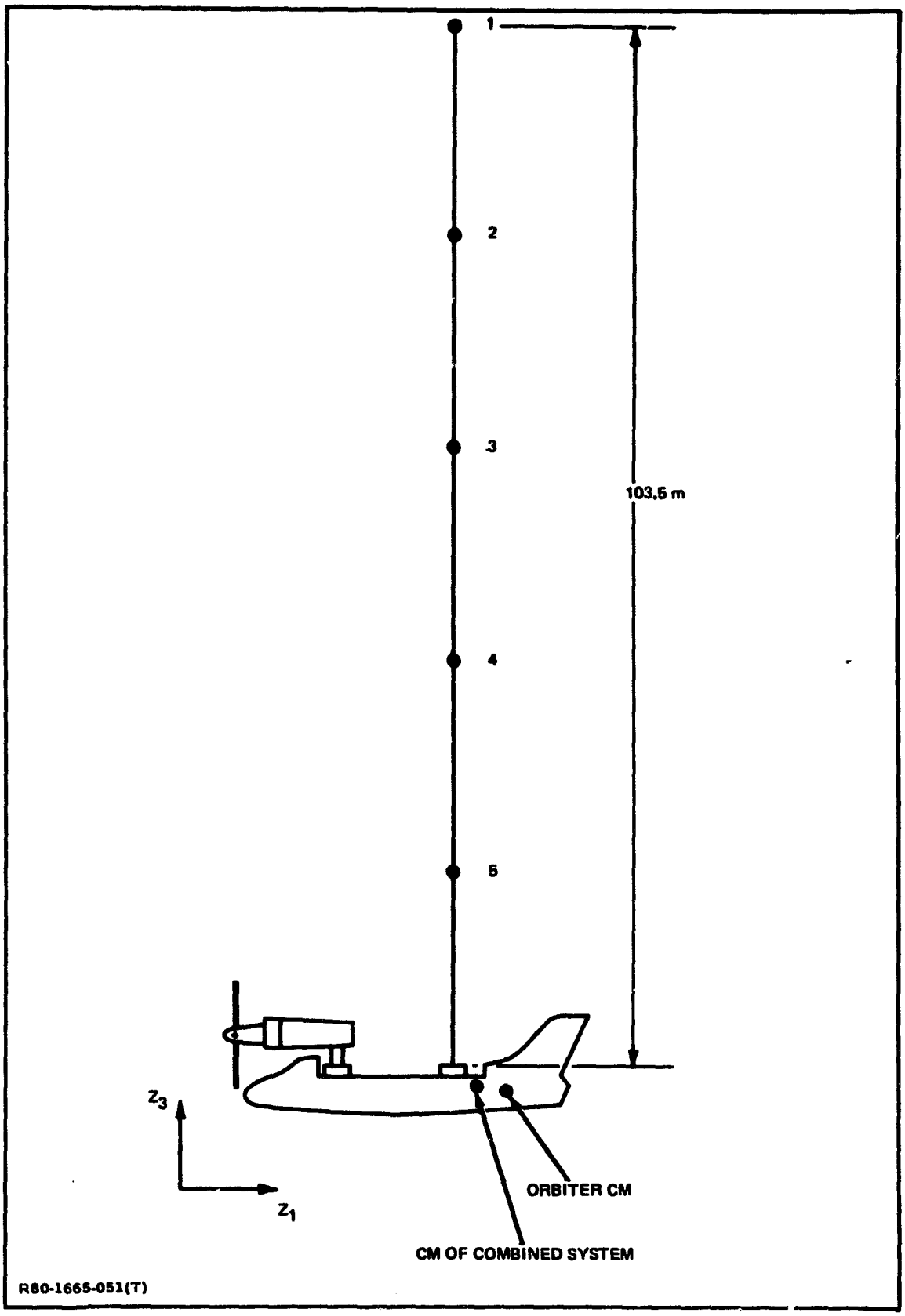

Fig. 2.18 Finite-Element Representation of Beam at Start of Seven-Bay Fabrication Run - Elevation View

influence of an emerging beam node. The history of the beam growth, shown in Fig. 2.19, is based on the performance of the Grumman ground-demonstration ABB.

When a module is first expelled ($\ddot{L} > 0$), the beam pushes down on the ABB. Since the total system cm is aft of the ABB, this causes the orbiter to pitch down slightly. As the expulsion of the module stops ($\ddot{L} < 0$), the beam pulls on the ABB, and the result is a braking effect on the pitching motion. The angular displacement of the orbiter is shown in Fig. 2.20. During the interim period, when the beam does not grow, the average angular motion of the system is zero since the total angular momentum must be equal to its initial value which is zero. The orbiter has cross products of inertia, and this mass coupling causes some small angular displacement in roll and yaw; however the amount is too small to be noticed in the curves.

The linear displacement of beam Node 1, the beam tip, is shown in Fig. 2.21. The result is mostly rigid-body motion, with some small superimposed vibration. Fig. 2.22 shows the vibration of the beam tip relative to axes fixed in the orbiter. Most of the response is at the first mode. The amplitude changes every time a beam-growth acceleration pulse occurs (see Fig. 2.19). The frequency of vibration varies from .078 Hz (at the beginning of the run) to .067 Hz (at the end of the run) in accordance with Fig. 2.17. A damping coefficient, α, of .01 was used. In accordance with Appendix F, the higher frequency modes are damped more than the lower frequency modes. The lateral vibration is very small. Since the lateral and fore-and-aft fundamental bending frequencies are nearly equal, some energy transfer, or beating, occurs between these response components.

Figure 2.23 shows the total fore-and-aft displacement and the pitch rotation of Node P_3, the tip of the left solar panel, and Fig. 2.24 shows the same quantities relative to axes fixed in the orbiter. As indicated by Fig. 2.25 which shows the response at the tip of the right solar panel, the motion of the solar panels is almost precisely symmetric.

The bending-moment components at the root of the beam are shown in Fig. 2.26. They are well within the 13,600 in-lb maximum allowable bending moment.

2.8.3 Average-Length Technique

The vector $-\{g\}$ that appears on the right side of the equations of motion

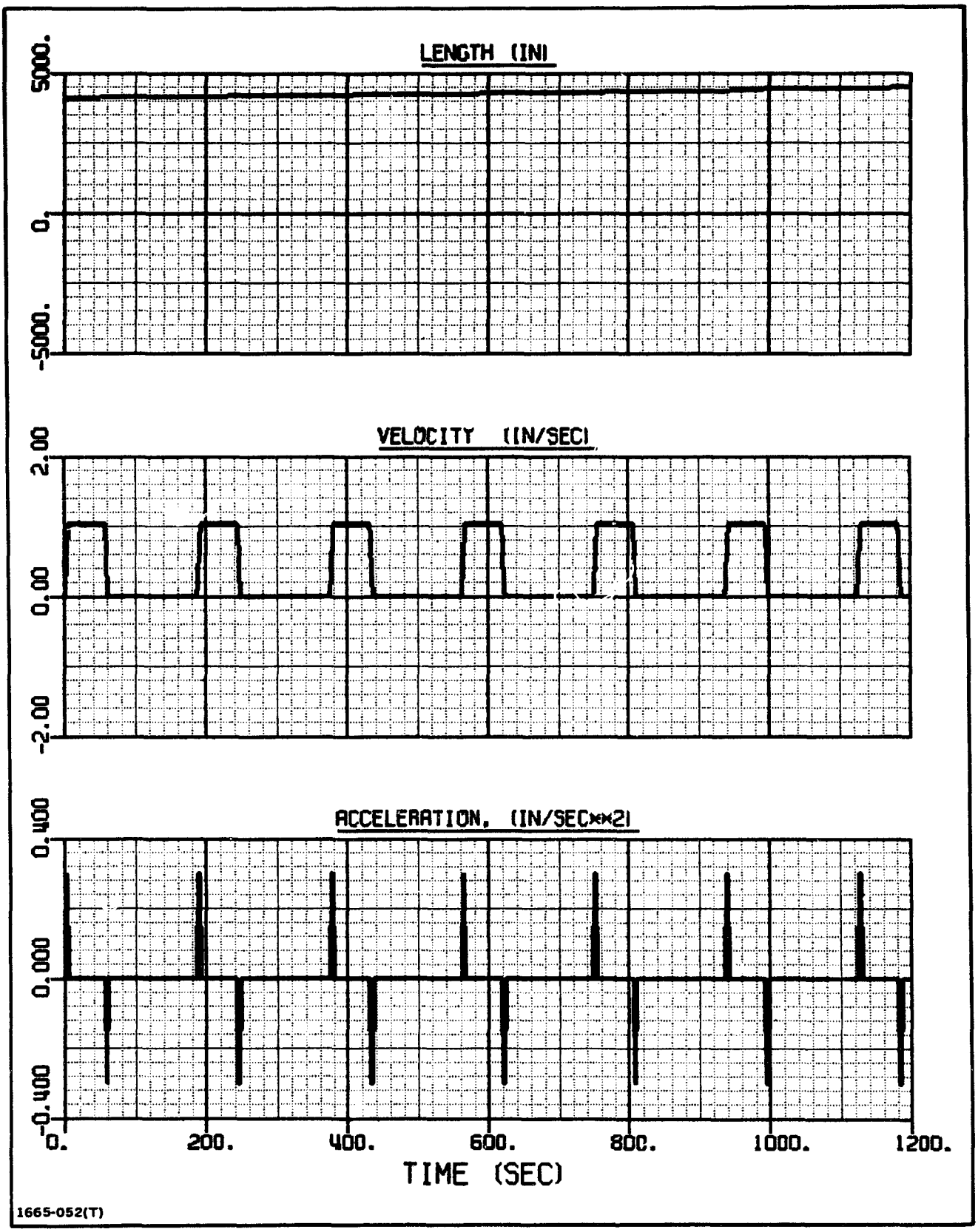

Fig. 2.19 Growth of Beam During Expulsion of Seven Bays.

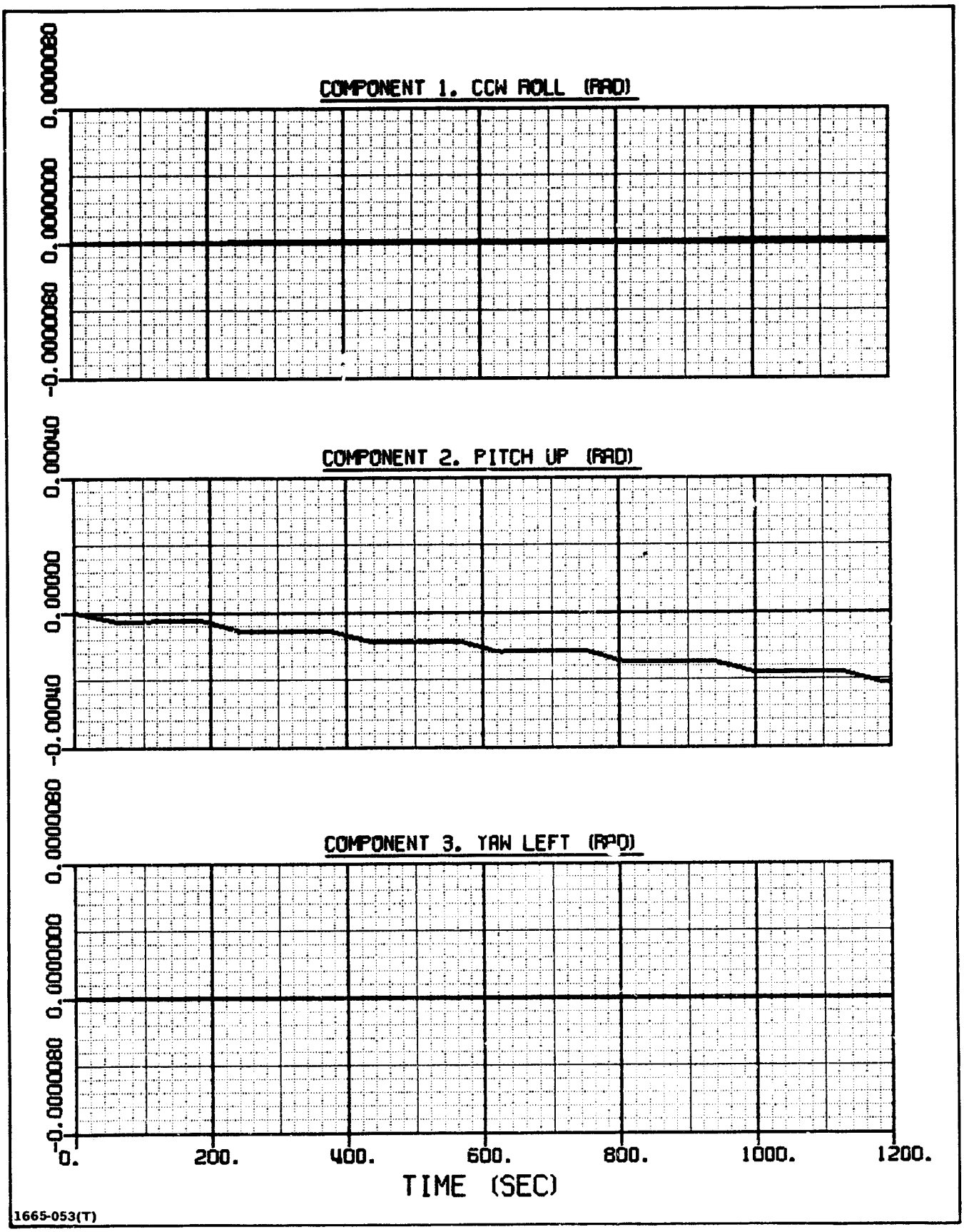

Fig. 2.20 Angular Displacement of Orbiter During Expulsion of Seven Bays.

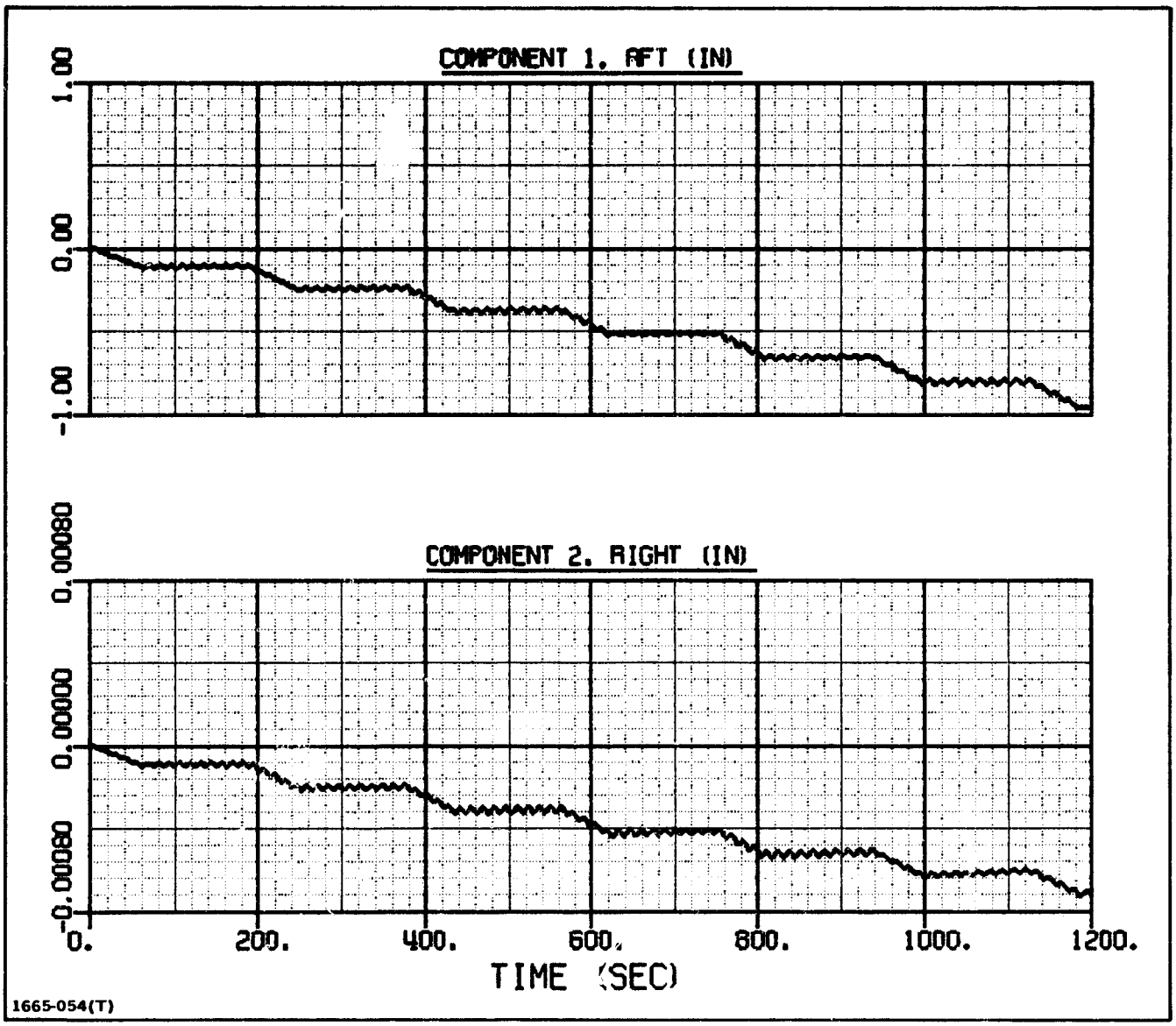

Fig. 2.21 Linear Displacement of Beam Tip, Node 1, During Expulsion of Seven Bays.

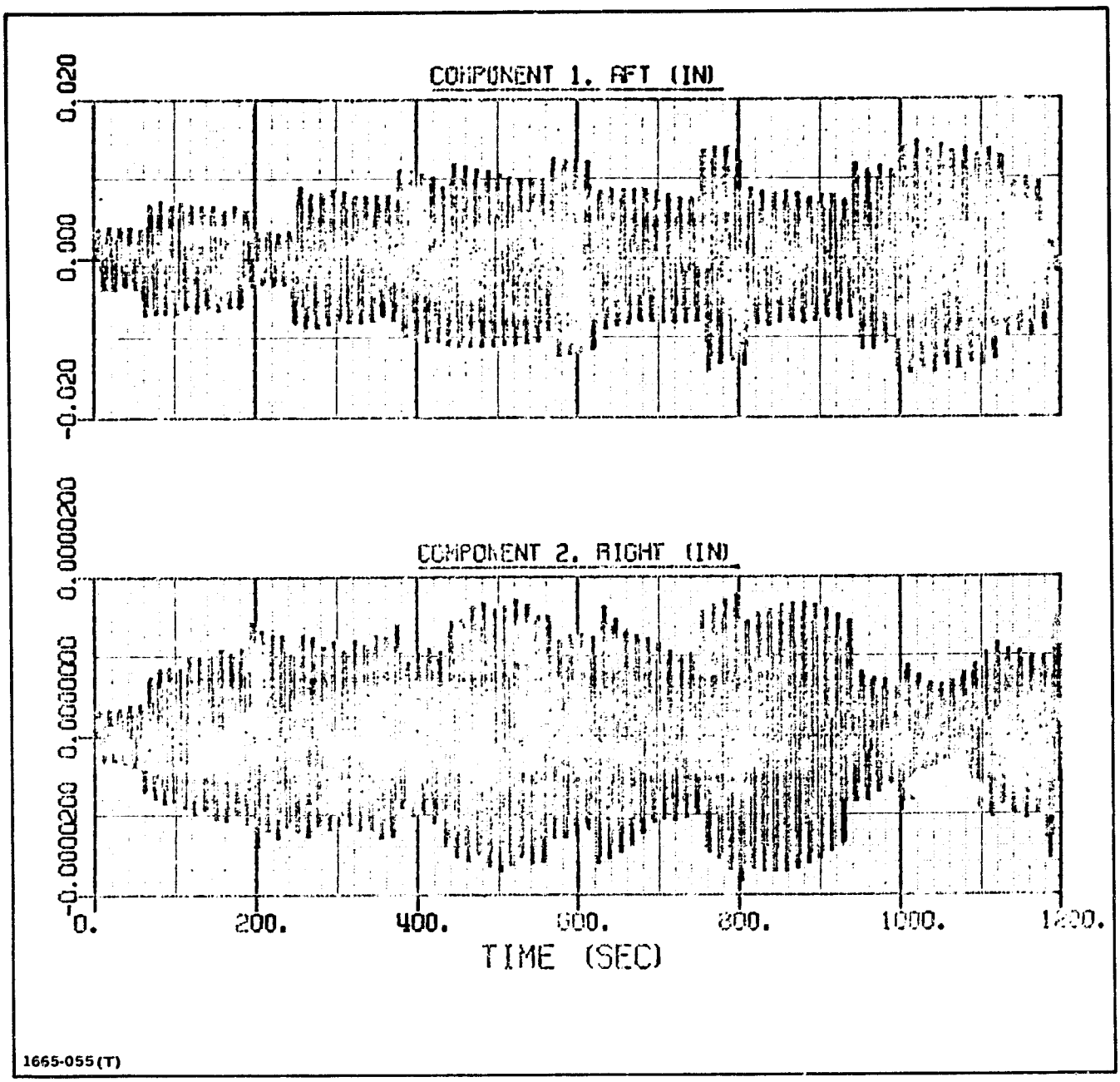

Fig. 2.22 Linear Displacement of Beam Tip, Node 1, Relative to Axes Fixed in Orbiter, During Expulsion of Seven Bays

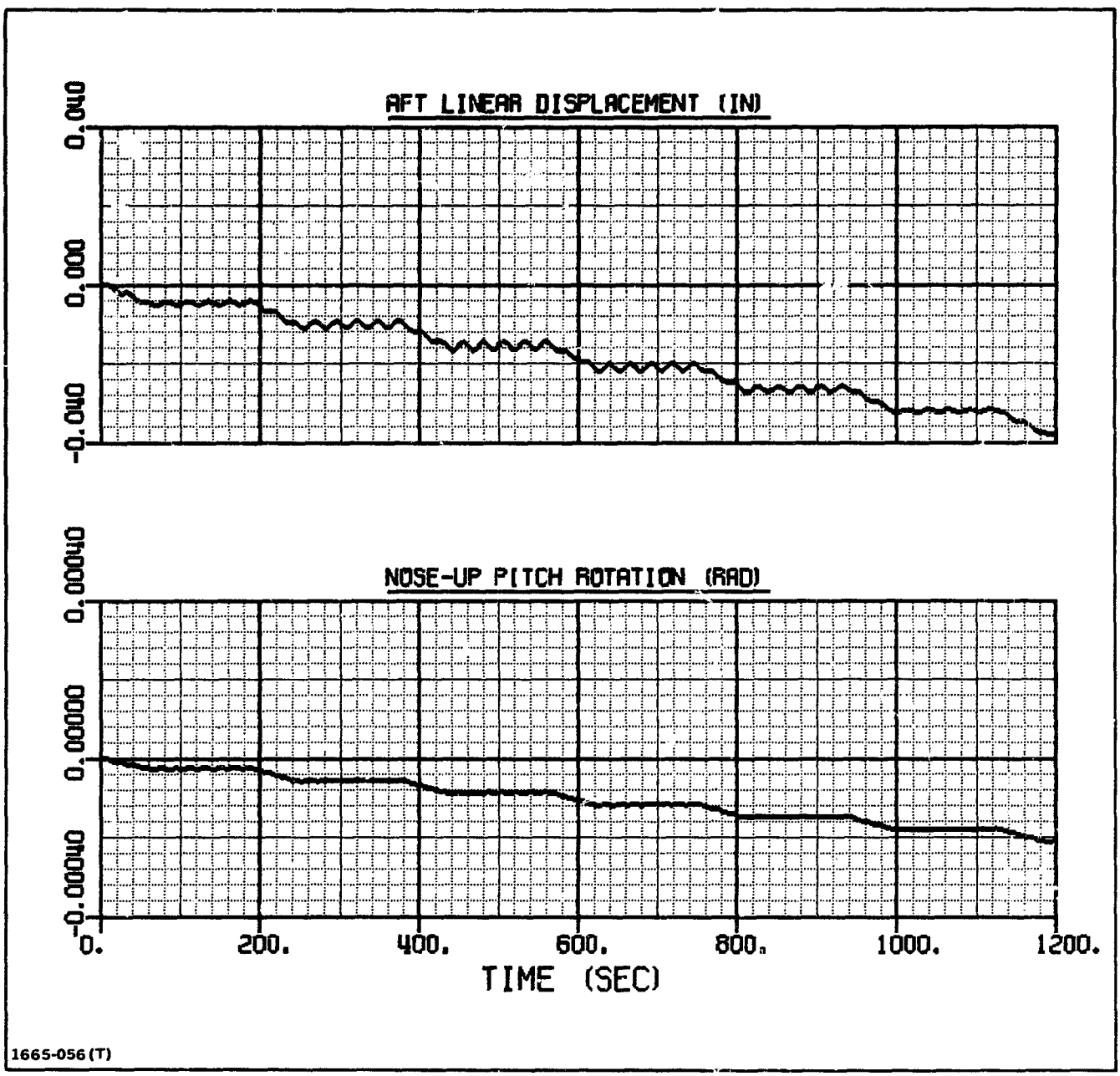

Fig. 2.23 Motion of Node P_3, Tip of Left Solar Panel, During Expulsion of Seven Bays

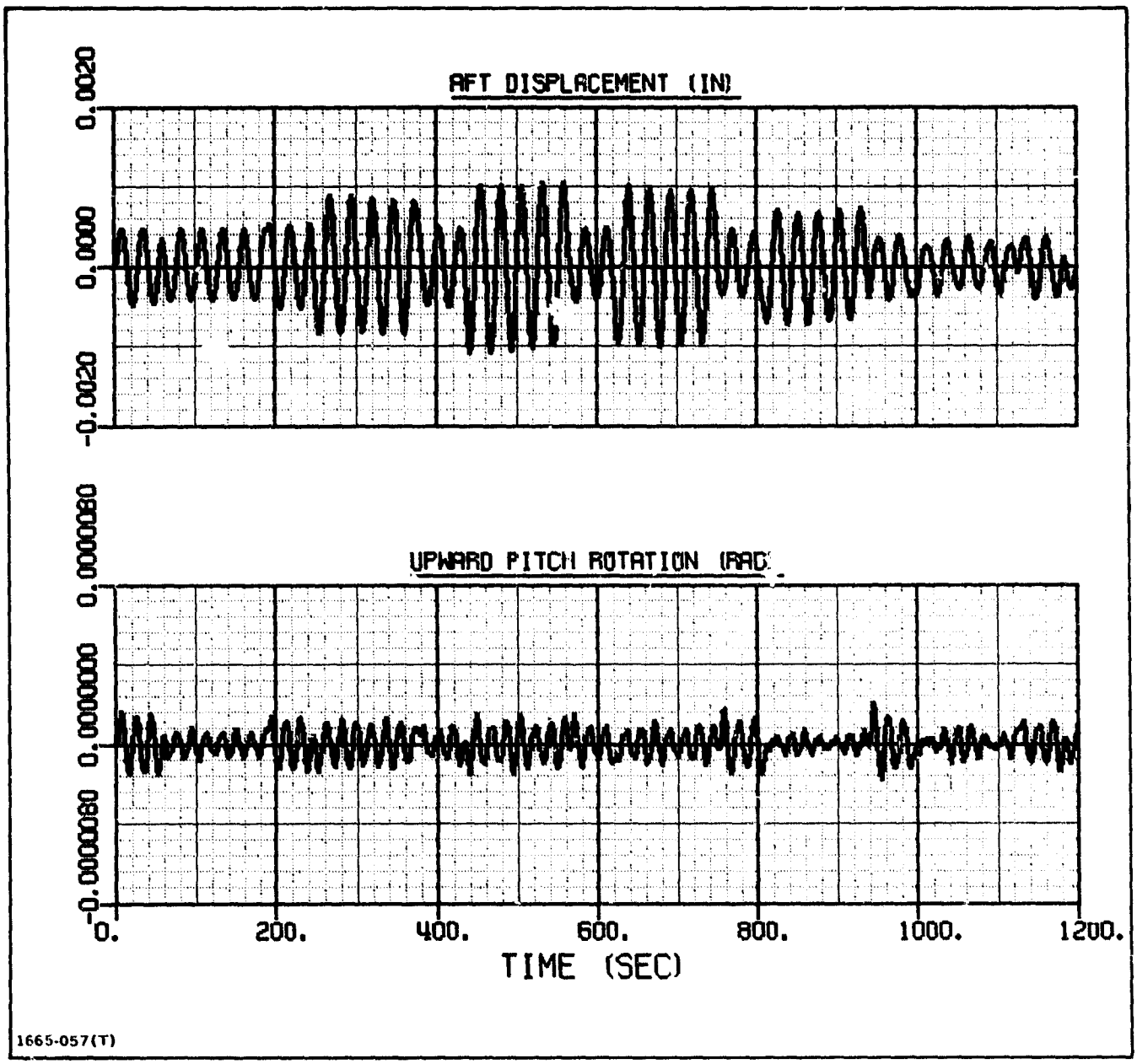

Fig. 2.24 Motion of Node P_3, Tip of Left Solar Panel, Relative to Axes Fixed in Orbiter During Expulsion of Seven Bays

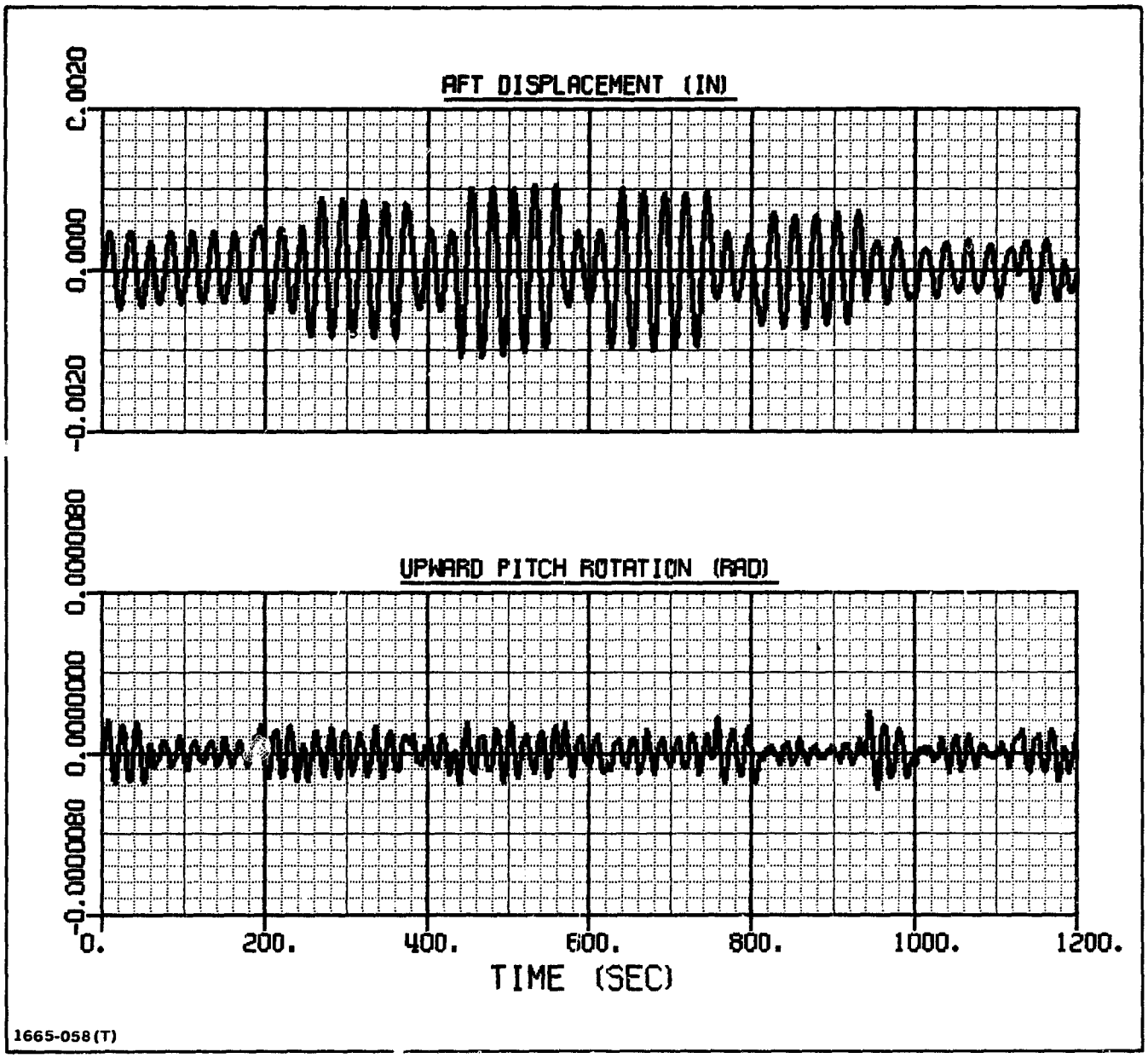

Fig. 2.25 Motion of Node P_6, Tip of Right Solar Panel, Relative to Axes Fixed in Orbiter During Expulsion of Seven Bays

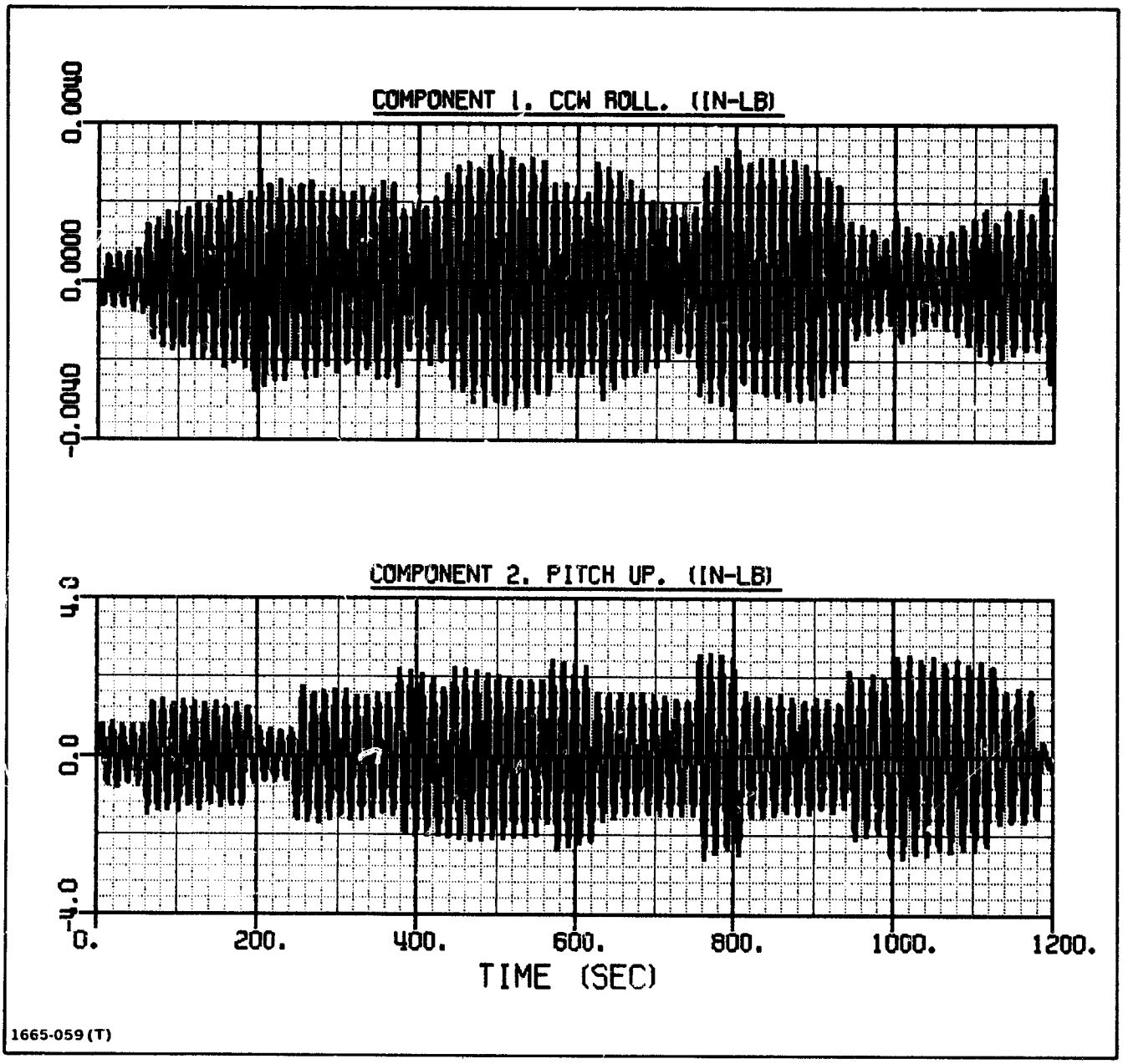

Fig. 2.26 Torques Applied by ABB to Beam During Expulsion of Seven Bays

(2-18) contains inertia loads, i.e., rigid-body mass-times-acceleration terms given by (E53) - (E55).

These inertia loads are equal in magnitude, but opposite in direction, to the upward acceleration of the beam relative to the orbiter times the mass of the beam nodes. This observation led to the formation of the following approximate technique which can be performed with a conventional fixed-geometry transient-response program such as NASTRAN. The beam length is held fixed during the run at its average value and the above described inertia forces are applied as loads on the structure.

This technique, which will be referred to as the Average-Length-Method, was explored to determine its limitations. Several runs were made, starting with a beam length of 103.5 m (69 bays), the same length as the run described in Section 2.8.2. It was found that reasonably accurate results could be obtained as long as the change in length of the beam was small.

Figure 2.27 illustrates the beam growth during one run in which two bays are constructed. By comparing the results shown in Figure 2.28, it is seen that the overall motion of the beam tip can be approximated fairly well by the average-length method. The vibration of the beam tip relative to coordinates fixed in the orbiter can also be approximated fairly well by using the new method (See Fig. 2.29). The approximate motions of the other nodes in the structure were even more accurate than the motion of the beam tip. Good agreement was also obtained for the rigid-body motion (e.g. see Fig. 2.30) and the torque at the root of the beam.

However, when more than two bays were constructed, the average-length method provided unacceptable results for the beam motion. For example, consider the case studied in Section 2.8.2 where seven bays are emitted (Fig. 2.19). Figure 2.31 shows that the flexible vibration of the beam tip is poorly represented by the average-length fixed-geometry approximation for this case. The primary reason is that the frequency of the structure varies as the beam grows; consequently the exact and approximate solutions are out of phase. The pulse exerted on the system whenever the beam is accelerated out of the beam builder will either amplify the beam vibration or decrease it depending on the phase of the vibration relative to the pulse. However, since the vibrations are small, the overall motion of the beam tip, which is primarily attributable to rigid-body motion, is reasonably well represented by the approximate method (see

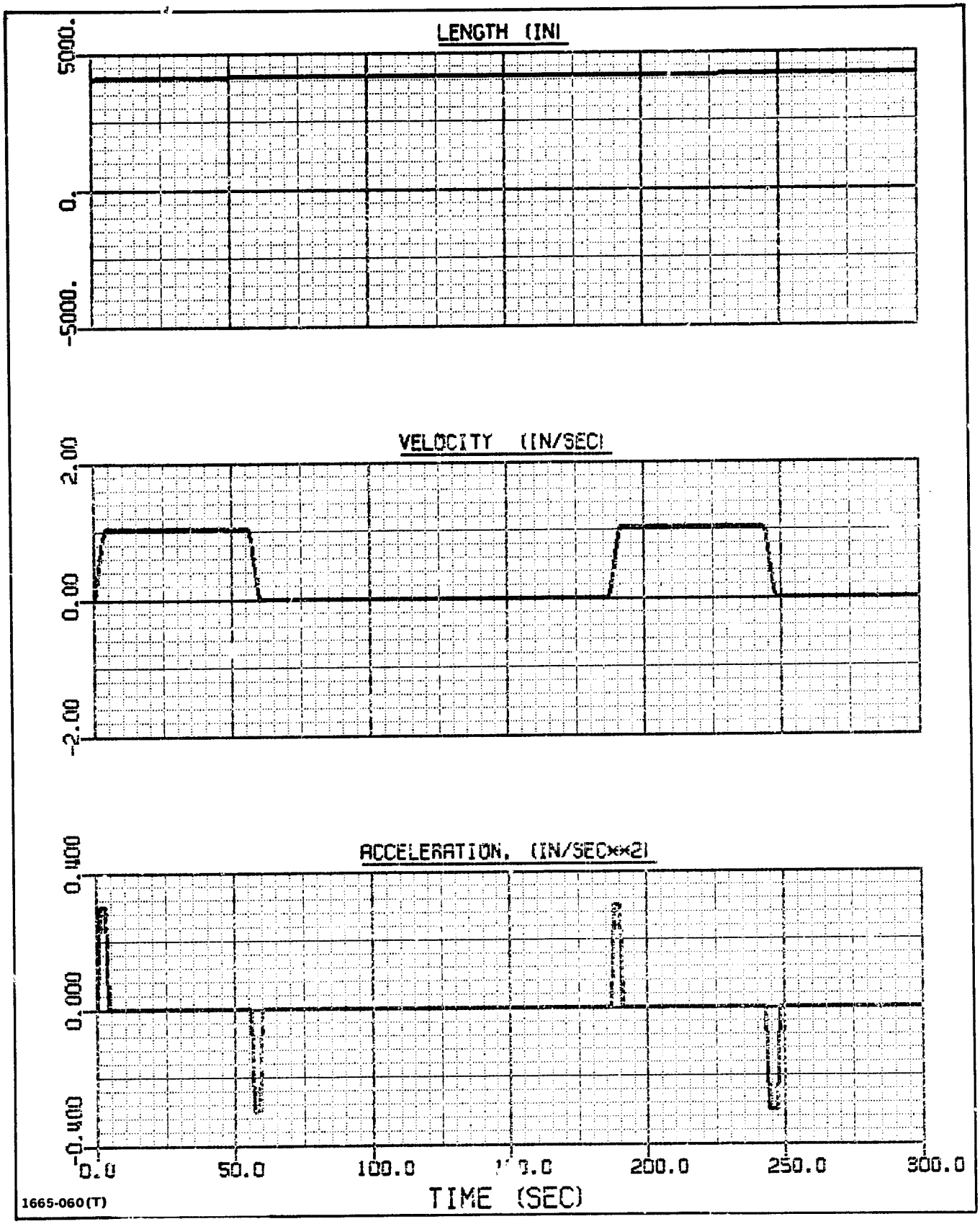

Fig. 2.27 Beam Growth During Expulsion of Two Bays

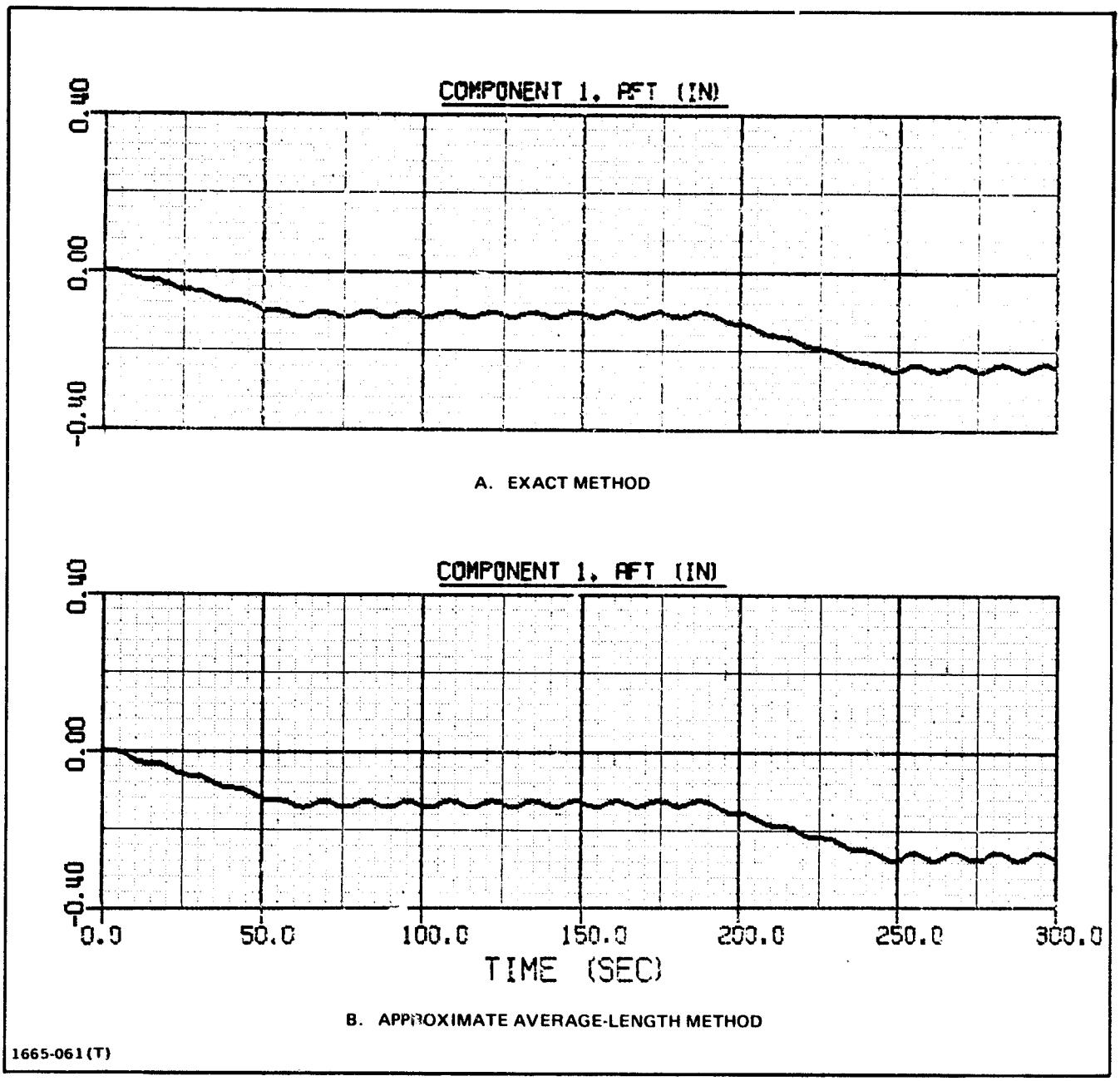

Fig. 2.28 Comparison of Fore and Aft Motion of Beam Tip During Expulsion of Two Bays Using Exact and Average-Length Methods

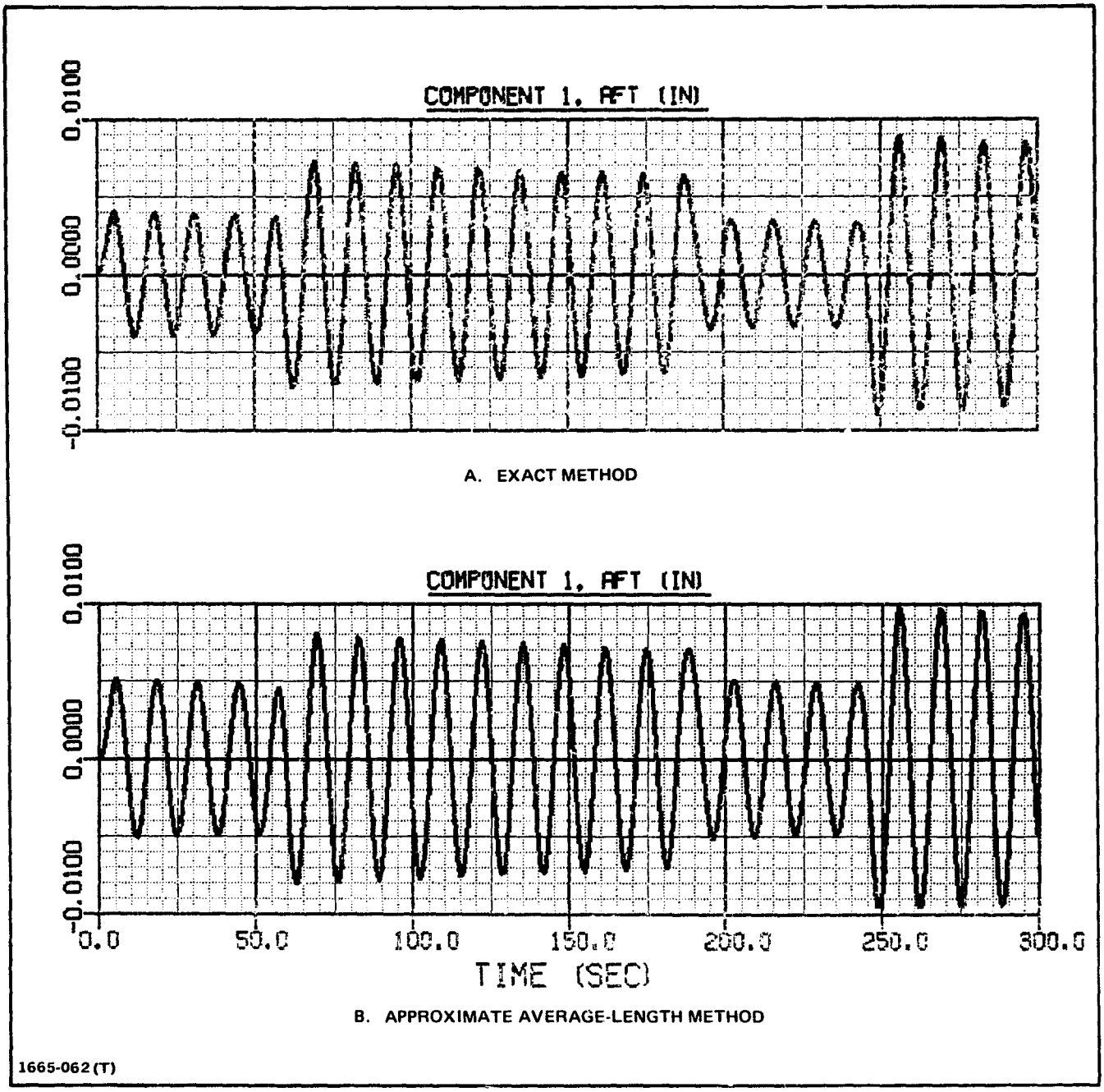

Fig. 2.29 Comparison of Fore and Aft Motion of Beam Tip Relative to Axes Fixed in Orbiter During Expulsion of Two Bays Using Exact and Average-Length Methods

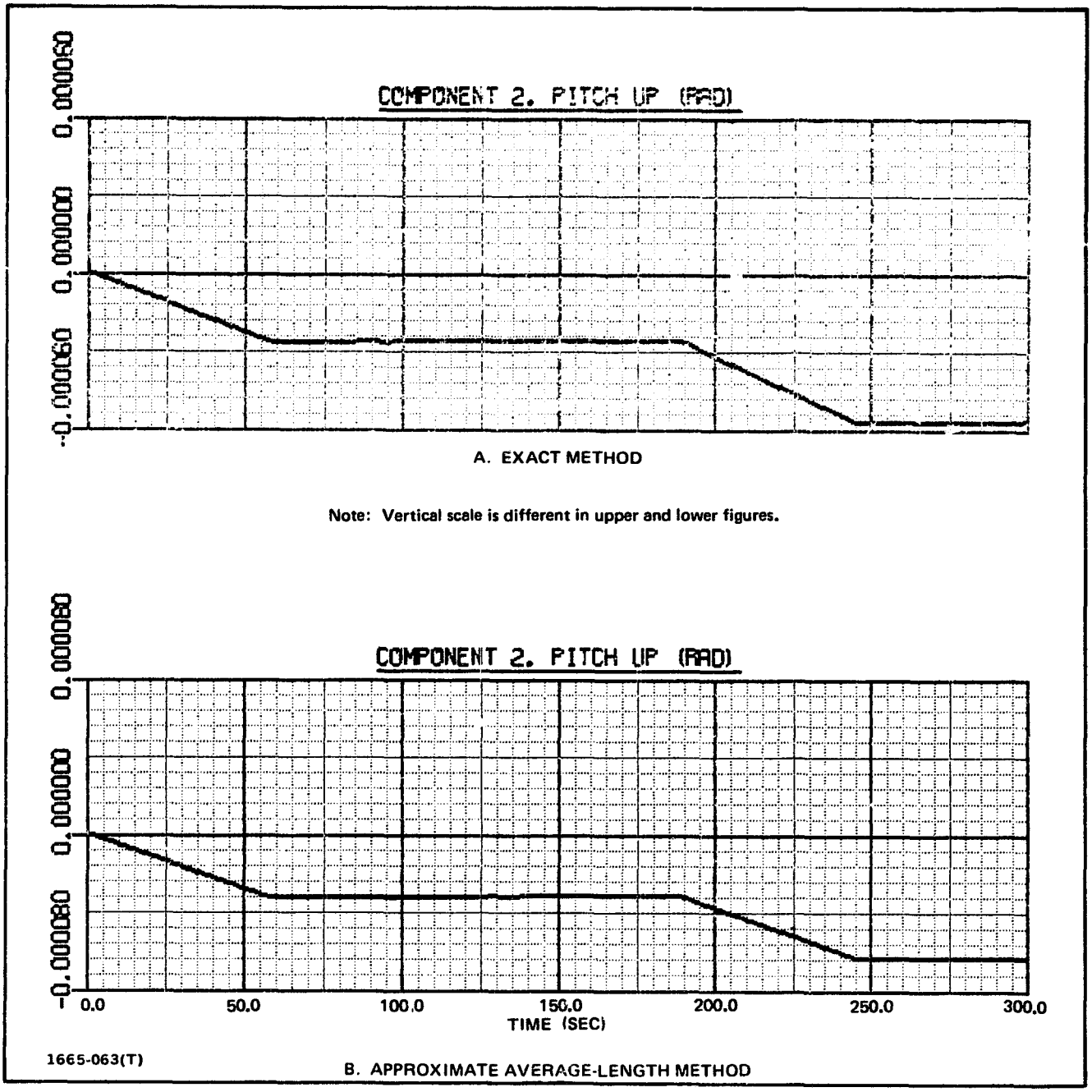

Fig. 2.30 Comparison of Pitch Motion of Orbiter During Expulsion of Two Bays Using Exact and Average-Length Methods

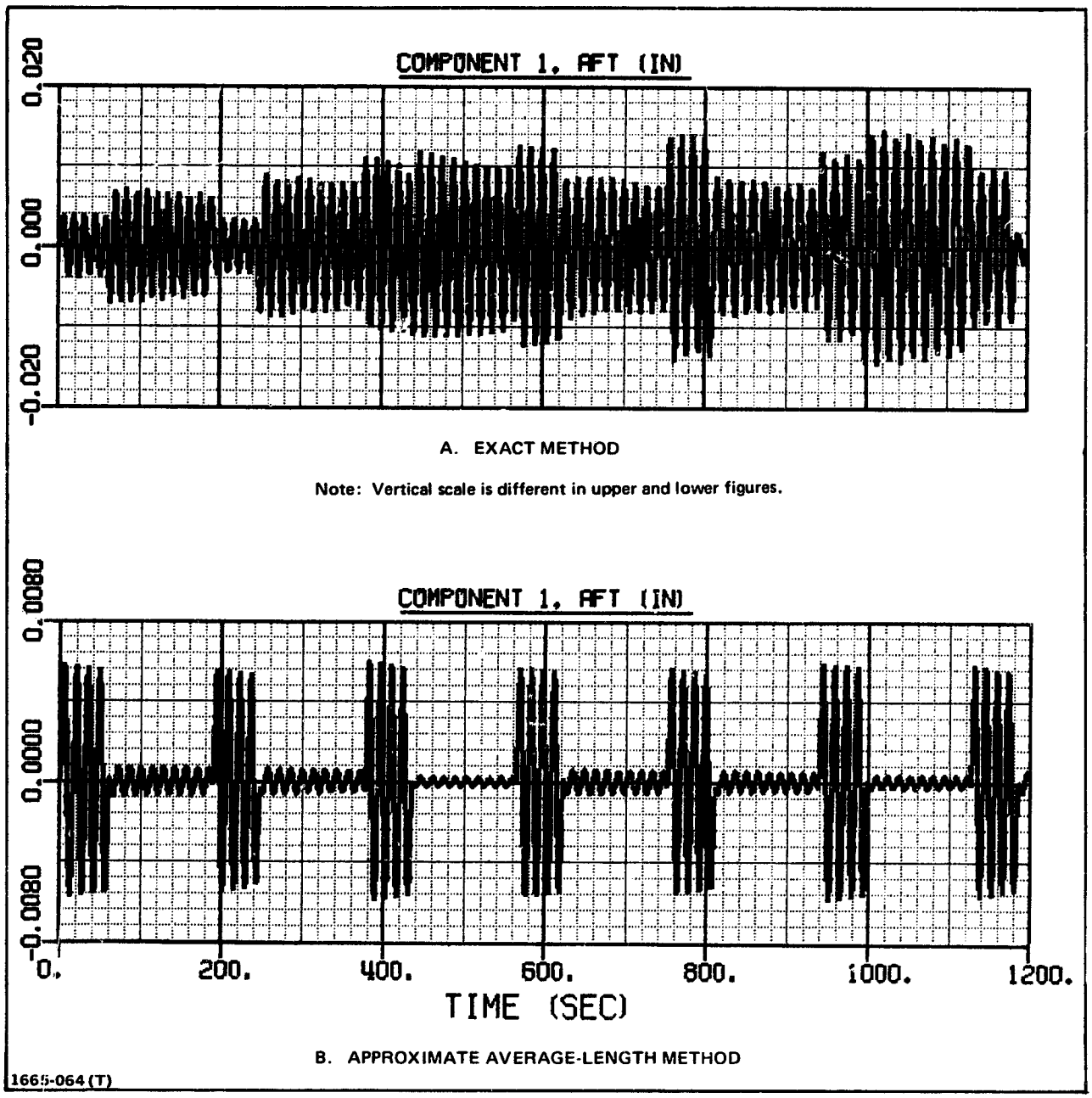

Fig. 2.31 Comparison of Fore and Aft Motion of Beam Tip Relative to Axes Fixed in Orbiter During Expulsion of Seven Bays Using Exact and Average-Length Methods

Fig. 2.32). Also, the motion of the solar panels is well approximated by the new method (see Fig. 2.33). This occurs because the orbiter is relatively massive and there is therefore very little coupling between the beam and the solar-panel vibrations. Each panel is excited by the motion of the orbiter which is induced by the beam as it is periodically pushed out of the ABB.

Computer runs were made for different quantities of emitted beam length using the Average-Length Method and the exact method. The beam vibration frequencies in each average-length run are of course slightly different, since the average fixed beam length is different from run to run. The error, the peak deflection of the beam tip, measured relative to an axis system fixed in the orbiter at the root of the beam, was used as an indication of the accuracy of the method. The results are shown in Table 2.2 and pictorially in Fig. 2.34. As indicated, runs were also made with beam densities equal to ten times the nominal value. The results show that as long as the beam length does not vary more than two or three percent, reasonably accurate results can be obtained with the average-length method. The method can therefore be used to evaluate short-duration disturbances such as a sudden variation in the system's geometry. In addition, the method may be useful as the basis for a technique in which longer-duration motion is computed by making several runs with a conventional program. The average length would be updated in each run, and the final motion of the previous run would be the initial conditions of the current run.

2.8.4 Effect of Large Beam Growth

In order to study the effect of a large quantity of the beam emanating from the orbiter without using an extravagent amount of computer time, the rate at which bays are expelled was increased from one bay every 187.5 sec to one bay every 6 sec. The hypothetical rate of change of beam length is shown in Fig. 2.35. The maximum beam velocity of 29.5 in/sec is computed by the program so that one bay, 1.5 m (59 in), is expelled during the first 3 sec. portion of each cycle. Initially, the beam is 37.5 m long (1476 in). The beam grows during the run until 645 sec. elapse when fabrication of the 199.5 m (7854 in) beam is complete. Figure 2.36 illustrates the fore and aft motion of the beam tip, and Fig. 2.37 illustrates the motion of Node 4 which does not emerge from the ABB until 102 sec have elapsed. Figure 2.38 shows the aft acceleration of the beam tip and the pitch torque at the root of the beam. This figure also contains a schedule of events (See Table 2.3 for more detail). As the beam is expelled, its frequencies drop

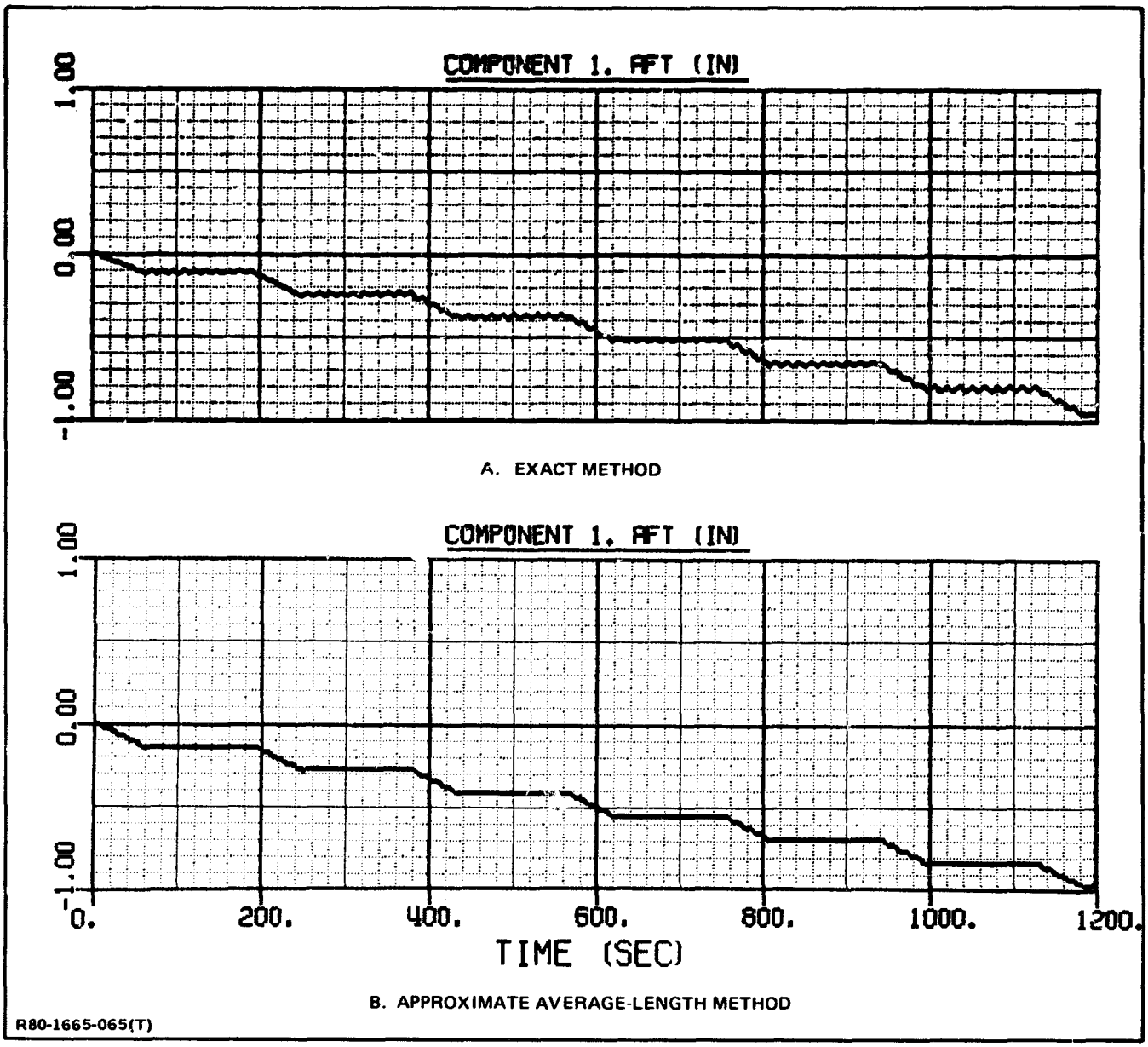

Fig. 2.32 Comparison of Fore and Aft Motion of Beam Tip During Expulsion of Seven Bays Using Exact and Average-Length Methods

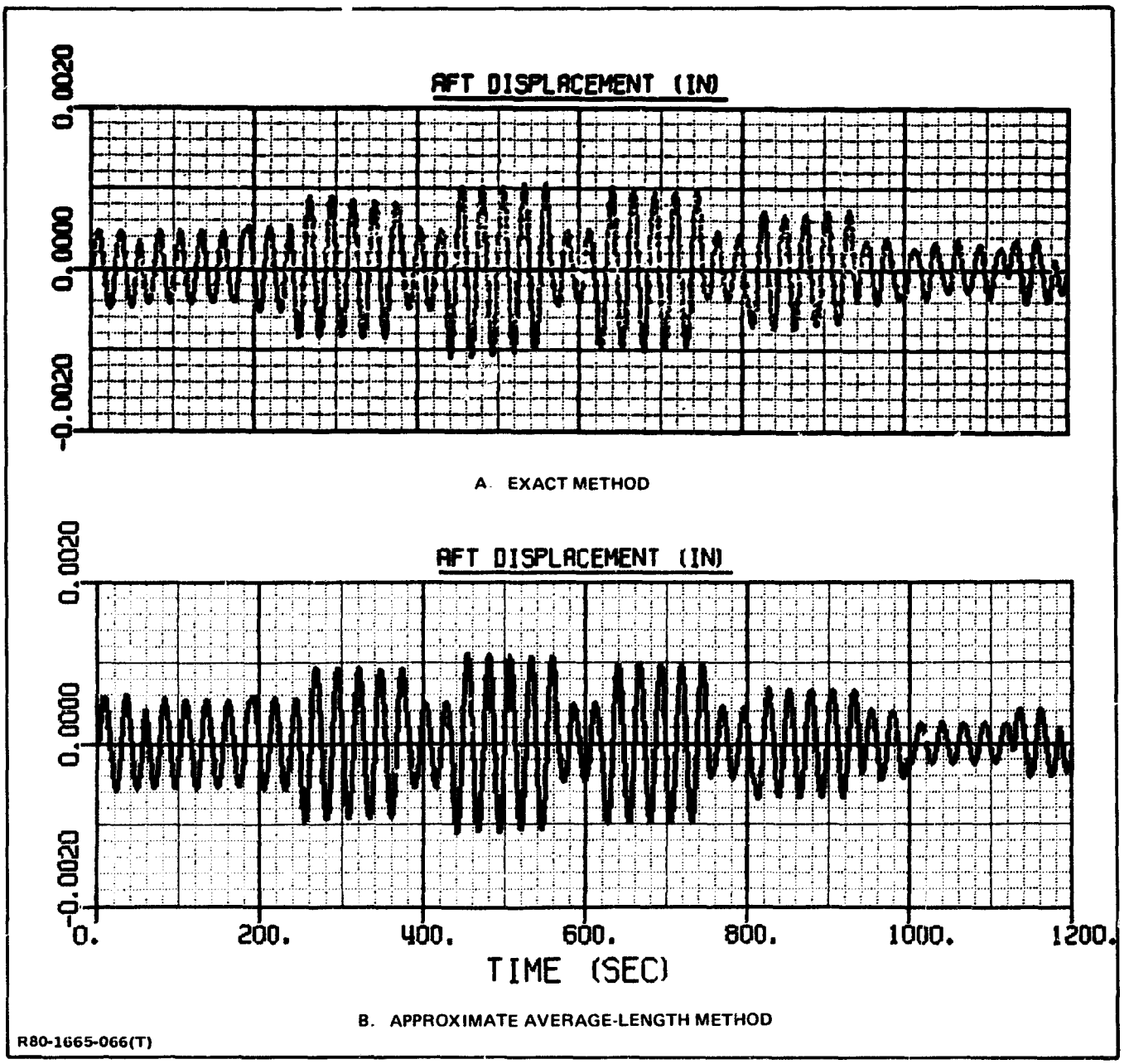

Fig. 2.33 Comparison of Fore and Aft Motion of Left Solar Panel Tip Relative to Axes Fixed in Orbiter During Expulsion of Seven Bays Using Exact and Average-Length Methods

TABLE 2.2 VARIATION IN ERROR, OF APPROXIMATE AVERAGE-LENGTH METHOD, WITH BEAM LENGTH EXPOSED DURING RUN

NUMBER OF BAYS EXPOSED	AVERAGE BEAM LENGTH DURING RUN, L (IN)	CHANGE IN BEAM LENGTH ΔL (IN)	$\frac{\Delta L}{L_{AVG}}$ (%)	ERROR, % (NOTE 3)	
				NOMINAL BEAM DENSITY ρ	DENSITY = 10ρ
1	4104	59.1	1.44	1.45	1.13
1.6	4123	96.5	2.34	6.09	7.67
2	4134	118.1	2.86	11.46	7.60

NOTES:
1. INITIAL LENGTH IN EACH CASE IS 4074.8 IN. (103.5 m).
2. NOMINAL BEAM MASS PER UNIT LENGTH IS 1.843×10^{-4} LB SEC^2/IN^2
3. THE ERROR INDICATED IS THE PERCENT ERROR IN PEAK DEFLECTION OF BEAM TIP RELATIVE TO AXES FIXED IN ORBITER.

1665-139(T)

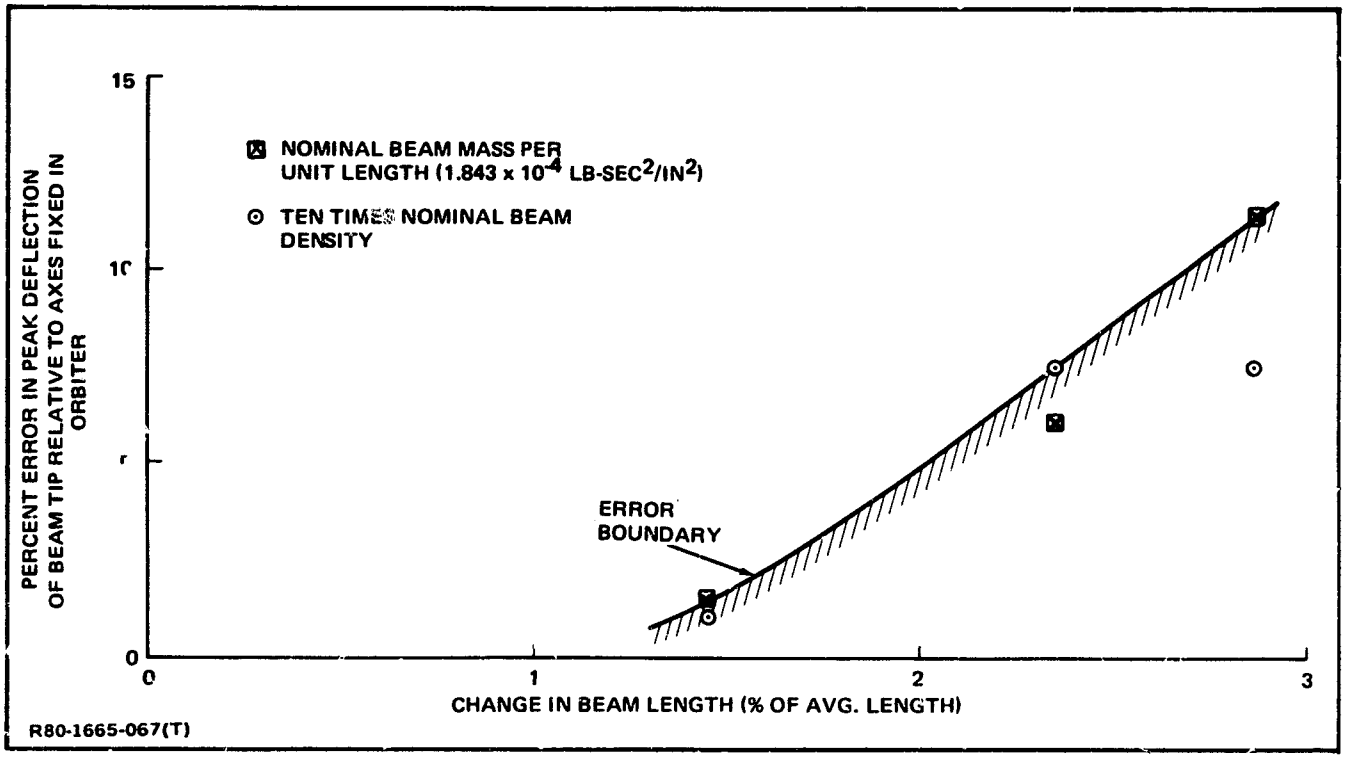

Fig. 2.34 Variation in Error of Approximate Average-Length Method with Change in Length of Beam During Run

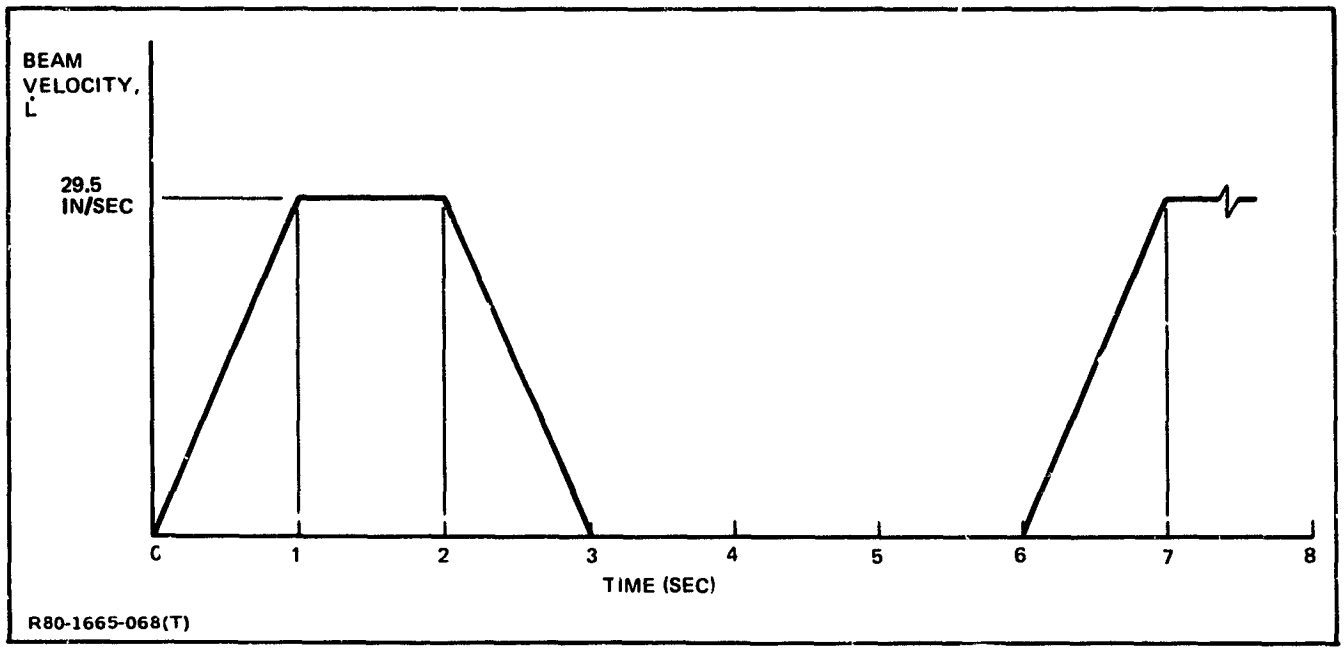

Fig. 2.35 Beam Velocity for Run with Large Growth

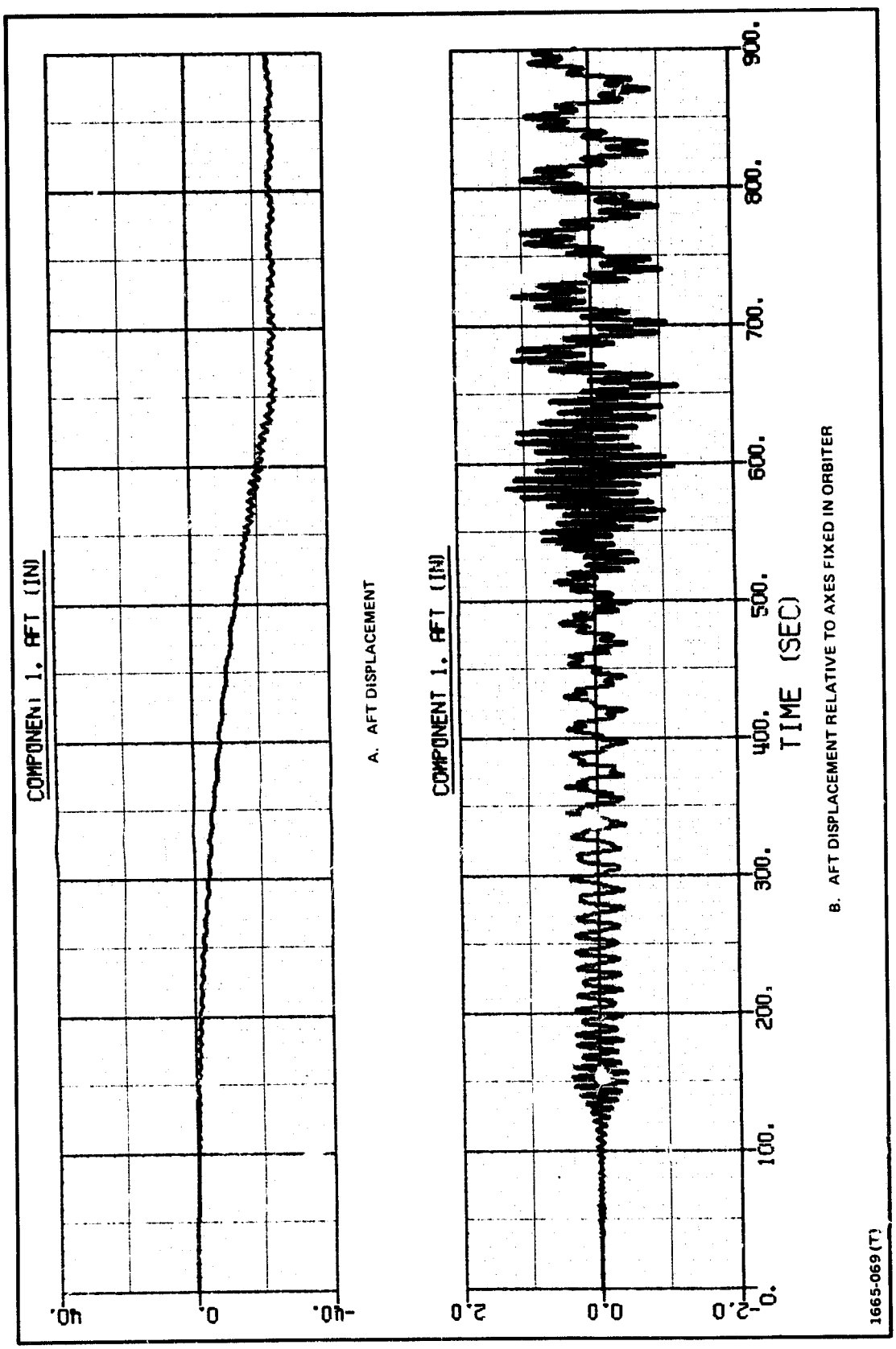

Fig. 2.36 Fore and Aft Displacement of Beam Tip During Run With Large Beam Growth

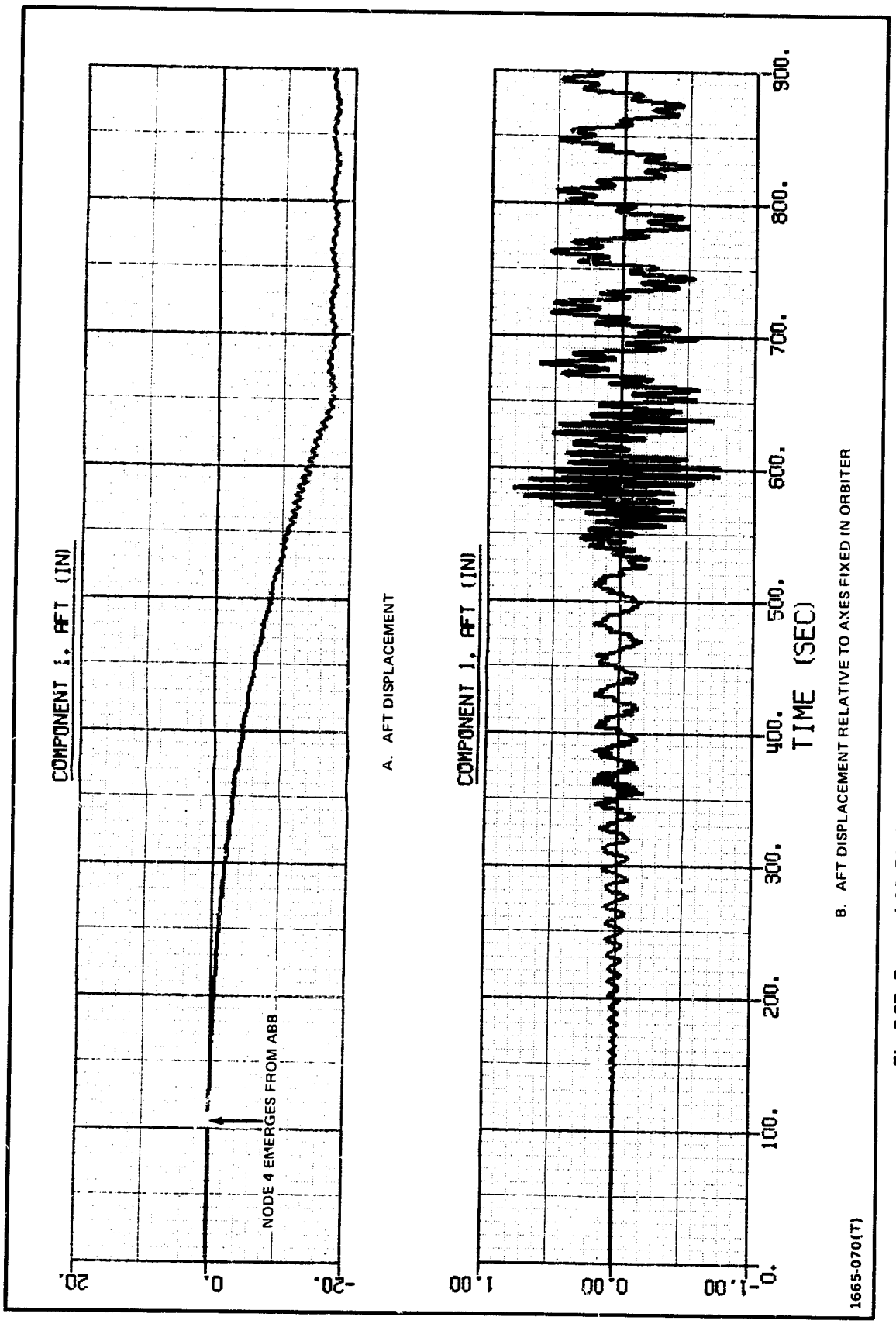

Fig. 2.37 Fore and Aft Displacement of Beam Node Four During Run with Large Beam Growth

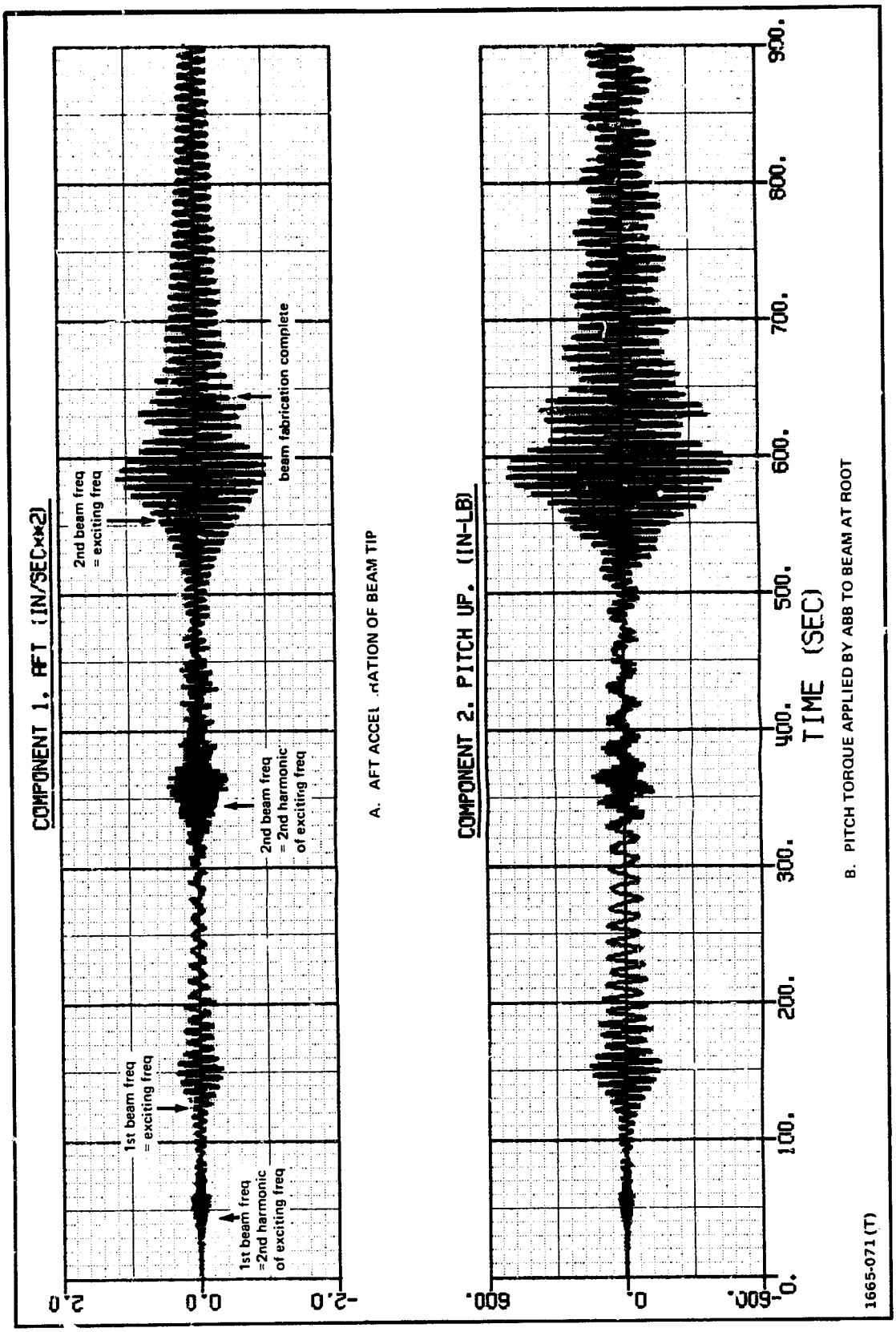

Fig. 2.38 Fore and Aft Acceleration of Beam Tip and Pitch Torque at Root of Beam During Run with Large Beam Growth

TABLE 2.3 SCHEDULE OF EVENTS FOR RUN WITH LARGE BEAM GROWTH

TIME (SEC)	BEAM LENGTH (IN)	FIRST BEAM FREQUENCY (Hz)	EVENT
0	1476	.50	START OF RUN (25 BAYS EXPOSED)
43	1900	.333	FIHST BEAM FREQUENCY EQUALS SECOND HARMONIC OF EXCITING FREQUENCY
122	2700	.167	FIRST BEAM FREQUENCY EQUALS EXCITING FREQUENCY
343	4867	.050	SECOND FORE AND AFT BEAM FREQUENCY EQUALS SECOND HARMONIC OF EXCITING FREQUENCY (.333 Hz)
452	5950	.0382	FIRST BEAM FREQUENCY EQUALS FIRST SOLAR-PANEL FREQUENCY
553	6930	.028	SECOND FORE AND AFT BEAM FREQUENCY EQUALS EXCITING FREQUENCY (.167 Hz)
645	7854	.0232	FABRICATION OF BEAM IS COMPLETE

R80-1665-140(T)

in accordance with Fig. 2.17, and resonances begin to form at the times when the first and second beam frequencies are equal to the .167 Hz exciting frequency of the pulse shown in Fig. 2.35. This pulse may be decomposed into its Fourier-series harmonics, and resonances also begin to form when the beam frequencies are equal to the second harmonic (.333 Hz) of the pulse. The amplitudes never grow too large since the beam frequency varies as the beam grows and passes through the resonant frequency. Also, the formulation contains a damping matrix which is equal to one percent of the stiffness matrix. As indicated in Figure 2.39, some of the beam energy is transferred to the solar panels near 452 sec, when the beam frequency becomes equal to the solar-panel frequency. If the beam frequency remained fixed, a beat would be expected to form. This effect is explored further in the next subsection.

When this run was repeated with the influence of the pulsating axial load on the stiffness included, it was found that the character of the motion was basically the same although some differences in the response amplitudes could be measured. This was the only run in which this effect had any influence which could be discerned by overlaying the response graphs. There is the possibility of a primary instability (similar to resonance) due to parametric excitation when the pulsating axial load has a frequency which is twice the beam frequency (Ref. 17). This would be expected to occur at t = 224 sec when the beam length is 3700 in and the fundamental beam frequency is .0833 Hz; however the instability was not observed. According to the theory, the instability will not occur in the presence of damping if the amplitude of the axial load is sufficiently small relative to the buckling load. Also, the beam frequency falls through .0833 Hz, and the instability requires time to develop.

2.8.5 Solar Panel- and Beam-Frequency Crossover

A run was made starting with a beam length of 5669.29 in (144 m or 96 bays) and ending with a beam length of 6259.84 in (159 m or 106 bays). The beam growth is a function of the ABB kinematic characteristics as illustrated in Fig. 2.40. As the beam grows, its frequency drops, and at 794 sec into the run the beam length is 5950 in and the fundamental beam frequency becomes equal to .0382 Hz, the fundamental solar-panel frequency (See Table 2.1 and Fig. 2.17). The transverse bending frequency drops, but remains higher than, the solar-panel frequency during the run.

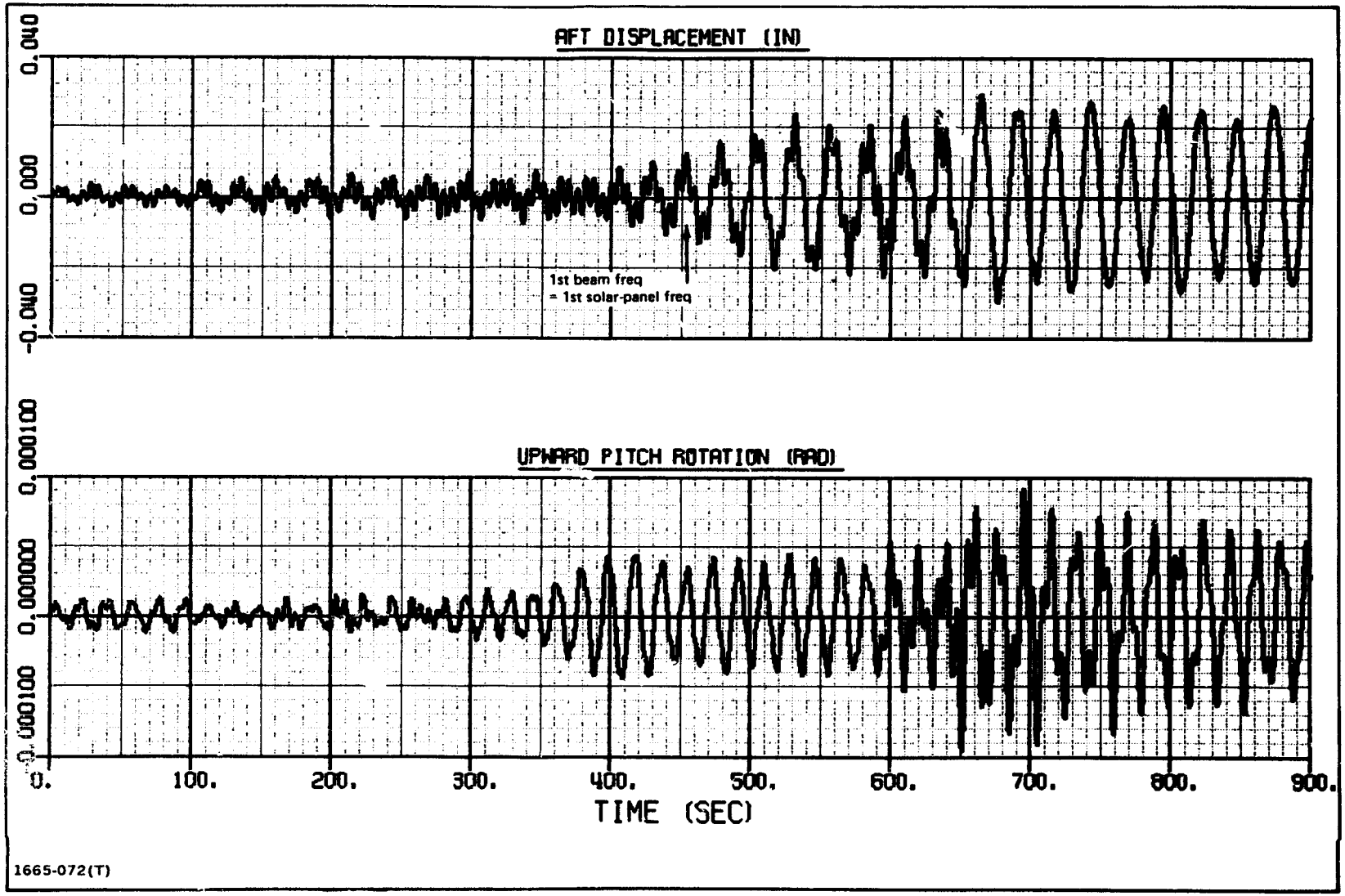

Fig. 2.39 Motion of Tip of Left Solar Panel Relative to Axes Fixed in Orbiter During Run with Large Beam Growth

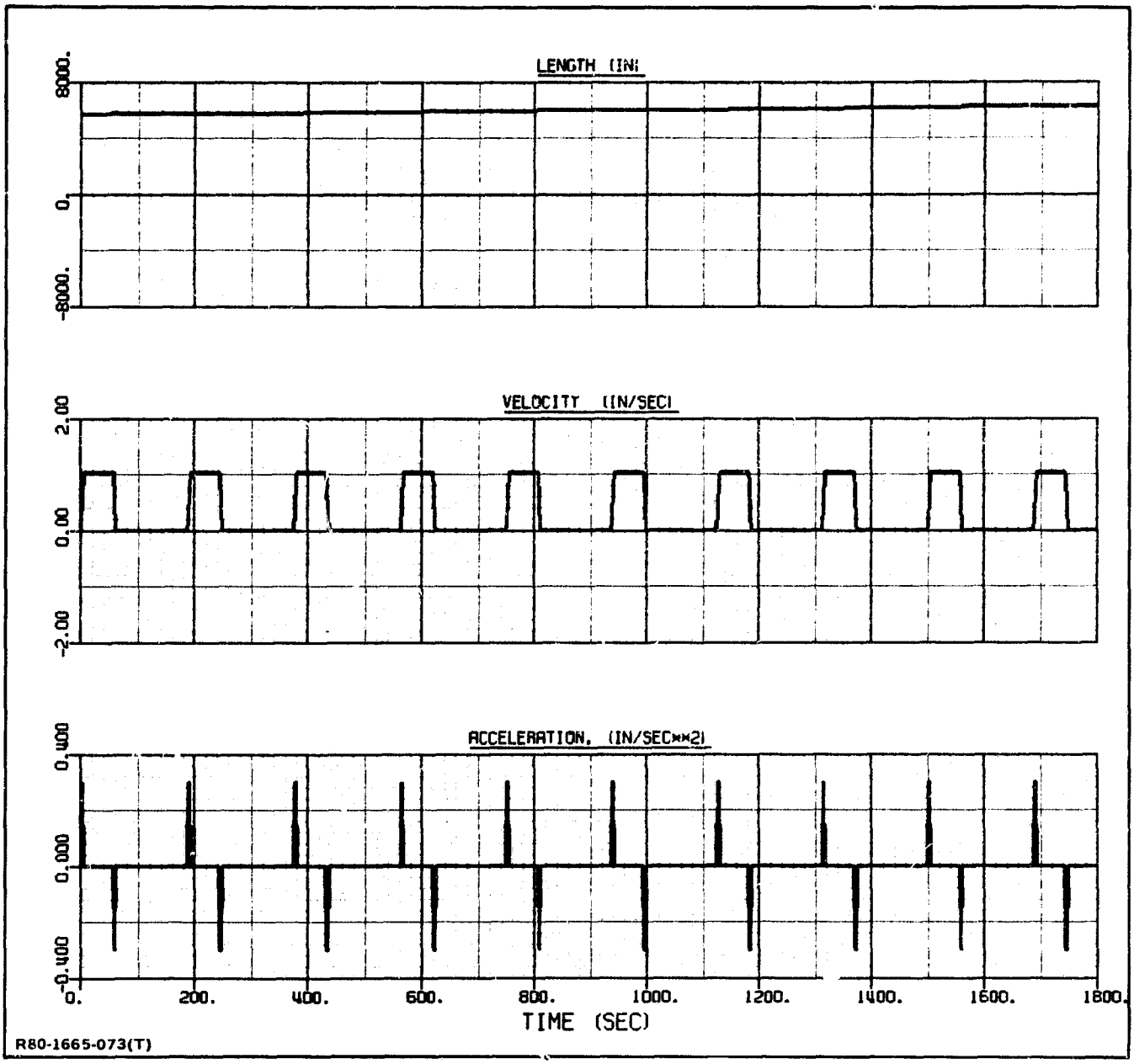

Fig. 2.40 Growth of Beam. Run Illustrating Solar Panel- and Beam-Frequency Crossover

The motions at the tip of the beam and at the tip of the left solar panel are shown in Figs. 2.41 and 2.42, and the torque at the root of the beam is shown in Fig. 2.43. There is some evidence of energy transfer in the form of beats occurring between the small lateral components of the beam motion and the solar-panel motion; however, it is not conclusive since the times of maximum amplitude of one component of the motion do not always coincide with the times of minimum amplitude of another component. This may be due to the fact that there are three nearly equal frequency components in the run, fore and aft beam motion, lateral beam motion, and solar-panel bending. In addition, the motion is complicated by the beam-growth pulsing effect (Fig. 2.40).

2.8.6 Control System

In this run, the initial beam length is 3897.64 in (99 m or 66 bays). As indicated in Fig. 2.44, three bays are expelled from the orbiter during the run. The control-system sample time τ, which is equal to the minimum thruster pulse time, was taken as .125 sec, and the numerical-integration step size was .0125 sec for this run. Actually, the orbiter control-system sample time is .080 sec; however, .125 sec was assumed so that the pulse time could be represented by 10 integration steps with a somewhat larger step size than .008 sec.

The system was given an initial orientation error of 1 deg (.017 rad) about each axis. The control system deadband was .1 deg for each axis. Fig. 2.45 shows that the angular motion of the orbiter is well controlled. The torques exerted by the control system are shown in Fig. 2.46. The impulses are high at the beginning of the run when the initial error is being corrected, and then they become smaller when the errors are small and the system drifts into the deadband boundary. As indicated in Fig. 2.47, the beam-tip displacement is under 8 in. and the bending moment at the root of the beam is under 2000 in-lbs (Fig. 2.48), well under the 13,600 in-lb allowable moment.

2.8.7 Variable Modes

Several runs were made with variable modes, and good correllation was obtained with direct numerical-integration solutions. The set of runs described in this section is typical. The initial length of the beam in these runs is 3897.64 in (99 m or 66 bays), and the final length is 4015.75 in (102 m or 68 bays). The beam growth is illustrated in Fig. 2.49. In addition to this variable-geometry effect, a pitch torque of 20,000 in lbs is applied to the orbiter in the positive

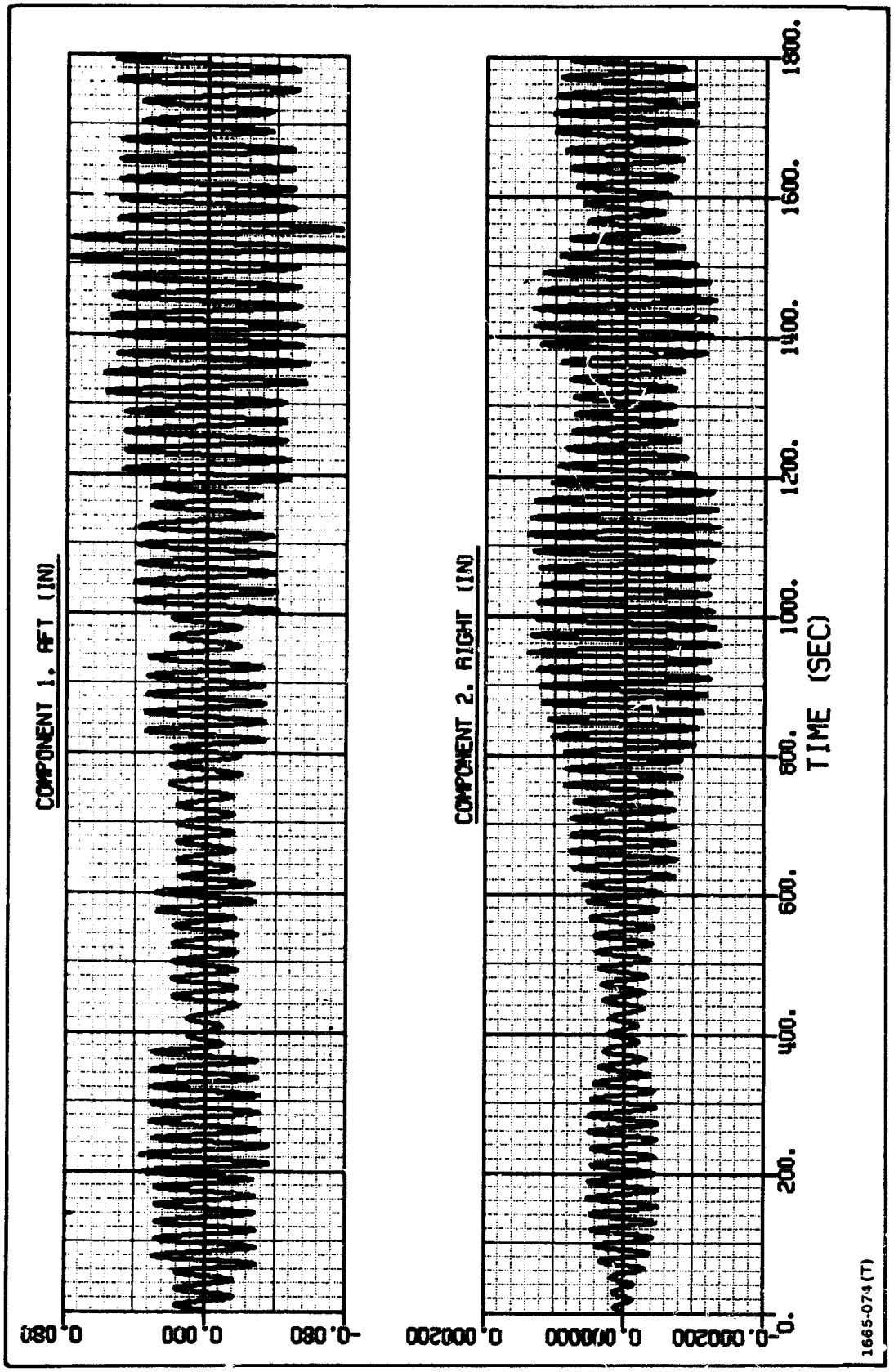

Fig. 2.41 Linear Displacement of Beam Tip, Node 1, Relative to Axes Fixed in Orbiter. Run Illustrating Solar-Panel- and Beam-Frequency Crossover

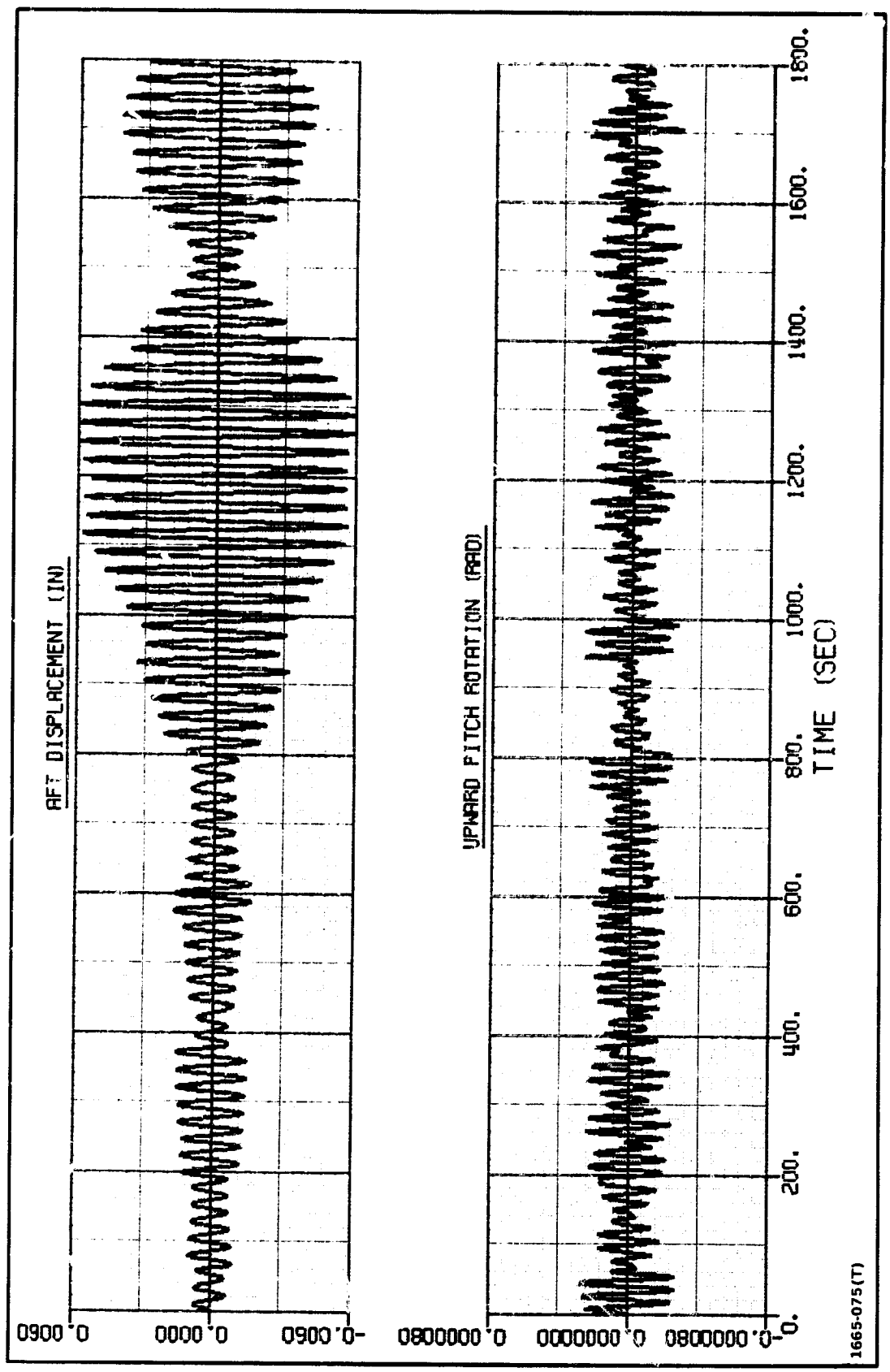

Fig. 2.42 Motion of Tip of Left Solar Panel, Node P_3, Relative to Axes Fixed at Orbiter CM. Run Illustrating Solar-Panel and Beam-Frequency Crossover

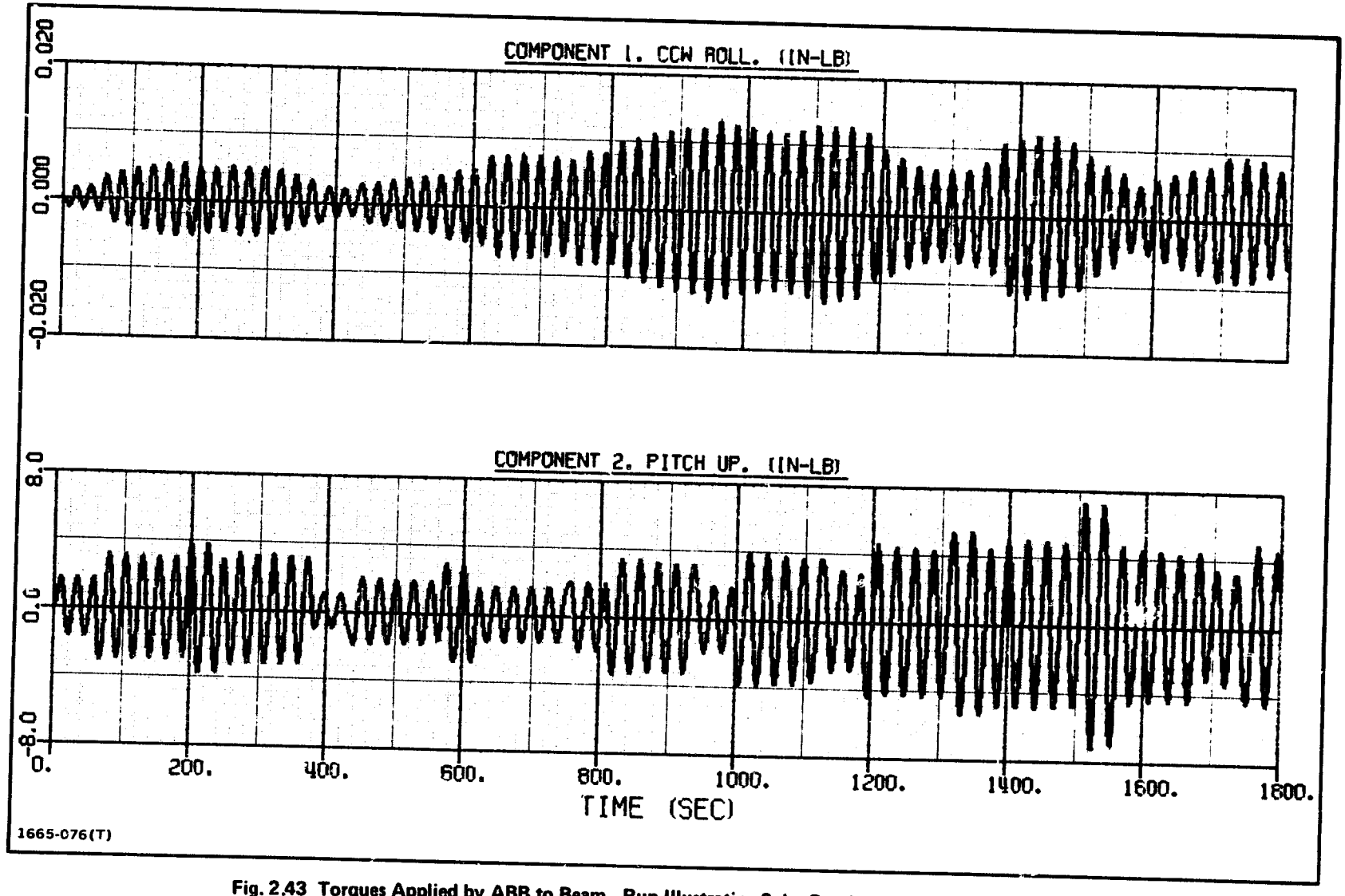

Fig. 2.43 Torques Applied by ABB to Beam. Run Illustrating Solar-Panel- and Beam-Frequency Crossover

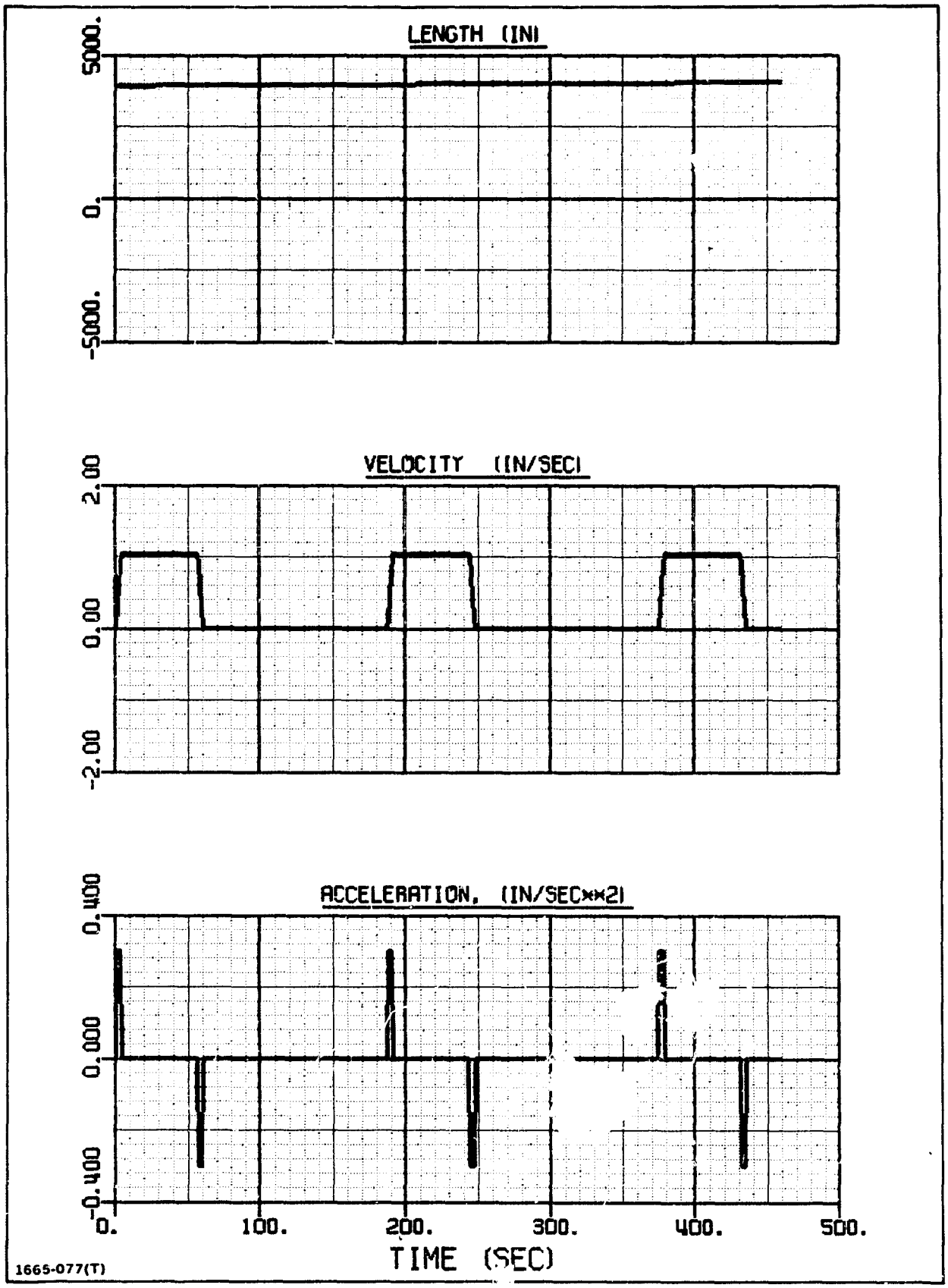

Fig. 2.44 Beam Growth. Control System Active

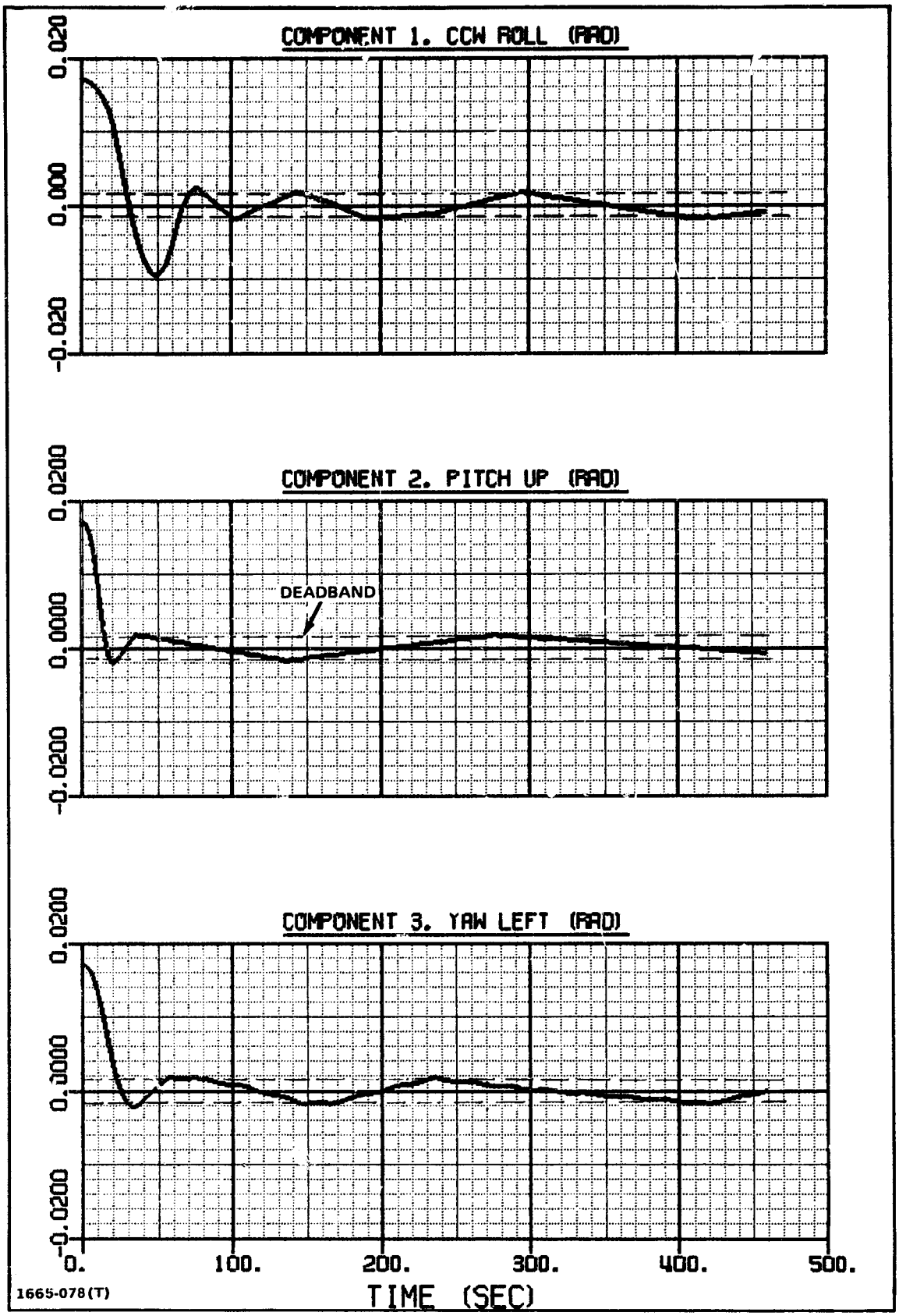

Fig. 2.45 Angular Displacement of Orbiter. Control System Active

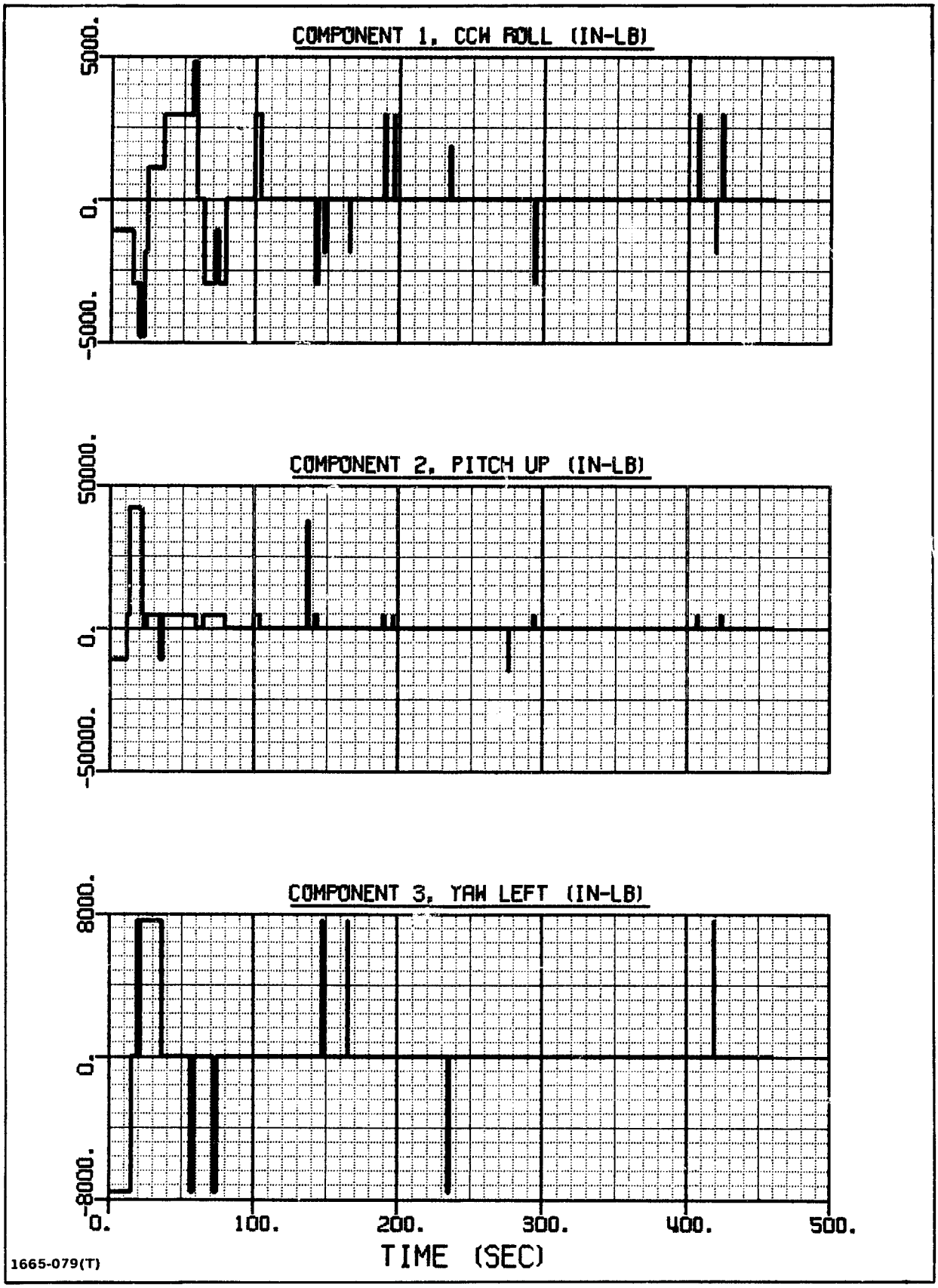

Fig. 2.46 Total Control Torque About Orbiter Center of Mass

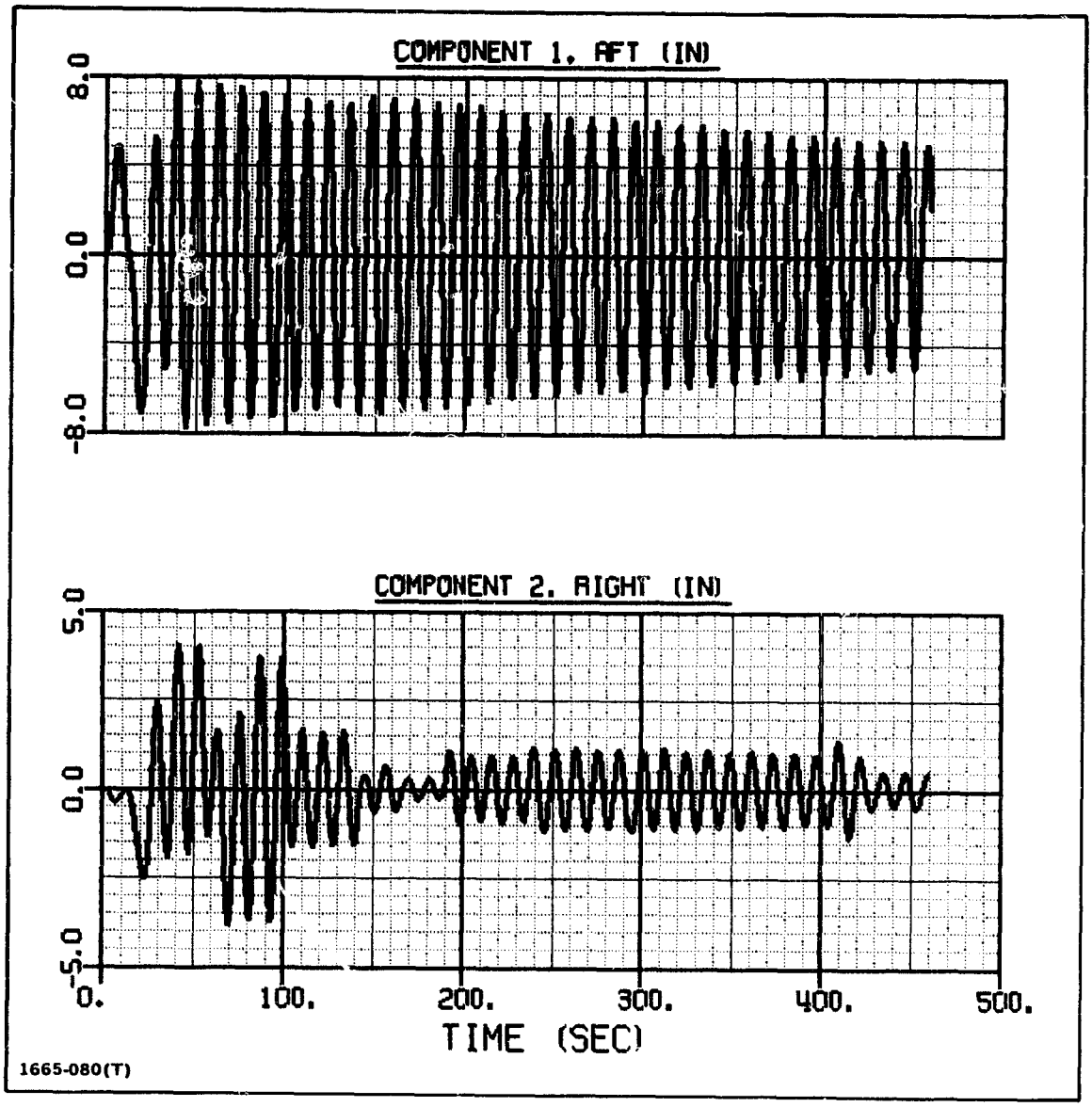

Fig. 2.47 Linear Displacement of Beam Tip Relative to Axes Fixed in Orbiter. Control System Active

ORIGINAL PAGE IS
OF POOR QUALITY

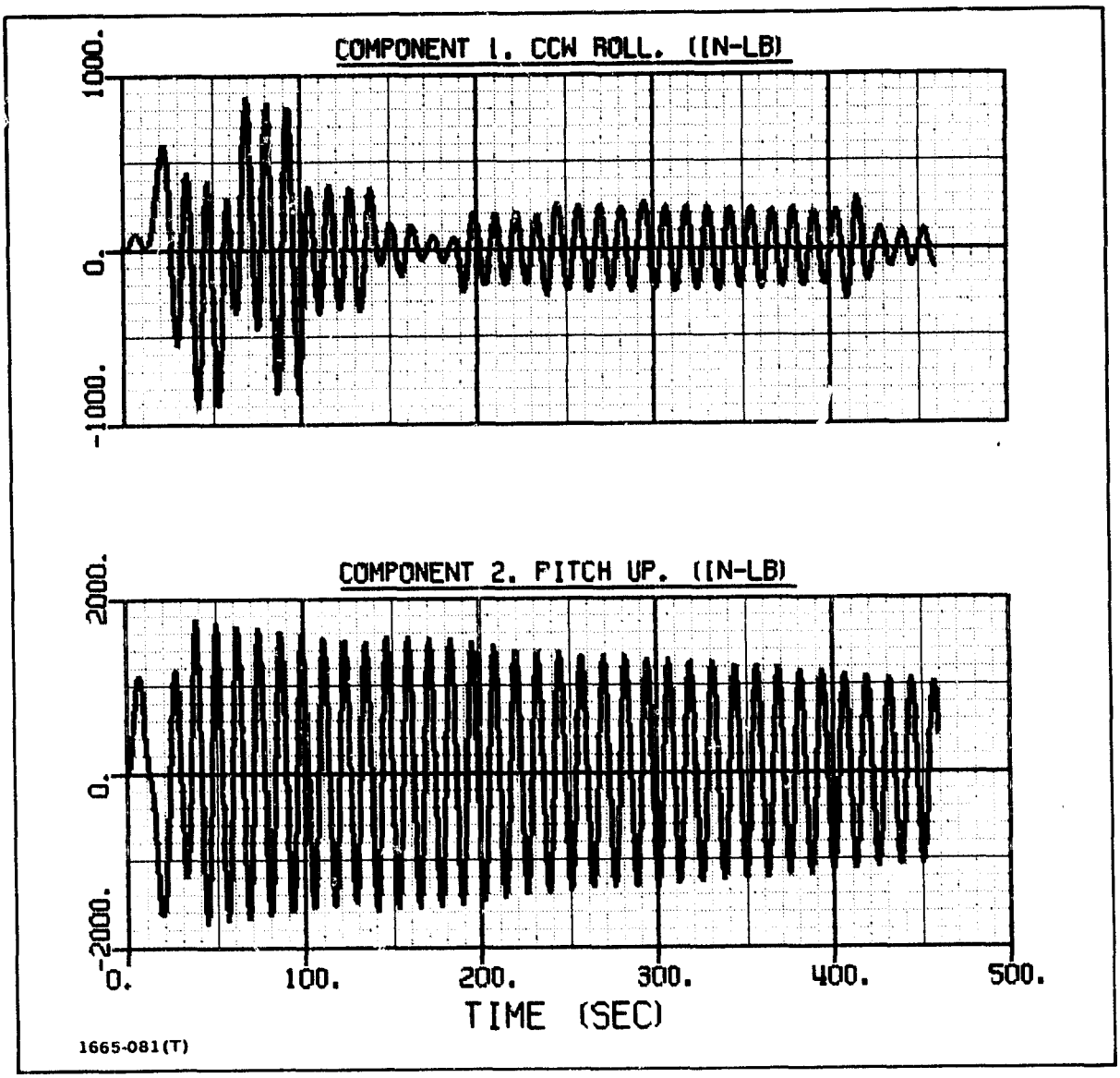

Fig. 2.48 Torques Applied by ABB to Beam. Control System Active

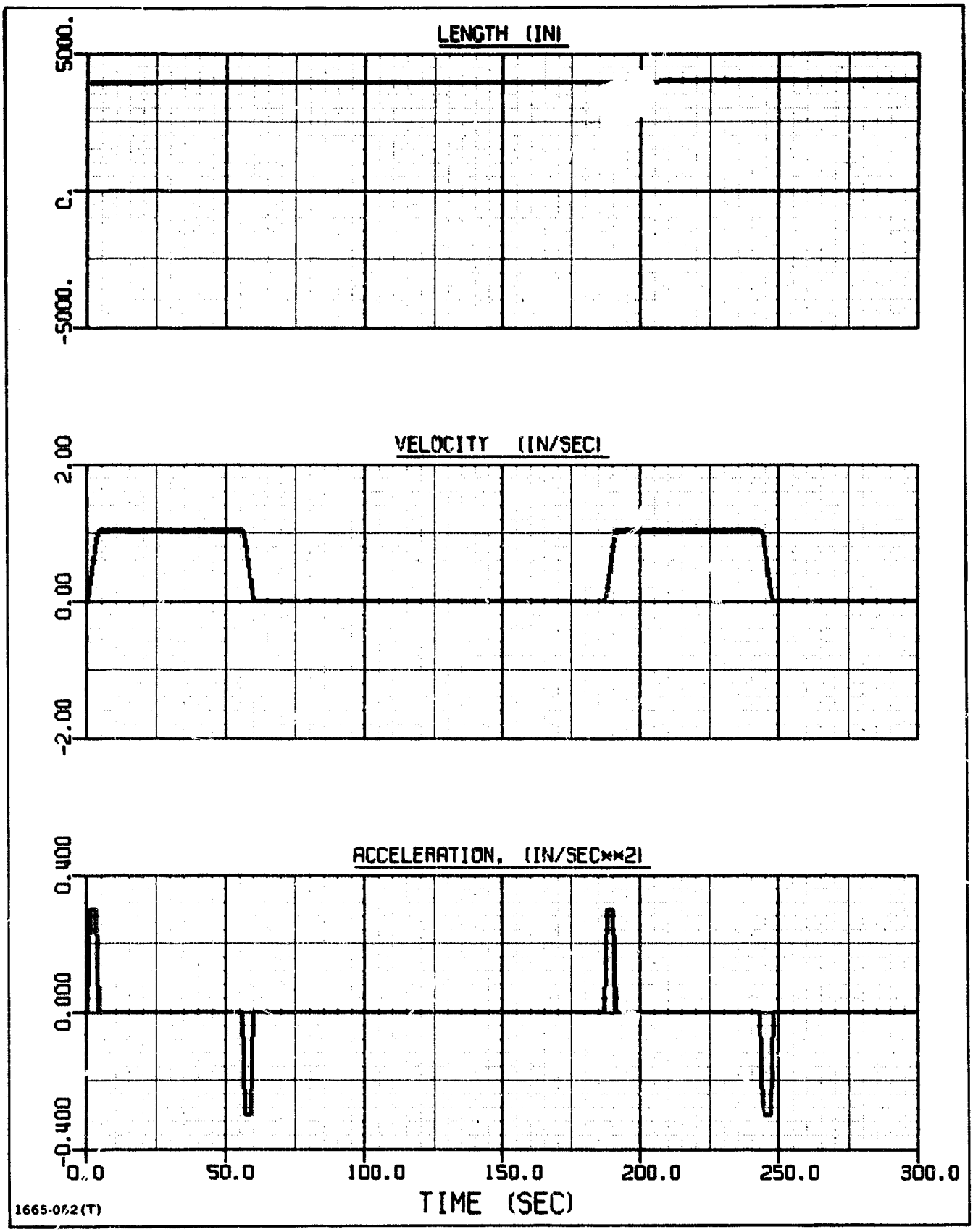

Fig. 2.49 Beam Growth. Direct Numerical Integration Run for Comparison with Variable-Mode Technique

direction for 10 sec and then in the negative direction for 10 sec (see Fig. 2.50). Three sets of modes were used in the run for the interpolation. These modes were computed for the system with the beam length set at the initial value in the run, the final value, and the average value. Figures 2.51 - 2.56 show typical response curves done by direct numerical integration and by the variable-mode technique. It is seen that very good agreement was obtained with the new technique.

Additional data and results are presented in Table 2.4. The above runs correspond to 37A and 37C in the table. As indicated, in Run 37C, the peak deflection at the beam tip was in error by only .80%. The variable-mode techniques saved 85% of the computer time. In a similar run (37B), twice as many modes (24) were used with an integration step size that was one-half as large (.10 sec). However, the additional accuracy obtained generally would not warrant the expenditure associated with the additional computer time required. In another run, 37D, modes were only calculated for the initial and final structural geometries; thus the interpolation interval was double that used for Runs 37B and 37C. This saved very little additional computer time. Although the maximum beam deflection was a little more accurate than the value for Run 37C, this was not indicative of the overall accuracy of the response. During most of the time history, the responses generated in Run 37C were more accurate. In summary, the new method appears to be very accurate, and has the potential to save a significant amount of computer time.

2.8.8 Variable Modes with Control-System Active

The final run that will be discussed is a repeat of the run described in Section 2.8.6, except that the variable-mode method is used. The system has a 1 deg initial error that is corrected by the control system, and three bays are expelled during the run; however, the variable-mode technique is used. The first twenty-four modes were used with an integration step-size of 0.0125 sec. These interpolated modes were obtained from three sets of modes that were computed from eigenvalue analyses. The system geometry for the interpolated modes was the initial geometry (corresponding to a beam length, $\bar{L}_1 = 3898$), the average geometry ($\bar{L}_2 = 3986$), and the final geometry ($\bar{L}_3 = 4075$).

Selected response curves are shown in Figs. 2-57 - 2-60. Again, good control was achieved, and the overall solution is roughly the same as that achieved using direct numerical integration (Figs. 2.45 - 2.48); e.g. the peak values of the responses agreed in both runs. In the early part of the run the correlation

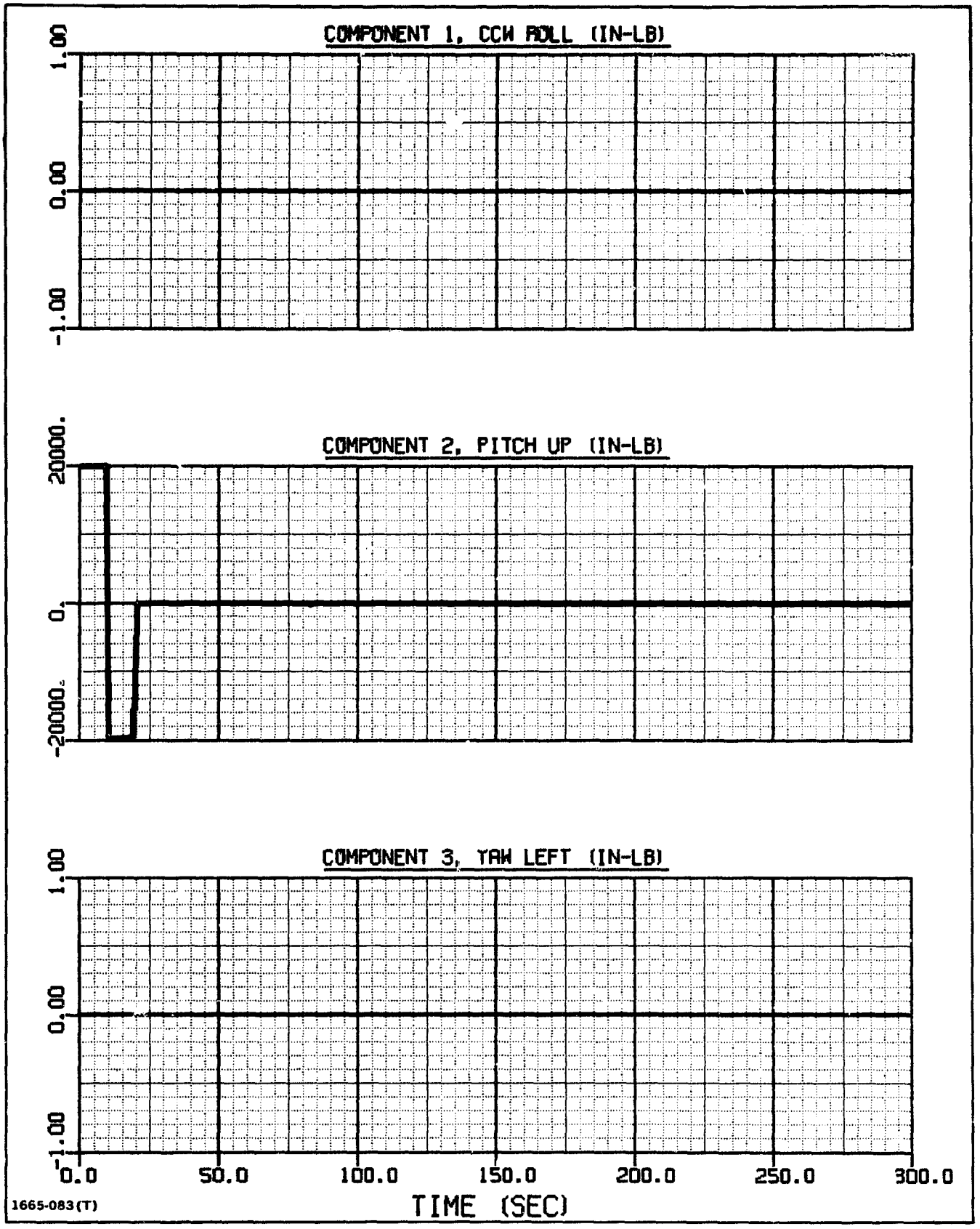

Fig. 2.50 External Torque Applied to Orbiter. Direct Numerical-Integration Run for Comparison with Variable-Mode Technique

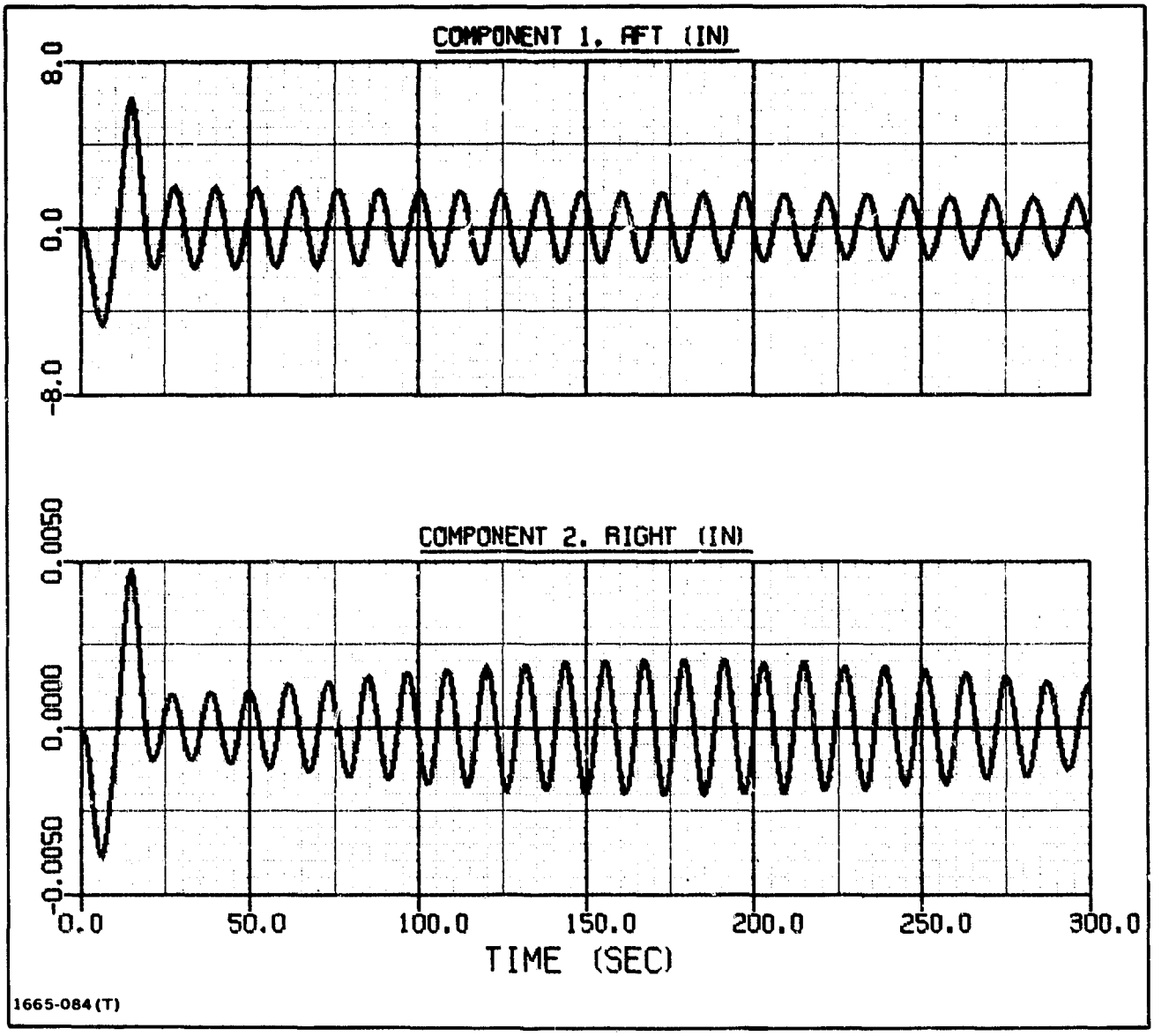

Fig. 2.51 Linear Displacement of Beam Tip Relative to Axes Fixed in Orbiter. Direct Numerical Integration

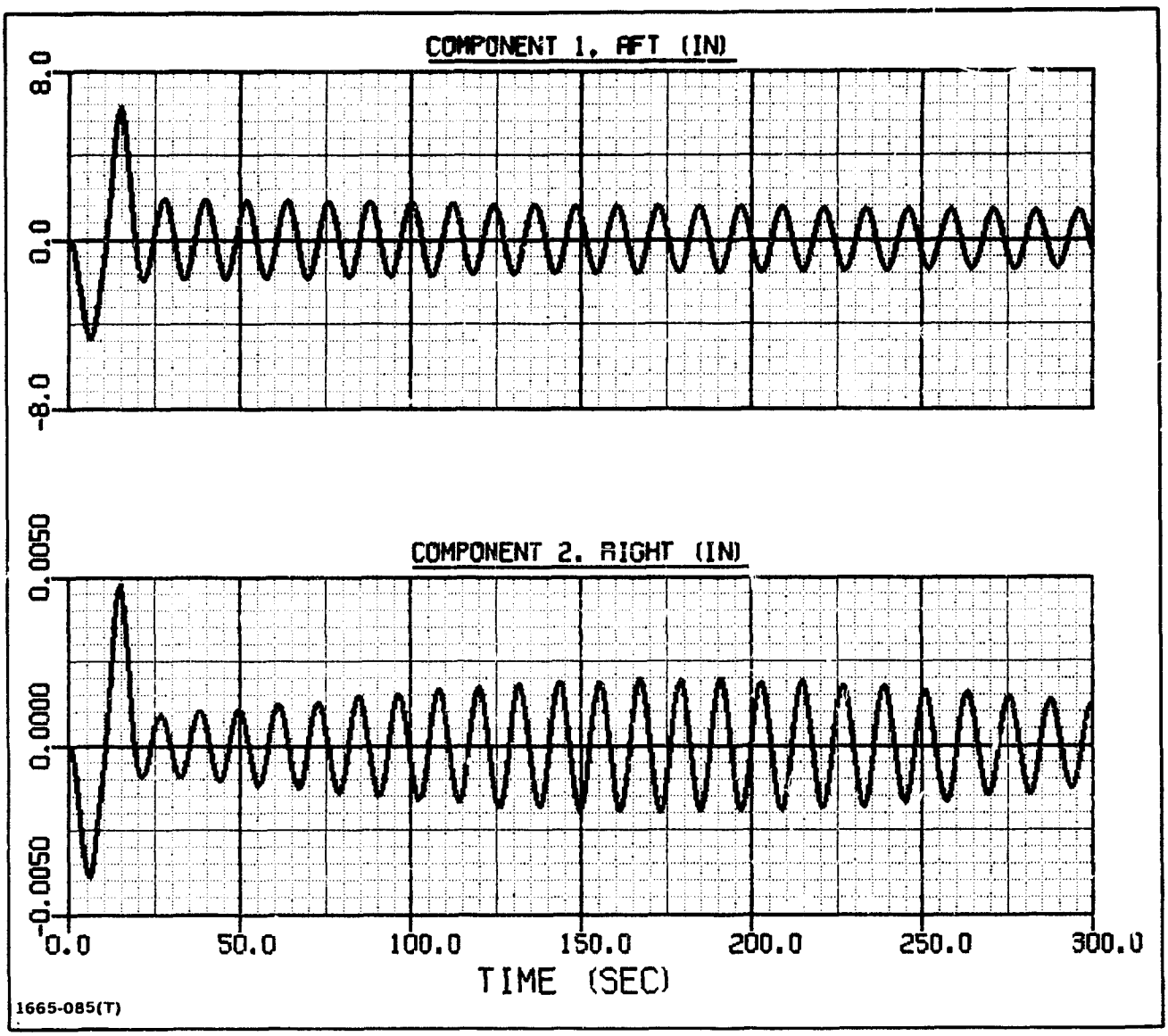

Fig. 2.52 Linear Displacement of Beam Tip Relative to Axes Fixed in Orbiter. Variable-Mode Technique

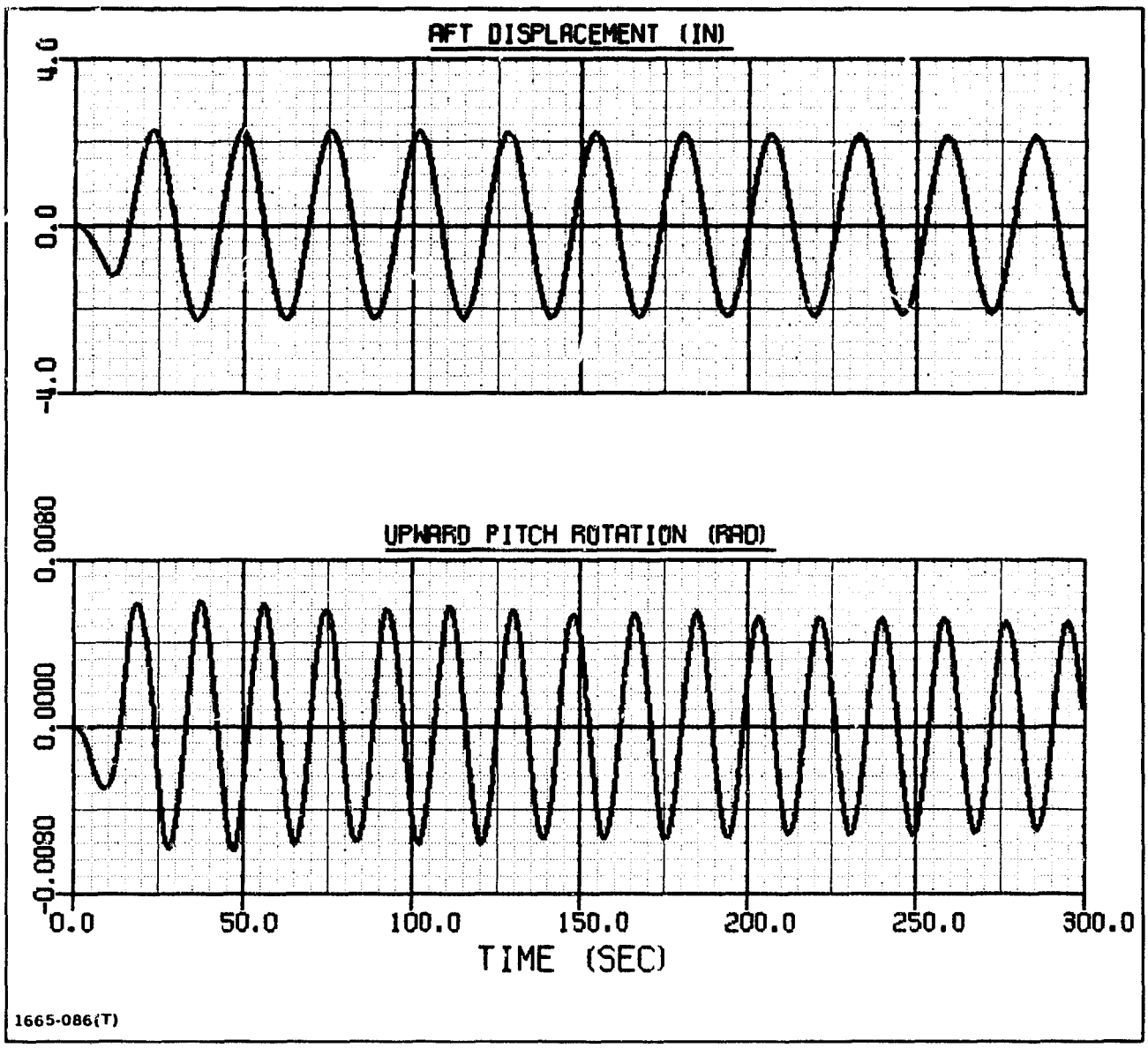

Fig. 2.53 Motion of Tip of Right Solar Panel Relative to Axes Fixed in Orbiter. Direct Numerical Integration

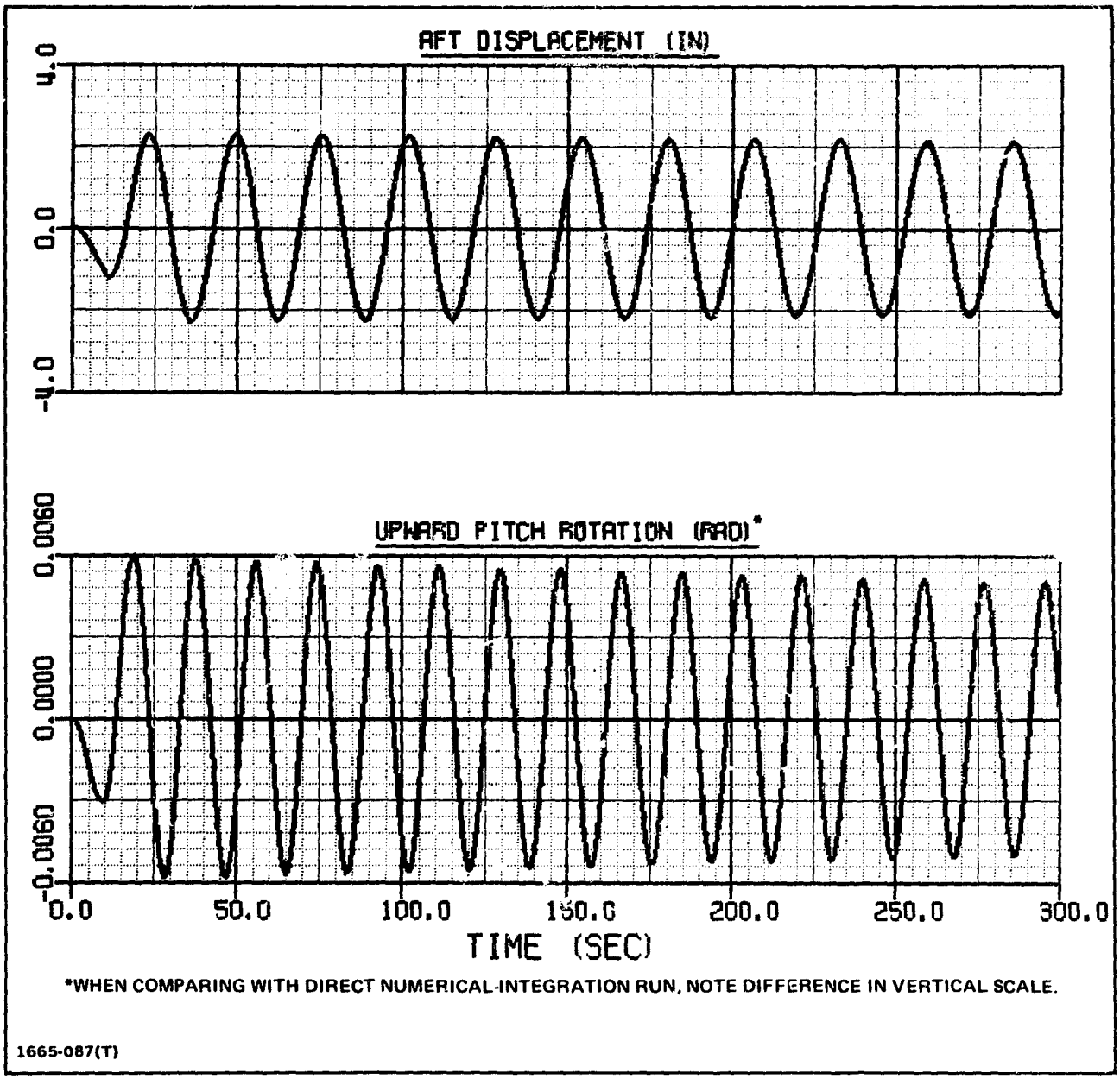

Fig. 2.54 Motion of Tip of Right Solar Panel Relative to Axes Fixed in Orbiter. Variable Mode Technique

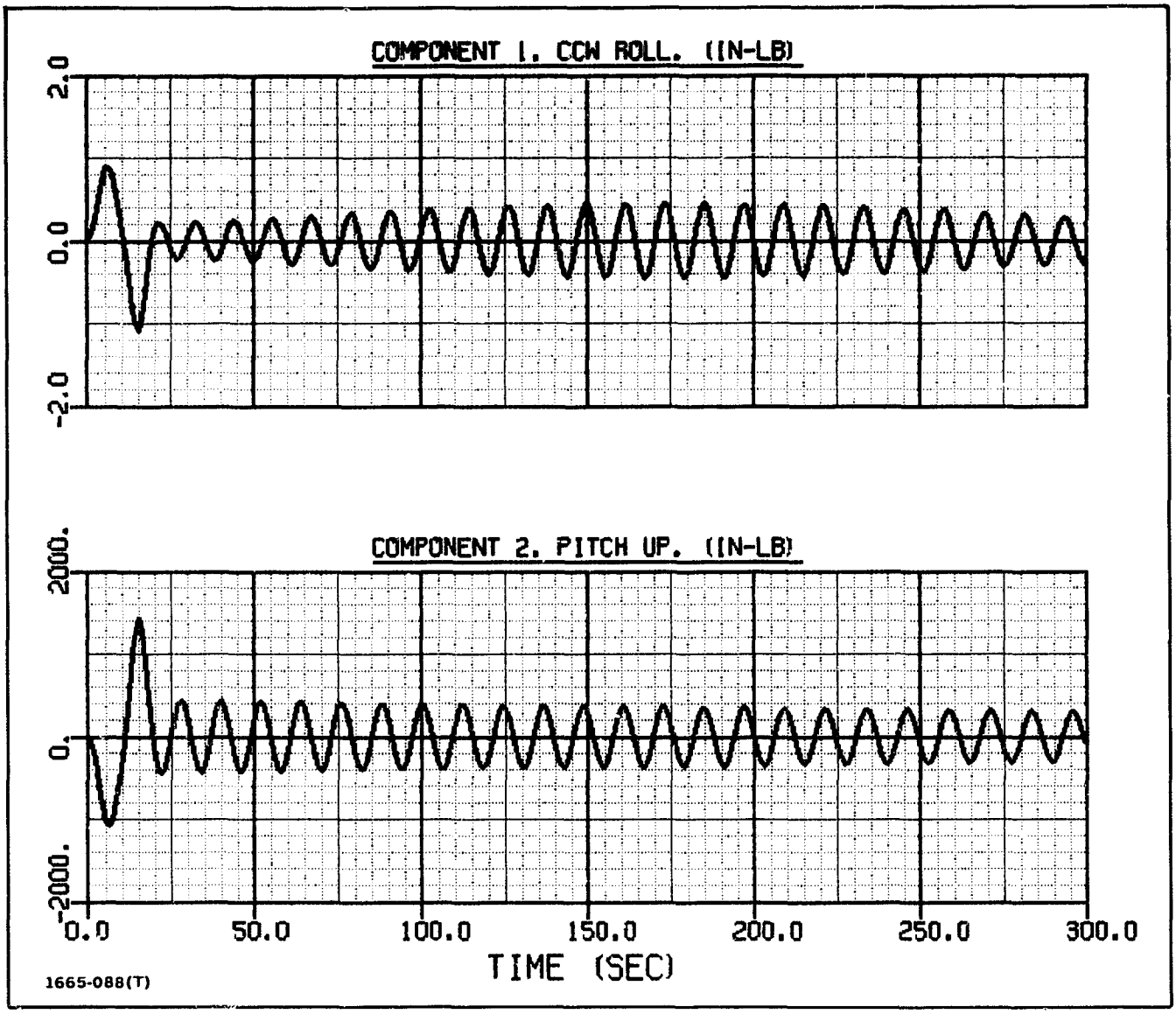

Fig. 2.55 Torques Applied by ABB to Beam. Direct Numerical Integration

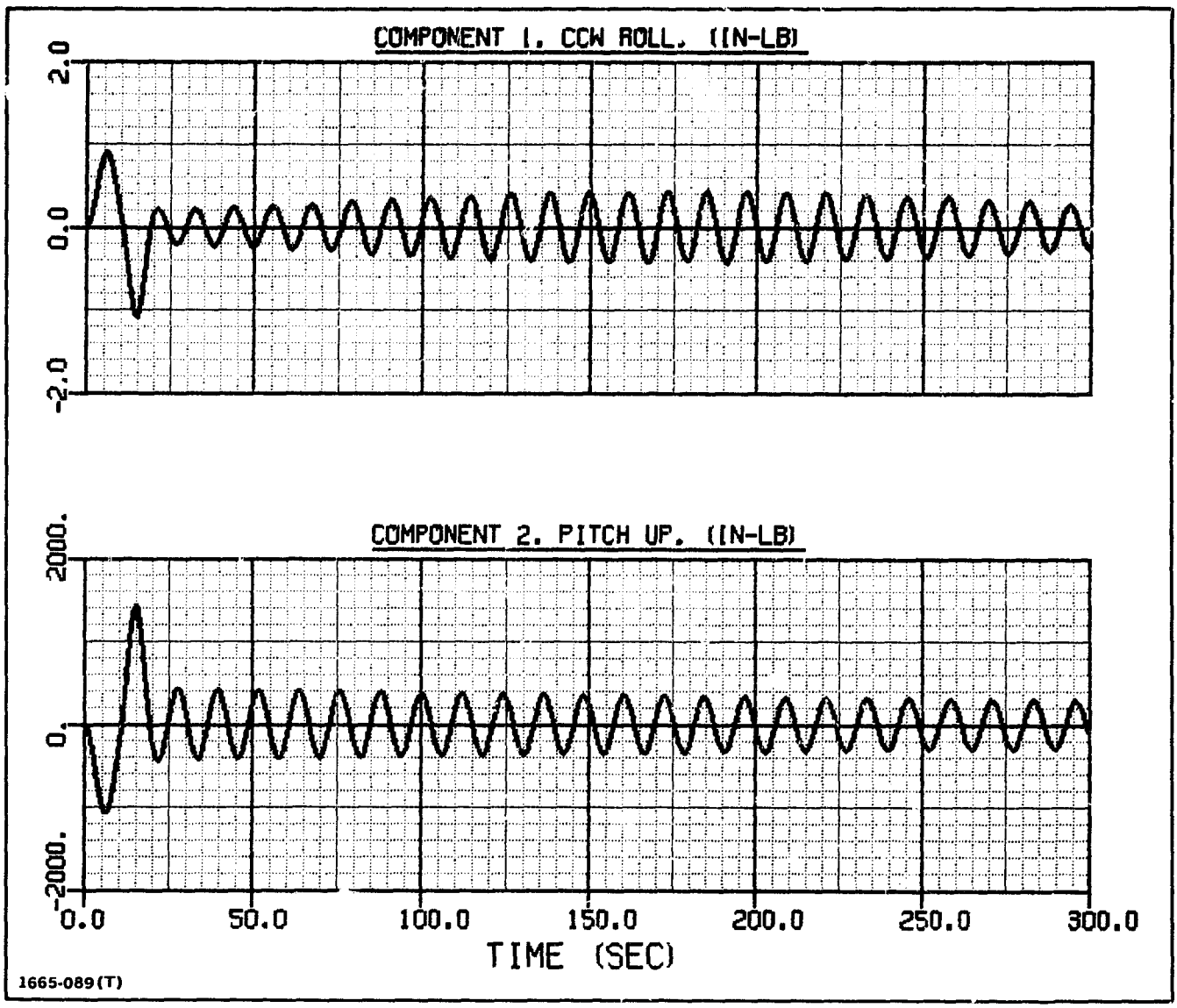

Fig. 2.56 Torques Applied by ABB to Beam. Variable Mode Technique

TABLE 2.4 COMPARISON OF VARIABLE-MODE TECHNIQUE WITH DIRECT NUMERICAL INTEGRATION

RUN NO.	TYPE	NUMBER OF MODES[1]	BEAM LENGTHS FOR COMPUTED MODES	MAXIMUM BEAM TIP DEFLECTION		NUMERICAL INTEGRATION STEP SIZE (SEC)	COMPUTER TIME[2]	
				(IN)	% ERROR		CPU SEC ON IBM 3033	% SAVINGS
37A	DIRECT NUMERICAL INTEGRATION	–	–	6.231	–	.10	257.2	–
37B	VARIABLE-MODE TECHNIQUE	24	3898 3957 4016	6.241	.16	.10	88.3	66
37C	VARIABLE-MODE TECHNIQUE	12	3898 3957 4016	6.281	.80	.20	37.8	85
37D	VARIABLE-MODE TECHNIQUE	12	3898 4016	6.277	.74	.20	36.3	86

(1) ALL LOWER-FREQUENCY MODES WERE USED. NUMBER INCLUDES RIGID-BODY MODES.
(2) INCLUDES TIME TO COMPUTE MODES.

R80-1685-141(T)

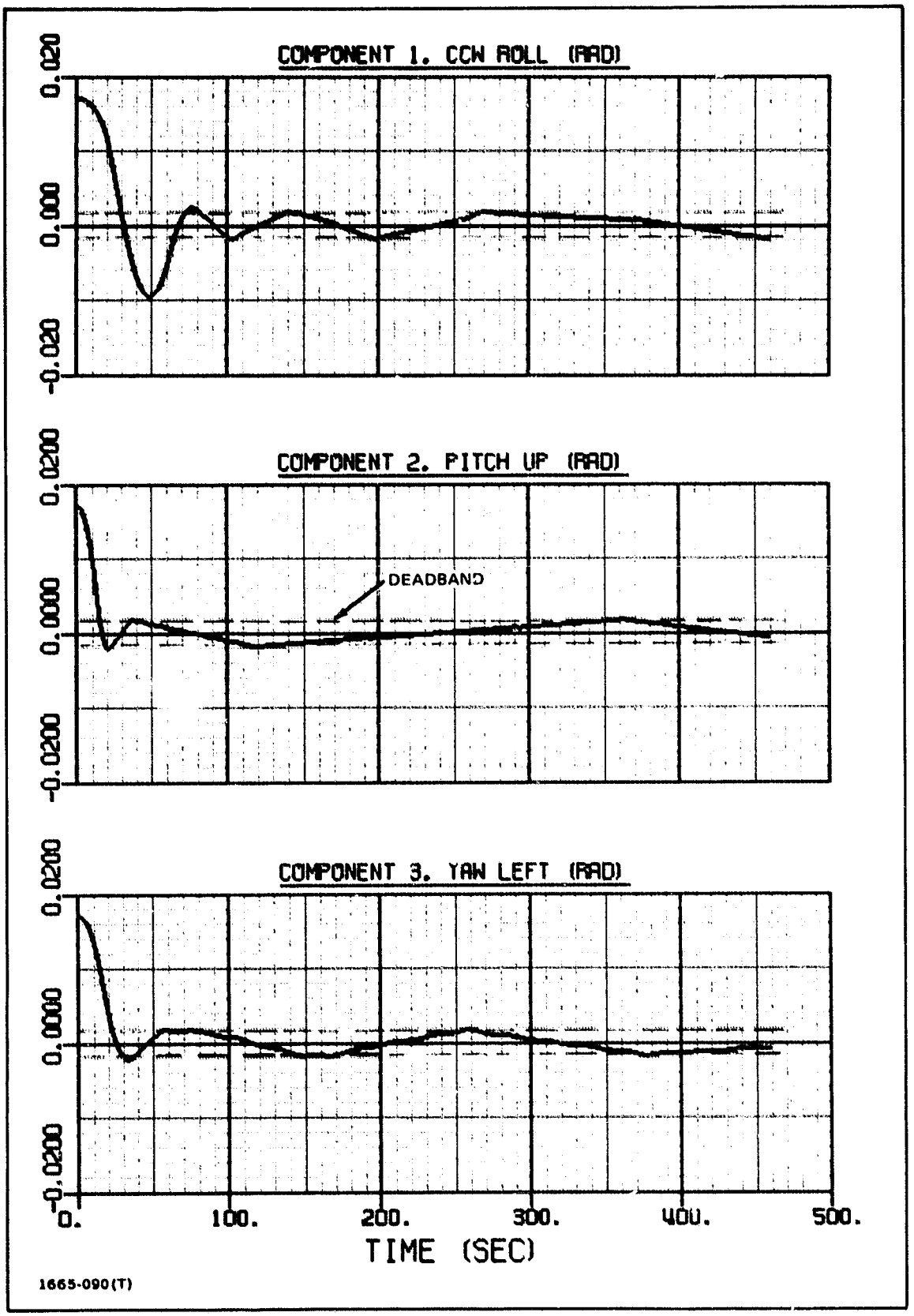

Fig. 2.57 Angular Displacement of Orbiter. Variable-Mode Method with Control System Active

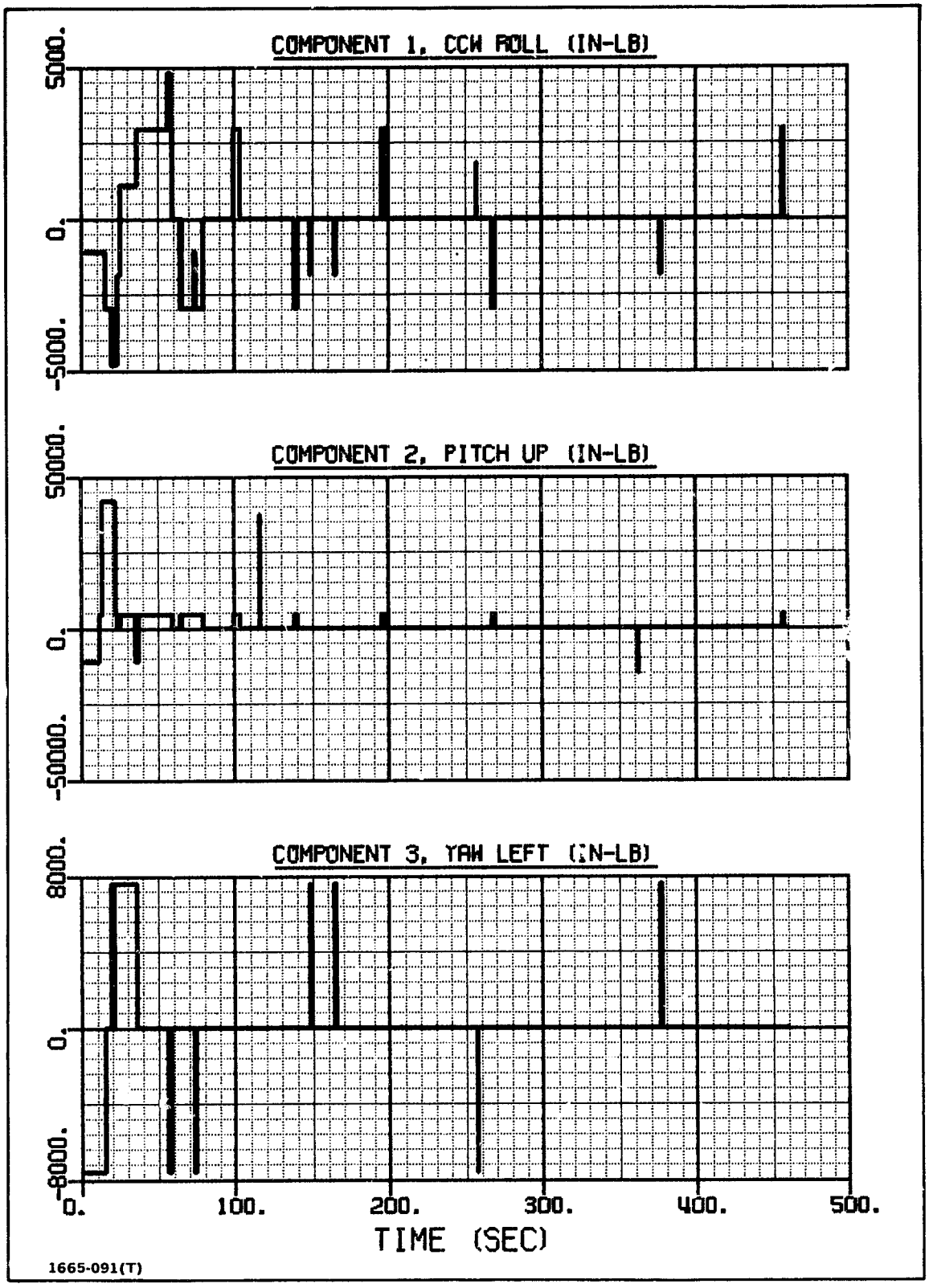

Fig. 2.58 Total Control Torque About Orbiter CM. Variable-Mode Method

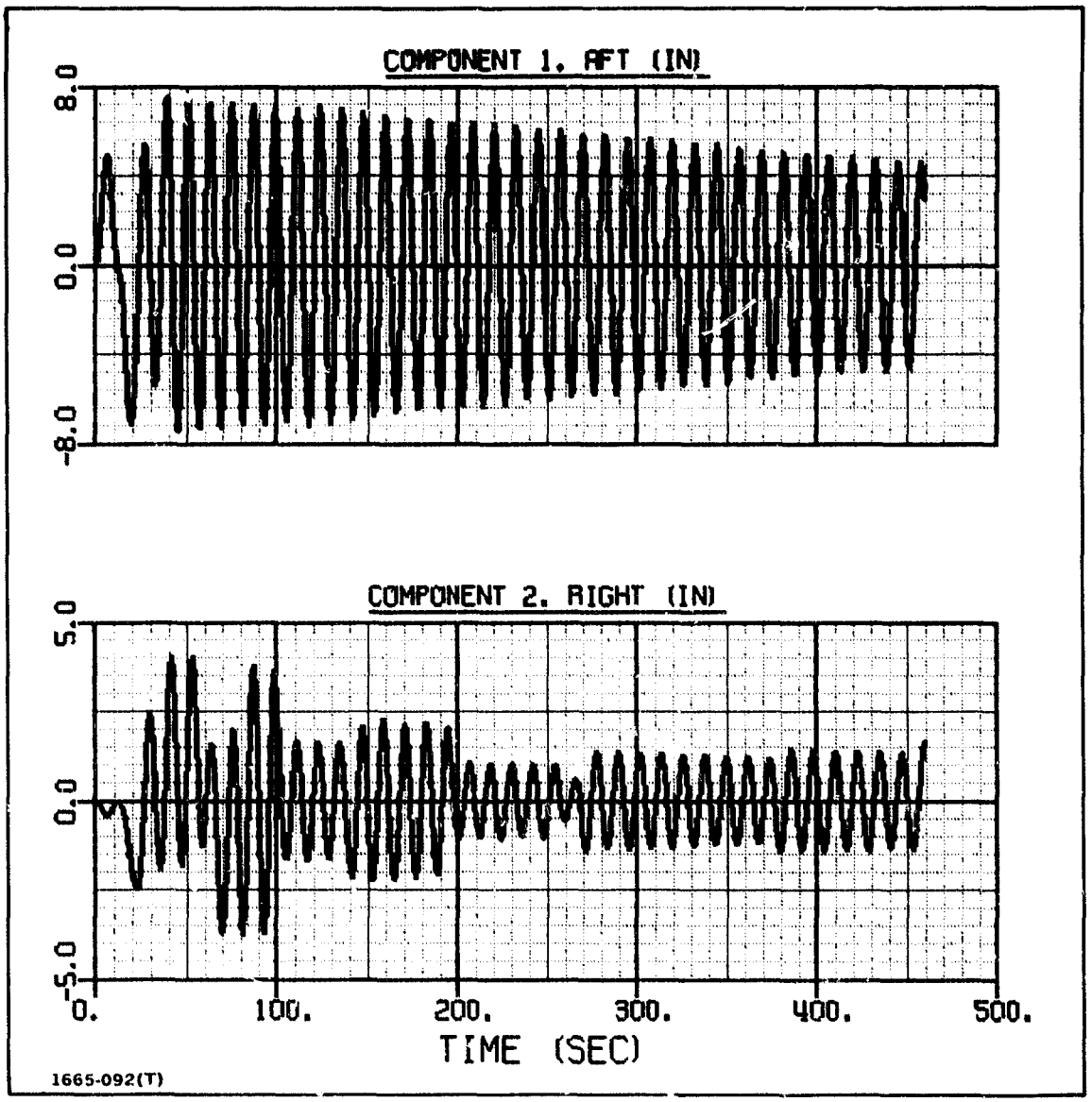

Fig. 2.59 Linear Displacement of Beam Tip Relative to Axes Fixed in Orbiter. Variable Mode Method with Control System Active

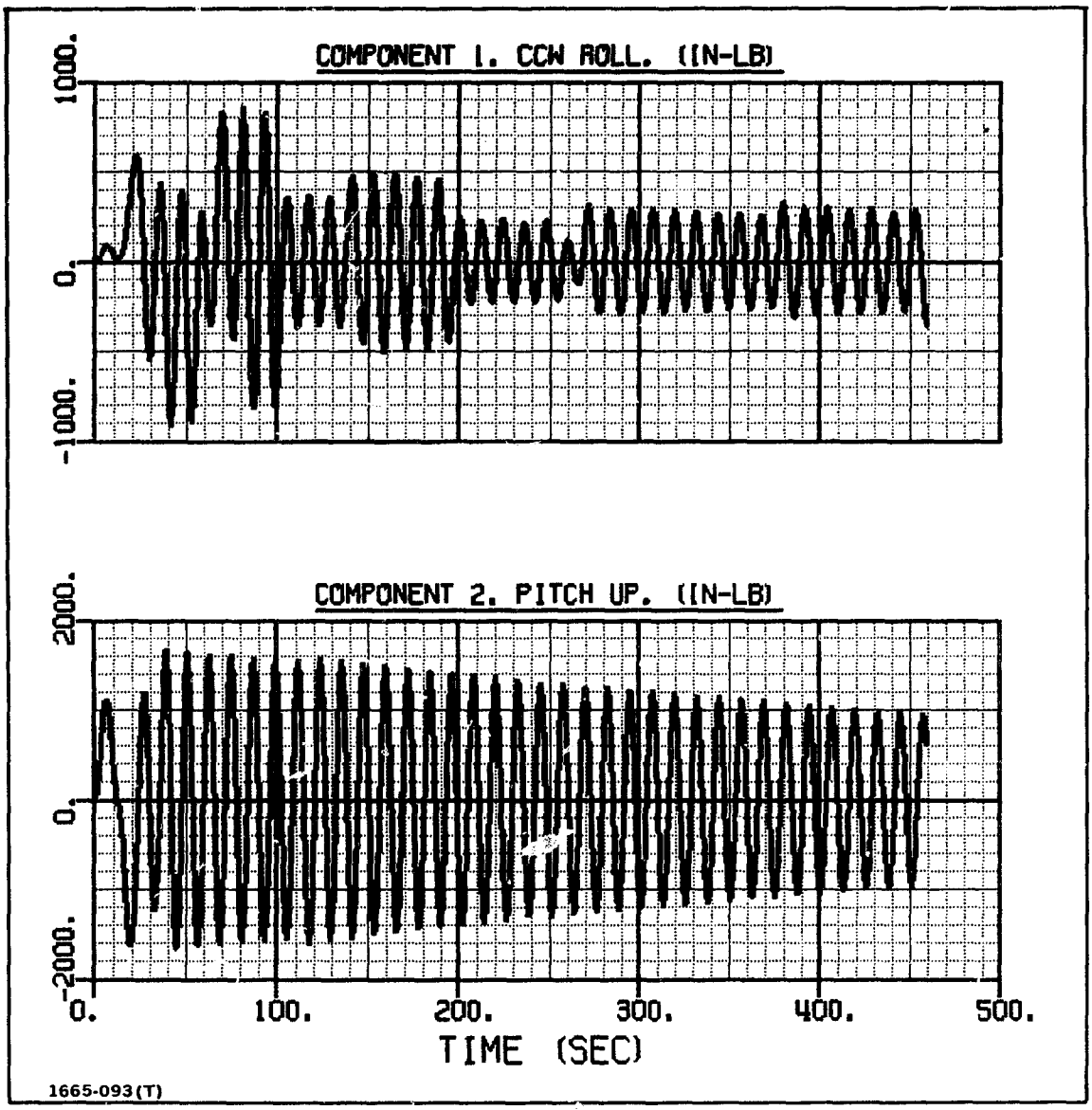

Fig. 2.60 Torques Applied by ABB to Beam. Variable-Mode Method with Control System Active

is very good; however, after some time passes, as the system drifts back and forth across the deadband, the correlation becomes inexact. The reason is that a very small difference in the solutions will cause the thrusters to turn on and off at slightly different times. This accentuates the difference in the motion, and the next time the thrusters turn on, the difference in the turn-on time in the two runs will be larger. This effect is cumulative, and after a while the thrusters turn on and off at very different times (compare Fig. 2.46 and 2.58). The effect occurs when the system drifts back and forth across the deadband because the thruster pulses are small and the minimum pulse width is .125 sec which is only represented by ten numerical-integration time intervals. In consequence, a theoretical small delay in the time to switch a thruster off could result in an impulse error which is as large as ten percent. It is not practical to use a much smaller integration time interval for the entire run; however, this could be corrected by reprogramming to use two intervals: one when all thrusters are off, and a smaller interval when any thruster is on. This technique has been successfully used in the SPACE12B program which is an updated version of SPACE10 described in Ref. 2. It should be noted that the correlation problem is not related to the variable-mode technique. The problem occurred when correlations between direct numerical-integration and conventional modal analysis were attempted with the beam length held fixed. Also, it was demonstrated that more of the run correlates when the numerical-integration step size is decreased. The step size of .0125 sec, used in the two runs that are presented, was the smallest step size that was used.

3 - BEAM RELOCATION

In the beam relocation problem, the completed beam is grasped by the RMS and moved through a large angle by a rotation about the shoulder joint (Point h in Fig. 2 of the Summary and Introduction). The power module with its solar panels is present but is not shown in the figure.

3.1 Derivation of Equations of Motion

The general idealization shown in Fig. 3.1 is used to derive the equations of motion. The platform, Body A, is composed of the orbiter and the power supply including its solar panels. Body B consists of the RMS and the beam. The two bodies are connected by the hinge h located on the orbiter by the coordinates $\{a_h\}$ relative to the orbiter mass center, Node 100. As previously, a set of axes $\underset{\sim}{Z}$, consisting of the Z_1, Z_2, and Z_3 axes, is fixed in space. The $\underset{\sim}{X}$ axes are fixed in the orbiter at Node 100, and the $\underset{\sim}{Y}$ axes are fixed in Body B in the rotating part of the hinge. The vector $\{a_h\}$ is expressed in the $\underset{\sim}{X}$ axes. The deformation of any node m_i in Body A is $\{u_i\}$, and the deformation of any node m_j in Body B is $\{v_j\}$. The undeformed locations of these nodes are $\{a_i\}$ and $\{b_j\}$, respectively. $\{a_i\}$ and $\{u_i\}$ are expressed in $\underset{\sim}{X}$ axes, and $\{b_j\}$ and $\{v_j\}$ are expressed in $\underset{\sim}{Y}$ axes.

The method used in developing the equations of motion is summarized in this section; a detailed derivation is presented in Appendix J. First, the equations of motion are written for Body A and Body B, separately. In this step, the loads that each body exerts on the other, at point h, are considered to be externally applied loads.

The equations for Body B are written using coordinates that are relative to the rotating $\underset{\sim}{Y}$ axis system which has its origin at point h. Very stiff areas in the structure are idealized as rigid areas in order to eliminate high-frequency effects so that direct numerical integration would be practical. In accordance with the constraint procedure of Appendix D, the equations are first rearranged and combined so that they are in the Lagrangian form, i.e., with a symmetric mass matrix. Then the constraint procedure is used to delete the forces of constraint due to the rigidities and to reduce the number of coordinates by the number of constraint equations.

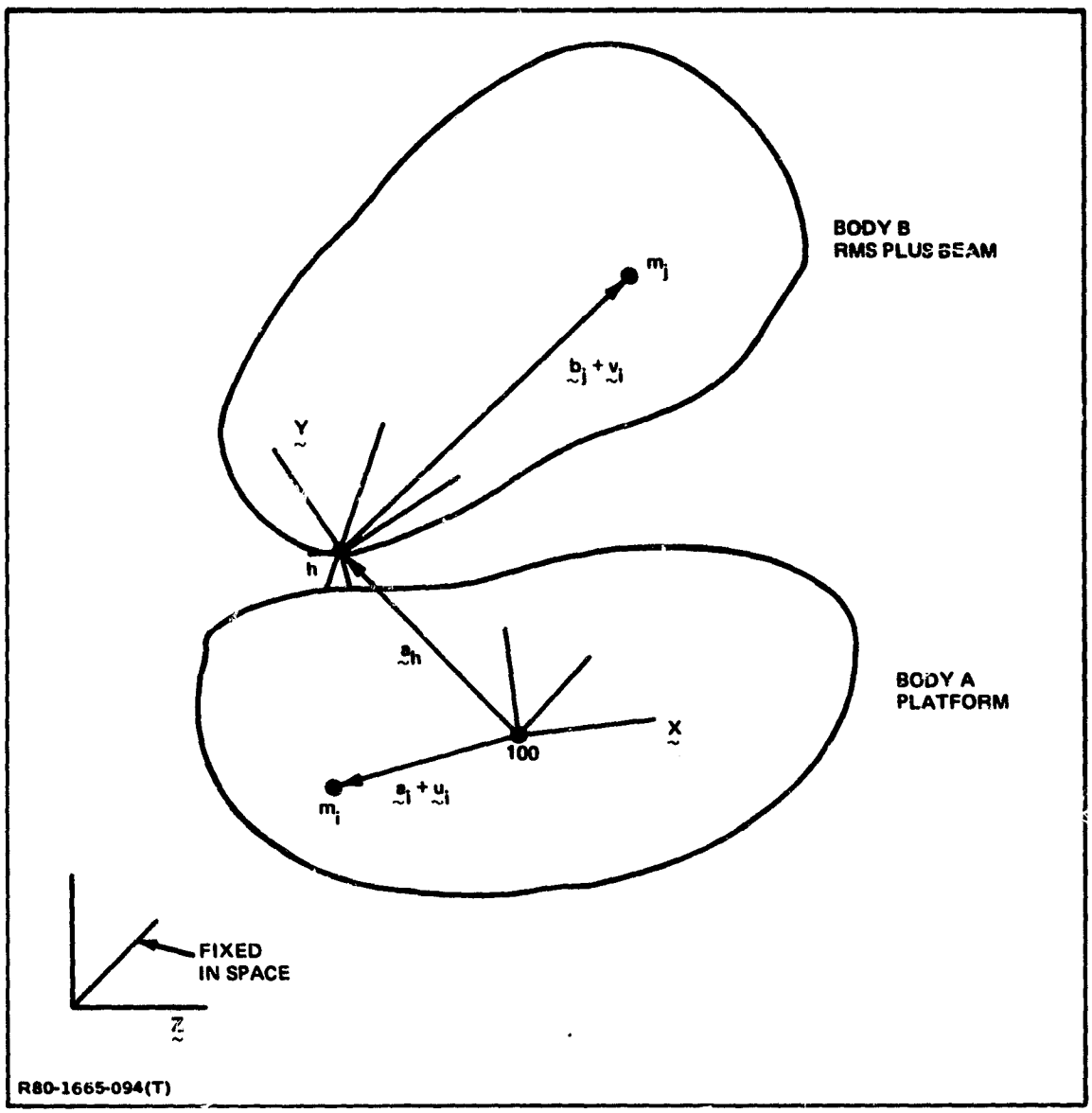

Fig. 3.1 General Idealization for Beam Relocation Problem

The equations of motion for Body A, taken as a free body, are obtained from the equations of motion for the Beam Fabrication Problem by setting the beam terms to zero. The equations for Body B and Body A are combined into the following matrix equation:

$$\left[\begin{array}{ccc|cc|c} M'_{bb} & M'_{bt} & M'_{br} & & & \\ M'^{T}_{bt} & M'_{tt} & M'_{tr} & & & \\ M'^{T}_{br} & M'^{T}_{tr} & M'_{rr} & & & \\ \hline & & & \bar{V}_1 & \bar{V}_2 & \\ & & & \bar{V}_3 & \bar{V}_4 & \\ & & & & & M_{pp} \end{array}\right] \left\{\begin{array}{c} \ddot{w} \\ \ddot{u}_h \\ \ddot{\omega} \\ \ddot{u}_{100} \\ \ddot{\theta}_{100} \\ \ddot{u}_p \end{array}\right\} + \left[\begin{array}{ccc|cc|c} K_{bb} & & & & & \\ & 0 & & & & \\ & & 0 & & & \\ \hline & & & & & \\ & & & & & \\ & & & & & K_A \end{array}\right] \left\{\begin{array}{c} w \\ 0 \\ 0 \\ u_{100} \\ \theta_{100} \\ u_p \end{array}\right\} = \left\{\begin{array}{c} \bar{d}_b \\ \bar{d}_t \\ \bar{d}_r \\ \bar{F}_R \\ \bar{T}_R \\ f_p \end{array}\right\} \quad (3\text{-}1)$$

where the upper equations represented in (3-1) are the equations for Body B and the lower equations are the equations for Body A. {w} contains those deformation components in the $\{v_i\}$'s (for Body B) that are independent after the rigidity constraints are applied (see (K6) of Appendix K); i.e.,

$$\{w\} = \begin{Bmatrix} v_{11} \\ v_{12} \\ \hline v_{21} \\ v_{22} \\ \hline \vdots \\ \hline v_{q-2,1} \\ v_{q-2,2} \\ \hline v_{q-1,2} \\ v_{q-1,3} \\ \hline v_{q1} \\ v_{q2} \end{Bmatrix} \tag{3-2}$$

The node numbering scheme for Body B is shown in Fig. 3.2. As indicated all of the v_{i3}'s except $v_{q-1,3}$ have been eliminated as independent coordinates. Also $v_{q-1,1}$ and $v_{q,3}$ were eliminated by rigidization-constraint equations. The vector $\{u_p\}$ in (3-1) contains the solar-panel deformations; i.e.,

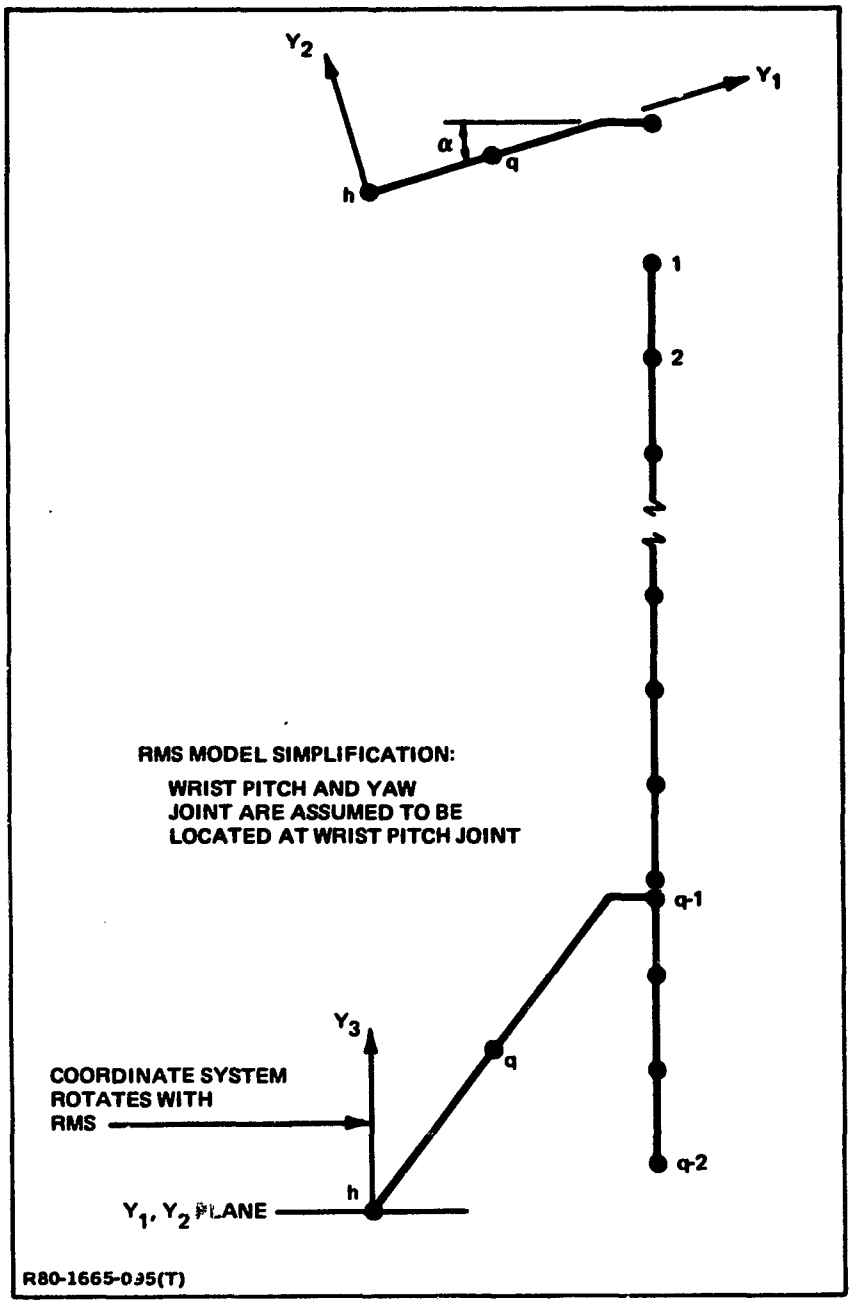

Fig. 3.2 Node Numbering Scheme for Body B

$$\{u_p\} = \begin{Bmatrix} u_{p_1} \\ \theta_{p_1} \\ \hline u_{p_2} \\ \theta_{p_2} \\ \hline \vdots \\ \hline u_{p_6} \\ \theta_{p_6} \end{Bmatrix} \qquad (3\text{-}3)$$

The other terms in (3-1) are as follows:

$\{u_h\}$ = deformation vector of hinge, Node h, expressed in $\underset{\sim}{Z}$ axes

$\{\omega\}$ = total angular velocity of $\underset{\sim}{Y}$ axes expressed in $\underset{\sim}{Y}$ axes

$[K_{bb}]$ = stiffness matrix of Body B cantilevered at point h for deformation components along $\underset{\sim}{Y}$ axes.

$[K_A]$ = stiffness matrix of Body A, taken as an unsupported body, for deformation components along $\underset{\sim}{Z}$ axes

and the vector on the right side of (3-1) contains externally applied loads, forces of constraint exerted at Point h, and lower-derivative mass-times-acceleration terms.

In the program developed for this project, the manipulator rotation angle ϕ at the hinge, or shoulder joint, (see Fig. 3.3) is prescribed as a function of time. Consequently, from geometry, the hinge linear and angular acceleration can be expressed in terms of the orbiter coordinates by using an equation of the following form (see (J59)):

$$\begin{Bmatrix} \ddot{u}_h \\ \dot{\omega} \end{Bmatrix} = \begin{bmatrix} I_3 & U_q \\ 0 & D \end{bmatrix} \begin{Bmatrix} \ddot{u}_{00} \\ \ddot{\theta}_{00} \end{Bmatrix} + \begin{Bmatrix} 0 \\ K \end{Bmatrix} \qquad (3\text{-}4)$$

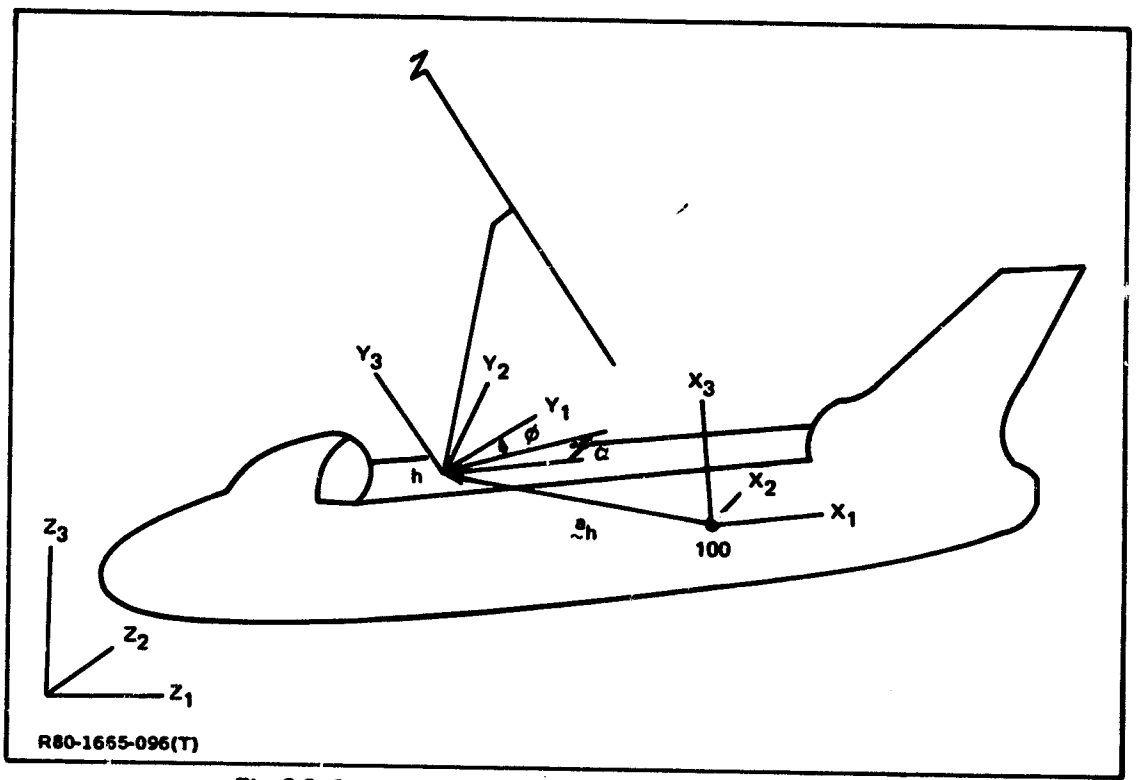

Fig. 3.3 Coordinates Used in Development of Hinge Equations

where $\{\psi\}$ is a function of ϕ, $\dot{\phi}$, and $\ddot{\phi}$ which are prescribed quantities. Thus, the acceleration vector in (3-1) can be expressed in terms of fewer coordinates as follows:

$$\begin{Bmatrix} \ddot{w} \\ \ddot{u}_h \\ \dot{\omega} \\ \ddot{u}_{100} \\ \ddot{\theta}_{100} \\ \ddot{u}_P \end{Bmatrix} = \begin{bmatrix} I_\nu & & & & \\ & I_3 & U_\psi & & \\ & & D & & \\ & I_3 & & & \\ & & I_3 & & \\ & & & & I_{12} \end{bmatrix} \begin{Bmatrix} \ddot{w} \\ \ddot{u}_{100} \\ \ddot{\theta}_{100} \\ \ddot{u}_P \end{Bmatrix} + \begin{Bmatrix} 0 \\ 0 \\ \psi \\ 0 \\ 0 \\ 0 \end{Bmatrix} \tag{3-5}$$

where ν are the number of independent coordinates in Body B, i.e., the dimension of $\{w\}$. Also, the displacement vector in (3-1) can be contracted by the equation

$$\begin{Bmatrix} w \\ 0 \\ 0 \\ u_{100} \\ \theta_{100} \\ u_P \end{Bmatrix} = \begin{bmatrix} I_\nu & & & \\ & & & \\ & I_3 & & \\ & & I_3 & \\ & & & I_{12} \end{bmatrix} \begin{Bmatrix} w \\ u_{100} \\ \theta_{100} \\ u_P \end{Bmatrix} \tag{3-6}$$

The constraint procedure of Appendix D is also applicable to the case where angular velocities appear among the derivatives of the coordinates. The procedure is the substitute (3-5) and (3-6) into (3-1) and to premultiply the result by the transpose of the acceleration-vector coefficient matrix on the right side of (3-5). The resulting equation is

$$[\Lambda]\{\ddot{y}\} + [C]\{\dot{y}\} + [K_T]\{y\} = \{s\} \tag{3-7}$$

where the damping terms $[C]\{y\}$ have been added at this stage to attenuate the response, the form of the mass matrix $[\Lambda]$ is specified in Appendix J, $\{s\}$ contains lower derivative mass-times-acceleration terms as well as external loads

and its form is also specified in Appendix J. The hinge constraint loads have been eliminated by the constraint procedure and do not appear in (3-7). Also, in (3-7)

$$\{y\} = \begin{Bmatrix} \underset{\sim}{w} \\ \underset{\sim}{u}_{100} \\ \underset{\sim}{\theta}_{100} \\ \underset{\sim}{u}_{p} \end{Bmatrix} \tag{3-8}$$

$$[K_T] = \begin{bmatrix} \underset{\sim}{K}_{bb} & \\ & \underset{\sim}{K}_{A} \end{bmatrix} \begin{matrix} \nu \\ 18 \end{matrix} \tag{3-9}$$

and, as in the Beam-Fabrication Problem, the damping was assumed to be proportional to the stiffness matrix; i.e.,

$$[C] = \alpha [K] \tag{3-10}$$

The solutions are generated by solving (3-7) for $\{\dot{y}\}$ and numerically integrating $\{\dot{y}\}$ and $\{\dot{y}\}$ to obtain $\{\dot{y}\}$ and $\{y\}$ at the next time point. The same fixed-interval Runge-Kutta scheme was used for this purpose as was used for the Beam Fabrication Problem.

Once these solutions are obtained, the loads in the RMS at the shoulder and at the wrist can be obtained. Equations for these quantities are presented in Appendix L.

If the hinge control torque is specified instead of the hinge angle ϕ, this angle becomes an unknown and the number of equations increase by one. The derivation of the equations of motion for this case is similar to the derivation in this section. The equations are developed in Appendix M; however they were not programmed. A special case of this problem is the freewheeling situation where the hinge control torque is specified as zero.

3.2 Motion of Hinge Angle

The specified motion of the hinge angle at the RMS shoulder is indicated in Fig. 3.4. It consists of a constant angular-acceleration phase, followed by a constant angular-velocity cruise, and then a constant angular deceleration until $\dot{\phi} = 0$. The equations describing this motion are analogous to those developed for beam growth in the Beam Fabrication Problem (see Appendix C), except that only one velocity pulse occurs.

3.3 Numerical Results

Properties of the structure and the assumed characteristics of the RMS motion are presented in Appendix I. The idealization of Body A, the platform, is the same as the idealization for the platform used in the beam-fabrication problem. The idealization for Body B is shown in Fig. 3.5. The beam is 105 m long. The stiffness matrix of Body B cantilevered at the hinge $[K_{bb}]$ was obtained by using NASTRAN and was transferred to the FORTRAN program.

3.3.1 Modes of Vibration

The vibration modes of Body B were computed by using NASTRAN. The first six modes are illustrated in Figs. 3.6 - 3.11. As indicated, the lower-frequency modes are primarily beam bending. Significant manipulator deformations occur in Modes 5 and 6.

Modes were also computed for the total system with the RMS handling a 39 m beam. This was done for manipulator angles ϕ of 0 and 90 deg. It was found that the frequencies of the modes associated with platform motion did not change with manipulator angle. They remained fixed at the values presented in Table 2.1. Also, the change in the frequencies of the modes involving motion of Body B was small. The system with the 105 m beam will probably also have these modal characteristics with the modes primarily involving motion of Body B being very close to the modes of Figs. 3.6 - 3.11.

3.3.2 Average-Angle Technique

In addition to the direct numerical-integration solutions, results will be presented for an approximate technique which will be referred to as the Average-Angle Technique. This method is analagous to the Average-Length Technique that was evaluated for the Beam Fabrication Problem. In the Average-Angle Technique, the manipulator angle ϕ is held fixed at its average

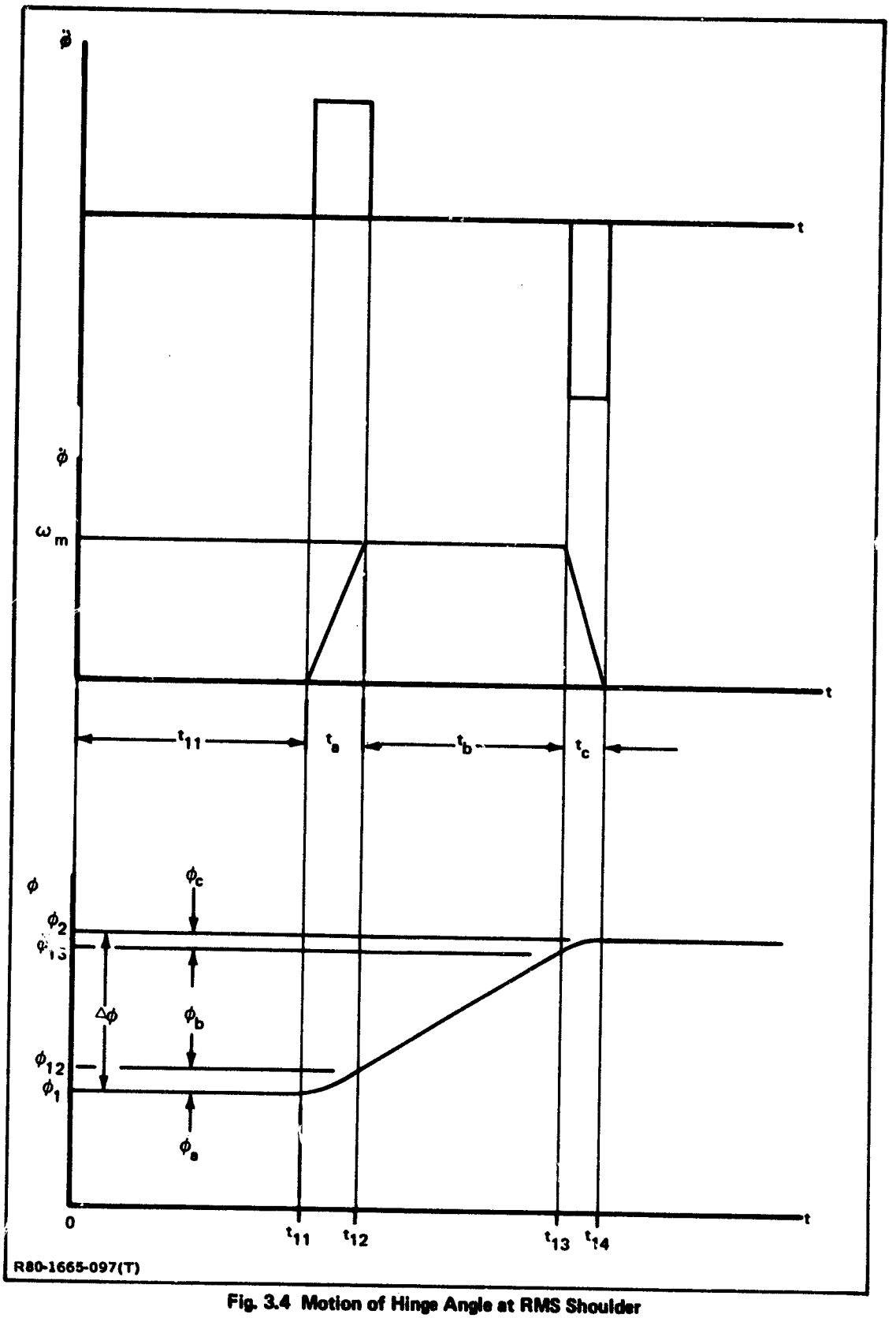

Fig. 3.4 Motion of Hinge Angle at RMS Shoulder

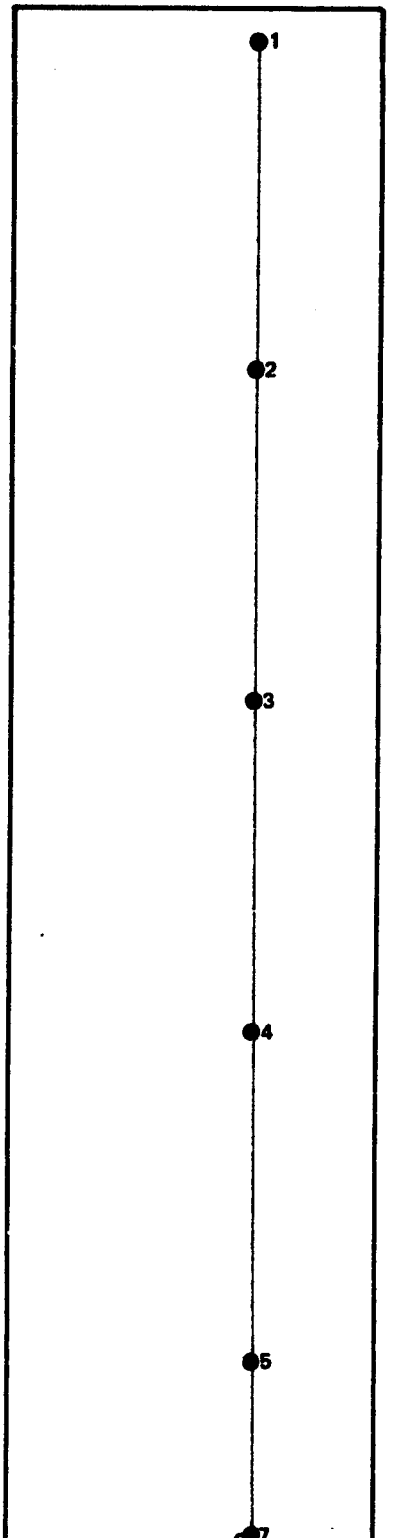

Fig. 3.5 Idealization of Body B

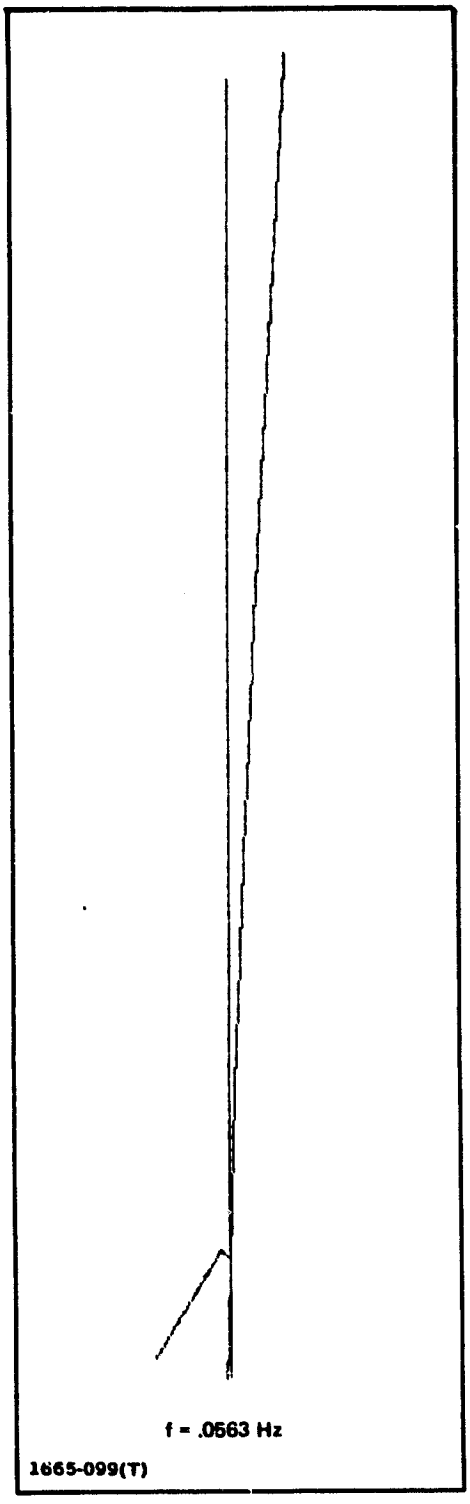

Fig. 3.6 Mode 1 of Body B, Lateral Bending

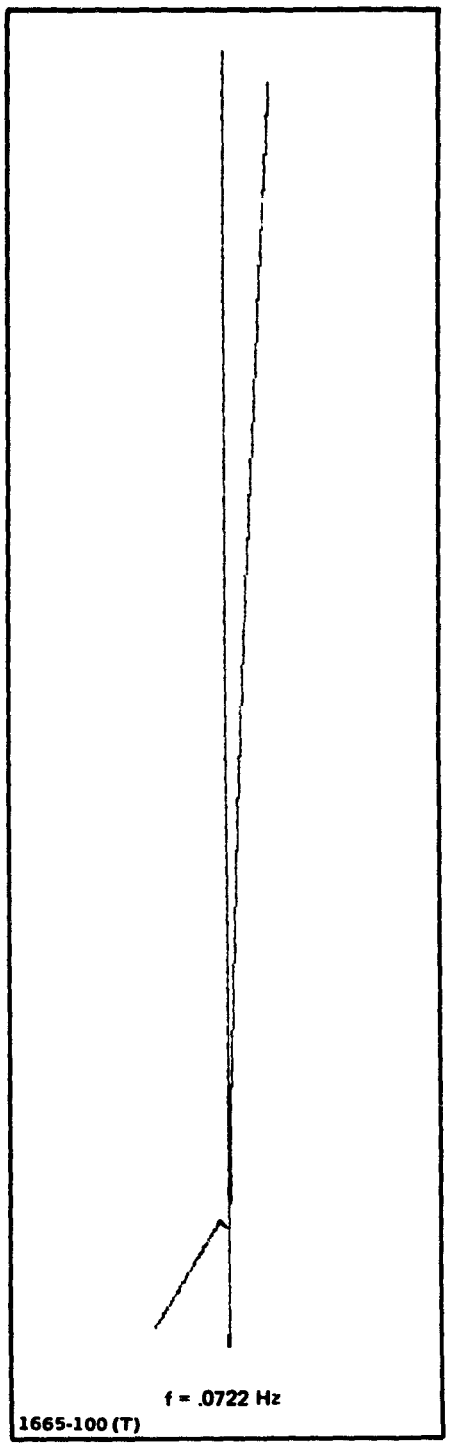

Fig. 3.7 Mode 2 of Body B, Fore-and-Aft Bending

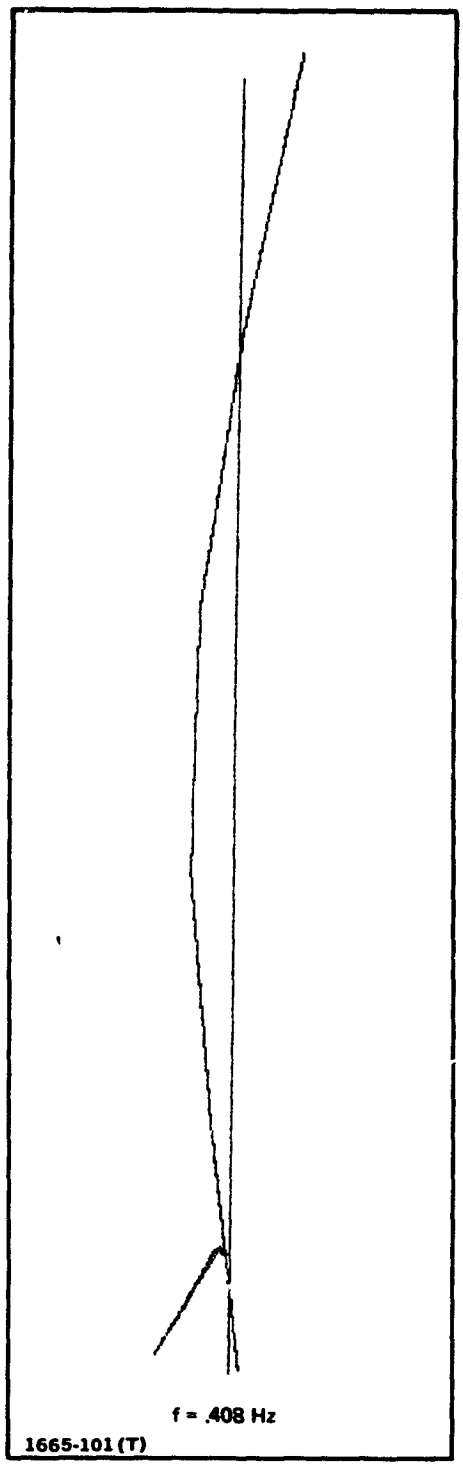

Fig. 3.8 Mode 3 of Body B, Second Lateral Bending Shape

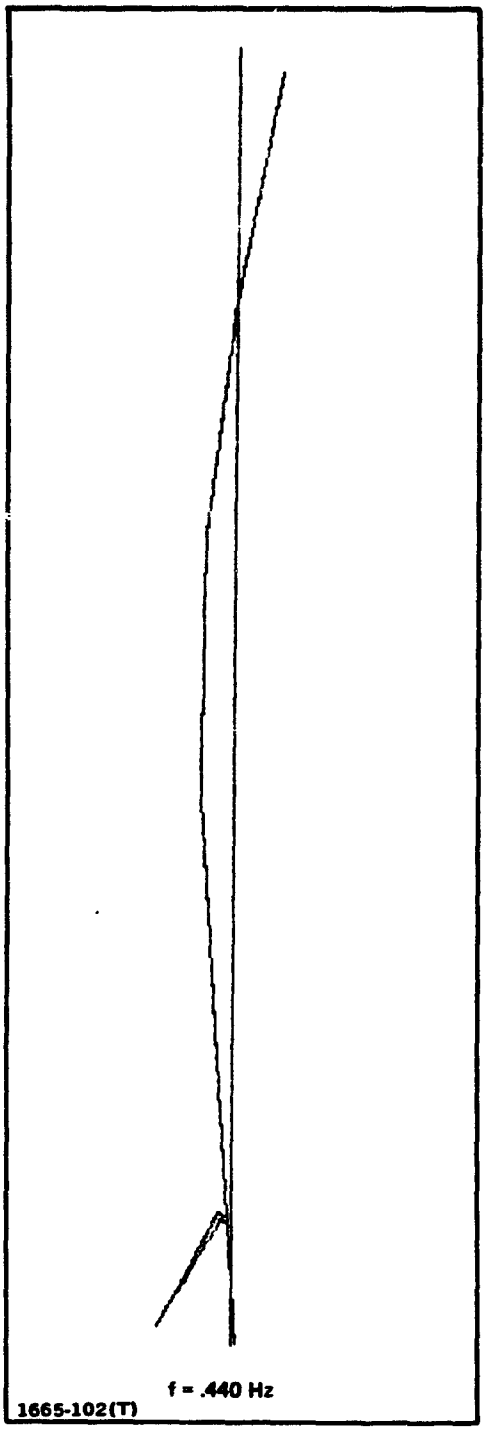

Fig. 3.9 Mode 4 of Body B, Second Fore-and-Aft Bending Shape

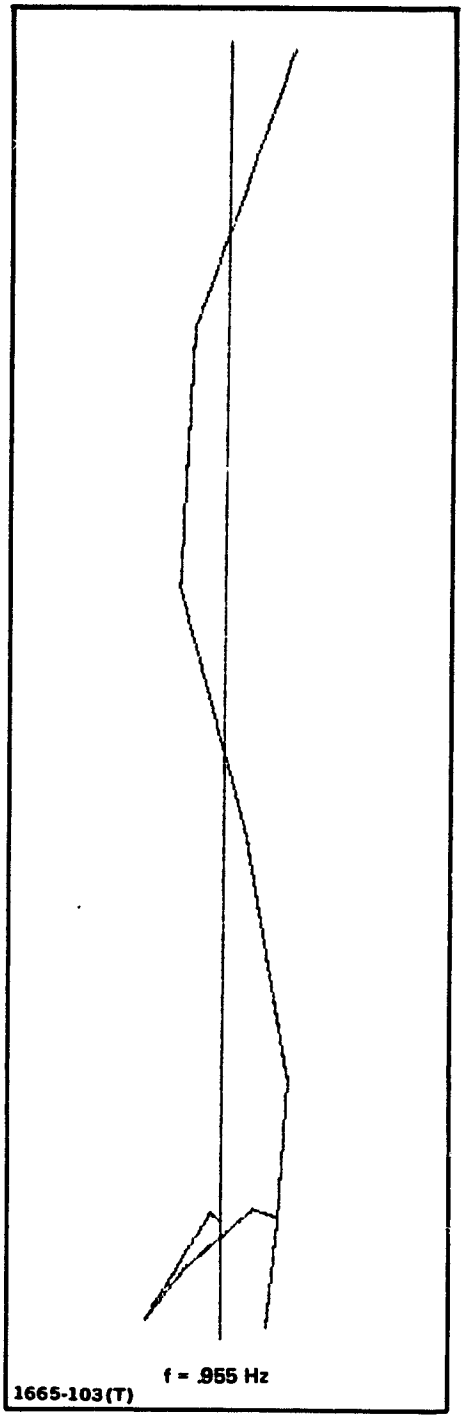

Fig. 3.10 Mode 5 of Body B

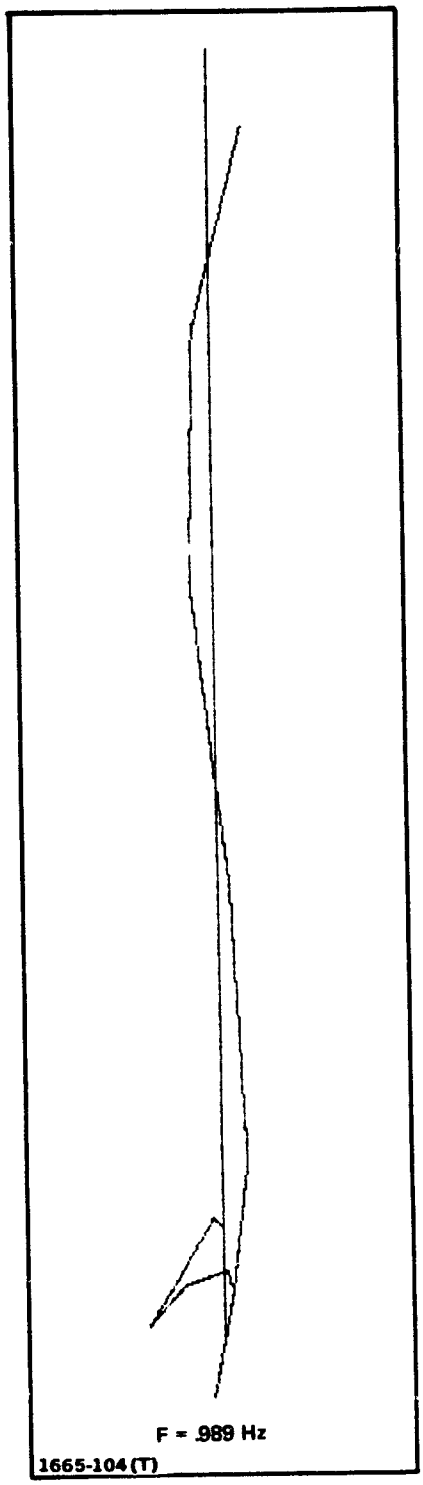

Fig. 3.11 Mode 6 of Body B

value during the run. Loads that are equal to the inertia loads (reverse mass-times acceleration loads) due to varying geometry are applied to the nodes on Body B only. The accelerations that are used in computing the inertia loads are the accelerations that Body B would experience if it were rigid and rotated at the angular acceleration $\ddot{\phi}$ of the $\underset{\sim}{Y}$ axes with the orbiter held fixed. Centrifugal forces were not included, although it is believed that they would improve the results. This technique was attempted because an analysis of the terms on the right side of the equations of motion indicated that they would be well approximated by applying the described inertia loads.

3.3.3 Illustration for 20 Degree Rotation of Shoulder and Comparison With Average-Angle Technique

In the run which will be illustrated, the RMS is moved from a shoulder-rotation angle ϕ = 30 deg to ϕ = 50 deg as indicated in Fig. 3.12. In this run, the angular velocity does not reach the cruise rate of .0062 rad/sec (.36 deg/sec); therefore, there is only an acceleration and a deceleration phase.

The maximum linear deflection at the tip of the beam is in the fore and aft direction and is under 4.5 in as indicated in Fig. 3.13. It is seen that the pitching deformation is biased in accordance with the applied acceleration at the hinge shown in Fig. 3.12. The same deformation components obtained by the Average-Angle Technique are shown in Fig. 3.14. By comparing Figs. 3.13 and 3.14, it is seen that the new technique provides a very good approximation to the solution.

The roll and pitch rotations of the orbiter are shown in Fig. 3.15. The yaw rotation is small and is not shown. After the RMS motion has been completed at about 133 sec, the average angular motion of the orbiter becomes a constant. This is consistent with the conservation of angular momentum. By comparing Figs. 3.15 and 3.16, it is seen that, the Average-Angle Technique provides a good approximation to the rigid-body motion of the system.

Figures 3.17 - 3.20 show that the wrist and hinge (or shoulder) torques in the RMS can also be well approximated by the Average-Angle Technique. The wrist torque is under 800 in-lbs and the hinge torque is under 1000 in-lbs. These torques are well below the slip torques of 2770 in-lbs and 9260 in-lbs, respectively.

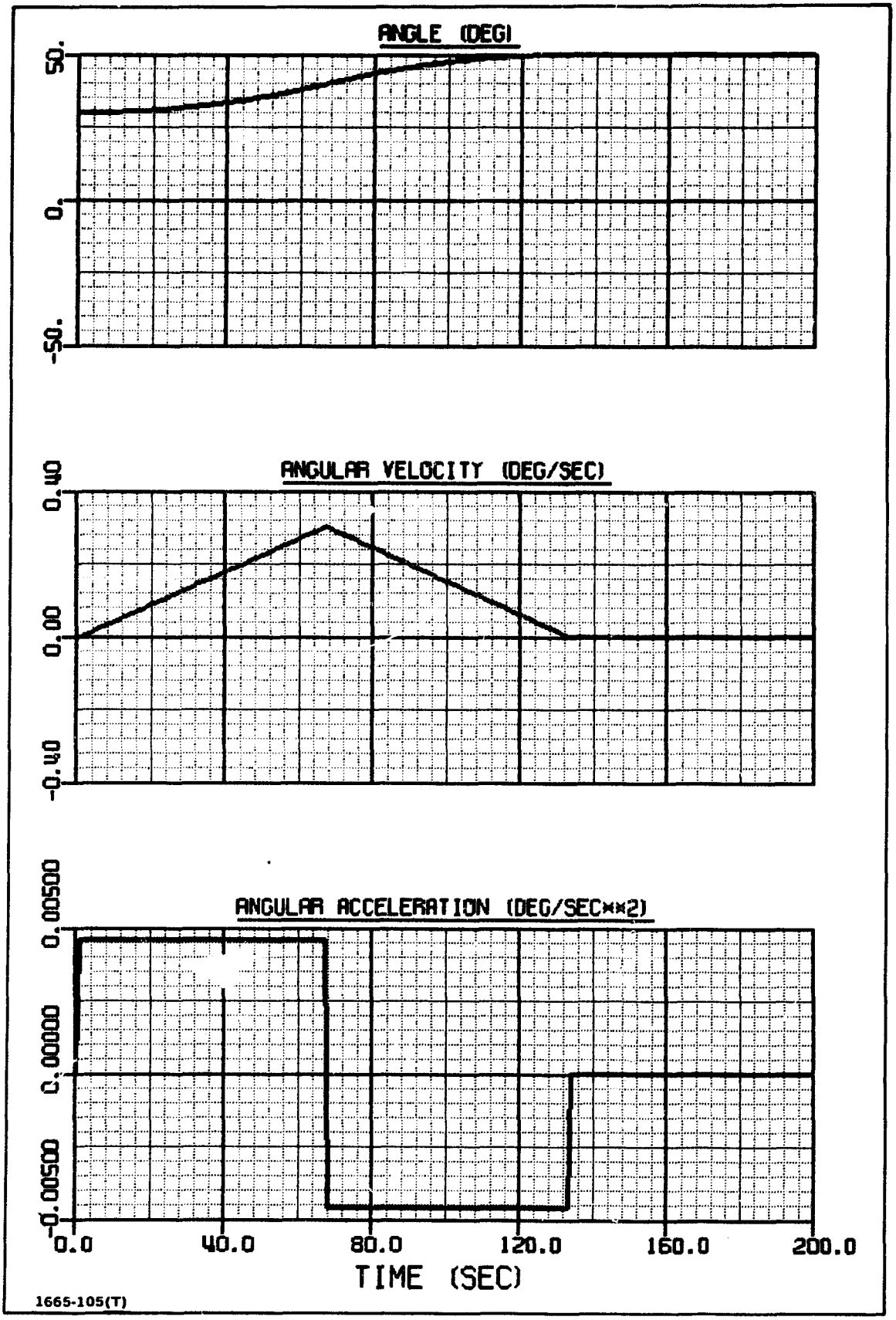

Fig. 3.12 Manipulator Motion. Hinge Angle Rotates From 30 to 50 Deg.

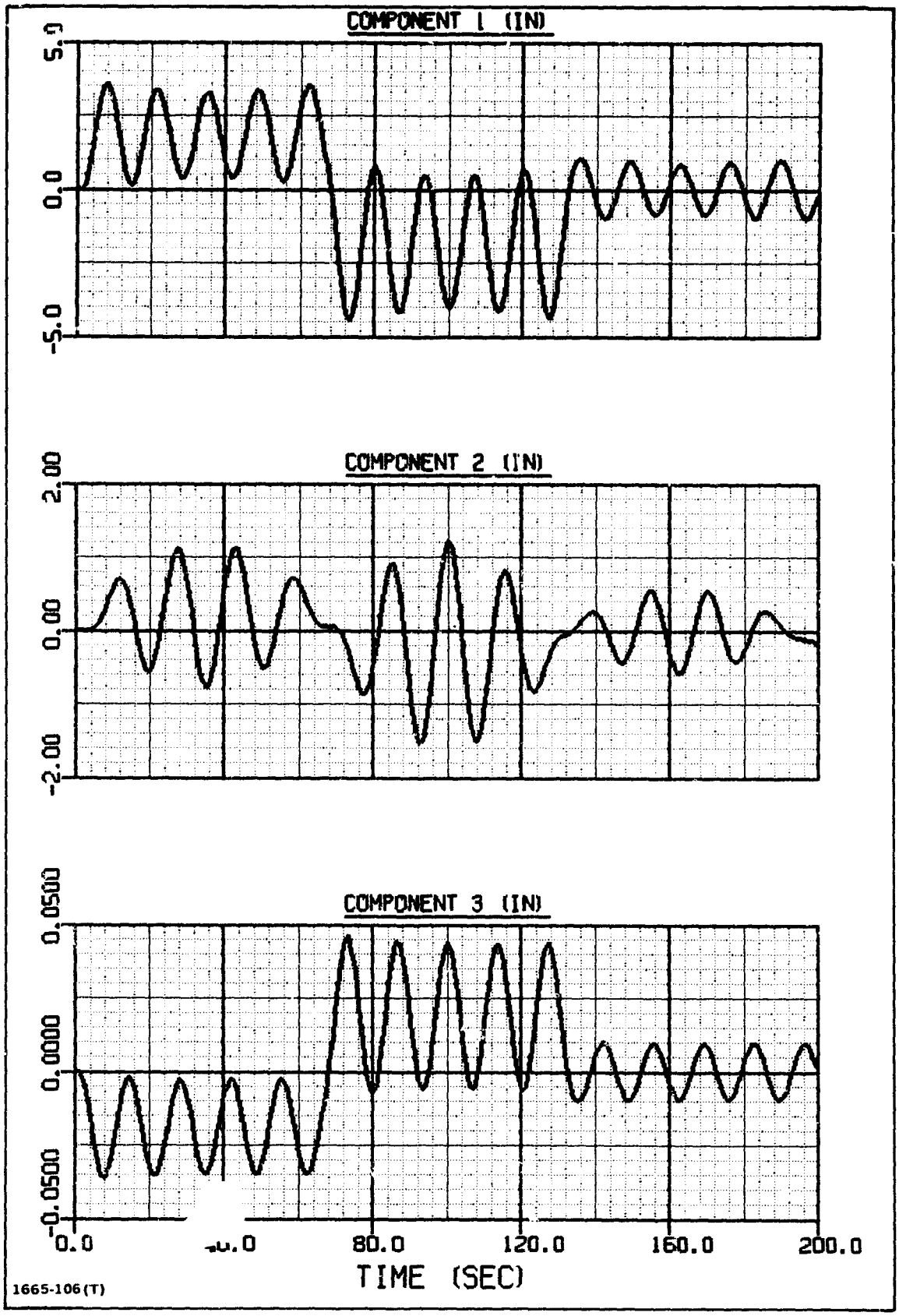

Fig. 3.13 Linear Displacement of Beam Tip in Y Axes. Hinge Angle Rotates From 30 to 50 Deg.

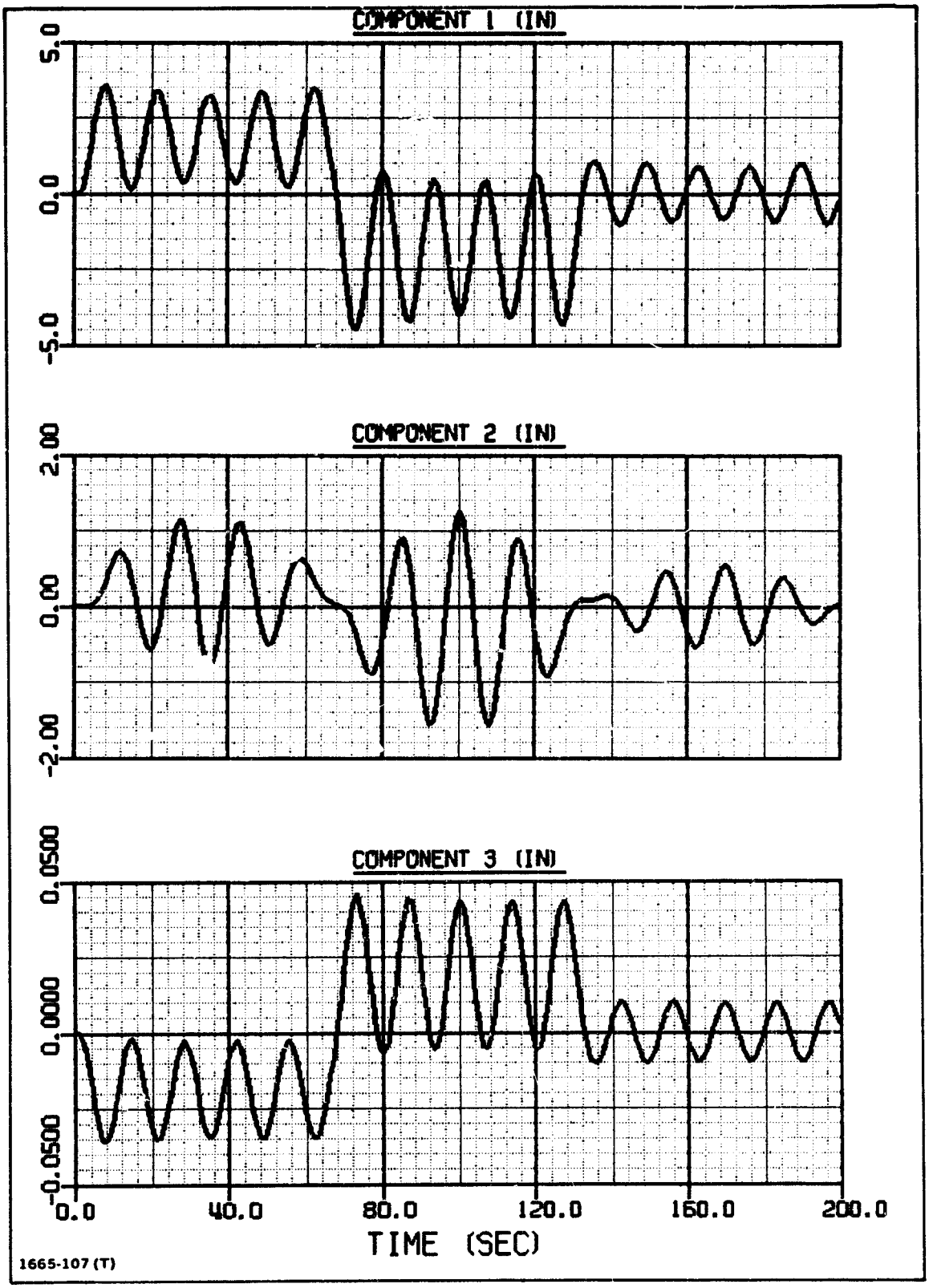

Fig. 3.14 Linear Displacement of Beam Tip in Y Axes. Hinge Angle Rotates From 30 to 50 Deg. Approximate Average-Angle Technique

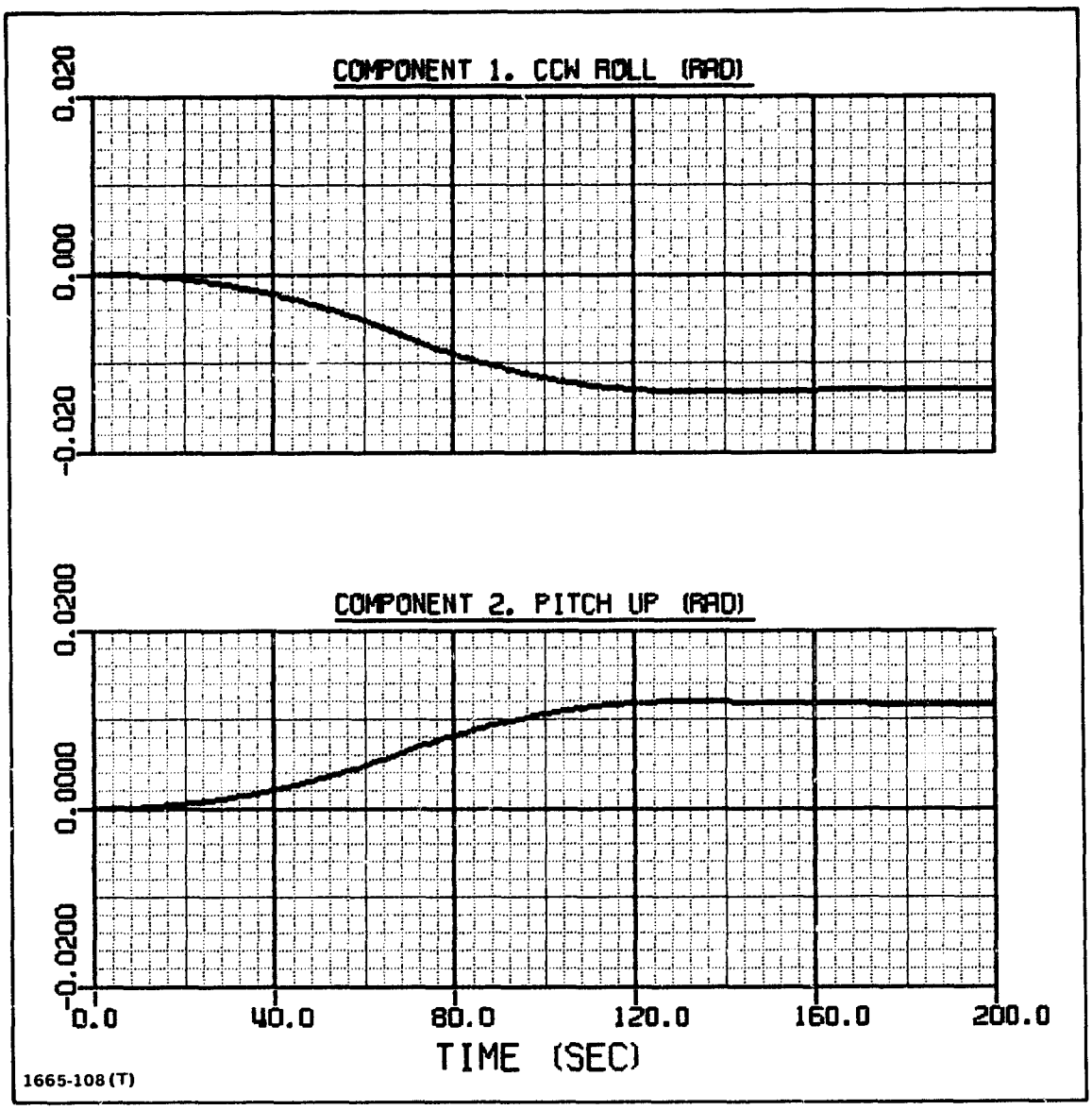

Fig. 3.15 Angular Displacement of Orbiter. Hinge Angle Rotates From 30 to 50 Deg.

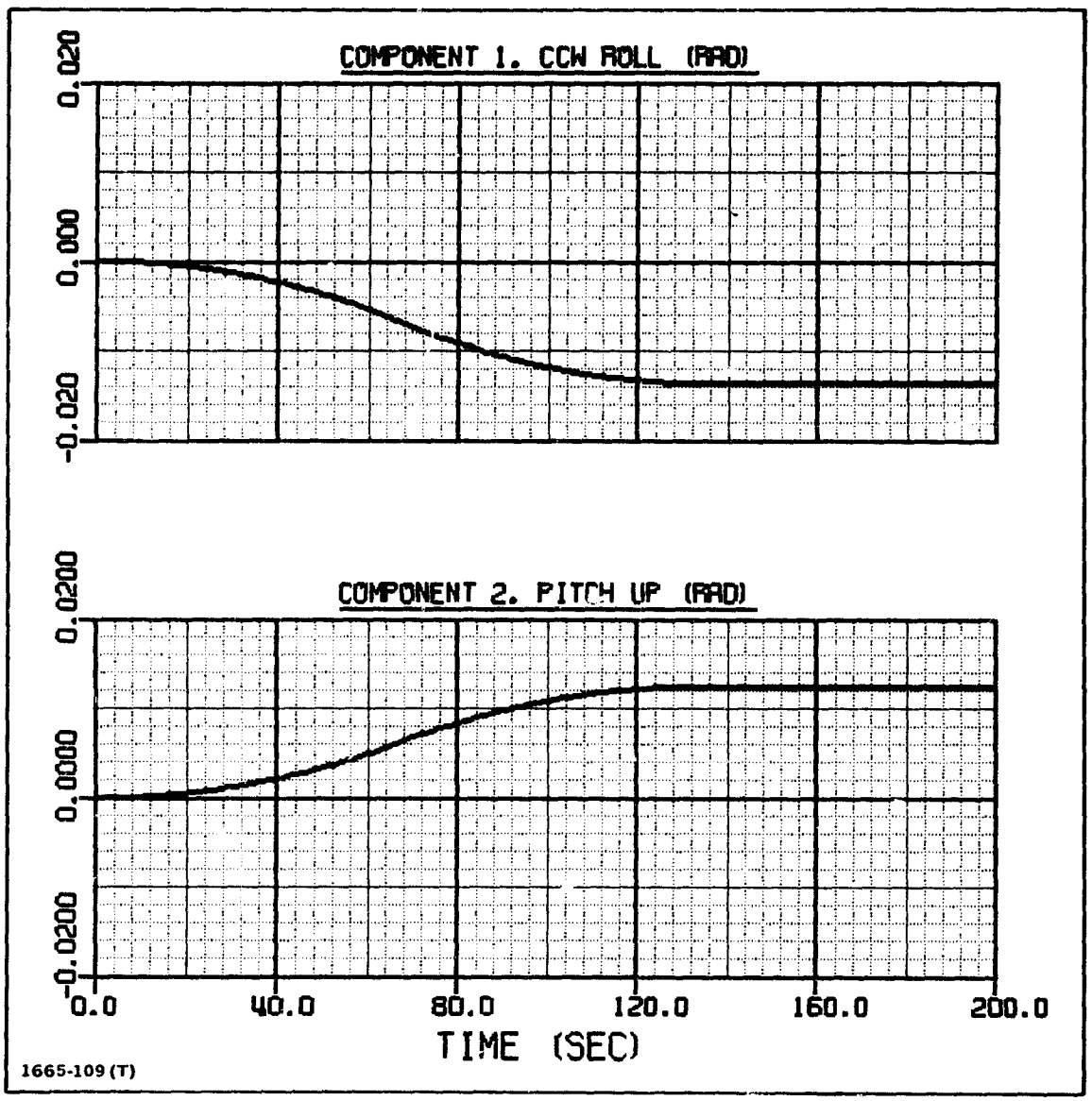

Fig. 3.16 Angular Displacement of Orbiter. Hinge Angle Rotates From 30 to 50 Deg. Approximate Average-Angle Technique

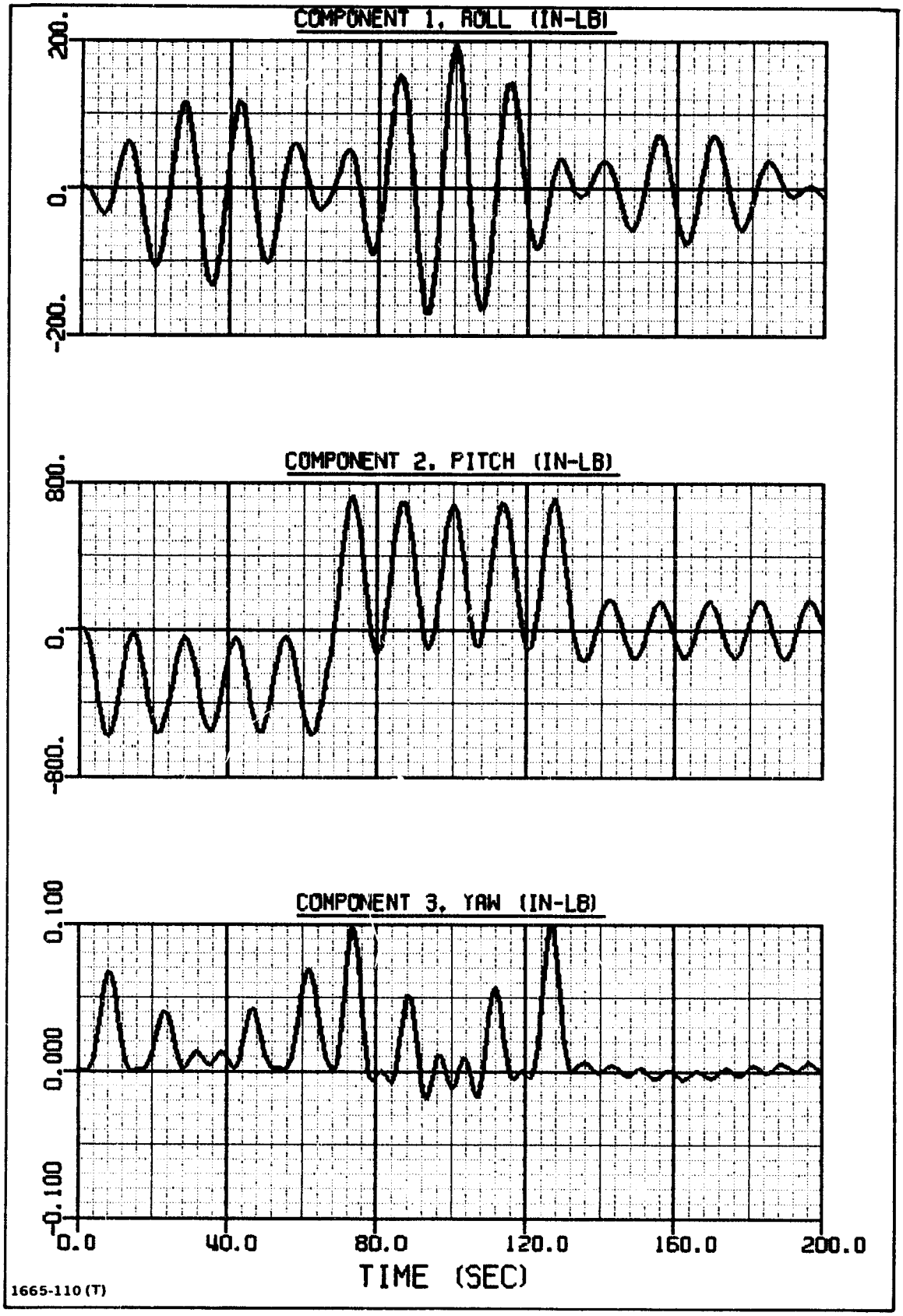

Fig. 3.17 Torque Exerted by Wrist on Beam in Y Axes. Hinge Angle Rotates From 30 to 50 Deg.

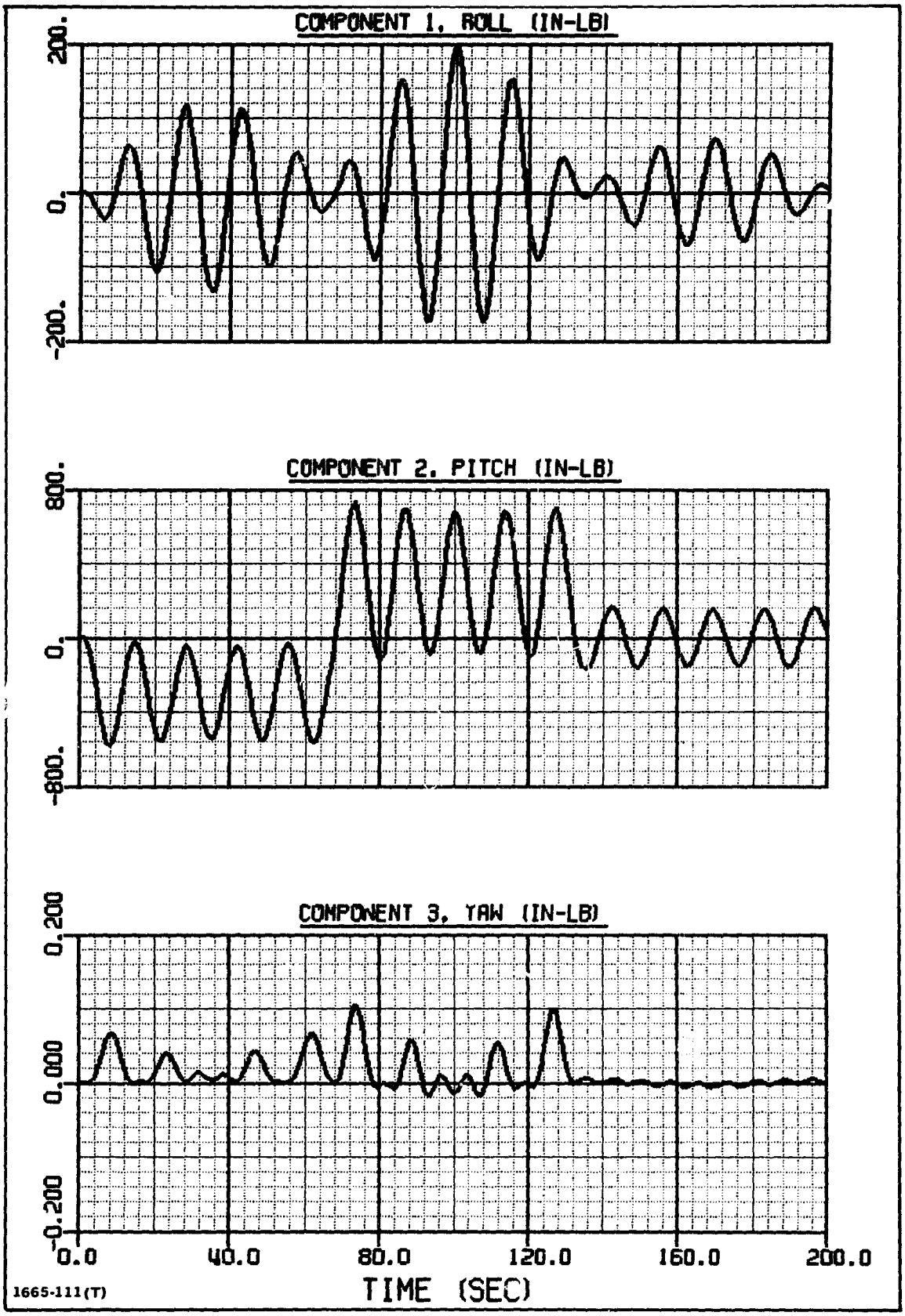

Fig. 3.18 Torque Exerted by Wrist on Beam in Y Axes. Hinge Angle Rotates From 30 to 50 Deg. Approximate Average-Angle Technique

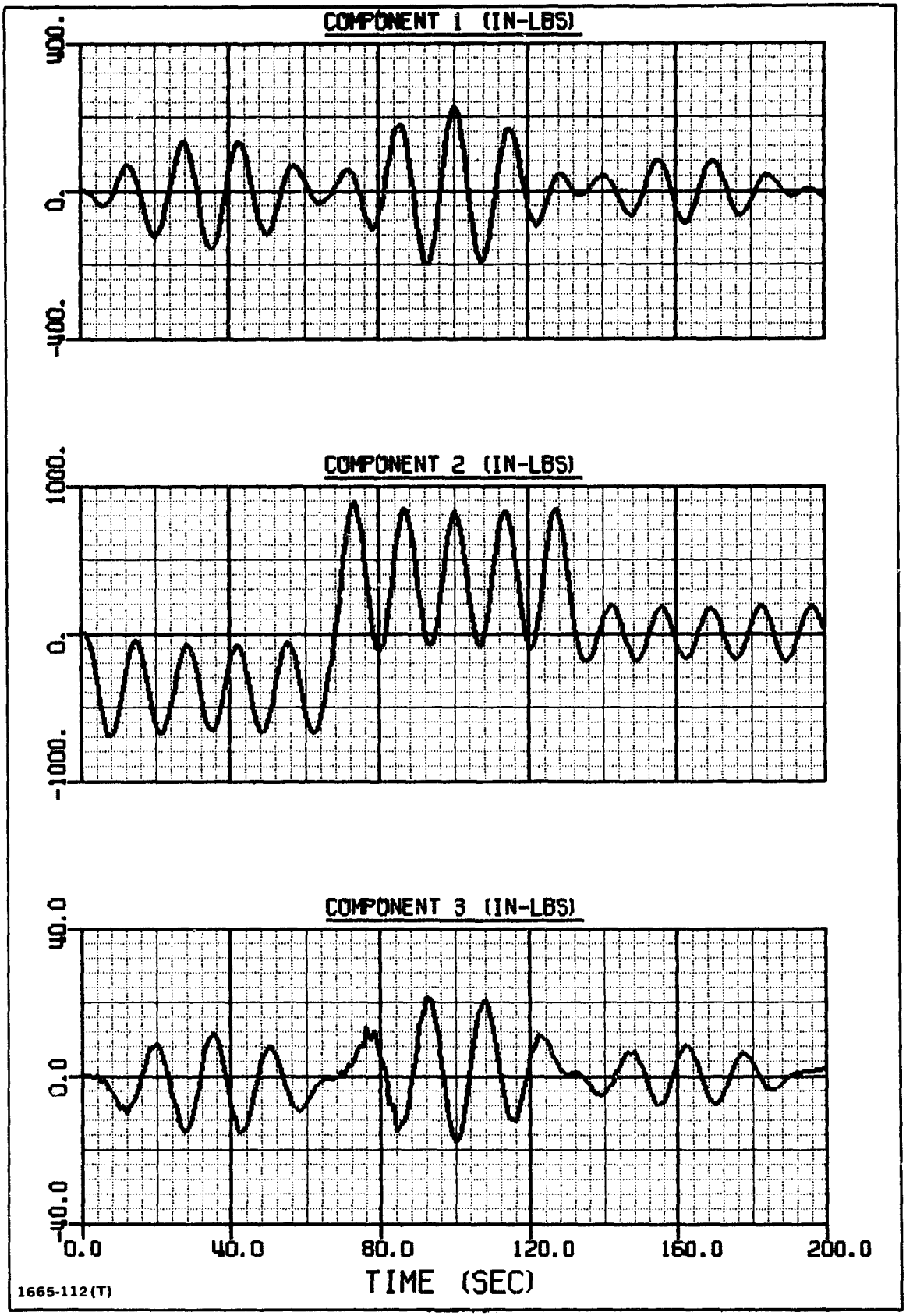

Fig. 3.19 Torque on Body B at Hinge in Y Axes. Hinge Angle Rotates From 30 to 50 Deg.

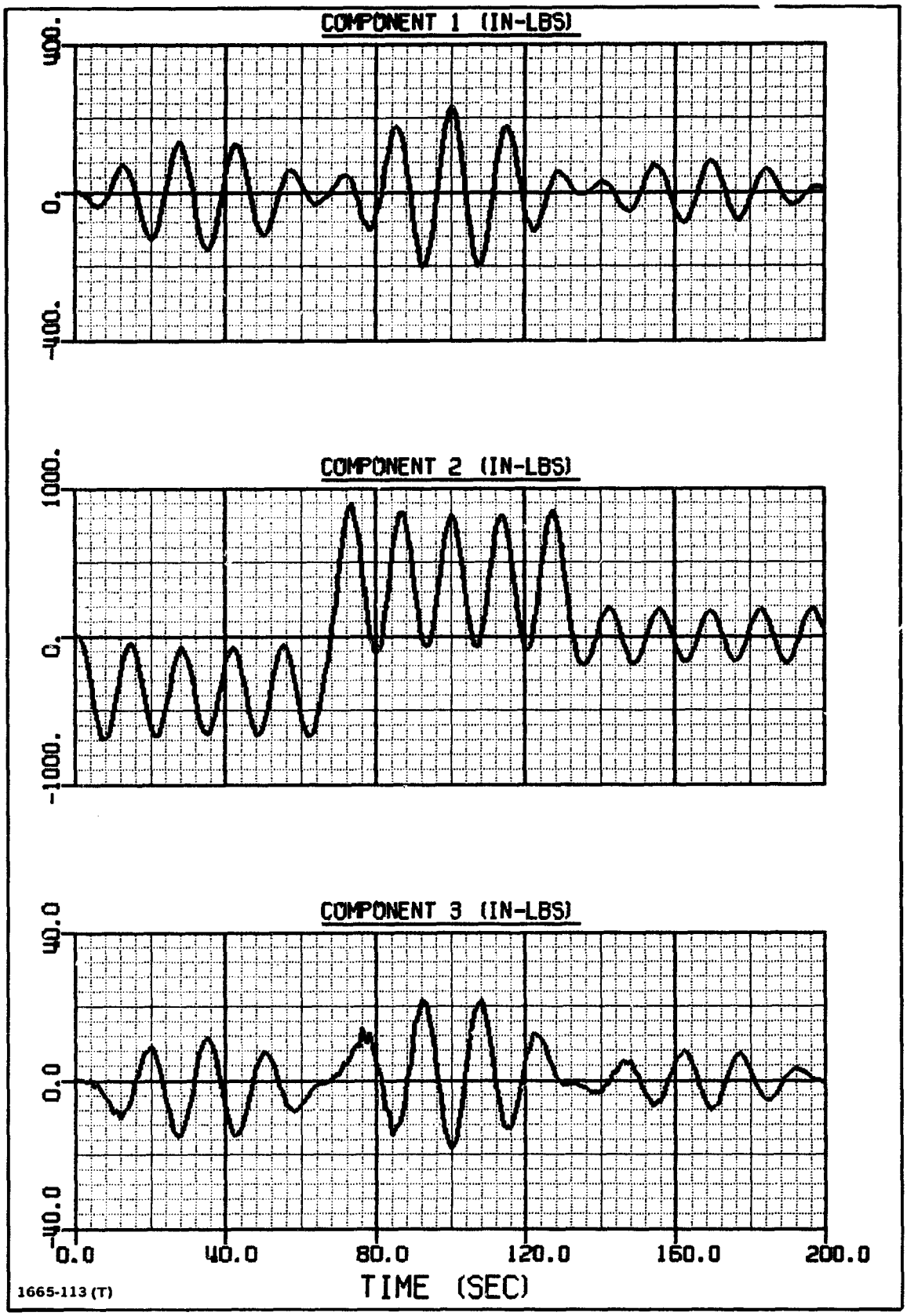

Fig. 3.20 Torque on Body B at Hinge in Y Axes. Hinge Angle Rotates From 30 to 60 Deg. Approximate Average-Angle Technique

SO

3.3.4 Evaluation of Average-Angle Technique

Additional runs were made by direct numerical integration and the Average-Angle Technique for the manipulator angle ϕ changing to 40, 60, and 70 deg. In each case the starting angle was 30 deg. In all of these runs the Average-Angle Technique provided a good approximation to the motion. The peak beam-tip deflection v_{11} was used as an indicator of the quality of the approximate solution. As seen in Table 3.1, the peak beam-tip deflection is closely approximated by the Average-Angle Technique in all cases. Also, the time of occurrence of the peak response is nearly the same in all cases. The per cent error for $\Delta\phi$ = 30 deg is lower than the value for $\Delta\phi$ = 20 deg because the peak response happens to occur very early in time for the 30 deg angle.

The closeness of the approximation for large changes in the manipulator angle is truly remarkable, especially since the quality of the solutions obtained by the approximate method deteriorated rapidly in the Beam-Fabrication Problem for changes in geometry greater than three percent. It is believed that the greater accuracy achieved in the Beam-Relocation Problem is attributable to the fact that the vibration frequencies of the system (especially the lower frequencies) remain nearly constant as the manipulator angle ϕ is changed. Consequently, there is almost no phase difference between the exact and approximate solutions; therefore, inertia loads due to geometry changes affect both solutions in the same way.

It is possible that the technique would not work so well if the orbiter were not so massive in comparison with the RMS and the beam. This question has not been addressed.

3.3.5 Hinge Angle Rotates From Zero To 90 Deg. - With and Without Control System Active

Figure 3.21 shows the motion of the manipulator hinge angle ϕ for the case to be discussed, a 90 deg rotation of the RMS at the shoulder joint. Figures 3.22 to 3.24 show the linear displacement of the beam tip and the torques at the wrist and shoulder (or hinge).

The run was repeated with the control system active. A control-system sample time τ of .1 sec was used. Figure 3.25 shows the orbiter orientation as a function of time. Most of the time the pitch and roll angles drift back and forth across the deadband. The yaw angle drifts within the deadband and never reaches the deadband boundary. Figure 3.26 shows the torques exerted by the

TABLE 3.1 EVALUATION OF AVERAGE-ANGLE TECHNIQUE

CHANGE IN MANIPULATOR ANGLE $\Delta\phi$ (DEG)	PEAK BEAM-TIP DEFLECTION v_{11} (IN)				% ERROR IN v_{11}
	DIRECT NUMERICAL INTEGRATION		APPROXIMATE AVERAGE-ANGLE TECHNIQUE		
	VALUE (IN)	TIME (SEC)	VALUE (IN)	TIME (SEC)	
10	-6.9475	54.75	-6.9745	54.75	.39
20	-4.4696	72.95	-4.5021	72.95	.73
30	3.6013	7.850	3.5874	7.850	.39
40	-4.4761	122.9	-4.5631	122.8	1.94

NOTE: MANIPULATOR ANGLE ϕ IS INITIALLY 30 DEG IN EACH RUN.

1665-142(T)

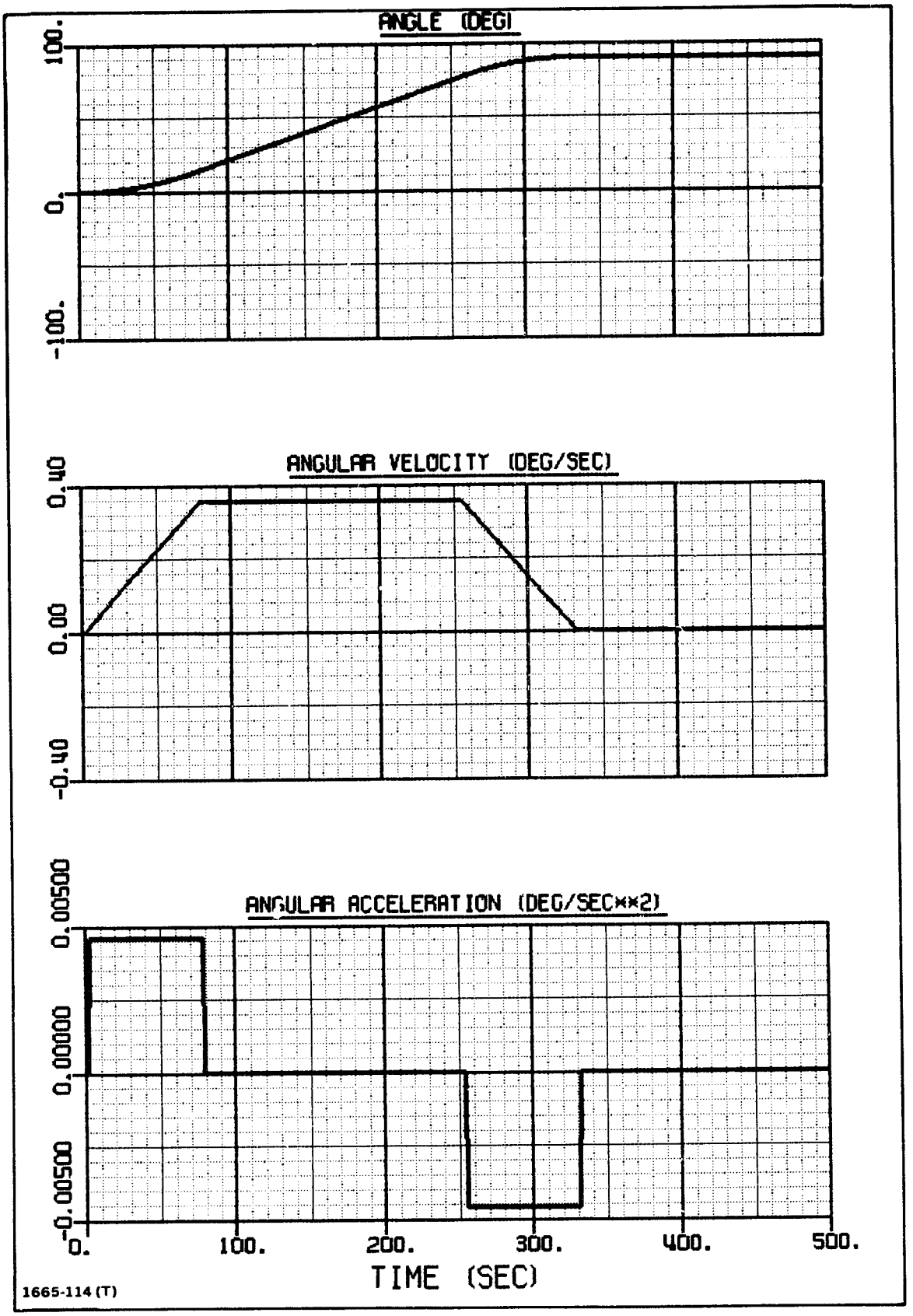

Fig. 3.21 Manipulator Motion. Hinge Angle Rotates From Zero to 90 Deg.

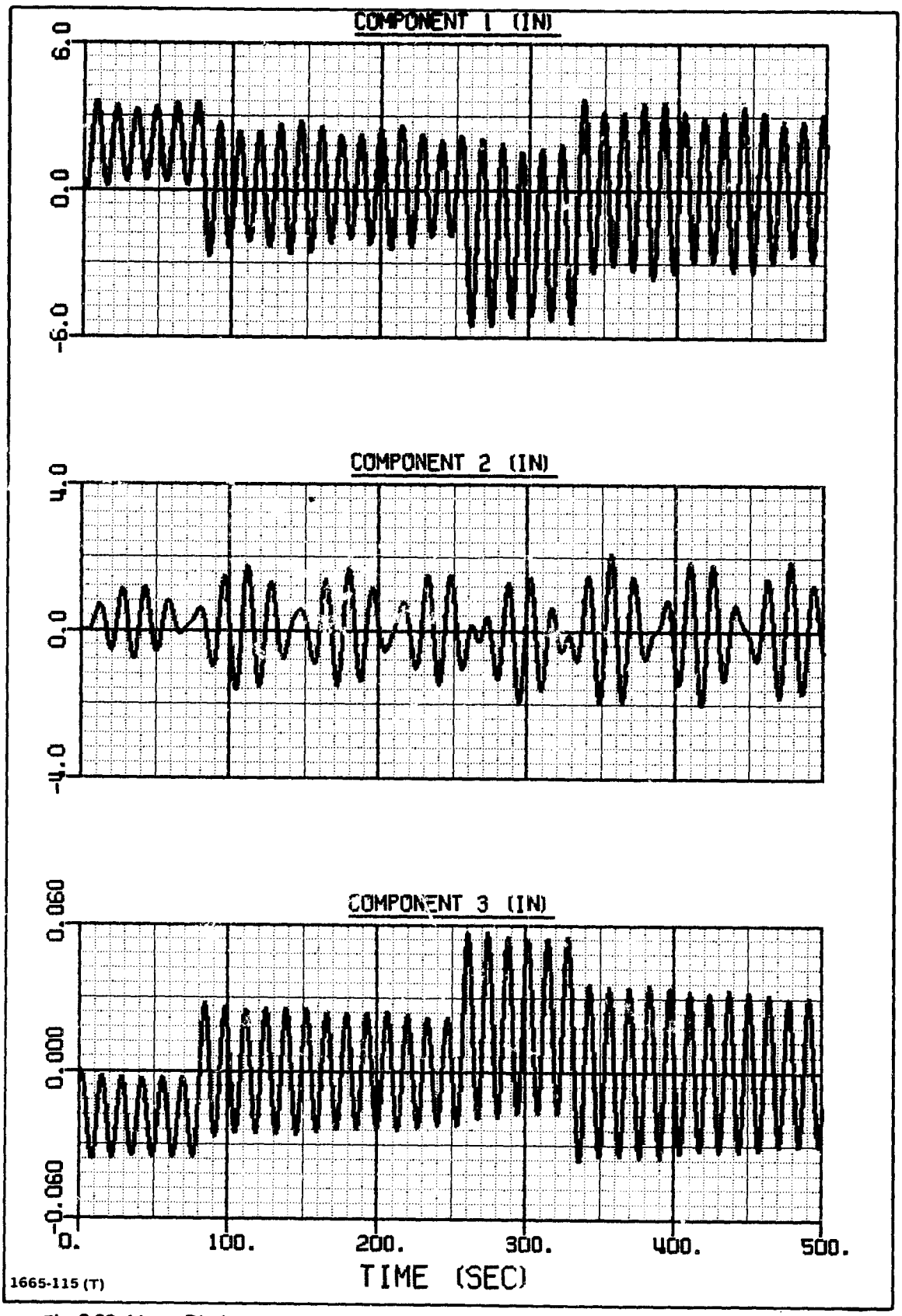

Fig. 3.22 Linear Displacement of Beam Tip in Y Axes. Hinge Angle Rotates From Zero to 90 Deg.

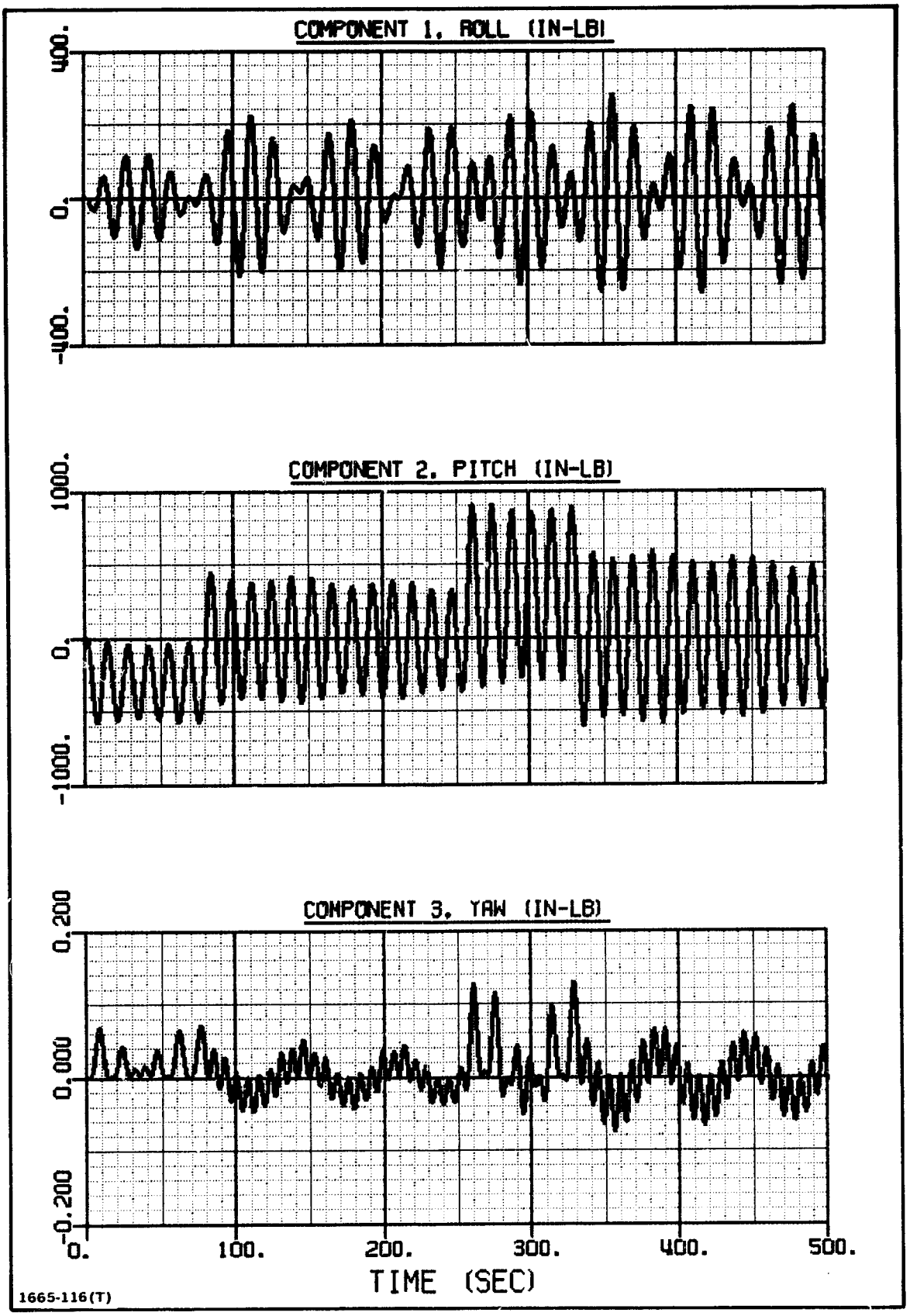

Fig. 3.23 Torque Exerted by Wrist on Beam in Y Axes. Hinge Angle Rotates From Zero to 90 Deg.

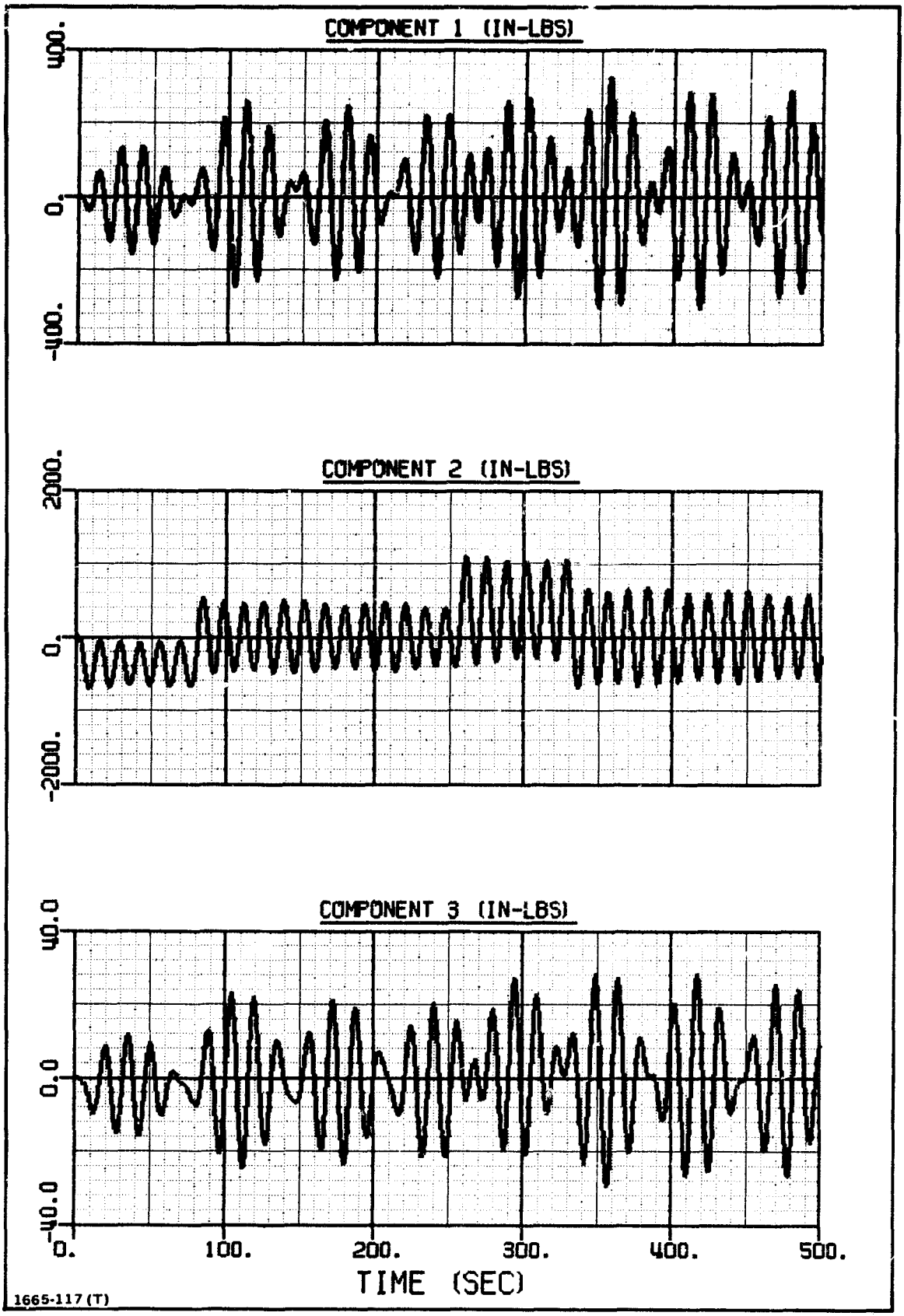

Fig. 3.24 Torque on Body at Hinge in Y Axes. Hinge Angle Rotates From Zero to 90 Deg.

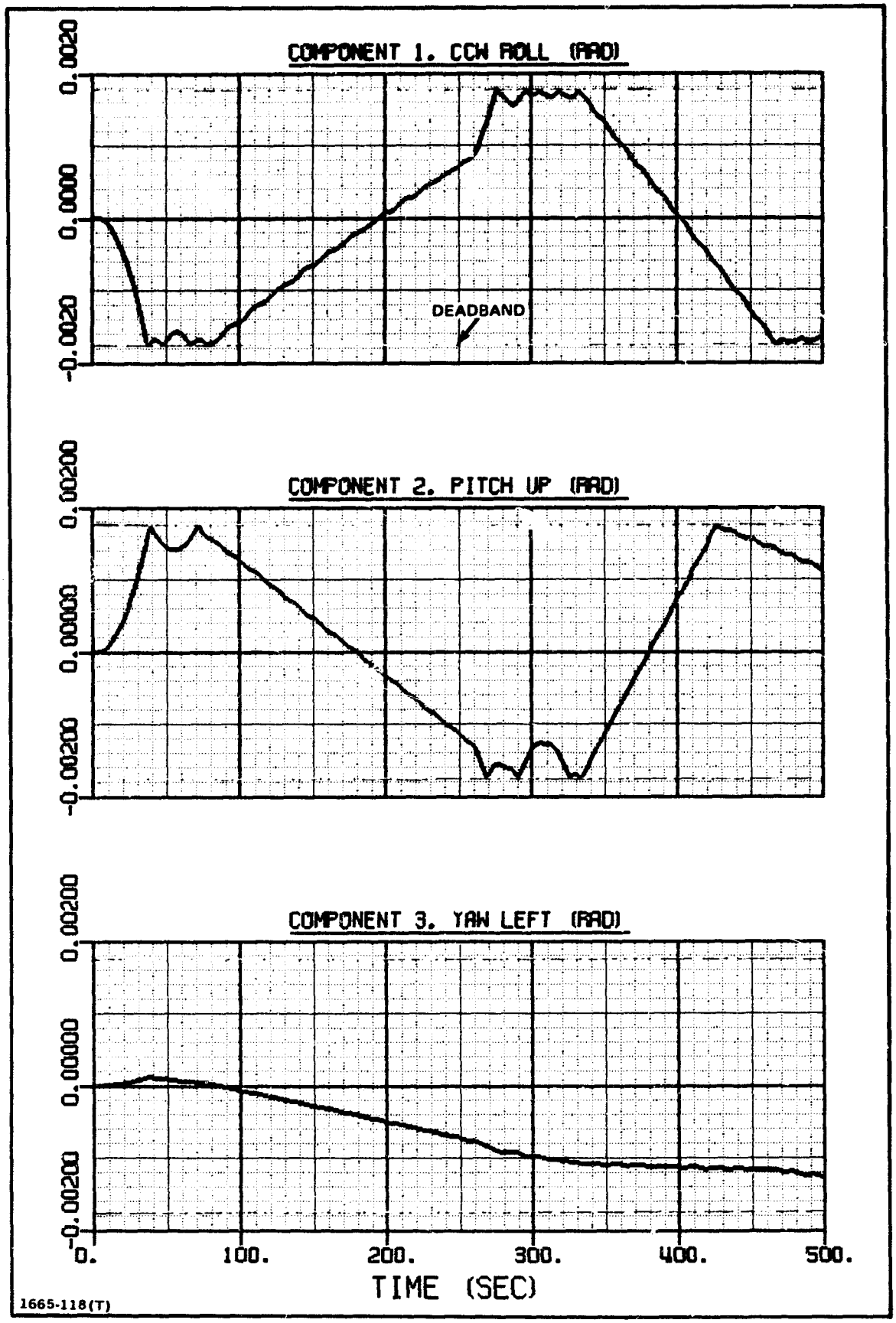

Fig. 3.25 Angular Displacement of Orbiter. Hinge Angle Rotates From Zero to 90 Deg. Control System Active

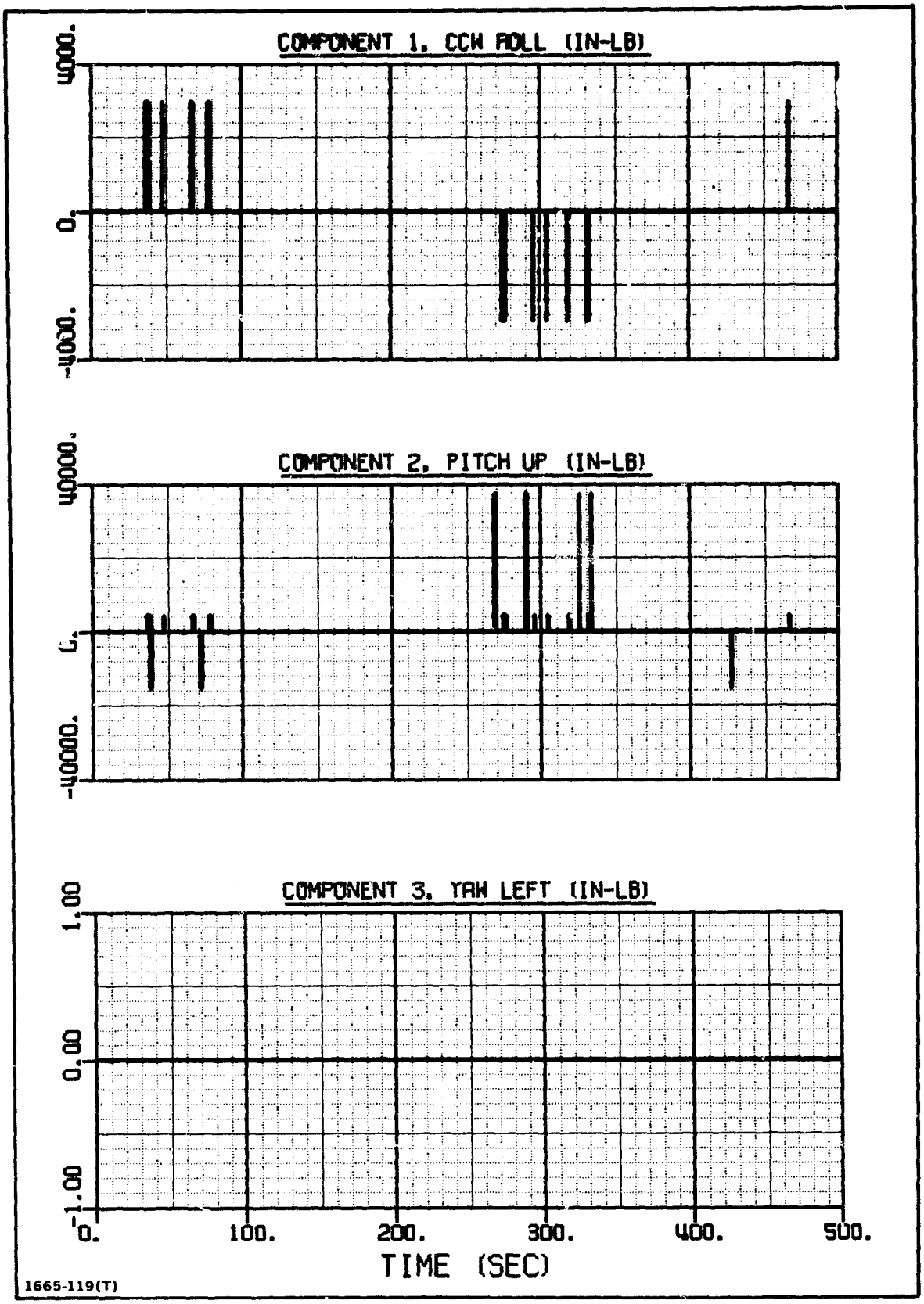

Fig. 3.26 Total Control Torque About Orbiter CM. Hinge Angle Rotates From Zero to 90 Deg. Control System Active

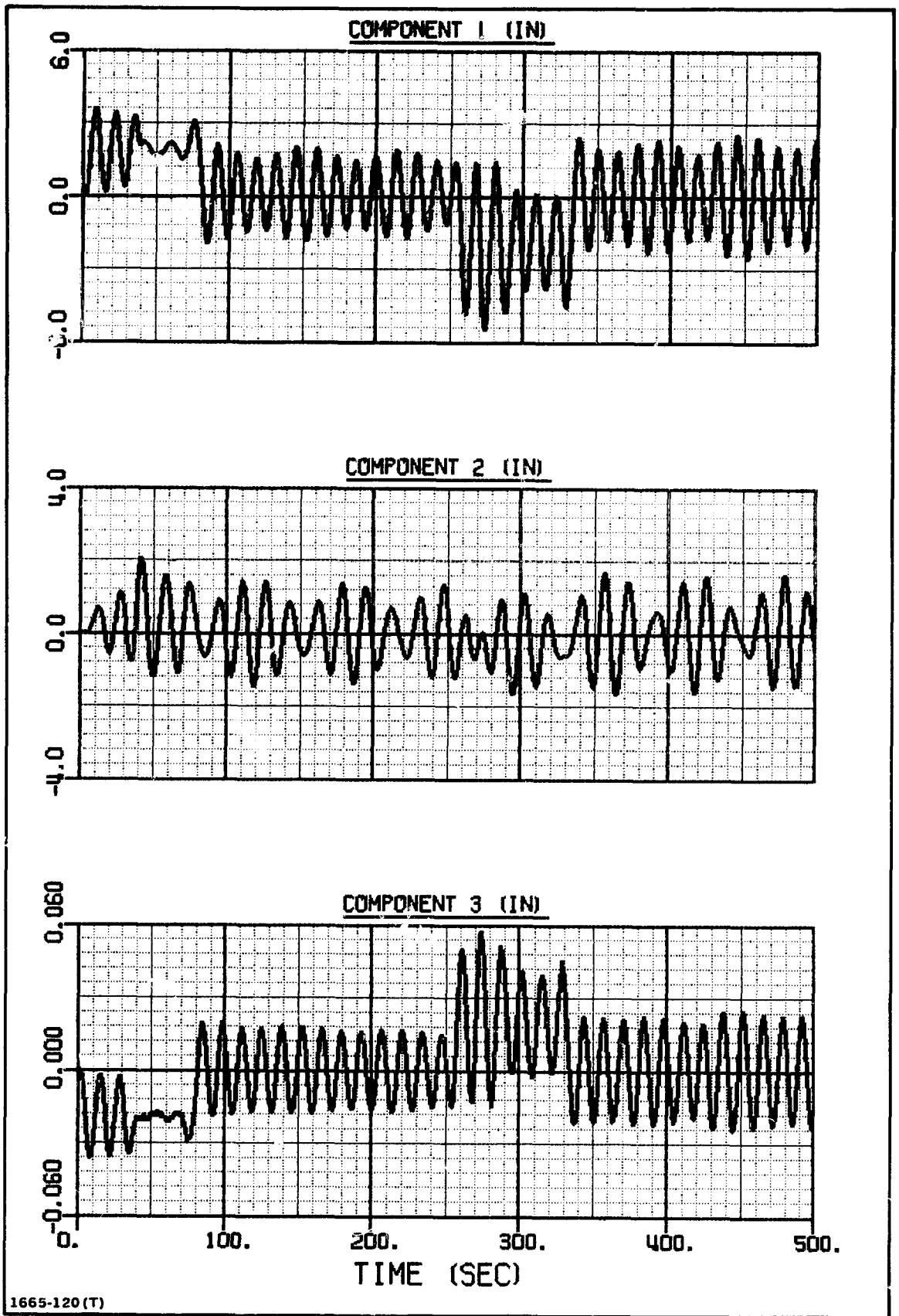

Fig. 3.27 Linear Displacement of Beam Tip in Y Axes. Hinge Angle Rotates From Zero to 90 Deg. Control System Active

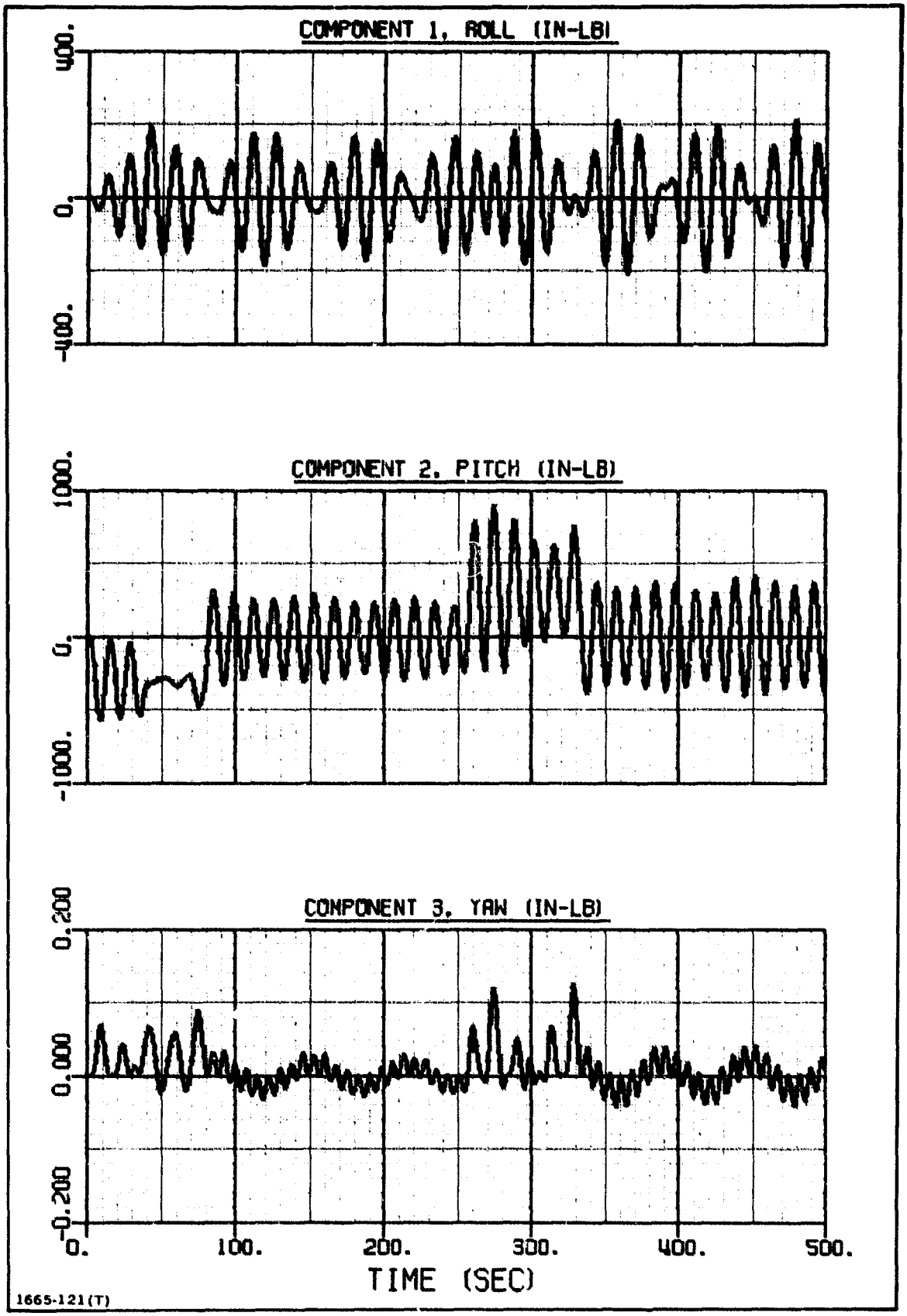

Fig. 3.28 Torque Exerted by Wrist on Beam in Y Axes. Hinge Angle Rotates, From Zero to 90 Deg. Control System Active

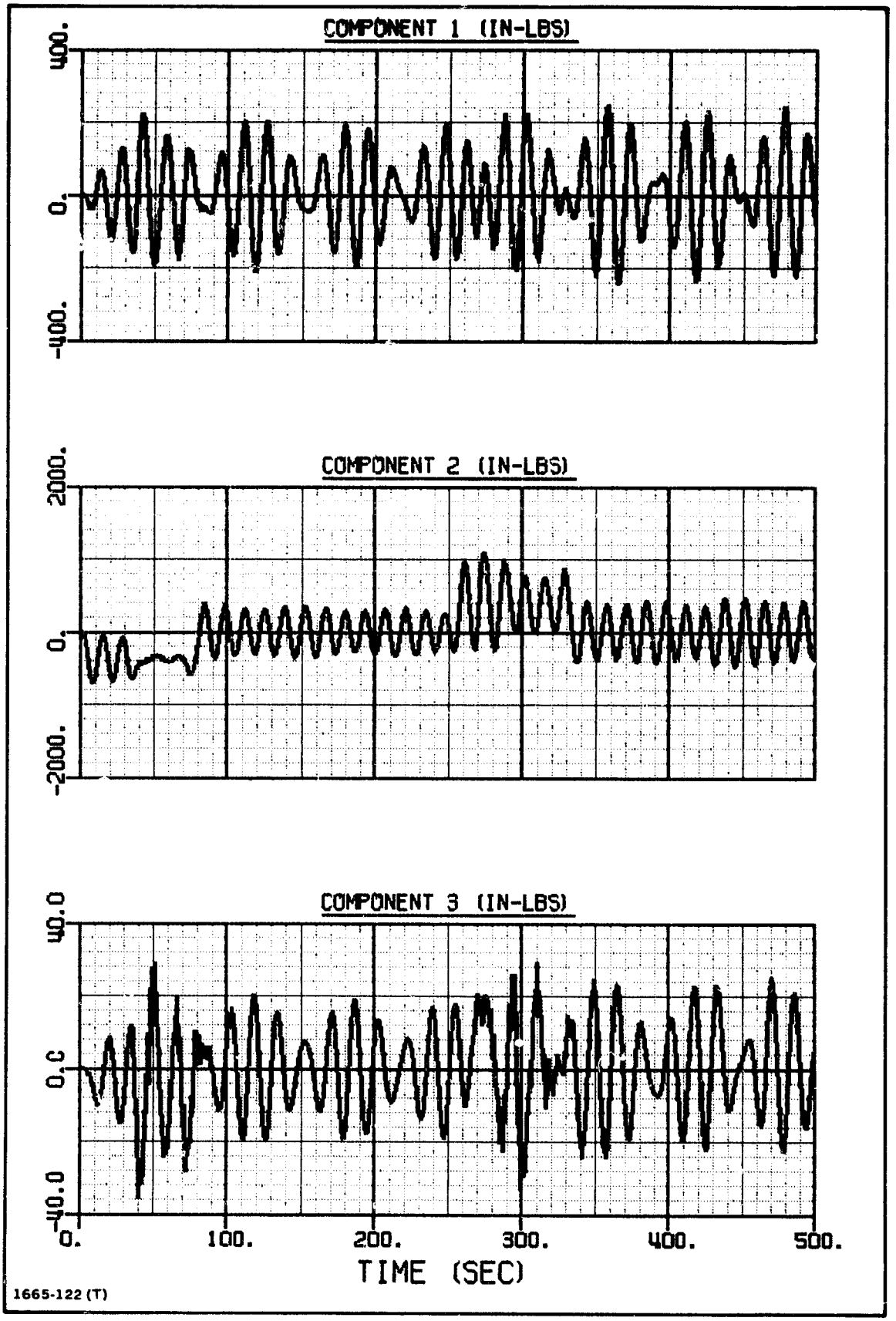

Fig. 3.29 Torque on Body B at Hinge in Y Axes. Hinge Angle Rotates From Zero to 90 Deg. Control System Active

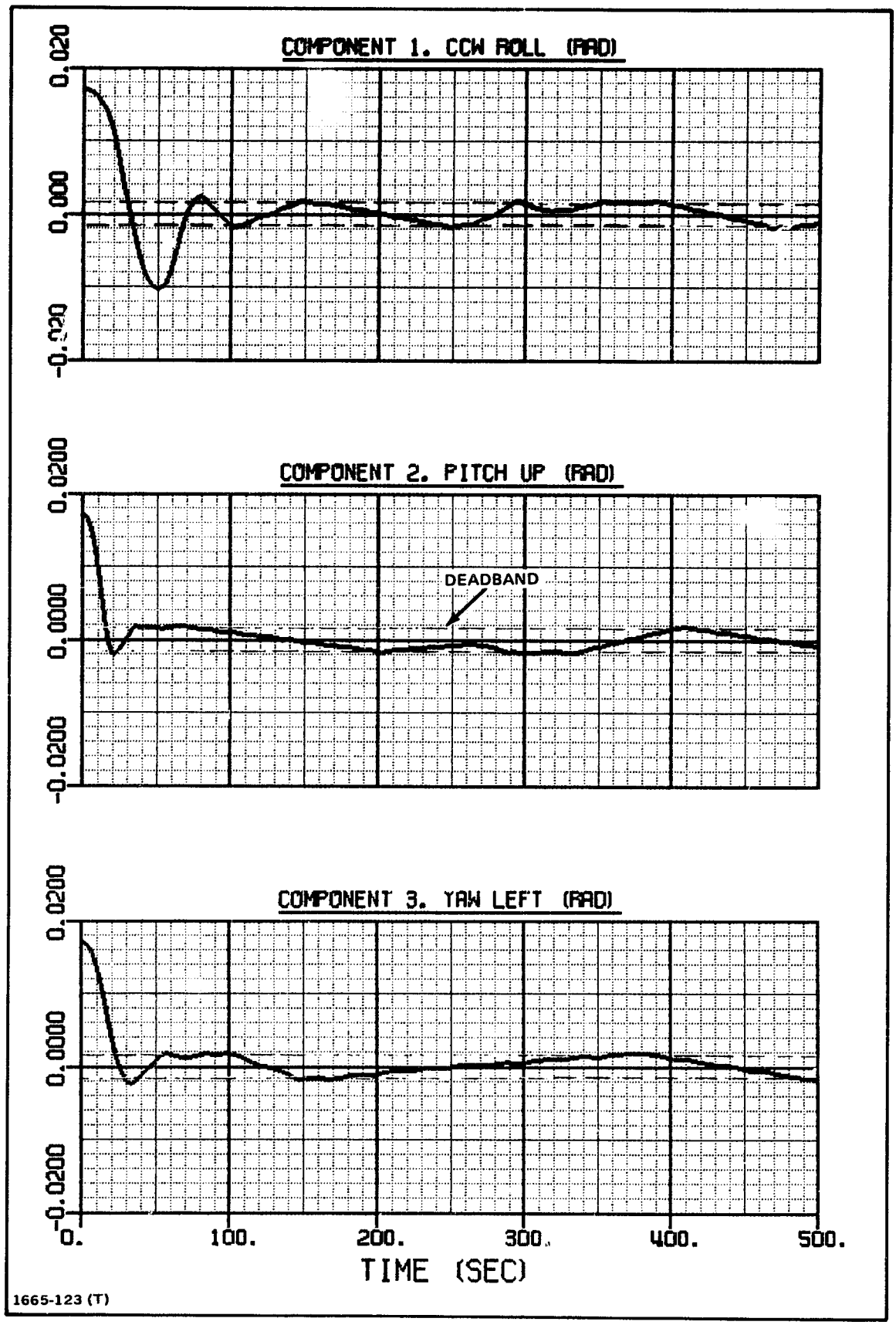

Fig. 3.30 Angular Displacement of Orbiter. Hinge Angle Rotates From Zero to 90 Deg. One Deg. Initial Error About Each Axis. Control System Active

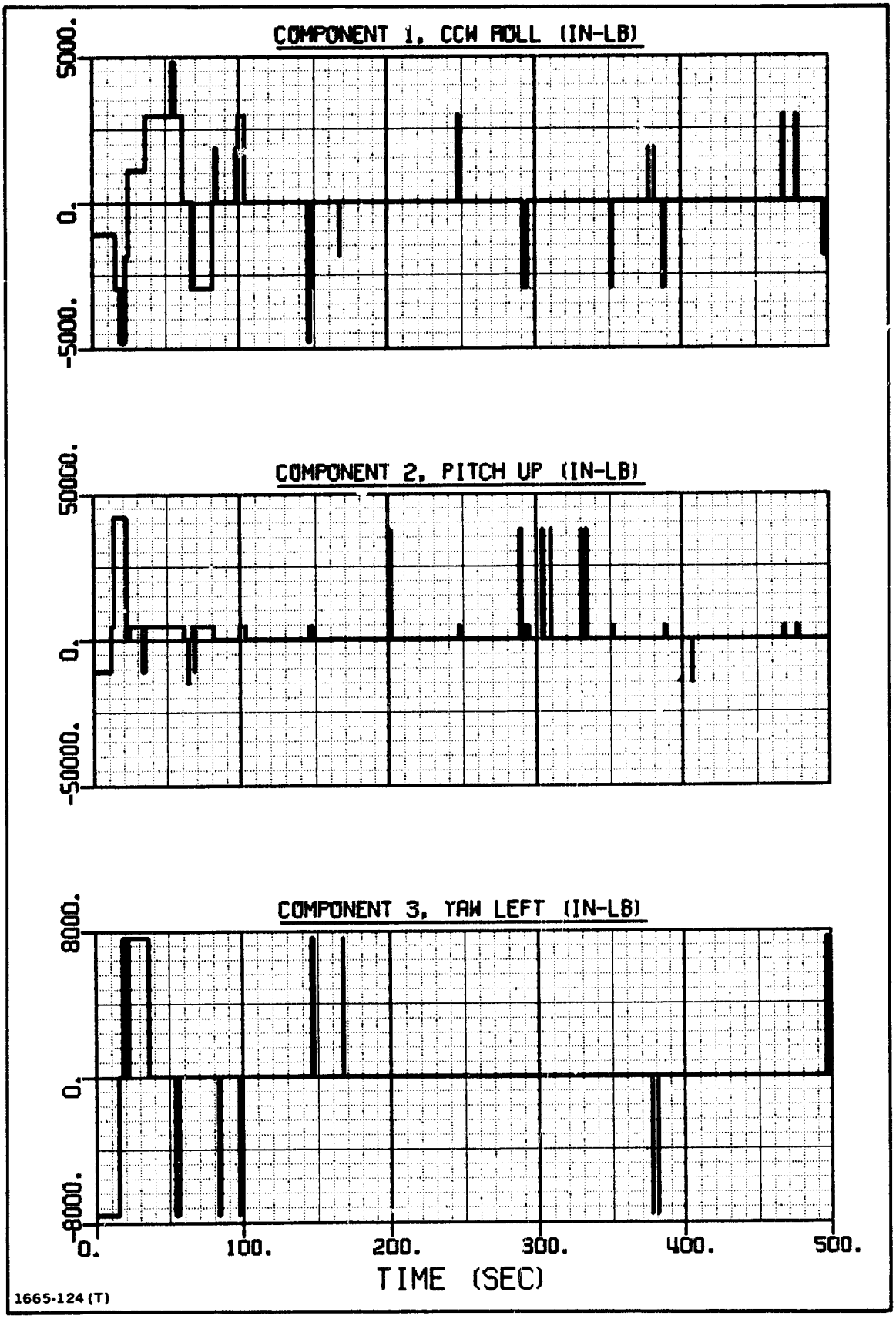

Fig. 3.31 Total Control Torque. Hinge Angle Rotates From Zero to 90 Deg. One Deg. Initial Error About Each Axis. Control System Active

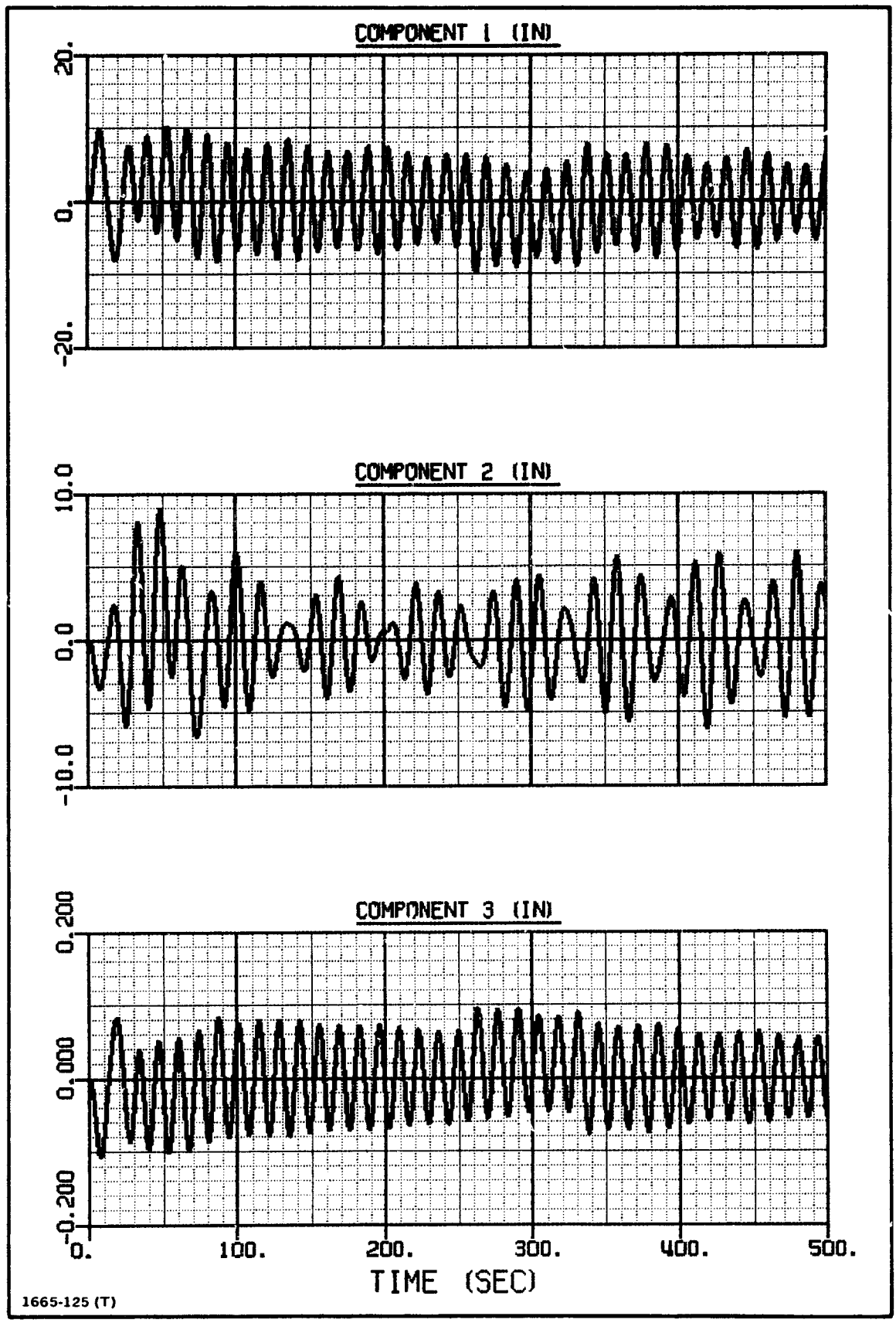

Fig. 3.32 Linear Displacement of Beam Tip in Y Axes. Hinge Angle Rotates From Zero to 90 Deg. One Deg. Initial Error About Each Axis. Control System Active

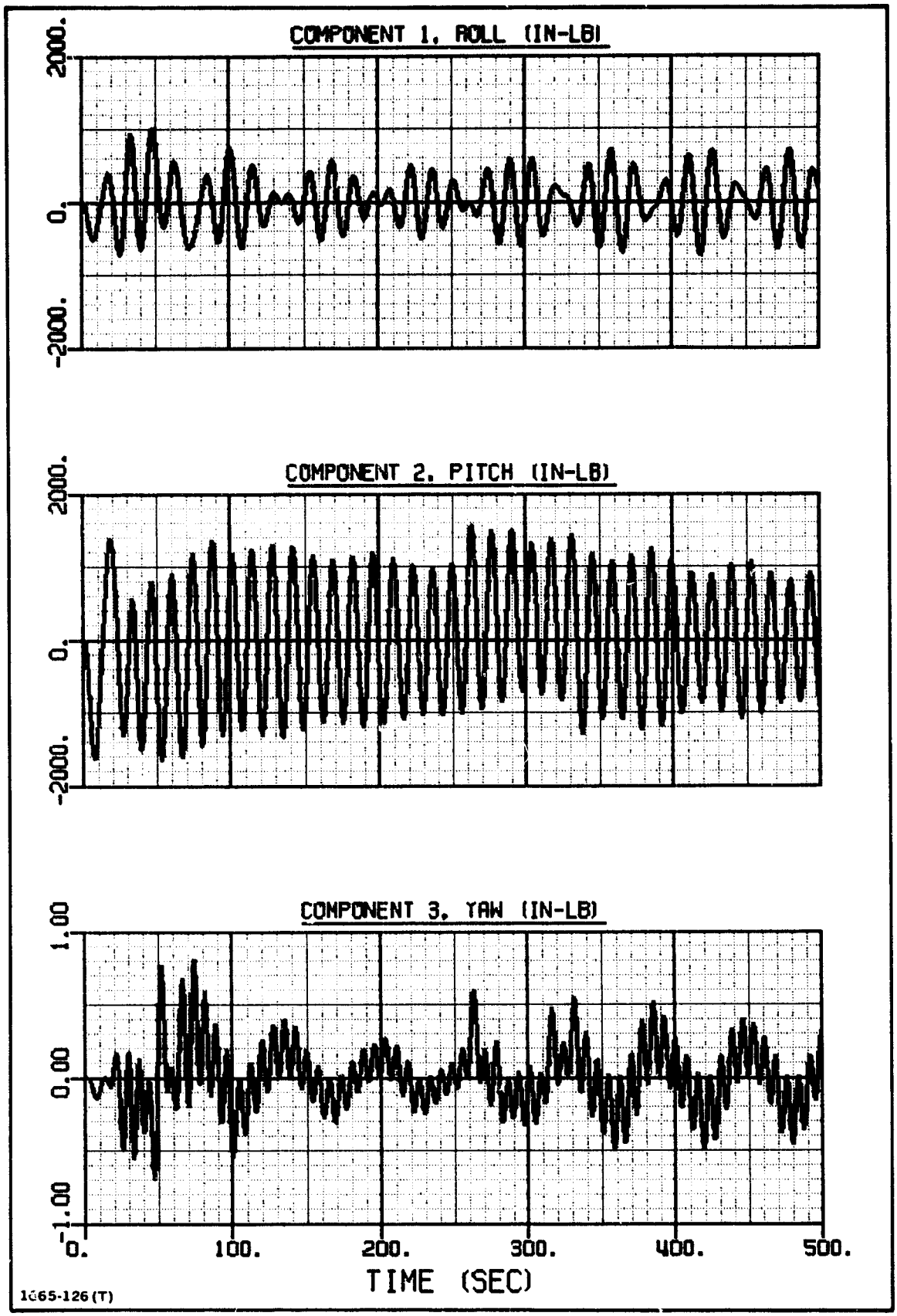

Fig. 3.33 Torque Exerted by Wrist on Beam in Y Axes. Hinge Angle Rotates From Zero to 90 Deg. One Deg. Initial Error About Each Axis. Control System Active

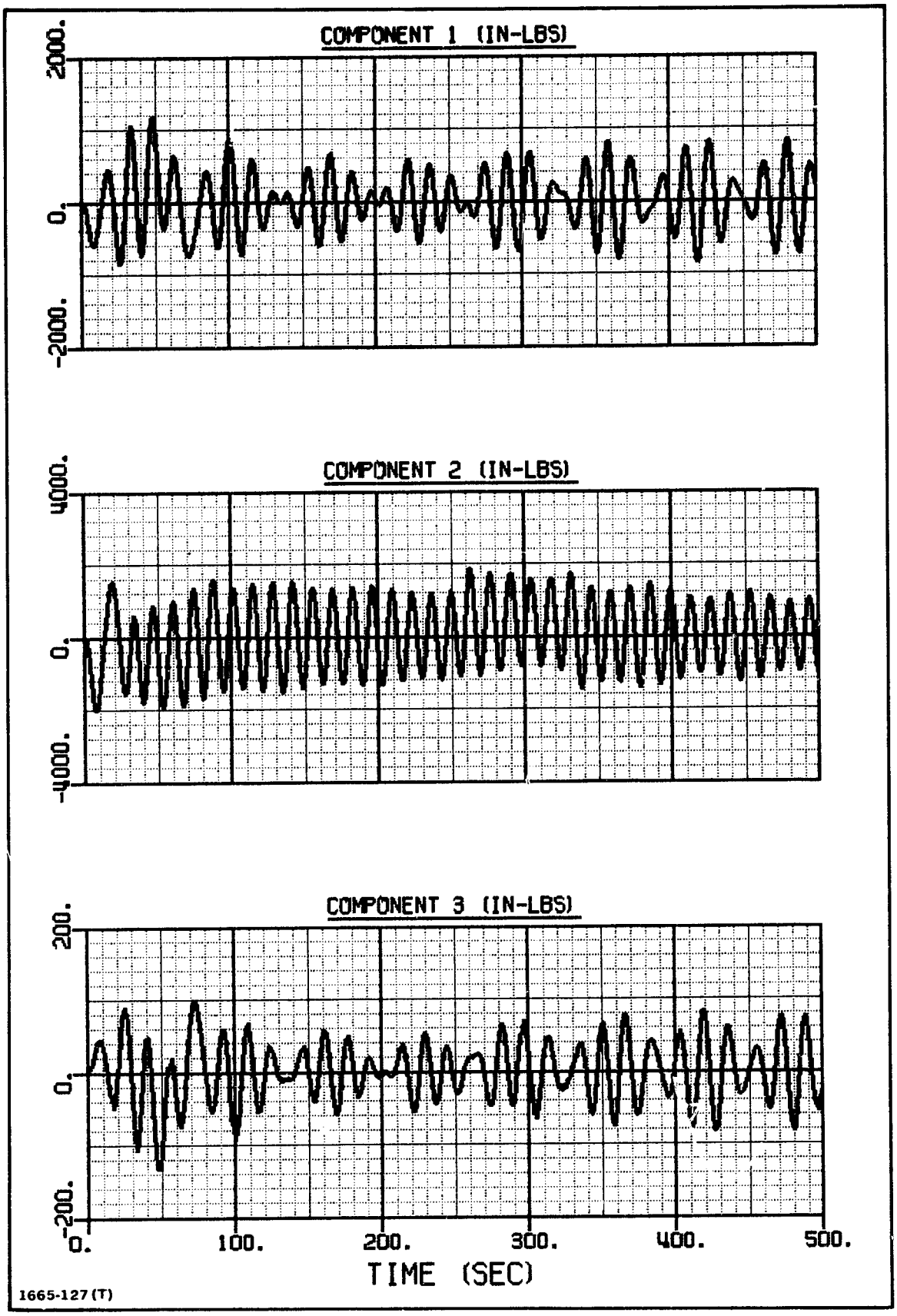

Fig. 3.34 Torque on Body B at Hinge in Y Axes. Hinge Angle Rotates From Zero to 90 Deg. One Deg. Initial Error About Each Axis. Control System Active

control-system actuators about the orbiter cm. The linear displacement of the beam tip and the torques at the wrist and shoulder (or hinge) are shown in Figs. 3.27 - 3.29.

The run was then repeated, but this time an initial error of 1 deg (.017 rad) was introduced about each axis. Typical response curves are illustrated in Figs. 3.30 - 3.34. From Fig. 3.30, it is seen that good control is achieved early in the run.

Peak responses for the three runs are compared in Table 3.2. It is seen that when there is no initial error, the control-system loads do not have a significant influence on the peak responses. This occurs because the thrusters are only on for short time periods (see Fig. 3.26) since only small disturbances must be corrected; consequently, the impulses applied by the control system are small. However, the impulses required to correct the one degree initial error are much larger (see Fig. 3.31); therefore, larger responses occur. Nevertheless, the torques at the wrist and the shoulder are below the slip torques of 2770 in-lbs and 9260 in-lbs, respectively.

TABLE 3.2 PEAK VALUES OF SELECTED RESPONSES DURING 90 DEG ROTATION OF RMS AT SHOULDER JOINT

CASE	PEAK VALUE		
	LINEAR DISPLACEMENT OF BEAM TIP (IN)	TORQUE AT WRIST (IN-LBS)	TORQUE AT SHOULDER (OR HINGE) (IN–LBS)
UNCONTROLLED	-5.65	910.	1090.
CONTROLLED	-5.53	896.	1110.
CONTROLLED. INITIAL ERROR OF 1 DEG ABOUT EACH AXIS	10.28	-1650	-2040

1665-142(T)

Appendix A

CONFIGURATION REVIEW AND SELECTION OF PROBLEMS

A1. Configuration Review

A review of selected large space-structure configurations was conducted in order to define associated dynamic analysis problem areas. This review includes near-term (1980's) structures that are intermediate in size with lengths in the order of hundreds of meters. These structures could be constructed or deployed from the orbiter. The review also includes ultra-large structures, with lengths in the order of kilometers, required for applications such as the Solar Power Satellite for the 1990's and beyond. All of these structures experience major changes in geometry during on-orbit fabrication, assembly or deployment. Finally, key construction machines, beam builders and the orbiter remote manipulator system, are discussed.

A1.1 Intermediate-Size Structures (orbiter assembled)

Typical intermediate size structures that can be fabricated from the orbiter are:

- Large Space Structures (LSS) Platform (Grumman, Ref. A1)
- Space Construction Automated Fabrication Experiment Definition Study (SCAFEDS) Ladder (General Dynamics, Ref. A2)
- Large Space Structures (LSS) - Lollipop (Grumman, Ref. A3)

Characteristics of these structures are summarized in Fig. A1. All structures are assembled from a triangular beam which is fabricated on-orbit using an Automatic Beam Builder (ABB). Similar structures could also be assembled from beams which are prefabricated on the ground and assembled in orbit.

The purpose of the LSS Platform program is a demonstration of space construction. The structure also has potential use as a spacecraft or space platform (i.e., a structure that is designed to be connected to a spacecraft). Figure A2 shows the assembly sequence for the LSS Platform. A spider-like fixture is erected and nine 10.5m-long beams fabricated by the Grumman ABB are placed in it to form one triangular shaped bay. Cross cables are attached to

	 GRUMMAN LSS PLATFORM	 GENERAL DYNAMICS LADDER	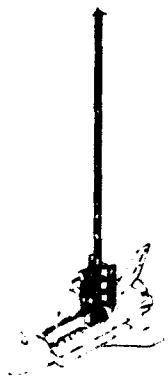 GRUMMAN LOLLIPOP
GEOMETRY			
LENGTH (m)	30.5	199.93	72.5
WIDTH (m)	10.5	10.68	4.5
DEPTH (m)	9.09	2.45	4.5
MASS			
STRUCTURE (kg)	500	996.6	279
STRUCTURE & EQUIP (kg)	3 164	2 143.6	5269
MOMENTS OF INERTIA			
ROLL-I_{XX} (kg-m^2)	3 013 000 (+139%)*	14 494 000 (+1134%)**	2 130 000 (+68%)
PITCH-I_{YY} (kg-m^2)	10 641 400 (+22%)	9 045 000 (+5%)**	9 488 000 (+10%)
YAW-I_{ZZ} (kg-m^2)	9 241 800 (+2%)	21 596 000 (+140%)**	9 104 000 (+1%)
(% INDICATES CHANGE RELATIVE TO ORBITER)			
NATURAL FREQUENCY			
FREQ. (Hz)	0.071	0.0338 – 0.072	.096
PERIOD (SEC)	14.1	29.5 – 13.9	10.4
BASIC MEMBER	1 m TRIANGULAR BEAM (ALUMINUM)	1.225 m TRIANGULAR BEAM (COMPOSITE)	1 m TRIANGULAR BEAM (ALUMINUM)

* INCREASE TO ORBITER INERTIA

** INCREASE IS ABOVE ORBITER INERTIA WITH FIXTURE

1665-010(T)

Fig. A1 Orbiter-Constructed Space Structures

STEP 1

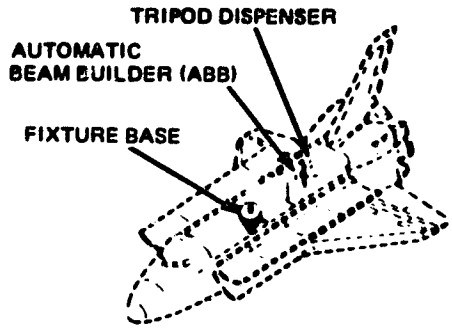

- AS LAUNCHED - ABB, TRIPOD DISPENSER & FIXTURE BASE IN PLACE

STEP 2

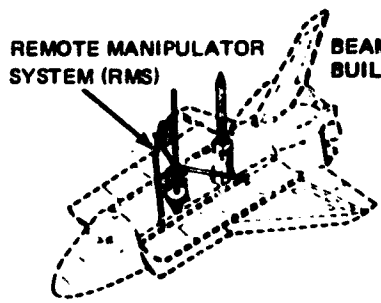

- TRIPOD DISPENSER IN OPERATIONAL POSITION
- COMMENCE BEAM MANUFACTURE
- COMPLETE FIXTURE ASSEMBLY USING RMS

STEP 3

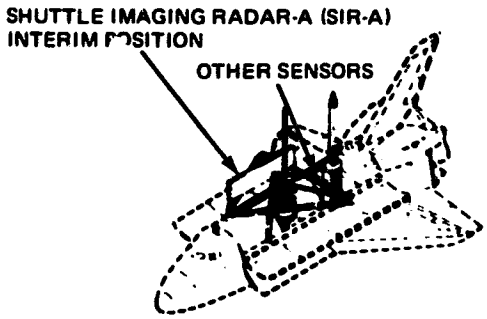

- ASSEMBLE FIRST (TOP) TRIANGULAR FRAME
- INTEGRATE SENSORS TO FIRST TRIANGULAR FRAME

STEP 4

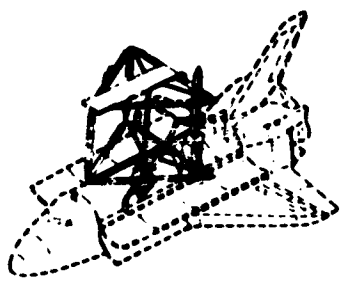

- "SLIDE" FIRST TRIANGULAR FRAME TO END OF CENTRAL FIXTURE TUBE
- ASSEMBLE TWO VERTICAL BEAMS
- ASSEMBLE SECOND TRIANGULAR FRAME
- ASSEMBLE THIRD VERTICAL BEAM
- ASSEMBLE & PRELOAD CABLES
- ORIENT SIR TO OPERATIONAL POSITION

STEP 5

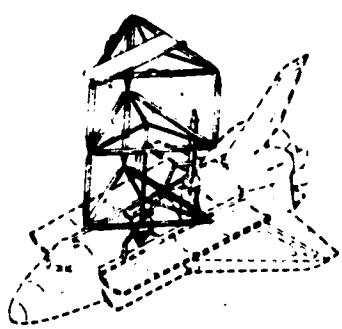

ASSEMBLE SECOND BAY TO FIRST

- INTEGRATE MATERIALS EXPERIMENTS ASSY (MEA)

STEP 6

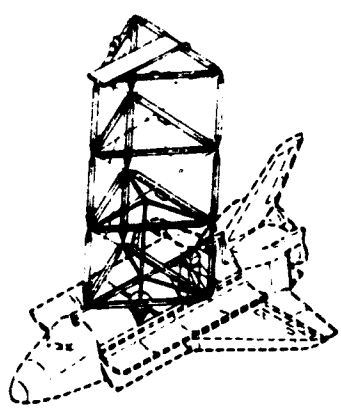

ASSEMBLE FINAL BAY TO SECOND BAY

1665-011(T)

Fig. A2 LSS Platform - Assembly

provide shear stiffness. After the completion of one bay, the assembly is vertically indexed and construction of the second bay is initiated. This process is repeated until the three-bay structure is completed. With equipment and payloads in place, the total inertia of the orbiter plus completed structure increases by 139% (Fig. A1). The natural frequency of the completed structure is 0.071 Hz.

The ladder assembly shown in Fig. A3 is another space demonstration project with potential use as the structure for a spacecraft or space platform. Assembly starts by erecting a fixture on which an ABB is mounted. Four longitudinal beams, 299m in length, are fabricated at an average rate of 1.1m/min. The four longitudinal beams are longitudinally indexed to enable the attachment of nine cross beams and equipment. Natural frequencies vary from 0.0338 Hz for the independently extended beams to 0.072 Hz for the completed structure. A major increase in roll inertia of the orbiter (1130%) occurs between the beginning and the end of construction.

The "Lollipop" shown in Fig. A4 is a gravity-gradient stabilized spacecraft with a radiometer experiment to measure soil moisture. A sequential representation of the assembly process is shown in the figure. Assembly begins with the fabrication of two 10.5m-long 1-m beams, which are then stored in the payload bay. A third ground-fabricated 10.5m-beam, fully instrumented, has already been stowed. A 72.5m-long boom is then manufactured by the ABB, and the three 10.5m beams are positioned. Then ground-fabricated verticals and diagonals are attached to complete the lower tri-beam structure. Next, structure is moved by the orbiter's Remote Manipulator System to an athwartship location to allow installation of the radiometer experiment. After assembly has been completed, the RMS is used to deploy the satellite. As indicated in Fig. A5, the natural frequencies of the vehicle are:

- Cantilevered from the orbiter - .096 Hz
- Captured by the RMS - .028 Hz
- Free - .18 Hz

In the cantilevered position, the roll moment of the orbiter plus completed structure increases by 69%.

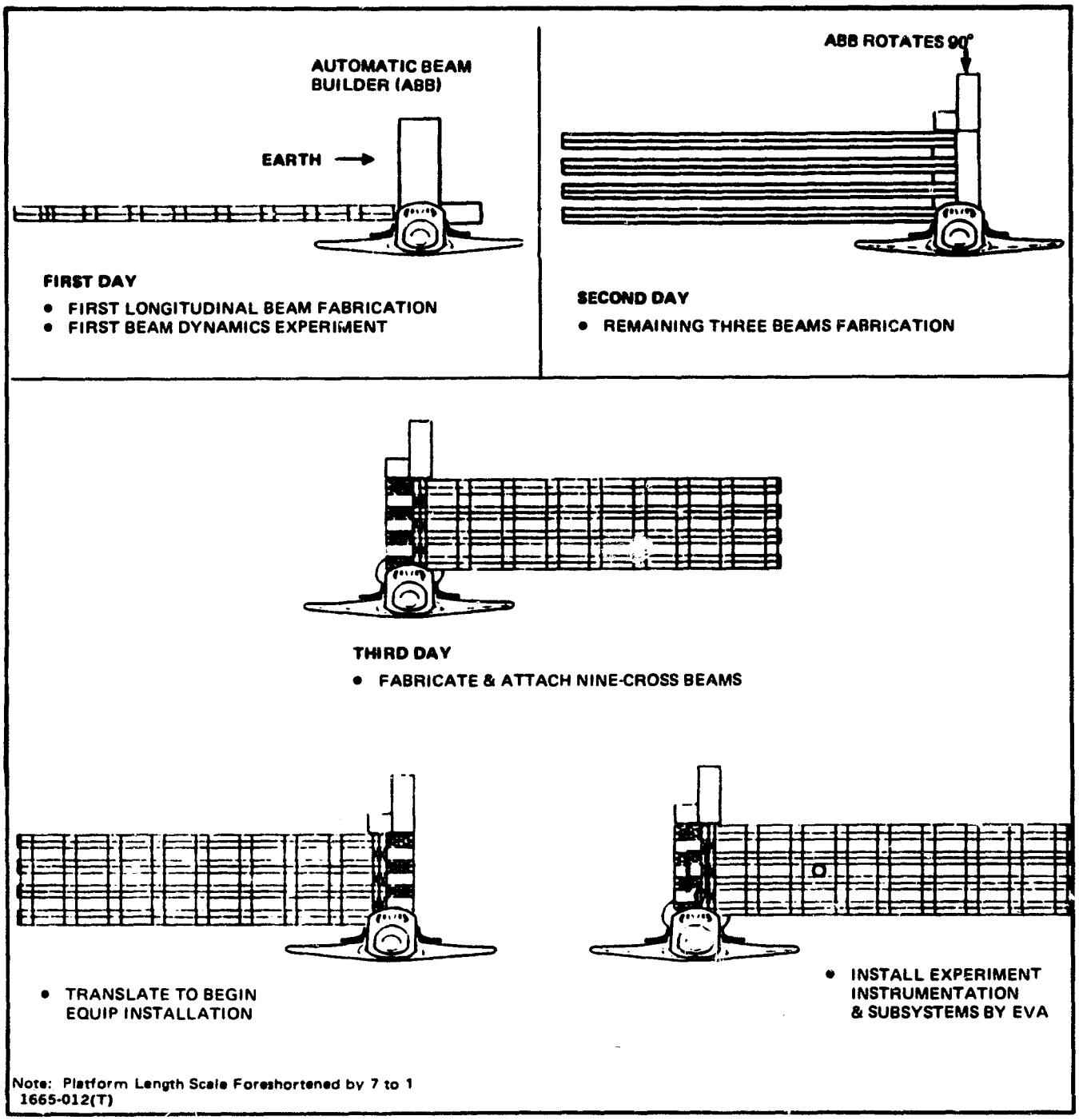

Fig. A3 SCAFEDS Ladder - Assembly

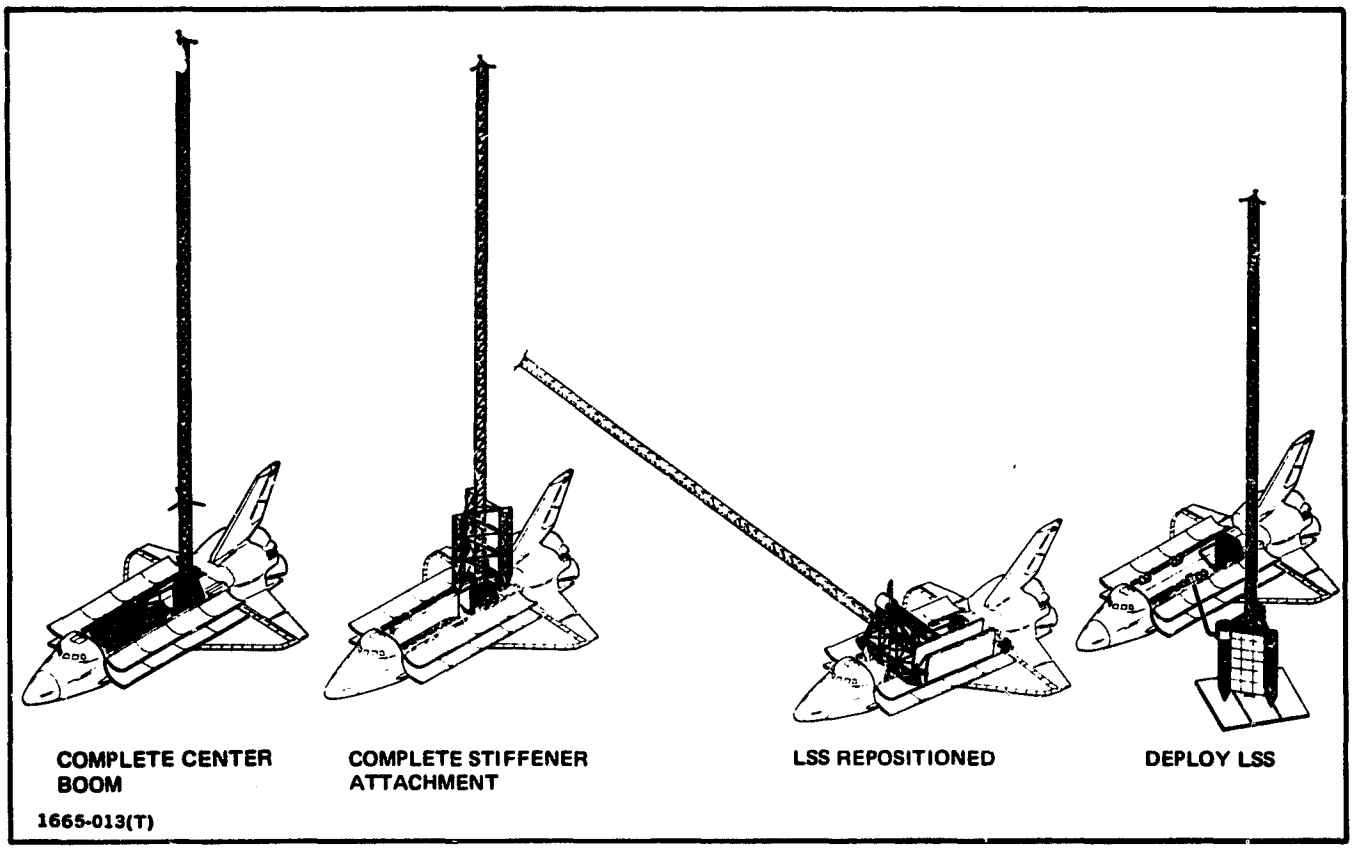

Fig. A4 LSS "LOLLIPOP" - Assembly

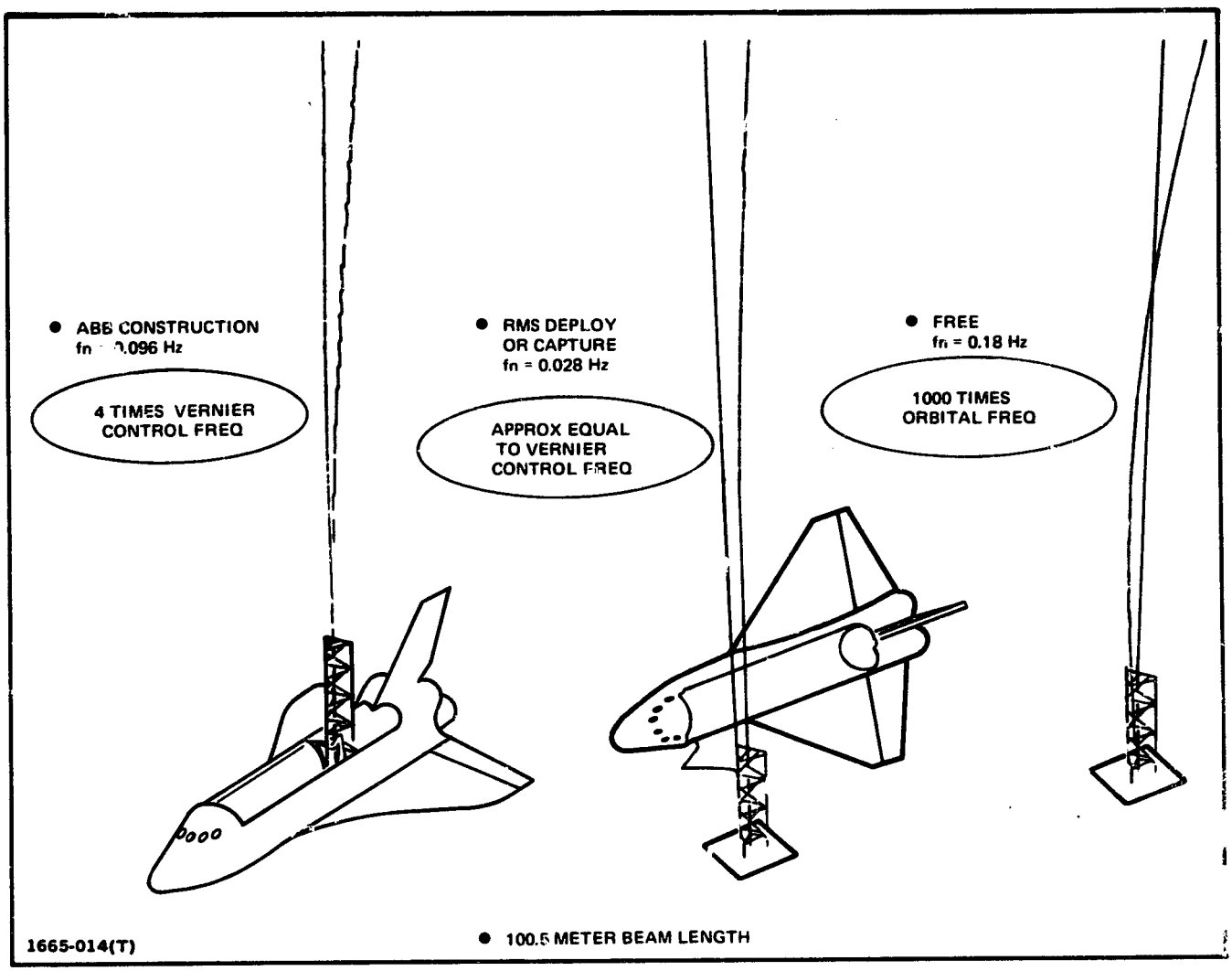

Fig. A5 Frequency Considerations - Orbiter VRCS Coupling

A1.2 Deployable Structures

Deployment techniques can be classified as follows:

- Controlled - motors and regulators determine deployment rates (rigid-body kinematics are known)
- Uncontrolled - there is no active system restraining deployment (rigid-body kinematics must be calculated)

The deployment of a Solar Electric Power System (SEPS) solar array where extension is regulated to occur at a relatively constant rate is an example of controlled deployment. A more complex controlled technique is used to deploy the Grumman Wire Wheel (Ref. A4), where synchronous motors are used to open hinges at a known rate. Uncontrolled deployment is typified by the tetrahedron building block structure deployment (Ref. A5), where the expansion is unrestrained; consequently, the deployment geometry must be calculated as a function of time, using joint-spring, friction and element-mass data.

The deployment sequence of the Power Extension Package (PEP) is shown in Fig. A6. This system is used to extend the possible STS mission times and to increase the power available for experiments. In the first phase of deployment, a packaged solar array is translated to its deployment location by the RMS. Each of the two wings of the solar array is deployed at a controlled rate by extending a central mast which pulls a solar array out. Each wing is 38m long by 4m wide and the total package weighs 1,668 lb. The fundamental frequency of the deployed array is approximately 0.02 Hz.

Another example of a configuration which used a controlled solar-array deployment is the 25 KW Power Module (Fig. A7). This free-flying module provides heat rejection, attitude stabilization, communications and data handling as well as power to docked modules. It is estimated that the solar-array deployment mast can provide sufficient stiffness to meet at least a .04 Hz frequency requirement at lengths of up to 150 feet.

The Grumman Wire-Wheel antenna (Ref. A4) shown in Fig. A8 has been used in designs of space-based radars, radiometers, and solar-power generation systems. Deployment of this structure is shown in the figure. A six-foot diameter engineering model was built to verify deployment feasibility and is shown partially deployed in Fig. A9. When packaged for shuttle launch, the

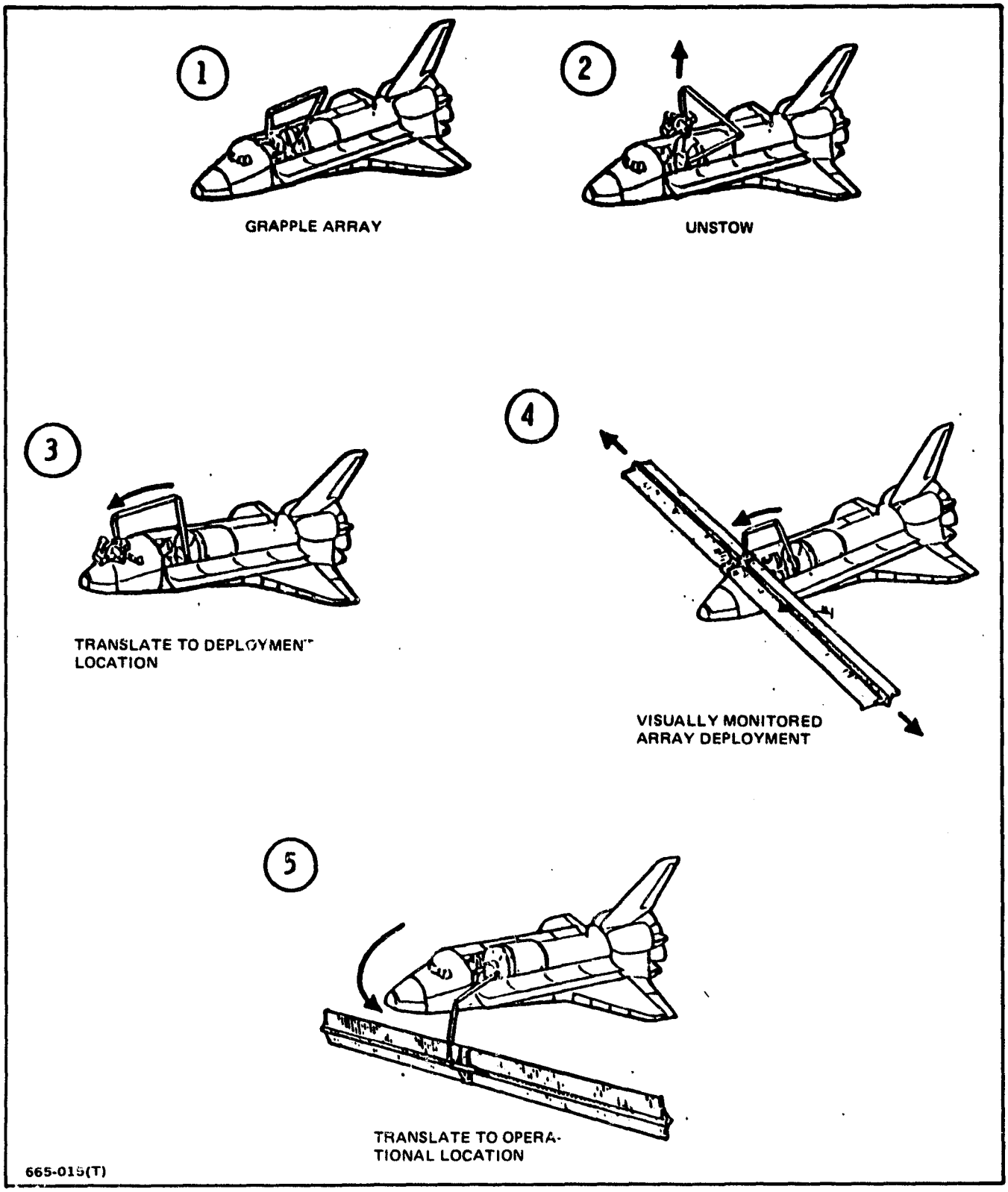

Fig. A6 PEP Deployment Sequence

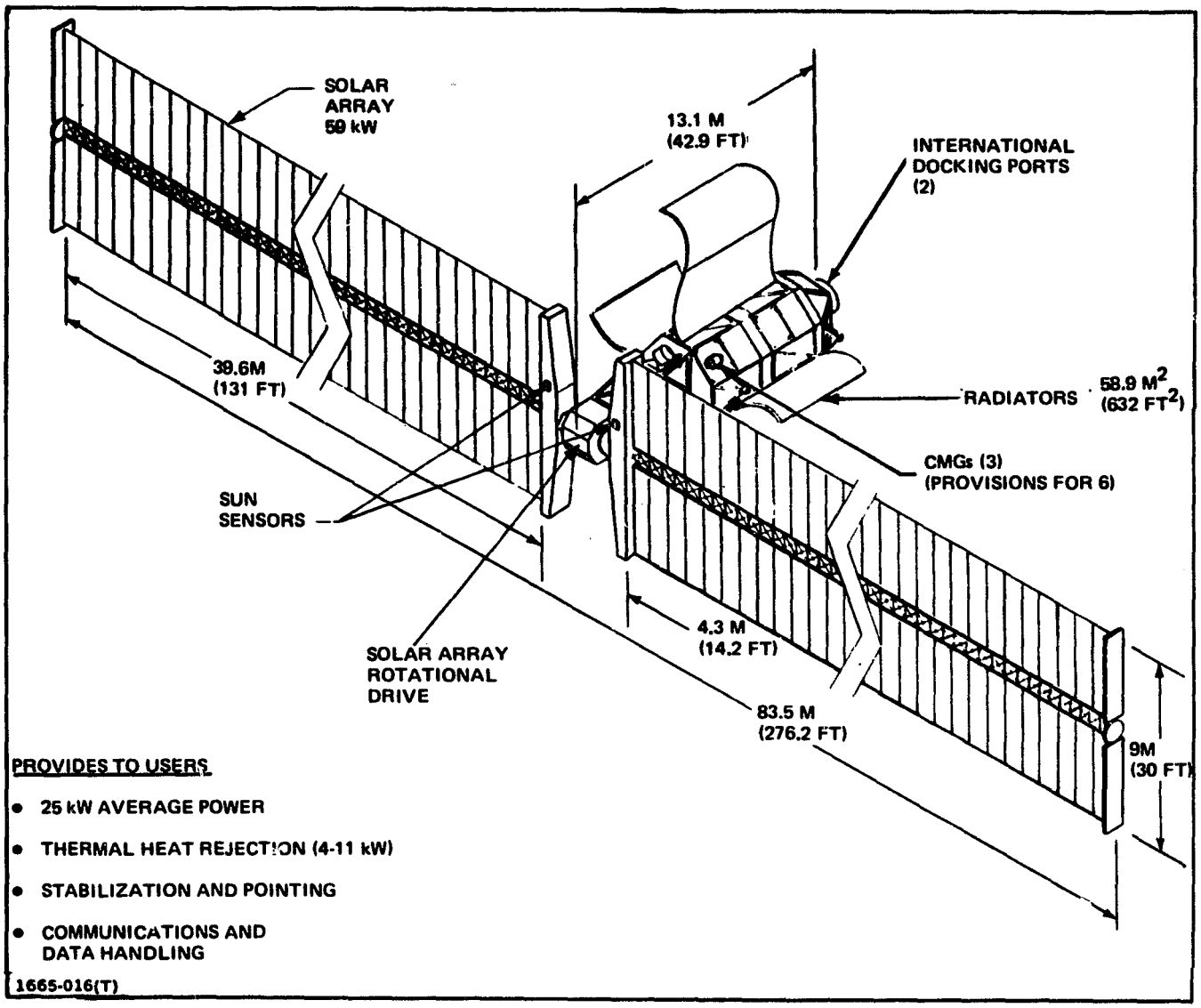

Fig. A7 Twenty-Five KW Power Module

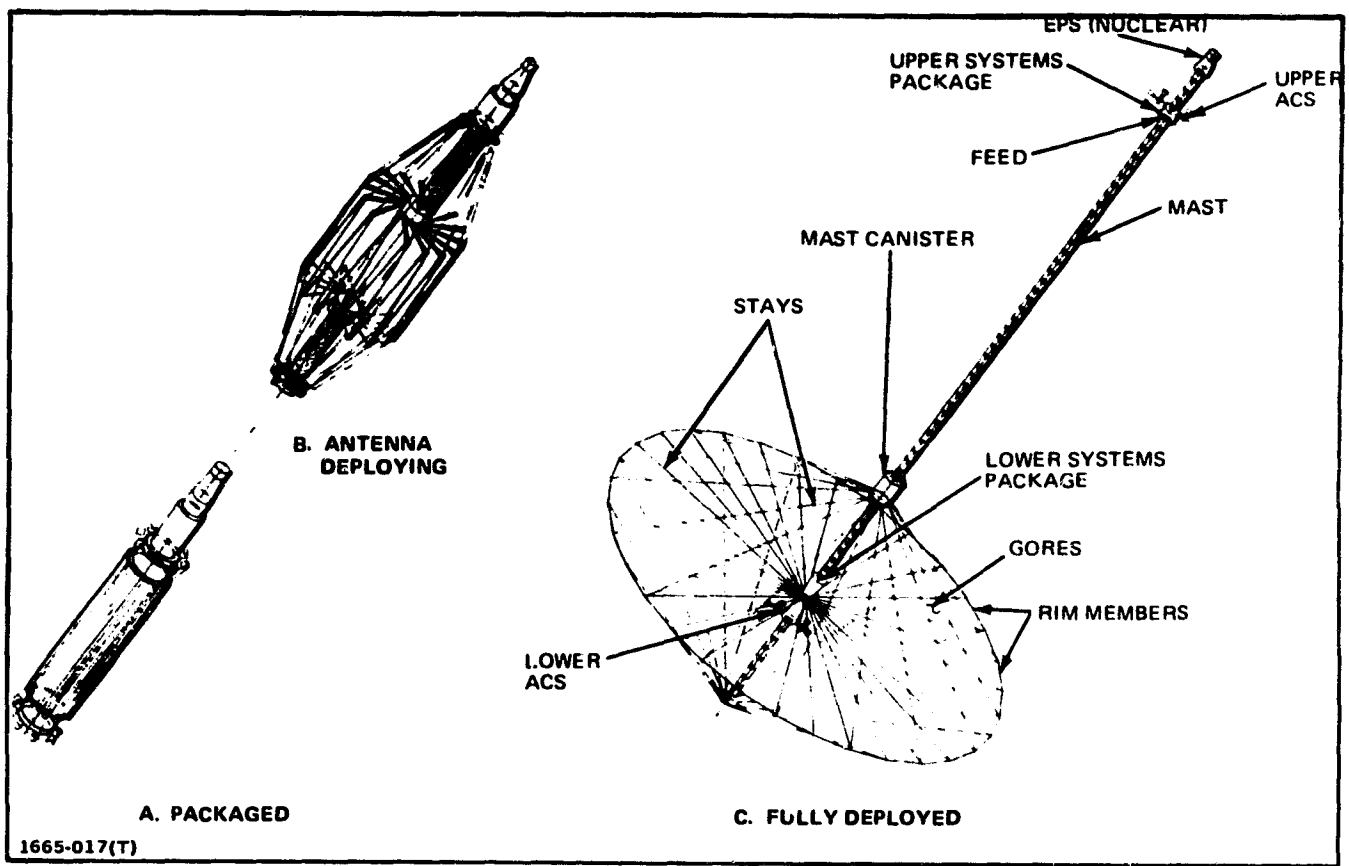

Fig. A8 Wire Wheel Deployment

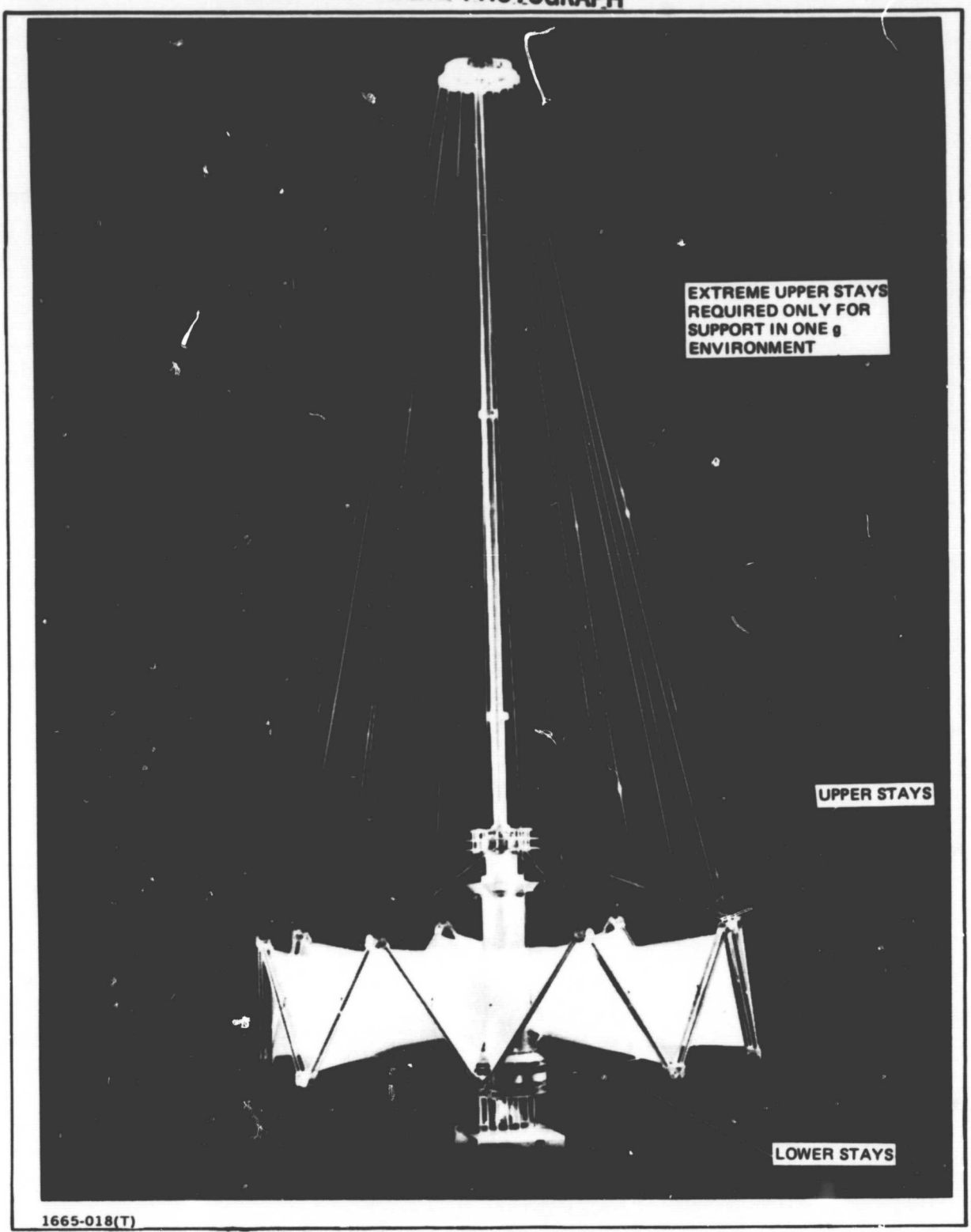

Fig. A9 Partially Deployed Wire Wheel Demonstration Model

rim members are almost parallel to the central drum axis. Membrane-like gore panels are wrapped around the drum and attached to the rim members. Synchronous motors in the hinge assemblies joining the rim members provide the power that deploys the rim and gores at a predetermined rate. After the rim is deployed, the central mast is extended. Antenna designs are available with diameters ranging from 71 to 300m with fundamental frequencies ranging from 0.035 to 0.00187 Hz.

The Tetratruss (Ref. A5) shown in Fig. A10 is a module of a general-purpose space structure. Fig. A10c shows the deployment geometry of a typical tetrahedraltruss element. The tetrahedron is driven open by rotational springs located at the midpoints of the upper and lower folding members (or alternatively by spin deployment). Times for deployment of the single tetrahedral truss vary from 1 to 10 seconds depending on deployment spring rate. The complete module is 103.49m long, 119.51m wide, and 3.48m deep and has a fundamental frequency of 1.14 Hz. The module consists of 5250 axial members, and, with variations of friction forces and spring tolerances at each joint, even a rigid-body deployment analysis of such a structure is a formidable task.

A1.3 Space Stations

Some space-station concepts extend orbiter experiment time. Others also serve as construction platforms for fabricating large space structures. One such configuration is the JSC Space Operations Center (SOC) described in Ref. A6. The basic SOC, which consists of four separate modules, is shown in Fig. A11. The service modules provide passageways between modules, control, electrical power, and thermal rejection. Two large solar arrays are mounted at each end of a long service-module boom. Antennas, radiators, and RCS units are also mounted to this boom. Two habitation modules provide crew living quarters while a logistics module is used to supply provisions. An orbiter is shown docked to the SOC. Figure A12 shows the SOC with a construction base in place to fabricate a solar-array structure. A similar SOC-mounted construction base can produce a tribeam structure such as the communication-platform concept shown in Fig. A13. A beam machine is used to form the truss members and a crane is provided to aid in the construction.

A summary of estimated natural frequencies is shown in Fig. A14. The range of frequencies is of the order of .01 Hz to 10 Hz for the indicated components of the SOC, while boom-mounted solar-array frequencies are of the order of .1 Hz.

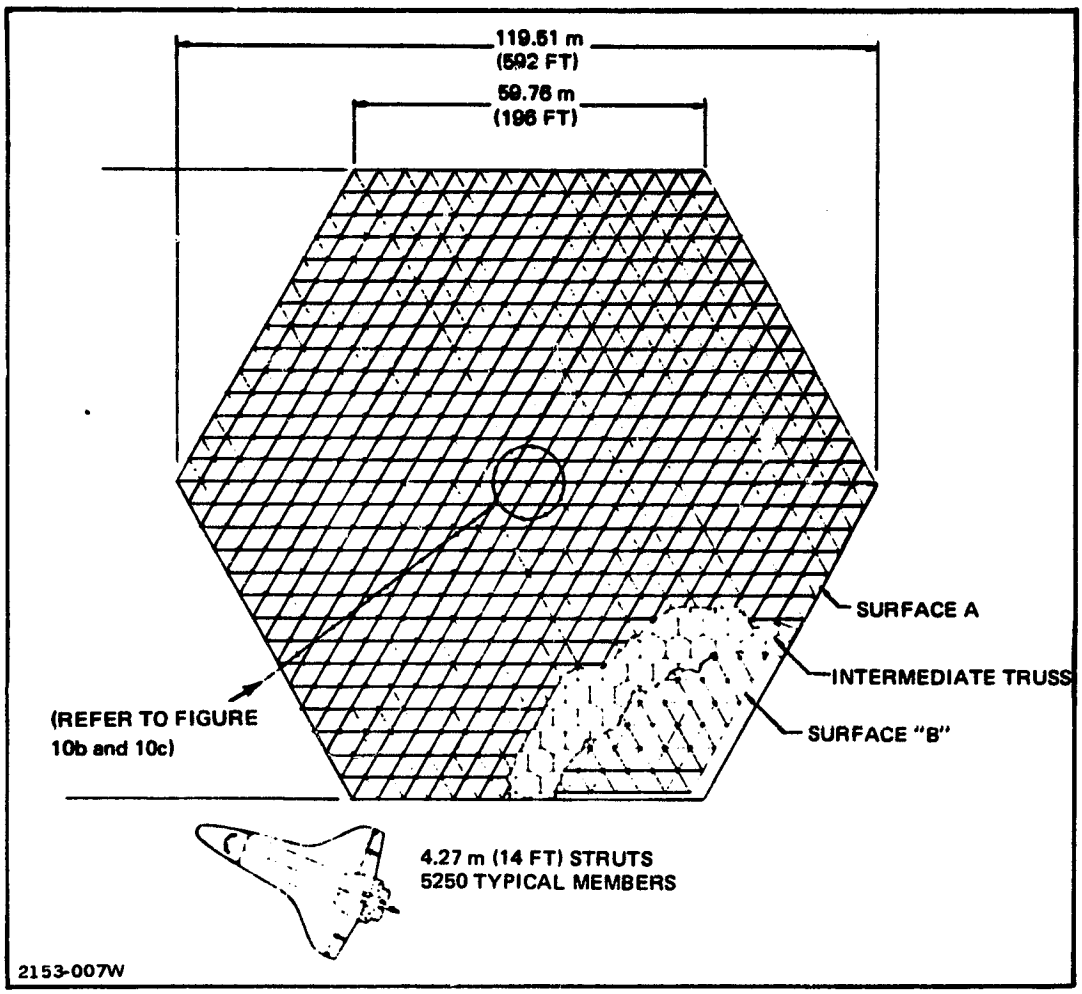

10a) TYPICAL TETRATRUSS MODULE

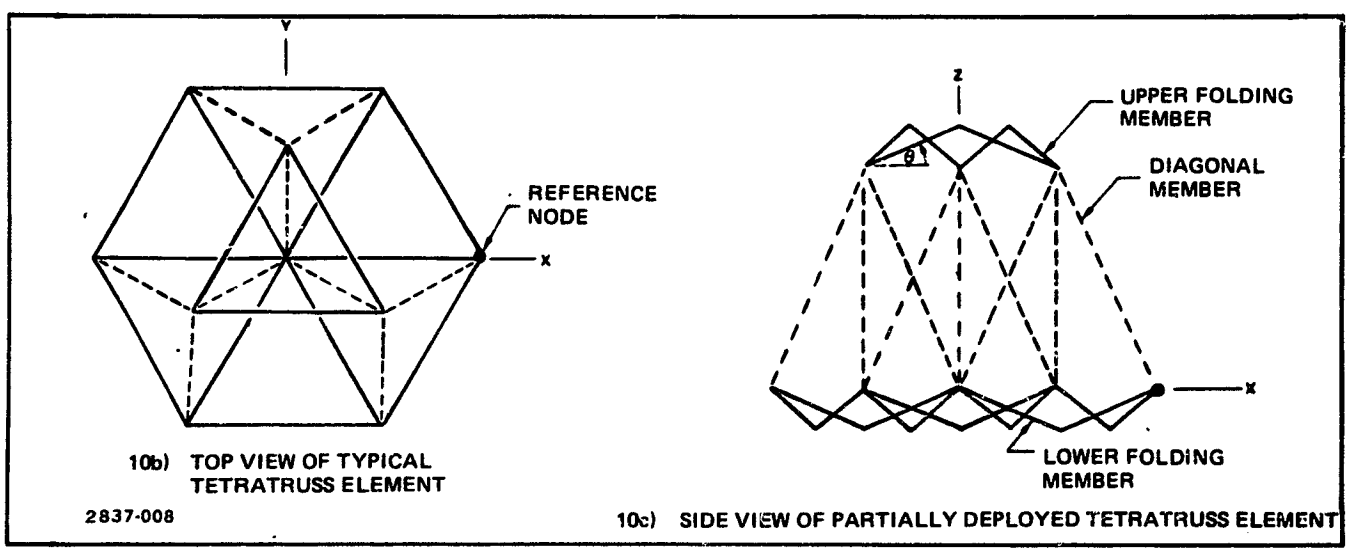

Fig. A10 Tetratruss

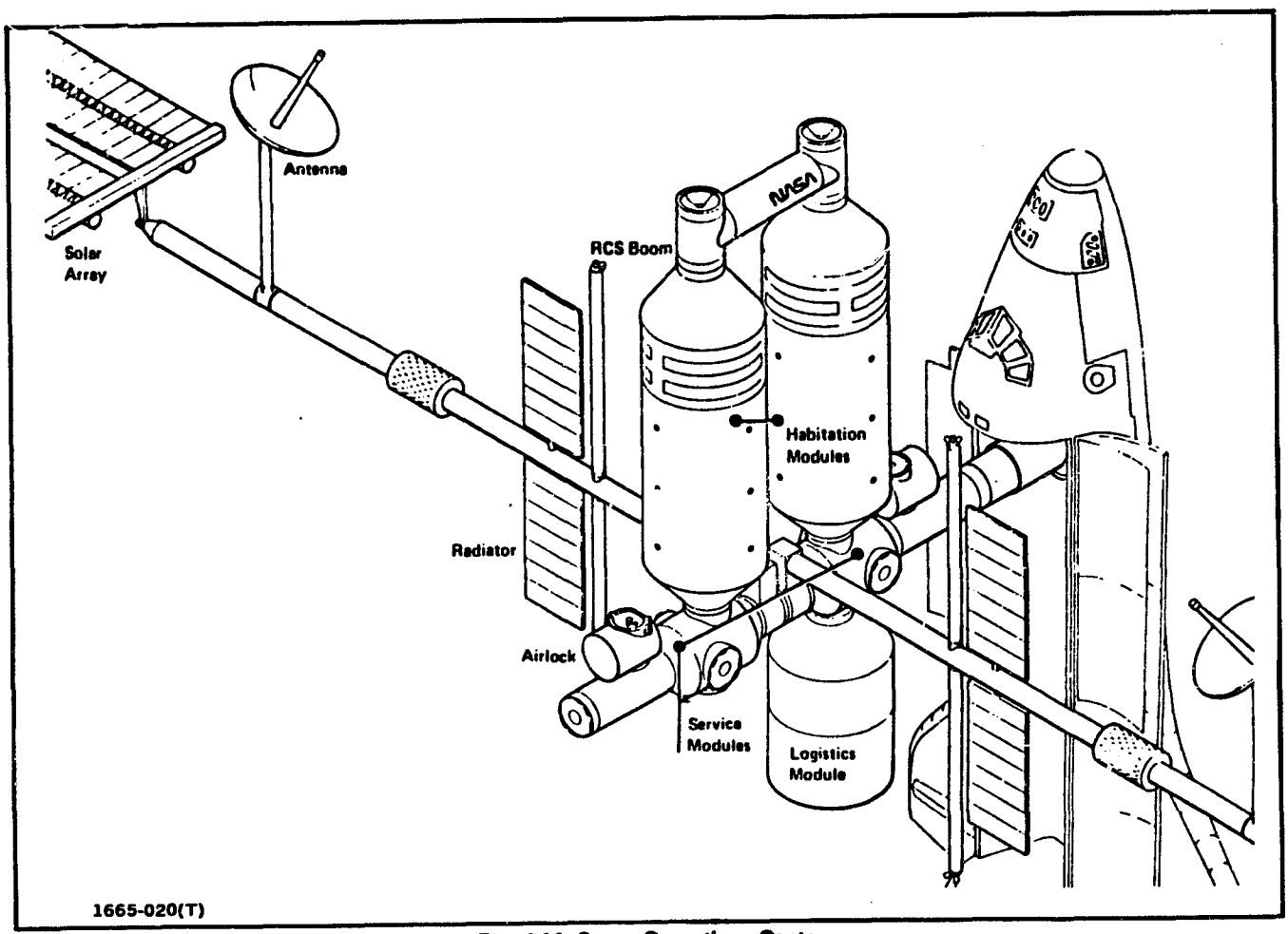

Fig. A11 Space Operations Center

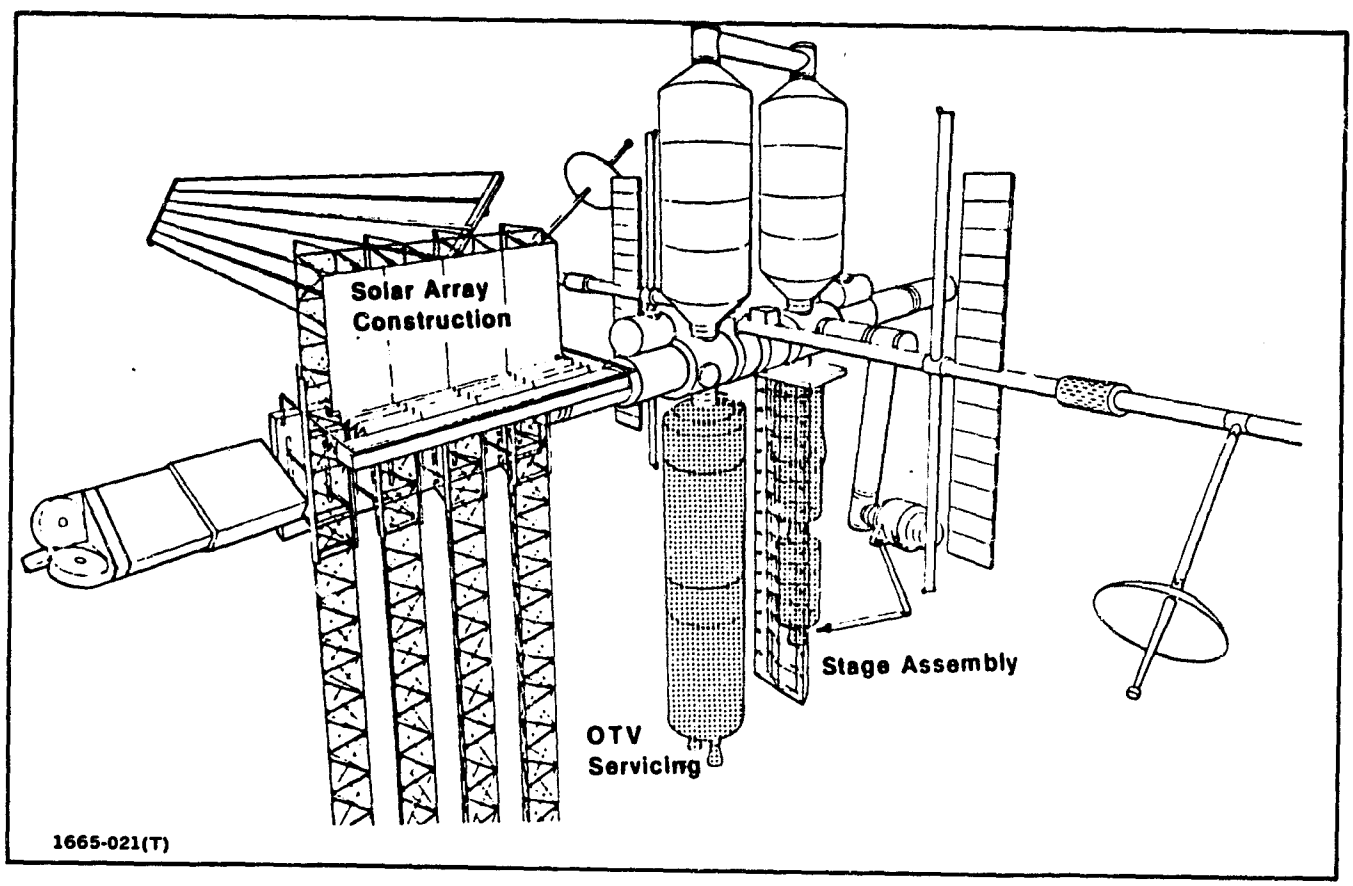

Fig. A12 Space Operations Center With Construction and Flight Support Facilities

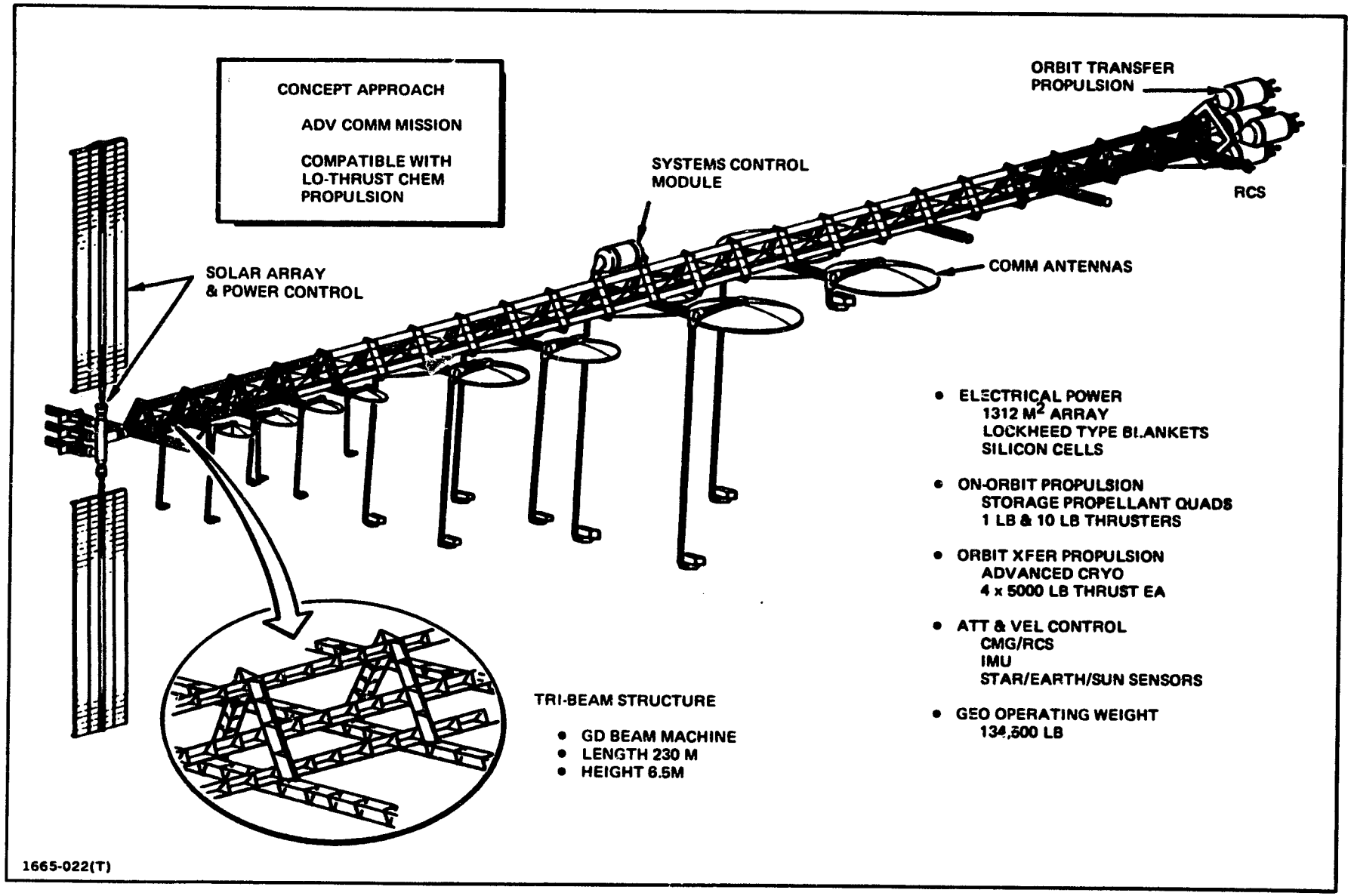

Fig. A13 Communications Platform Concept

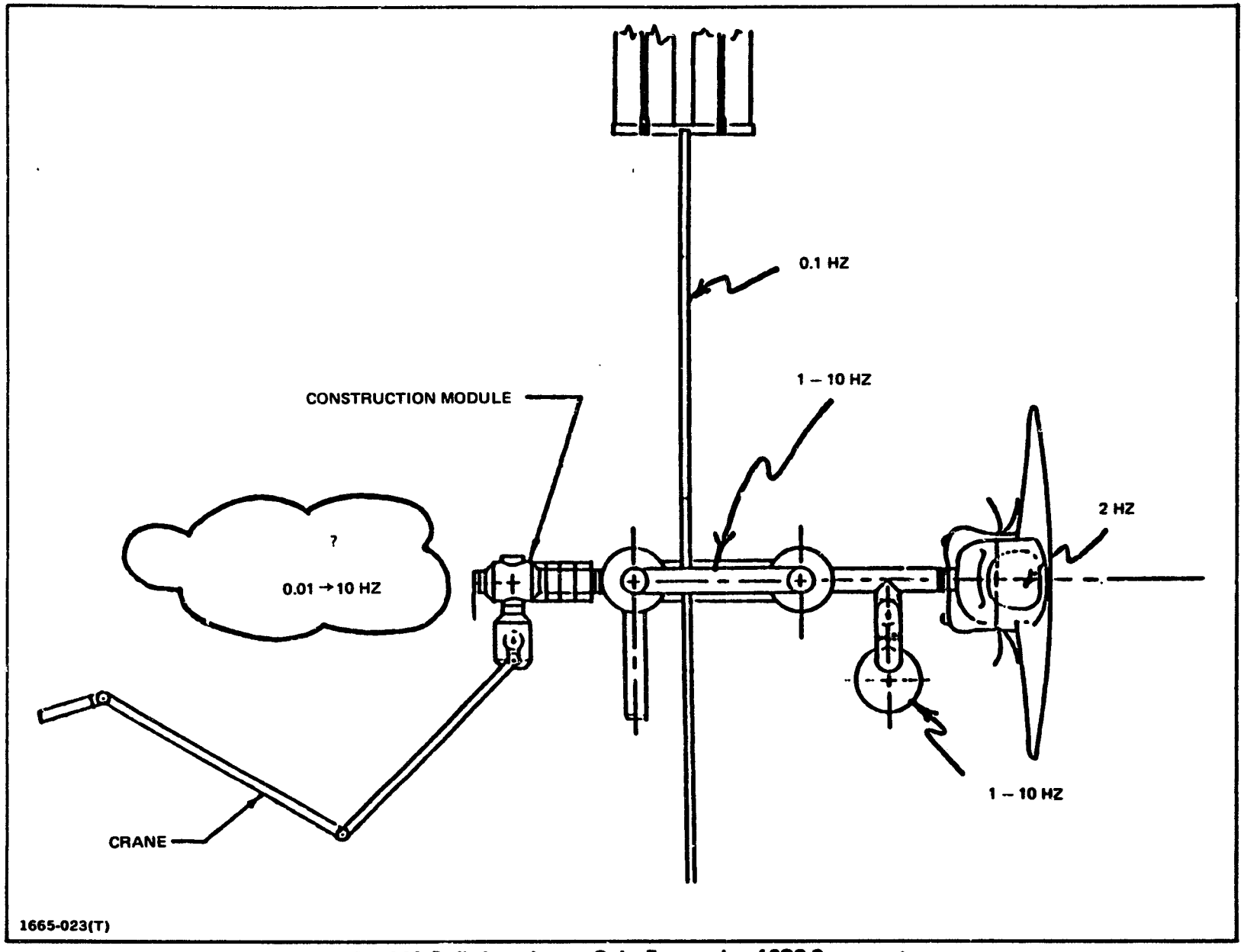

Fig. A14 Preliminary Lowest Order Frequencies of SOC Components

A1.4 Ultra-Large Space Structures

Ultra-large space structures are under investigation for use as Solar Power Satellites. Fig. A15 summarizes the characteristics of two versions developed by Boeing and Rockwell. Both versions have dimensions in the order of kilometers, masses of millions of kilograms, and require space construction bases.

The Boeing construction concept (Refs. A7 and A8) is depicted in Fig. A16. An end-builder is used in GEO to construct a four-bay strip. However, since the satellite is 8 bays wide, the end-builder must translate laterally across and then longitudinally down the first four-bay strip to complete the final four bays. Each bay will be indexed out at approximately .5m to 3m/minute. Indexing operations are also required for antenna construction (Fig. A17) which is occurring simultaneously. At completion, the fundamental frequency of the satellite and construction base is .0031 Hz.

Rockwell's construction sequence (Ref. A9) is similar. The major exception is that the satellite is constructed in one pass since both the end-builder (Fig. A18) and the satellite (Fig. A15) are 3 bays wide. The resulting satellite is longer and narrower. Beam machines produce longerons at a rate of 2m/min and solar array blankets are deployed on the fly. After completion of a bay, extension stops and transverse beams are attached. The completed satellite will have a frequency greater than 1 cycle/hour (.0003 Hz).

A1.5 Automatic Beam Builder (ABB)

Automatic beam builders are used to construct the basic elements for larger assembled structures such as the Platform, Ladder, and SPS configuration. Fig. A19 shows the Grumman ABB, which produces a 1m-deep triangular aluminum beam. As with the larger structures, the beam fabrication involves an indexing operation. Triangular caps are formed by the rolling mills for a length of one bay (1.5m). Longitudinal motion is stopped while preformed diagonal and vertical braces are welded in position. The completed bay is then extended while forming the caps for the next bay and the process is repeated. A ground demonstration unit has been built by Grumman and is operational. This unit fabricates beams at an average rate of 1.6 ft/min and extends the beam at a maximum rate of 5 ft/min. The ABB mounted in the orbiter is shown in Fig. A20. The composite beam builder (Ref. A2), used for the SCAFEDS Ladder assembly (Fig. A3), also operates in a stop-start fashion.

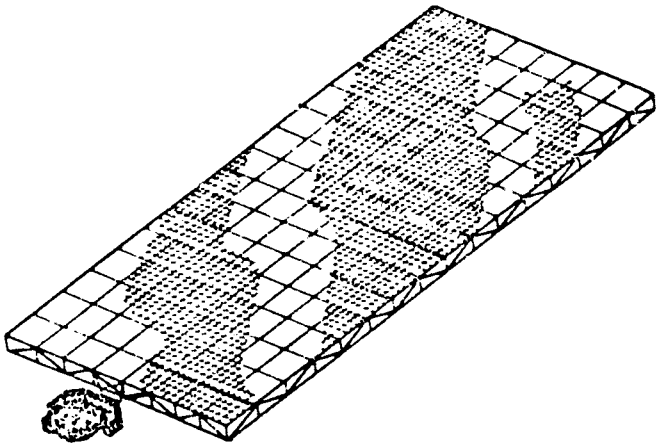

BOEING
SPS

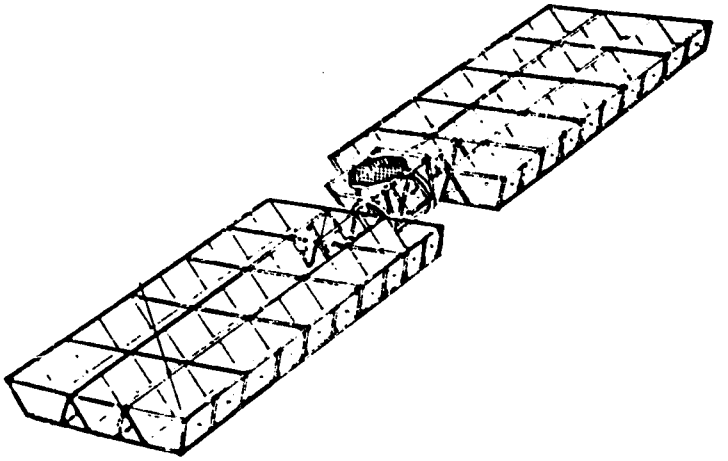

ROCKWELL
SPS

	BOEING SPS	ROCKWELL SPS
GEOMETRY		
LENGTH (km)	12.31	17.9
WIDTH (km)	5.352	3.9
DEPTH (km)	.47	.6
MASS (DRY)		
ARRAY (kg)	27 826 000	10 025 000
ANTENNA (kg)	12 234 000	14 532 000
GROWTH (kg)	8 413 000	6 137 000
TOTAL (kg)	48 473 000	30 694 000
BASIC MEMBER	7.5 M & 12.7 M TRIANGULAR BEAM (COMPOSITE)	2 M TRIANGULAR BEAM (COMPOSITE)
CONSTRUCTION SITE	GEO	GEO

1665 -024(T)

Fig. A15 SPS Concepts

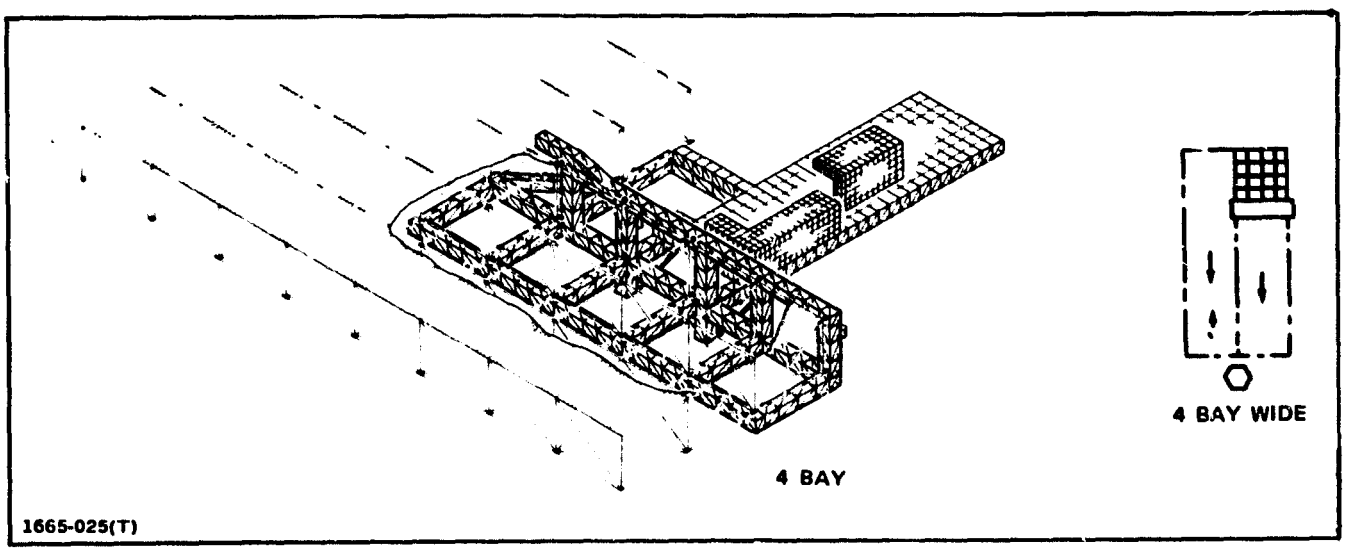

Fig. A16 End Builder Construction Base

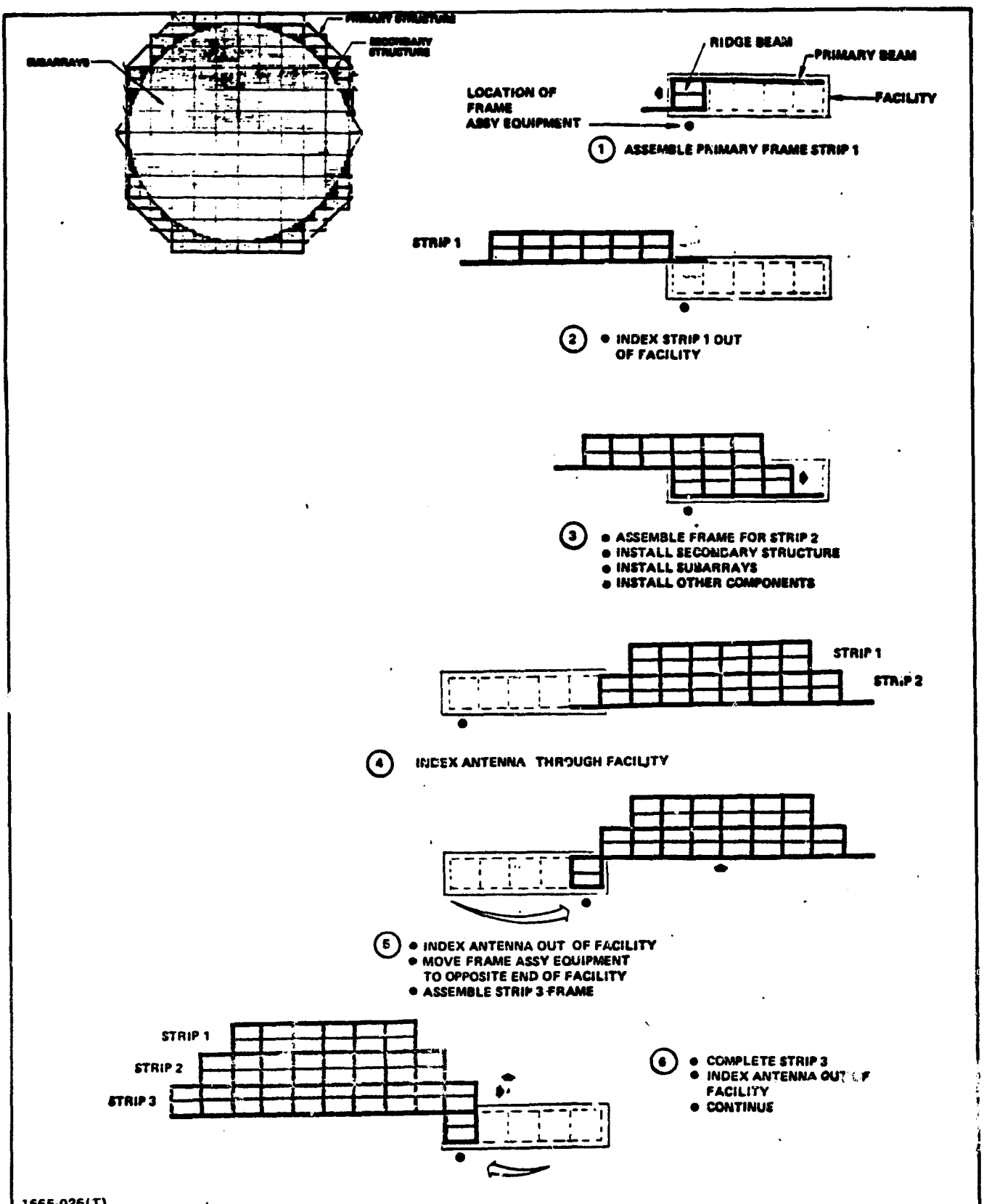

Fig. A17 SPS Antenna Assembly Sequence

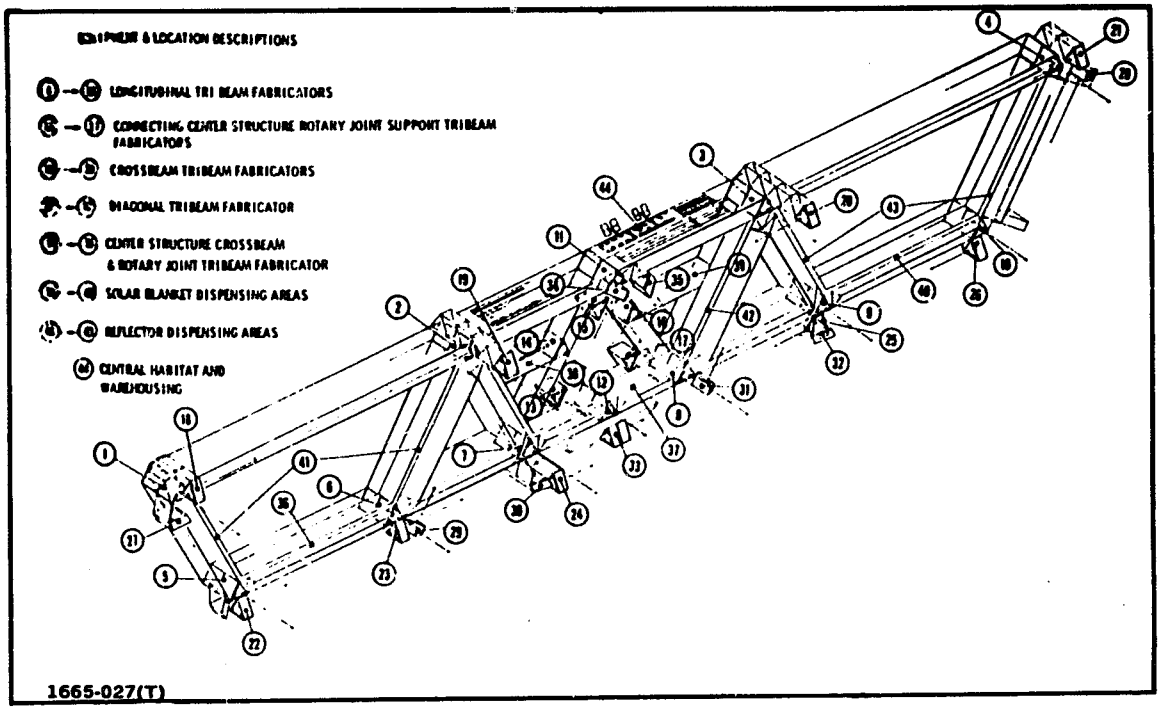

Fig. A18 Single-Pass Satellite Construction Base (SCB)

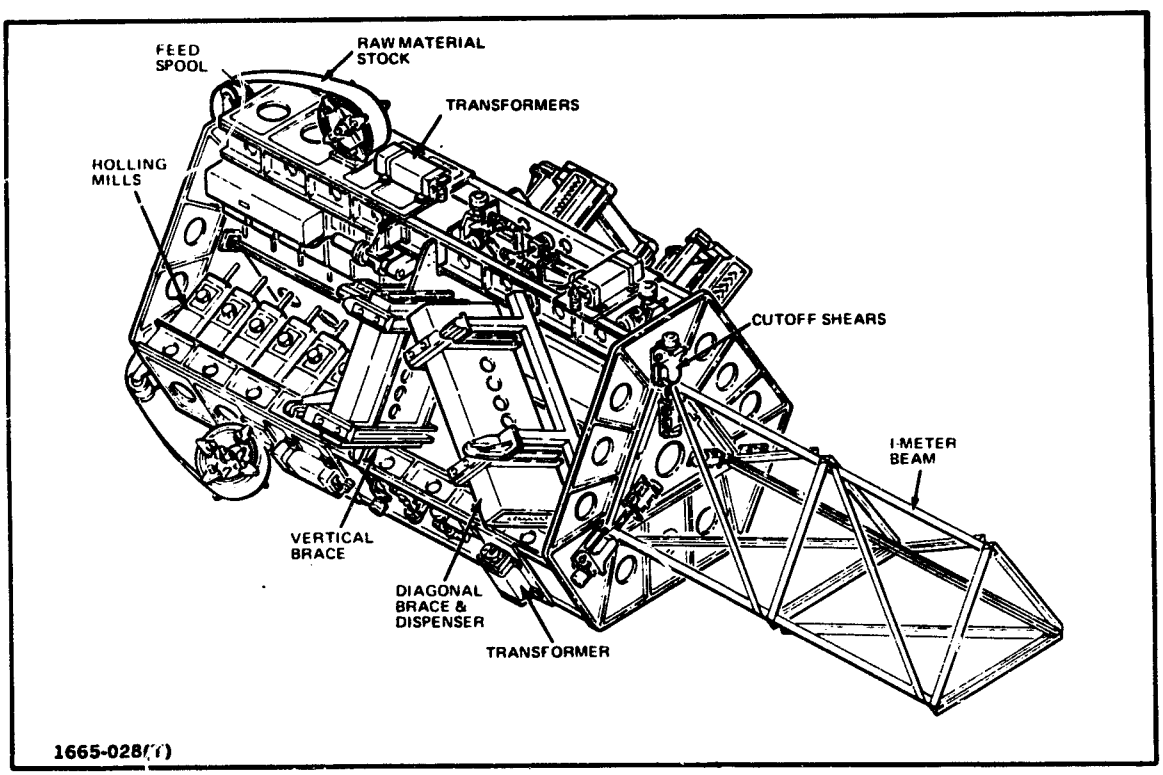

Fig. A19 Grumman Automatic Beam Builder

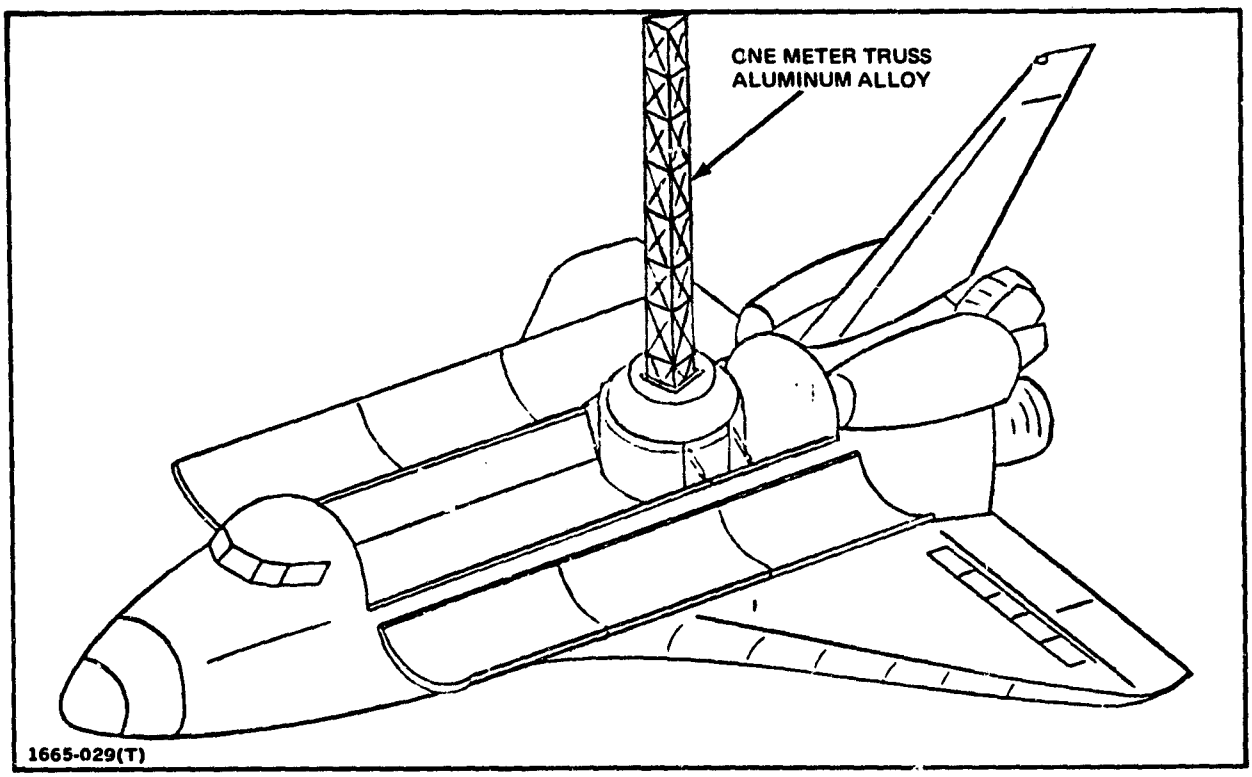

Fig. A20 ABB Mounted in Orbiter

A1.6 Remote Manipulator System

The orbiter is equipped with a 50 ft.-long Remote Manipulator System mounted on the port side of the vehicle. This arm (Fig. A21) can be used to deploy a 65,000 lb. payload and retrieve a 32,000 lb. payload. The RMS can be operated manually or automatically. It has 6 degrees-of-freedom, and it can move payloads through large translations and rotations. This system and extensions thereof, such as the crane shown in Fig. A12, will be used extensively in large space-structure construction. The boom and joints are relatively flexible; the RMS has a tip stiffness of 10 lb./in. when fully extended.

A2. Study Configuration Selection

In selecting a study configuration, the following ground rules were assumed:

- The configuration must exhibit characteristics of representative large space structures
- The configuration must be amenable to representation by a relatively coarse finite element model, so that it would be practical to generate solutions by direct numerical integration, using physical coordinates.

Table A1 contains a list of important dynamic characteristics and problem areas of large structures with variable geometry, cross referenced with typical configurations (discussed in Section A1). Some configurations such as the Wire Wheel display different characteristics during the various phases of construction or deployment. The analysis of each of these configurations requires an idealization employing a large number of degrees-of-freedom; consequently, each configuration requires a method for coordinate reduction. With the exception of the Tetratruss and RMS, these structures all have a construction phase where structure is extended linearly (along one axis) either continuously or by indexing. Prior to construction or deployment, these structures are very stiff (infinitely stiff if they are represented as rigid bodies), and their stiffness decreases drastically as they are extended. For most structures, the rigid-body shape can be defined as a function of time. On the other hand, Tetratruss expansion is an example of uncontrolled deployment where the rigid-body shape must be determined as a function of time, using a rigid-link dynamic analysis. Membrane deployment is required for the PEP, Power Module, and SPS configurations where solar-array blankets and reflectors are extended, and for the Wire Wheel where the gores unroll from the central drum. Differential stiffness

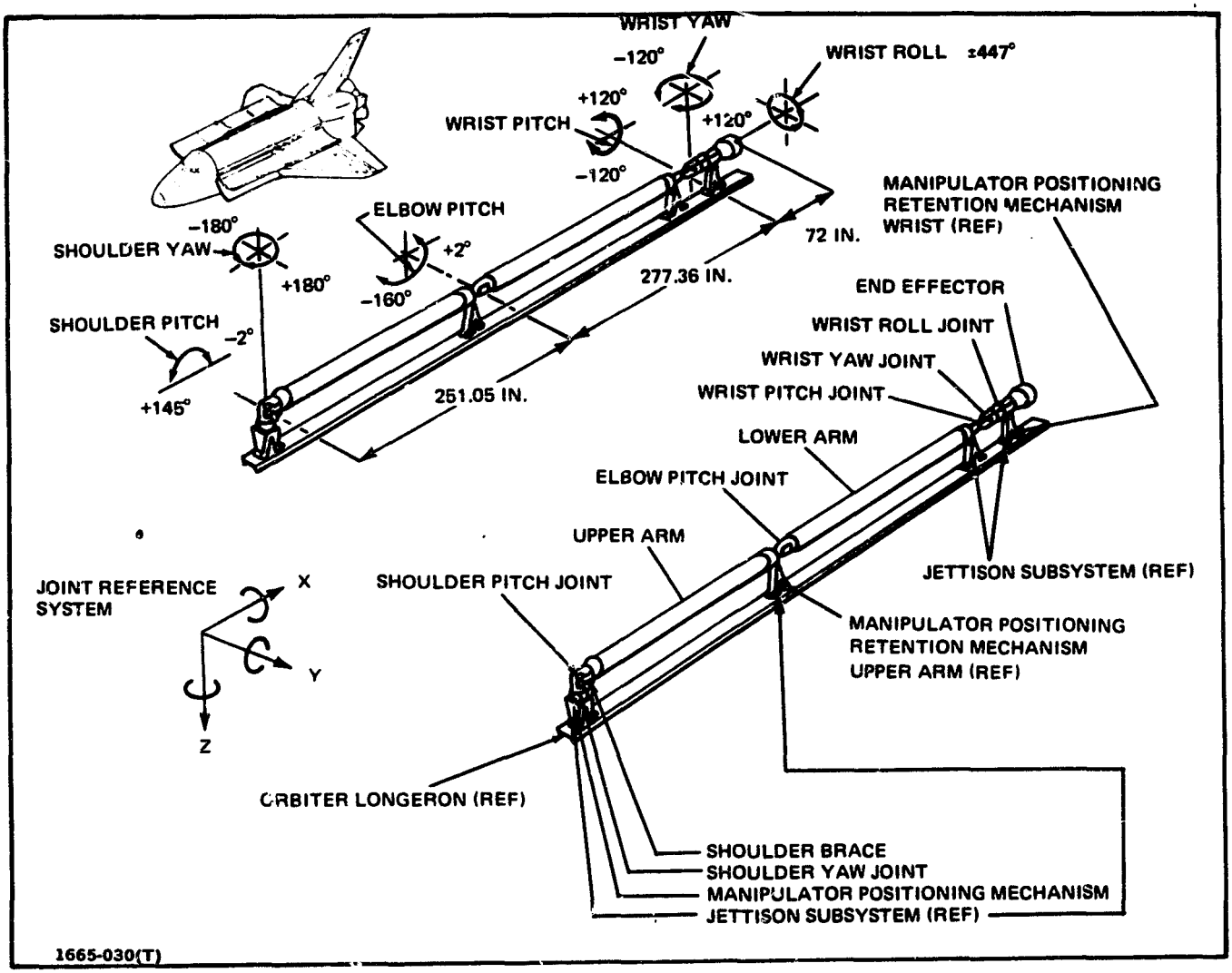

Fig. A21 Orbiter Remote Manipulator System

TABLE A1 CONFIGURATION EVALUATION

FEATURES AND PROBLEM AREAS	CONFIGURATION											
	LSS PLATFORM	LADDER	LOLLIPOP	PEP	POWER MODULE	WIRE WHEEL	TETRATRUSS	SOC	BOEING SPS	ROCKWELL SPS	ABB	RMS
COORDINATE-REDUCTION METHOD REQUIRED FOR ANALYSIS	X	X	X	X	X	X	X	X	X	X	X	X
LINEARLY EXTENDING STRUCTURE • CONTINUOUS • INDEXED	X X	X X	X X	X X	X X	X(1) X(1)		X X	X(2) X(2)	X X	X X	
CONTROLLED DEPLOYMENT (RIGID BODY MOTION KNOWN)	X	X	X	X	X	X		X	X	X	X	X
UNCONTROLLED DEPLOYMENT (RIGID BODY MOTION TO BE CALC)							X					
MEMBRANE DEPLOYMENT				X	X	X			X	X		
EMERGENCE FROM LARGE MASS	X	X	X		X	X(1)		X	X	X	X	
2- OR 3- DIMENSIONAL STRUCTURES						X(3)	X		X			X
MODULAR BUILDUP							X	X				
2- OR 3-DIMENSIONAL GEOM. CHANGES						X	X					X

(1) BOOM DEPLOYMENT
(2) LEO CONSTRUCTION
(3) ANTENNA DEPLOYMENT

1665-031(T)

would have to be included for such concepts. In six of the concepts, structures emerge from a large, relatively concentrated, variable mass, either the orbiter or a construction base. For the SOC and Boeing SPS, the construction base is relatively flexible. Certain configurations have two-dimensional (plate-like) structures. This effect is particularly important when cross coupling is induced by large offset masses. The buildup of a large structure by assembling large modules introduces a docking (or berthing) and joining problem.

Another problem occurs when a flexible structure is extended from a rigid base. As indicated in Fig. A22, when a node of the flexible structure first emanates from the rigid base, the structural member between the node and the base is differential in length, and therefore, infinitely stiff. This gives rise to an infinite-frequency component in the vibration solution.

A study configuration is proposed which will incorporate a linearly extending structure because this feature is used in the deployment or construction of most of the configurations. In addition, an idealization incorporating this feature can be used to investigate methods for treating the infinite-frequency phenomenon. The extending structure will emerge from a mass which has flexibility due to added appendages. In addition, large changes in geometry and natural frequency will be included. Figure 1 of the main text shows the basic configuration that was selected. It contains a 1-m aluminum beam that extends from a beam machine installed in the orbiter. This beam is a candidate for early experimental verification to determine modal properties, damping, and the effects of construction rates. A 25 KW power-module is attached to the orbiter to introduce flexible appendages.

In the first problem that is addressed, the beam is fabricated by the beam machine. The solar arrays are present in the deployed state; however, the RMS shown in Fig. 1 is stowed. The system flexibilities are selected so that the cantilever-beam frequency, which is initially infinite, will decrease to a value that is less than the initial system frequency.

In the second problem, the RMS is initially attached to the beam. In order to study the dynamic effects of large three-dimensional rotations, the beam is detached from the orbiter and rotated 90 deg. about the RMS-shoulder pitch-axis. Since this axis is located 19.6 deg. from the Z_2 axis (see Fig. 2), the beam is rotated out of the orbiter pitch plane.

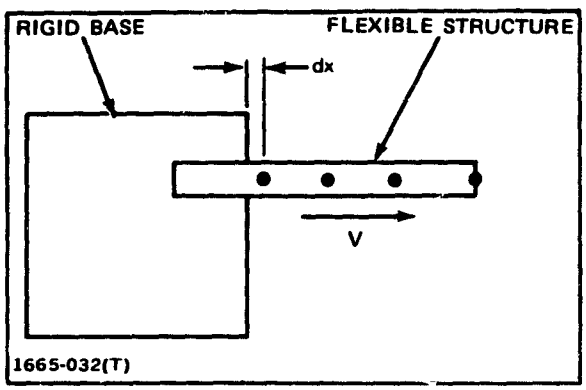

Fig. A22 Example of Infinite-Frequency Problem

Appendix B

DETAILS FOR FORMING THE STIFFNESS MATRIX FOR THE BEAM-FABRICATION PROBLEM

The computation procedure for the development of the stiffness matrix is outlined in Section 2.2. Further details are developed in subsequent sections of this appendix.

B1. Computation Procedure for the Development of the Structural Stiffness Matrix

The orbiter and power module, together, are the fixed-geometry portions of the structure, and are referred to as the platform. At t = 0, the platform stiffness $[K_p]$ is corrected for rigid-body drift (see Sections B6 and B7). If the beam has not been emitted, the structural stiffness matrix [K] is set equal to $[K_p]$. If 1) $t > 0$, 2) beam column effects are not being included, and 3) there has been no beam growth between the current and previous times, [K] has not changed from the previous time point, and the following procedure is therefore omitted at the current time point.

ABB Beam

If $\ell_n < \ell_c$: develop the beam stiffness matrix, assuming there are only n-1 nodes on the beam; set m = n-1, where m is the number of nodes on the beam. If n = 1, go to Step 5.

If $\ell_n \geq \ell_c$, set m = n.

1. Compute the element stiffness matrices in accordance with Section B2. These matrices are $[K^{(1)}]$, $[K^{(2)}]$, ..., $[K^{(m)}]$ ($[K^{(1)}] = [K^{(2)}] = \ldots = [K^{(m-1)}]$*)
2. Transform $[K^{(m)}]$ to the orbiter cm coordinates to obtain $[\bar{K}^{(m)}]$ (Section B2).
3. Assemble $[K^{(1)}]$, $[K^{(2)}]$, ..., $[K^{(m-1)}]$, $[\bar{K}^{(m)}]$ to obtain $[\bar{K}_B]$ using the displacement method of finite-element analysis (Ref. 14).
4. Use the Guyan reduction procedure (Section B4) to eliminate all rotation coordinates except those for the orbitor ($\theta_{100,1}$, $\theta_{100,2}$, $\theta_{100,3}$). Call the result $[K_B]$. If $\ell_n < \ell_c$, save the partition of [G] containing the last two rows, and call this matrix $[G_\theta]$.

If $\ell_n \geq \ell_c$, go to Step 6.

5. When $\ell_n < \ell_c$, it is necessary to obtain the deformations of node n and expressions to reduce node n from the mass matrix and applied load vector. This is accomplished by computing $[G_n]$ (see Section B5), and saving it for future use.

Final Assembly

6. Use the displacement method to assemble $[K_p]$ and $[K_B]$ to form $[K]$, the stiffness matrix for the entire structure.

7. Correct $[K]$ for rigid-body drift. (See Section B6).

B2. Beam-Member Stiffness Matrix

A program option has been incorporated to include the influence of the axial load on the stiffness of the beam. This axial load can have a different value for each beam member. The stiffness relation for the i-th element shown in Fig. B1 is as follows*:

$$\begin{Bmatrix} f_{i,1} \\ f_{i,2} \\ m_{i,1} \\ m_{i,2} \\ \hline f_{i+1,1} \\ f_{i+1,2} \\ m_{i+1,1} \\ m_{i+1,2} \end{Bmatrix} = \left[\begin{array}{cccc|cccc} K_2 & & & -K_8 & -K_2 & & & -K_8 \\ & K_3 & K_7 & & & -K_3 & K_7 & \\ & K_7 & K_5 & & & -K_7 & K_9 & \\ -K_8 & & & K_6 & K_8 & & & K_{10} \\ \hline -K_2 & & & K_8 & K_2 & & & K_8 \\ & -K_3 & -K_7 & & & K_3 & -K_7 & \\ & K_7 & K_9 & & & -K_7 & K_5 & \\ -K_8 & & & K_{10} & K_8 & & & K_6 \end{array}\right] \begin{Bmatrix} u_{i,1} \\ u_{i,2} \\ \theta_{i,1} \\ \theta_{i,2} \\ \hline u_{i+1,1} \\ u_{i+1,2} \\ \theta_{i+1,1} \\ \theta_{i+1,2} \end{Bmatrix} \quad \text{(B1)}$$

---

* See Ref. B1 for the basic stiffness and Ref. B2 for the incremental stiffness. Some of the signs differ from those of the references to account for differences in the coordinate systems.

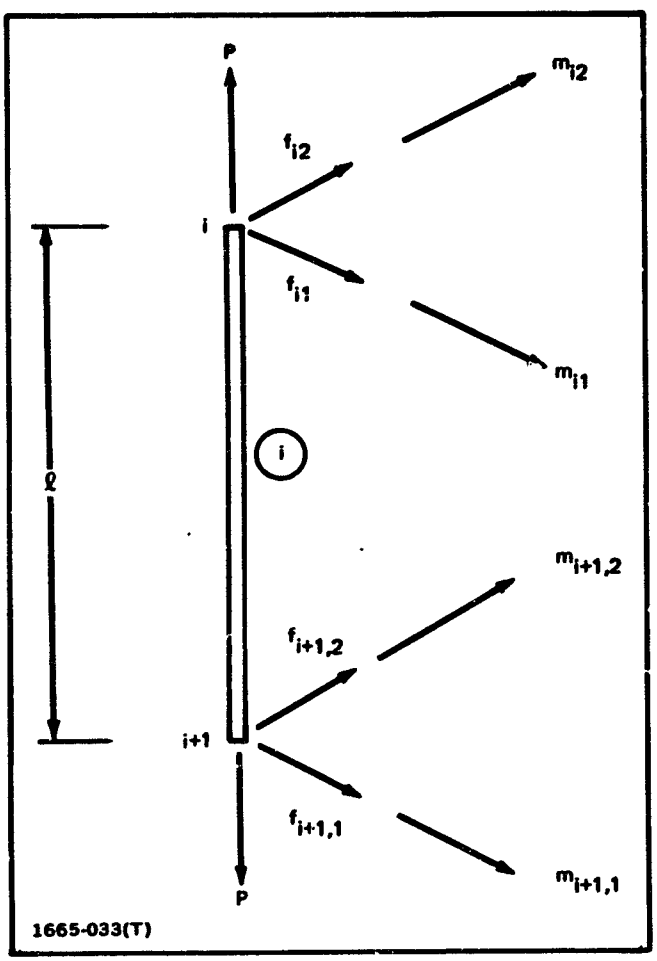

Fig. B1 Notation for Beam Element Stiffness Matrix

where

$$K_2 = \frac{12EI_2}{\ell^3} + 12\gamma \tag{B2}$$

$$K_3 = \frac{12EI_1}{\ell^3} + 12\gamma \tag{B3}$$

$$K_5 = \frac{4EI_1}{\ell} + \frac{4}{3}\ell^2\gamma \tag{B4}$$

$$K_6 = \frac{4EI_2}{\ell} + \frac{4}{3}\ell^2\gamma \tag{B5}$$

$$K_7 = \frac{6EI_1}{\ell^2} + \ell\gamma \tag{B6}$$

$$K_8 = \frac{6EI_2}{\ell^2} + \ell\gamma \tag{B7}$$

$$K_9 = \frac{2EI_1}{\ell} - \frac{\ell^2}{3}\gamma \tag{B8}$$

$$K_{10} = \frac{2EI_2}{\ell} - \frac{\ell^2}{3}\gamma \tag{B9}$$

where

$$\gamma = \frac{P}{10\ell} \tag{B10}$$

The above equations apply to member i, where E is its modulus of elasticity, I_1 and I_2 are its area cross-sectional moments of inertia about axes 1 and 2, respectively, ℓ is its length and P is its axial load. u_{ij} and θ_{ij} are the linear and rotational displacements of node i along axis j corresponding to the force and moment, f_{ij} and m_{ij}, shown in Fig. B1. The element stiffness matrices for the n beam members, as determined by the coefficient matrix in (B1) for each member, are called $[K^{(1)}]$, $[K^{(2)}]$, ..., $[K^{(n)}]$.

The deformation coordinates of the lower node of member n are the deformations of node 50, the ABB. Since the ABB is rigidly attached to the orbiter, the coordinates are transformed to the coordinates of node 00, the orbiter CM. The transformation between coordinates is

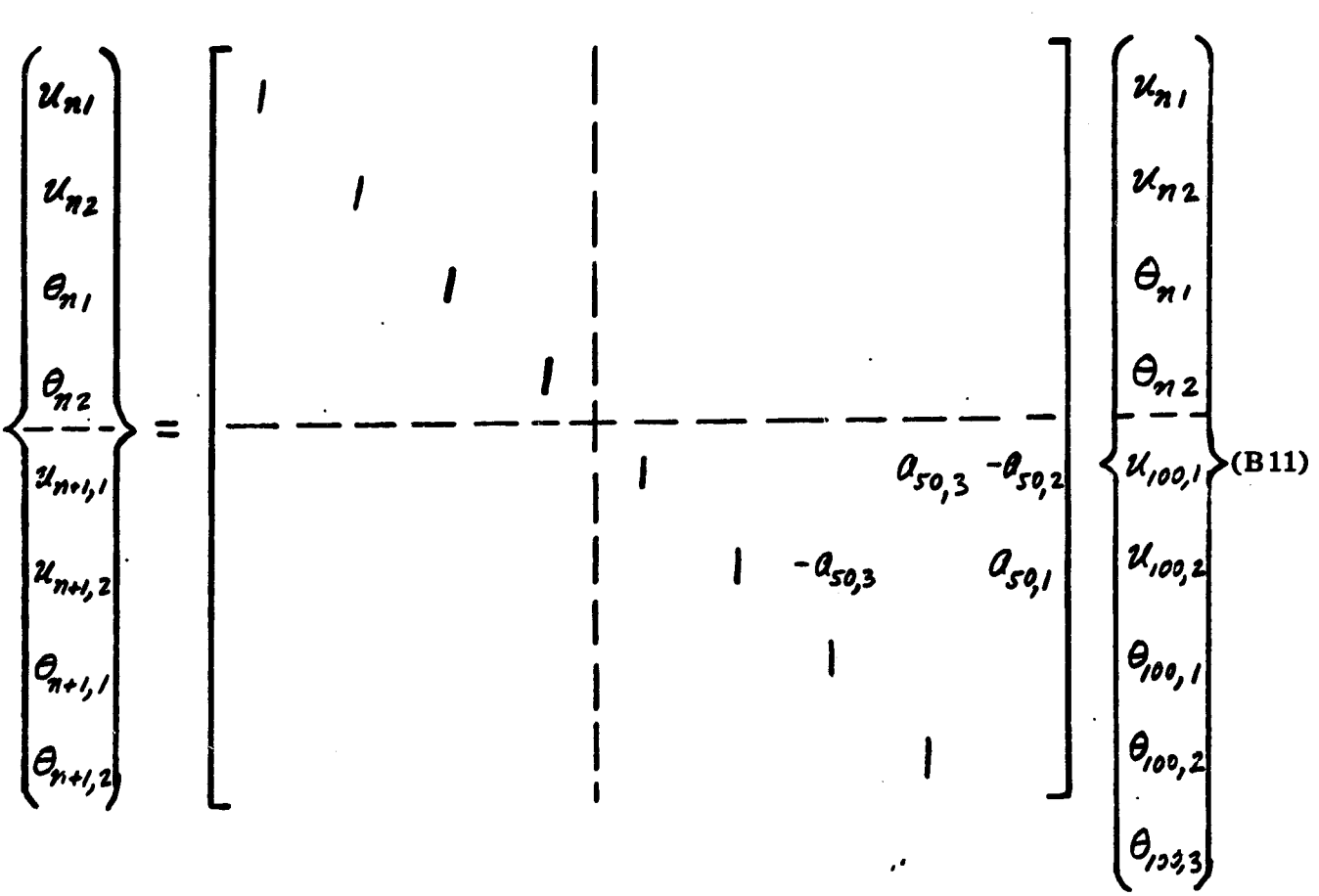

(B11)

where the $a_{50,j}$'s are the coordinates of node 50 relative to node 100. If $[T_n]$ is the coefficient matrix in (B11), as justified in Section B3, the transformation of the element stiffness matrix of member n to the coordinates on the right side of (B11) is

$$[\bar{K}^{(n)}] = [T_n]^T [K^{(n)}][T_n] \qquad \text{(B12)}$$

B3. Transformation of Stiffness Matrices

Assume $\{f_i\}$ and $\{q_i\}$ are the generalized loads and corresponding generalized deflections for a particular structure in coordinate system i; i.e., these quantities correspond to each other in the following sense. Consider alternative deflections that are consistent with the constraints but are so close to the current deflections that their difference is a differential quantity $\{\delta q_i\}$ known as a virtual displacement. Then $\{f_i\}$ and $\{q_i\}$ correspond to each other if the work done in moving $\{f_i\}$ through the displacement $\{\delta q_i\}$ is $\{f_i\}^T\{\delta q_i\}$. This quantity, known as the virtual work, is the same, regardless of the coordinate system so that, if the

C-3

subscript j corresponds to another coordinate system,

$$\{f_i\}^T\{\delta q_i\} = \{f_j\}^T\{\delta q_j\} \tag{B13}$$

The load-deflection relation in each coordinate system is

$$\{f_i\} = [K_i]\{q_i\} \quad \text{and} \quad \{f_j\} = [K_j]\{q_j\} \tag{B14}$$

Substition of (B14) into (B13) yields

$$\{q_i\}^T[K_i]\{\delta q_i\} = \{q_j\}^T[K_j]\{\delta q_j\} \tag{B15}$$

Assume that the matrix [T] relates the two deformation vectors; i.e.

$$\{q_i\} = [T]\{q_j\} \tag{B16}$$

The result of substituting (B16) into (B15) is

$$\{q_j\}^T[T]^T[K_i][T]\{\delta q_j\} = \{q_j\}^T[K_j]\{\delta q_j\} \tag{B17}$$

Thus, the transformation for the stiffness matrix is

$$[K_j] = [T]^T[K_i][T] \tag{B18}$$

which is symmetrical.

The transformation between loads may be obtained by substituting (B16) into (B13), yielding

$$\{f_i\}^T[T]\{\delta q_j\} = \{f_j\}^T\{\delta q_j\} \tag{B19}$$

so that $\{f_i\}^T[T] = \{f_j\}^T$, or

$$\{f_j\} = [T]^T\{f_i\} \tag{B20}$$

If (B16) involves a coordinate reduction (i.e., if there are fewer coordinates in $\{q_j\}$ than in $\{q_i\}$), the solution $\{q_i\}$ will be restricted to linear combinations of [T] and therefore will generally be approximate. Consequently, if (B16) is substituted into the first relation of (B14), forces of constraint are required to

maintain the solution in its approximate form; i.e.,

$$[K_i][T]\{q_i\} = \{f_i\} + \{f_i^{(c)}\} \tag{B21}$$

where $\{f_i^{(c)}\}$ represents the forces of constraint. It will be shown that multiplication of (B21) by $[T]^T$ not only transforms the problem, it also eliminates the forces of constraint. The virtual work done by the forces of constraint is always zero, so that

$$\{f_i^{(c)}\}^T\{\delta q_i\} = 0 \tag{B22}$$

and, from (B16),

$$\{f_i^{(c)}\}^T[T]\{\delta q_j\} = 0 \tag{B23}$$

for arbitrary, but differential $\{\delta q_j\}$'s. Consequently, the coefficient of $\{\delta q_j\}$, and, of course, its transpose in zero; i.e.,

$$[T]^T\{f_i^{(c)}\} = 0 \tag{B24}$$

It is seen from (B24) that if (B21) is pre-multiplied by $[T]^T$, the forces of constraint will not appear in the result.

$$[T]^T[K_i][T]\{q_i\} = [T]^T\{f_i\} \tag{B25}$$

If (B18) and (B20) are substituted into (B25), the result is the force deflection relation in j coordinates

$$[K_j]\{q_j\} = \{f_j\} \tag{B26}$$

which is in agreement with the second of Eqs. (B14).

In summary, the transformations (B18) and (B20):

a) transform the loads to generalized loads that are consistent with the new displacement coordinates

b) maintain the symmetry of the stiffness matrix

c) delete any constraint forces from the formulation

B4. Guyan Reduction of Stiffness Matrix

In the Guyan procedure (Ref. 13), certain coordinates of the structure are selected to be omitted. The procedure begins by rearranging the rows and columns of the stiffness matrix so that the coefficients corresponding to the omitted coordinates appear to the bottom and the right of the matrix. Both the rows and the columns are rearranged in the same way so that the symmetry of the matrix is retained. This step is equivalent to rearranging the force-displacement equations and the order of the coordinates. The force-displacement relation is

$$\begin{bmatrix} K'_{AA} & K_{AO} \\ K_{OA} & K_{OO} \end{bmatrix} \begin{Bmatrix} x_A \\ x_O \end{Bmatrix} = \begin{Bmatrix} F'_A \\ F_O \end{Bmatrix} \tag{B27}$$

where subscript A denotes the retained coordinates and O denotes the coordinates to be deleted. The displacements of the omitted coordinates, the elements of $\{X_O\}$, are assumed to be equal to the values they would have if F_O were zero; thus, from the lower equations embedded in (B27); $[K_{AO}]\{X_A\} + [K_{OO}]\{X_O\} = 0$, or

$$\{x_O\} = [G]\{x_A\} \tag{B28}$$

where

$$[G] = -[K_{OO}]^{-1}[K_{OA}] \tag{B29}$$

Thus

$$\begin{Bmatrix} x_A \\ x_O \end{Bmatrix} = \begin{bmatrix} I \\ G \end{bmatrix} \{x_A\} \tag{B30}$$

The method of Section B3 is used to transform the stiffness matrix and load vector. The resulting stiffness relation is in terms of the retained coordinates as follows:

$$[K_{AA}]\{x_A\} = \{F_A\} \tag{B31}$$

where

$$[K_{AA}] = [K'_{AA}] + [K_{A0}][G] = [K_{AA}'] - [K_{A0}][K_{00}]^{-1}[K_{0A}] \quad \text{(B32)}$$

and

$$\{F_A\} = \{F_A'\} + [G]\{F_0\} \quad \text{(B33)}$$

B5. Deformation of Beam Node that is Near ABB

As discussed in the main text, when the distance ℓ_n between the lowest beam node, Node n, and the ABB is less than a prescribed quantity ℓ_c, Node n does not appear in the stiffness matrix. The displacements of Node n are determined using a geometric relation. If n=1 and $\ell_1 < \ell_c$, the beam is assumed to be undeformed. Then the absolute displacement of Node 1 is

$$\begin{Bmatrix} u_{11} \\ u_{12} \end{Bmatrix} = [G_1] \begin{Bmatrix} u_{100,1} \\ u_{100,2} \\ \theta_{100,1} \\ \theta_{100,2} \\ \theta_{100,3} \end{Bmatrix} \quad \text{(B34)}$$

where u_{ij} is the linear displacement of Node i on the beam in direction j (see Fig. 2.6), θ_{ij} is the angular displacement of Node i about axis j, and

$$[G_1] = \begin{bmatrix} 1 & 0 & 0 & a_{13} & -a_{12} \\ 0 & 1 & -a_{13} & 0 & a_{11} \end{bmatrix} \quad \text{(B35)}$$

where the a_{ij}'s are the undeformed locations of Node i relative to Node 100; i.e.,

$$\{a_i\} = \{Z_i\} - \{Z_{100}\} \quad \text{(B36)}$$

When n is greater thai one, the deformation curve of the beam between Node n-1 and the ABB is assumed to be equal to the static deformation curve which is a cubic. The coefficients of the cubic can be evaluated in terms of the linear and angular deflections at Node 50 (the ABB) and Node n-1. The deflections of Node 50 are in turn related, by rigid-body equations, to the deflections of Node 100. The cubic equation is written separately for motion in the 1,3 plane and the 2,3 plane (Figs. 2.1 and 2.2). Once this is done, the linear deflections of Node n on the beam may be obtained. The result is

$$\begin{Bmatrix} u_{n1} \\ u_{n2} \end{Bmatrix} = \begin{bmatrix} b_3 & & b_1 & & b_5 & -b_6 & & b_4 \\ & b_3 & & b_1 & -b_5 & & b_7 & -b_4 \end{bmatrix} \begin{Bmatrix} u_{n-1,1} \\ u_{n-1,2} \\ u_{100,1} \\ u_{100,2} \\ \theta_{100,1} \\ \theta_{100,2} \\ \theta_{100,3} \\ \theta_{n-1,1} \\ \theta_{n-1,2} \end{Bmatrix} \tag{B37}$$

The b_i 's are defined by the following relations:

$$r = \frac{H_n}{H_{n-1}} \tag{B38}$$

where H_i is the height of Node i above the ABB ($H_n = \ell_n$) as shown in Fig. 2.4. Then

$$\left.\begin{aligned} b_1 &= 1 - 3r^2 + 2r^3 \\ b_2 &= H_{n-1}(r - 2r^2 + r^3) \\ b_3 &= 3r^2 - 2r^3 \\ b_4 &= H_{n-1}(-r^2 + r^3) \end{aligned}\right\} \qquad \text{(B39)}$$

$$\left.\begin{aligned} b_5 &= b_1 a_{50,3} + b_2 \\ b_6 &= b_1 a_{50,2} \\ b_7 &= b_1 a_{50,1} \end{aligned}\right\} \qquad \text{(B40)}$$

The beam rotation angles $\theta_{n-1,1}$ and $\theta_{n-1,2}$ are not coordinates that are among the generalized coordinates, the variables that are available from the numerical integration output, since all beam rotations are removed by the Guyan process. The rotations may be obtained as follows. In performing the Guyan procedure a matrix [G] is developed which relates the omitted to the retained coordinates (see B28). In this case the relation is

$$\begin{Bmatrix} \theta_{1,1} \\ \theta_{1,2} \\ \vdots \\ \theta_{n-1,1} \\ \theta_{n-1,2} \end{Bmatrix} = [G] \begin{Bmatrix} u_{1,1} \\ u_{1,2} \\ \vdots \\ u_{n-1,1} \\ u_{n-1,2} \\ u_{100,1} \\ u_{100,2} \\ \theta_{100,1} \\ \theta_{100,2} \\ \theta_{100,3} \end{Bmatrix} \tag{B41}$$

The last two rows of [G] are called $[G_\theta]$. The matrix $[G_\theta]$ provides expressions for θ_{n-1} and θ_{n-2} in terms of the variables in the vector on the right side of (B41), which are generalized coordinates. These expressions are substituted into (B37) and the result is

$$\{ q_n \} = [G_n] \begin{Bmatrix} q_1 \\ q_2 \\ \vdots \\ q_{n-1} \\ u_{100,1} \\ u_{100,2} \\ \theta_{100} \end{Bmatrix} \tag{B42}$$

where

$$\underset{\sim}{q}_i = \{q_i\} = \begin{Bmatrix} u_{i,1} \\ u_{i,2} \end{Bmatrix} \tag{B43}$$

$$\{\theta_{100}\} = \begin{Bmatrix} \theta_{100,1} \\ \theta_{100,2} \\ \theta_{100,3} \end{Bmatrix} \tag{B44}$$

and

$$[G_n] = \left[\begin{array}{ccc|ccccccc} \overleftarrow{3n-4} & & & & & & & & & \\ 0 & \cdots & 0 & b_3 & 0 & b_1 & 0 & 0 & b_5 & -b_6 \\ 0 & \cdots & 0 & 0 & b_3 & 0 & b_1 & -b_5 & 0 & b_7 \end{array}\right] + \begin{bmatrix} 0 & b_4 \\ -b_4 & 0 \end{bmatrix} \begin{bmatrix} & G_\theta & \end{bmatrix} \tag{B45}$$

Equation (B42) will be used to reduce Node n from the coordinates of the mass matrix as well as to determine the deformation of Node n.

B6. Adjustment of [K] to Eliminate Rigid-Body Drift

Small errors in the system stiffness matrix [K], due to computer round-off, cause the matrix to behave as if very small springs, with positive or negative rates, connect the structure to ground. In long computer runs, the structure therefore tends to slowly drift from the correct location after it experiences a

motion with a rigid-body component. In order to rectify this situation, a small matrix $[\varepsilon]$ is added to the stiffness matrix as follows:

$$[K] = [K_{OLD}] + [\varepsilon] \tag{B46}$$

$[\varepsilon]$ adjusts $[K]$ so that, if $[U_R]$ is the matrix of the six rigid-body modes,

$$[K][U_R] = ([K_{OLD}] + [\varepsilon])[U_R] = 0 \tag{B47}$$

Since $[U_R]$ contains six vectors, it is only necessary to adjust six columns in $[K_{OLD}]$. The six columns of $[K_{OLD}]$ corresponding to the orbiter degrees of freedom are selected for adjustment. To maintain the symmetry of $[K]$, $[\varepsilon]$ is made symmetric; thus the six corresponding rows of $[K_{OLD}]$ are also adjusted. Consequently, $[\varepsilon]$ has the following form:

$$[\varepsilon] = \begin{array}{c} \begin{array}{ccc} \vert\ 2m\ \vert & \vert\ 6\ \vert & \vert\ 12\ \vert \end{array} \\ \left[\begin{array}{ccc} \underset{\sim}{0} & \underset{\sim}{\varepsilon_1} & \underset{\sim}{0} \\ \underset{\sim}{\varepsilon_1}^T & \underset{\sim}{\varepsilon_2} & \underset{\sim}{\varepsilon_3}^T \\ \underset{\sim}{0} & \underset{\sim}{\varepsilon_3} & \underset{\sim}{0} \end{array}\right] \begin{array}{l} 2m \\ 6 \\ 12 \end{array} \end{array} \tag{B48}$$

where the subscript m is equal to the number of beam nodes represented in the stiffness matrix (m = n if $\ell_n \geq \ell_c$ and m = n-1 if $\ell_n < \ell_c$). By geometry, the matrix of rigid-body modes is

$$
[U_R] = \left[\begin{array}{cccccc}
1 & 0 & 0 & 0 & a_{1,3} & -a_{1,2} \\
0 & 1 & 0 & -a_{1,3} & 0 & a_{1,1} \\
\hline
1 & 0 & 0 & 0 & a_{2,3} & -a_{2,2} \\
0 & 1 & 0 & -a_{2,3} & 0 & a_{2,1} \\
\hline
 & & & \vdots & & \\
\hline
1 & 0 & 0 & 0 & a_{m,3} & -a_{m,2} \\
0 & 1 & 0 & -a_{m,3} & 0 & a_{m,1} \\
\hline
1 & 0 & 0 & 0 & 0 & 0 \\
0 & 1 & 0 & 0 & 0 & 0 \\
0 & 0 & 1 & 0 & 0 & 0 \\
0 & 0 & 0 & 1 & 0 & 0 \\
0 & 0 & 0 & 0 & 1 & 0 \\
0 & 0 & 0 & 0 & 0 & 1 \\
\hline
1 & 0 & 0 & 0 & a_{p_1,3} & -a_{p_1,2} \\
0 & 0 & 0 & 0 & 1 & 0 \\
\hline
1 & 0 & 0 & 0 & a_{p_2,3} & -a_{p_2,2} \\
0 & 0 & 0 & 0 & 1 & 0 \\
\hline
 & & & \vdots & & \\
\hline
1 & 0 & 0 & 0 & a_{p_k,3} & a_{p_k,2} \\
0 & 0 & 0 & 0 & 1 & 0
\end{array}\right]
\begin{array}{l}
\left.\vphantom{\begin{array}{c}a\\a\\a\\a\\a\\a\\a\\a\\a\\a\\a\\a\\a\\a\\a\\a\\a\\a\\a\\a\\a\\a\\a\end{array}}\right\} [U_R^{(1)}] \\
\left.\vphantom{\begin{array}{c}a\\a\\a\\a\\a\\a\\a\\a\\a\\a\\a\\a\\a\\a\\a\\a\\a\\a\\a\\a\\a\\a\\a\\a\end{array}}\right\} [I_6] \\
\left.\vphantom{\begin{array}{c}a\\a\\a\\a\\a\\a\\a\\a\\a\\a\\a\\a\\a\\a\\a\\a\\a\\a\\a\\a\\a\\a\\a\\a\end{array}}\right\} [U_R^{(3)}]
\end{array}
\qquad \text{(B49)}
$$

A matrix [S] is defined as follows:

$$\begin{array}{c} \\ \frac{2m}{6} \\ \frac{6}{12} \end{array} \begin{array}{c} \begin{array}{cc} & \begin{array}{|c|} \hline 6 \\ \hline \end{array} \end{array} \\ \begin{bmatrix} S_1 \\ S_2 \\ S_3 \end{bmatrix} \end{array} = -[K_{OLD}][U_R] \tag{B50}$$

Equations (B48) - (B50) are substituted into (B47) and the resulting equations for the matrix partitions are solved for the $[\varepsilon_i]$'s. The results are

$$\left.\begin{aligned} [\varepsilon_1] &= [S_1] \\ [\varepsilon_2] &= [S_2] - [S_1]^T[U_R^{(1)}] - [S_3]^T[U_R^{(3)}] \\ [\varepsilon_3] &= [S_3] \end{aligned}\right\} \tag{B51}$$

These quantities may be used in (B48), and the result is used in (B46) to adjust [K]. Since $[K_{OLD}]$ is, except for computer round-off, a free-free stiffness matrix, the $[S_i]$'s determined by (B50) are very small, and therefore the adjustments to [K] are very small. Nevertheless, this adjustment improved the solutions for the absolute deflections considerably in long computer runs.

B7. Adjustment of [Kp] to Eliminate Rigid-Body Drift

The platform stiffness [Kp] is also adjusted to eliminate rigid-body drift. The derivation of the required equations parallels that of the previous section. The results are

$$[\bar{U}_R] = \begin{bmatrix} I_6 \\ U_R^{(3)} \end{bmatrix} \tag{B52}$$

$$\begin{array}{c|c|} & 6 \\ \hline 6 \\ \hline 12 \end{array} \begin{bmatrix} \bar{S}_2 \\ \bar{S}_3 \end{bmatrix} = -[K_P][\bar{U}_R] \tag{B53}$$

$$[\bar{\varepsilon}] = \begin{array}{|c|c|} \multicolumn{1}{c}{6} & \multicolumn{1}{c}{12} \\ \hline \bar{\underset{\sim}{\varepsilon}}_2 & \bar{\underset{\sim}{\varepsilon}}_3^T \\ \hline \bar{\underset{\sim}{\varepsilon}}_3 & \underset{\sim}{0} \\ \hline \end{array} \begin{array}{c} 6 \\ \hline 12 \end{array} \tag{B54}$$

where

$$[\bar{\varepsilon}_2] = [\bar{S}_2] - [\bar{S}_3]^T [U_R^{(3)}] \tag{B55}$$

and

$$[\bar{\varepsilon}_3] = [\bar{S}_3] \tag{B56}$$

$[K_P]$ is adjusted by replacing it with $[K_P] + [\bar{\varepsilon}]$.

Appendix C

EQUATIONS FOR KINEMATICS OF BEAM EMISSION DURING BEAM FABRICATION

C1. Input Data

Many of the kinematics input-data quantities are indicated in Figs. 2.4 and 2.5. The data are as follows:

- L_1 length beam at reference time t_{11}
- h bay length
- n_p number of pulses; i.e., number of bays emitted during run
- n_b number of bays per node

The following data is only required if $n_p > 0$

- t_{11} time that first pulse starts (t_{11} is set to a negative number to begin the run in the middle of a pulse).
- t_a pulse acceleration time
- t_b pulse cruise time
- t_c pulse deceleration time
- τ pulse period (must be greater than $t_a + t_b + t_c$).

C2. Equations

Equations Used at t=0

The times at which the nature of the motion changes (see Fig. C1) are

$$\left.\begin{aligned} t_{k1} &= t_{11} + (k-1)\tau \\ t_{k2} &= t_{k1} + t_a \\ t_{k3} &= t_{k2} + t_b \\ t_{k4} &= t_{k3} + t_c \end{aligned}\right\} \quad \text{for } k = 1, 2, \ldots, n_p \qquad \text{(C1)}$$

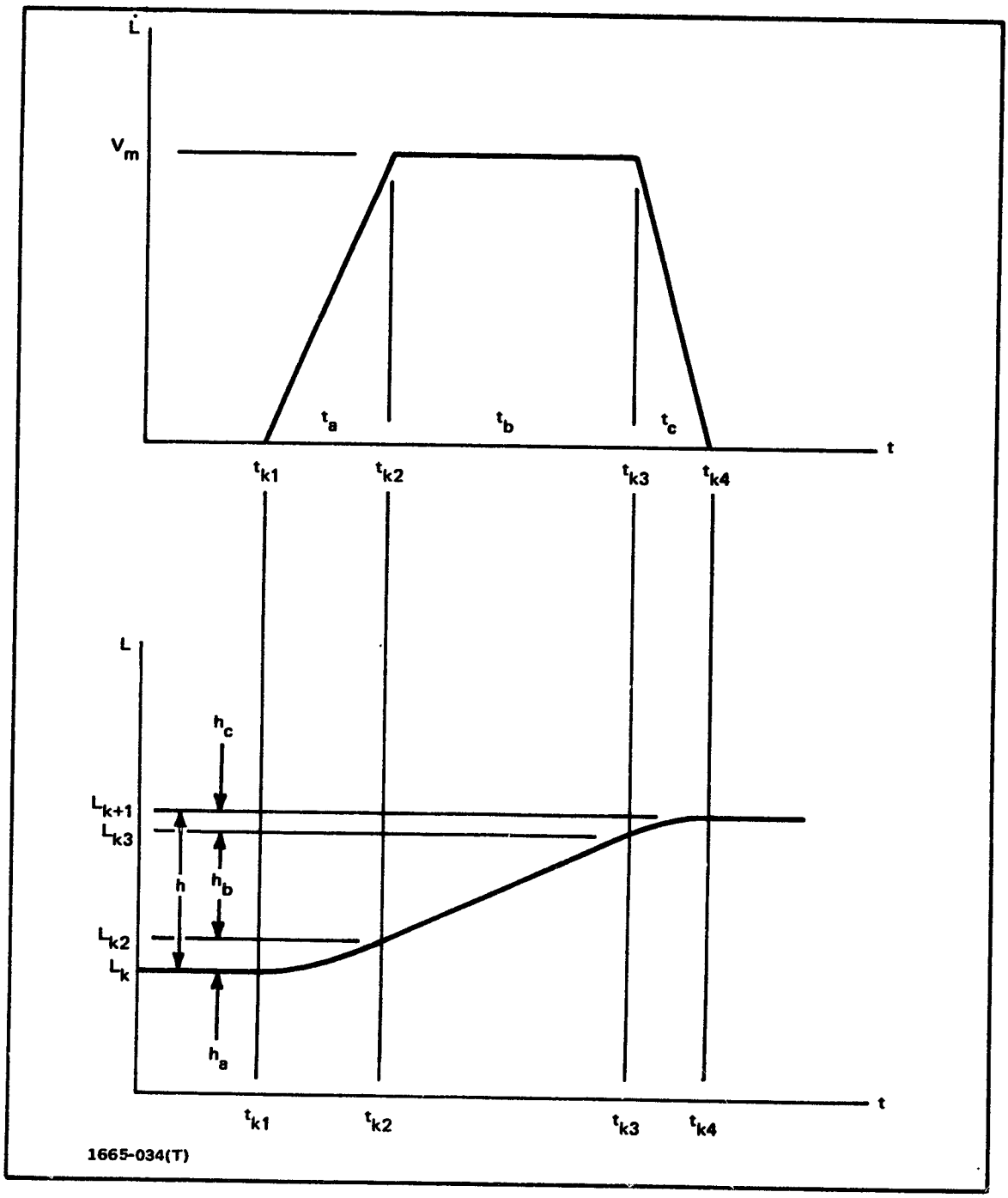

Fig. C1 Motion of L During k th Pulse

If V_m is the maximum velocity reached, the acceleration and deceleration are, respectively

$$a_r = \frac{V_m}{t_a} \tag{C2}$$

$$a_d = -\frac{V_m}{t_c} \tag{C3}$$

The increase in height during each phase of the motion is (refer to Fig C1)

$$\left.\begin{aligned} h_a &= \tfrac{1}{2} a_r t_a^2 \\ h_b &= V_m t_b \\ h_c &= V_m t_c + \tfrac{1}{2} a_d t_c^2 \end{aligned}\right\} \tag{C4}$$

and

$$h = h_a + h_b + h_c \tag{C5}$$

The beam length at the beginning of each phase of the motion is

$$L_k = L_1 + (k-1)h \qquad (k = 1, \ldots, n_p + 1) \tag{C6}$$

$$\left.\begin{aligned} L_{k2} &= L_k + h_a \\ L_{k3} &= L_{k2} + h_b \end{aligned}\right\} \quad (k = 1, \ldots, n_p) \tag{C7}$$

Equations (C2) and (C3) are substituted into (C4), and the result is substituted into (C5), yielding

$$V_m = \frac{h}{\frac{1}{2} t_a + t_b + \frac{1}{2} t_c} \tag{C8}$$

Also, for future use, it is noted that the distance between nodes is

$$\ell = n_b h \tag{C9}$$

The procedure at t=0 is to compute V_m from (C8), then a_r and a_d from (C2) and (C3), and h_a, h_b, and h_c from (C4). Then the times at which the pulse changes in shape are computed from (C1) and the corresponding beam lengths are computed from (C5) and (C6). Also, the distance between nodes is computed from (C9).

Equations Used at Each Time Point

In the intervals where the beam is stationary ($t_{k-1,4} \leq t \leq t_{k1}$ for k=1, 2, ..., n_p where $t_{0,4} \equiv 0$ and when $t > t_{n_p 4}$ for $k=n_p + 1$) the beam length and its derivatives are

$$\left.\begin{aligned} L &= L_k \\ \dot{L} &= 0 \\ \ddot{L} &= 0 \end{aligned}\right\} \tag{C10}$$

When the beam is accelerating ($t_{k1} < t < t_{k2}$ for k=1, 2, ..., n_p),

$$\left.\begin{aligned} L &= L_k + \tfrac{1}{2} a_r (t - t_{k1})^2 \\ \dot{L} &= a_r (t - t_{k1}) \\ \ddot{L} &= a_r \end{aligned}\right\} \tag{C11}$$

During the cruise portion of the cycle ($t_{k2} \leq t \leq t_{k3}$ for k=1, 2, ..., n_p),

$$\left.\begin{aligned} L &= L_{k2} + V_m (t - t_{k2}) \\ \dot{L} &= V_m \\ \ddot{L} &= 0 \end{aligned}\right\} \qquad \text{(C12)}$$

When the beam is decelerating ($t_{k3} < t < t_{k4}$ for k=1, 2, ..., n_p)

$$\left.\begin{aligned} L &= L_{k3} + V_m (t - t_{k3}) + \tfrac{1}{2} a_d (t - t_{k3})^2 \\ \dot{L} &= V_m + a_d (t - t_{k3}) \\ \ddot{L} &= a_d \end{aligned}\right\} \qquad \text{(C13)}$$

Once the beam length is determined, the number of beam nodes can be computed by deleting the digits to the right of the decimal point in the result of the following equation:

$$n = 1. - \varepsilon + L/\ell \qquad \text{(C14)}$$

(truncated to an integer)

where ε is a small number, typically 10^{-6}. Equation (C14) assures that even when a node just emerges from the ABB, it is counted as one of the total number of nodes, n.

Finally, from Fig. 2.4, the height of each beam node is

$$H_k = L - (k-1)\ell \qquad \text{(C15)}$$

$$(k = 1, 2, \ldots, n)$$

Appendix D

THE TREATMENT OF CONSTRAINTS IN THE DYNAMICS PROBLEM

D1. Linear Constraints

Consider a general dynamics formulation of the form

$$[M]\{\ddot{x}\} = \{g\} \tag{D1}$$

where {g} contains the loads and any lower-derivative terms. It is assumed that the equations embodied in (D1) have been arranged so that [M] is symmetric; therefore, these equations have the same form as Lagrange's equations. Assume a linear constraint relation of the form

$$\{x\} = [T]\{y\} + \{c\} \tag{D2}$$

where the number of coordinates in {y} are reduced from those in {x} by the number of constraints. {y} may contain some of the coordinates in {x}. The constraint matrix [T] can be used to describe such constraints as rigidization of a portion of the structure. In the general case [T] and {c} can be time-varying matrices. For example, this occurs when the motion of a joint is a prescribed function of time. Substituting (D2) into (D1) yields

$$[M][T]\{\ddot{y}\} = \{\bar{g}\} + \{F_c\} \tag{D3}$$

where $\{F_c\}$ has been added and represents the additional forces required to satisfy the constraints and

$$\{\bar{g}\} = \{g\} - 2[\dot{T}]\{\dot{y}\} - [\ddot{T}]\{y\}$$

The additional forces of constraint are eliminated by using the following method which is similar to the technique used in the derivation of Lagrange's equations. The procedure also has similarities to the method used in Section B3 to transform the stiffness matrix. Consider an alternate position of the system, consistent with the constraints, at the current time. {δx} represents the difference between that position and the current position; i.e., {δx} is the virtual displacement vector.

As in the derivation of Lagrange's equations, the virtual work of the forces of constraint vanishes; i.e., if (D1) is in the Lagrangian form, with the generalized coordinates corresponding to the generalized loads,

$$\{F_c\}^T\{\delta x\} = 0 \tag{D4}$$

Note that, from (D2)

$$\{\delta x\} = [T]\{\delta y\} \tag{D5}$$

Substituting (D5) into (D4) yields

$$\{F_c\}^T[T]\{\delta y\} = 0$$

Since the elements of $\{\delta y\}$ are independent and arbitrary

$$\{F_c\}^T[T] = 0 \quad \text{or} \quad [T]^T\{F_c\} = 0 \tag{D6}$$

Equation (D6) indicates that the forces of constraint can be eliminated from (D3) by multiplying through by $[T]^T$; i.e.,

$$[T]^T[M][T]\{\ddot{y}\} = [T]^T\{\bar{q}\} \tag{D7}$$

Equation (D7) represents the desired equations of motion in terms of the reduced coordinates with the forces of constraint eliminated.

In summary, to eliminate the constraints from the formulation, substitute the constraint equations (D2) into the formulation and premultiply the equations by the transpose of the constraint matrix.

D2. Nonlinear Constraints

Instead of (D2), if the constraints are nonlinear, they can be expressed in the following form:

$$\{x\} = \{h(\{y\})\} \tag{D8}$$

or

$$x_i = h_i(y_1, y_2, \ldots, y_r; t) \; ; \quad i = 1, 2, \ldots, n \tag{D9}$$

Defining δx_i as a differential virtual displacement,

$$\delta x_i = \sum_{j=1}^{r} \frac{\partial h_i}{\partial y_j}\,\delta y_j \; ; \quad \begin{matrix} i = 1, 2, \ldots, n \\ j = 1, 2, \ldots, r \end{matrix} \tag{D10}$$

or

$$\{\delta x\} = [T]\{\delta y\} \tag{D11}$$

where the elements of [T] are

$$T_{ij} = \frac{\partial h_i}{\partial y_j} \tag{D12}$$

The same derivation can be used as was used for the case of linear constraints. The resulting procedure is to reduce the number of coordinates by substituting (D8) into the equations of motion and to eliminate the forces of constraint by premultiplying the formulation by $[T]^T$, where the elements of [T] are defined by (D12).

Appendix E

REDUCTION OF EQUATIONS OF MOTION FOR BEAM-FABRICATION PROBLEM

E1. Deletion of Coordinates That are Dependent Because of Rigidity

The independent coordinates include u_{i1} and u_{i2}, the deflection components of Node i (i=1,2,...,n) on the beam in the 1 and 2 directions. The deflections are measured from node i on a hypothetical undeformed structure which has the same beam length as the deformed structure at the current time. The other independent coordinates are $\{u_{100}\}$, $\{\theta_{100}\}$, $u_{pj} \equiv u_{pj1}$ and $\theta_{pj} = \theta_{pj2}$ for j=1,2,...,6. All of the remaining coordinates are related to the above beam, orbiter, or solar-panel coordinates.

The acceleration components in (2-5) will be expressed in terms of derivatives of these coordinates. The components of $\{\ddot{r}_i\}$ in the 1 and 2 directions are

$$\left.\begin{aligned} \ddot{r}_{i1} &= \ddot{u}_{i1} \\ \ddot{r}_{i2} &= \ddot{u}_{i2} \end{aligned}\right\} \quad i = 1, 2, \ldots, n \tag{E1}$$

Since the beam is axially inelastic and node 50 is rigidly attached to the orbiter,

$$\ddot{r}_{i3} = \ddot{u}_{100,3} + a_{50,2}\,\ddot{\theta}_{100,1} - a_{50,1}\,\ddot{\theta}_{100,2} + \ddot{L} \tag{E2}$$

where the a_{ij}'s are the components of $\{a_i\}$ which is defined by (B36). The equation for the acceleration of node 50 is

$$\{\ddot{u}_{50}\} = \{\ddot{u}_{100}\} - [\Gamma(a_{50})]\{\ddot{\theta}_{100}\} \tag{E3}$$

where the notation $[\Gamma(\ )]$ is used for the cross-product matrix; i.e. given any vector $\{x\}$ with components x_1, x_2, x_3,

$$[\Gamma(x)] \equiv \begin{bmatrix} 0 & -x_3 & x_2 \\ x_3 & 0 & -x_1 \\ -x_2 & x_1 & 0 \end{bmatrix} \tag{E4}$$

Node 200 is also rigidly connected to the orbiter; therefore

$$\{\ddot{u}_{200}\} = \{\ddot{u}_{100}\} - [\Gamma(a_{200})]\{\ddot{\theta}_{100}\} \tag{E5}$$

and

$$\{\ddot{\theta}_{200}\} = \{\ddot{\theta}_{100}\} \tag{E6}$$

The solar panels are assumed to be rigid axially (in the Z_2 direction) and in the up-and-down (or Z_3) direction. Consequently,

$$\left.\begin{aligned} \ddot{u}_{p_j,2} &= \ddot{u}_{100,2} - a_{p_j,3}\,\ddot{\theta}_{100,1} + a_{p_j,1}\,\ddot{\theta}_{100,3} \\ \ddot{u}_{p_j,3} &= \ddot{u}_{100,3} + a_{p_j,2}\,\ddot{\theta}_{100,1} - a_{p_j,1}\,\ddot{\theta}_{100,2} \end{aligned}\right\} \quad j=1,2,\ldots,6 \tag{E7}$$

In view of (E1), (E2), (E3), (E5), (E6), and (E7), the acceleration vector of (2-5) can be expressed in terms of the independent coordinates as follows:

$$\{\ddot{Z}_G\} = [U]\{\ddot{Z}_F\} + \{v_G\} \tag{E8}$$

where

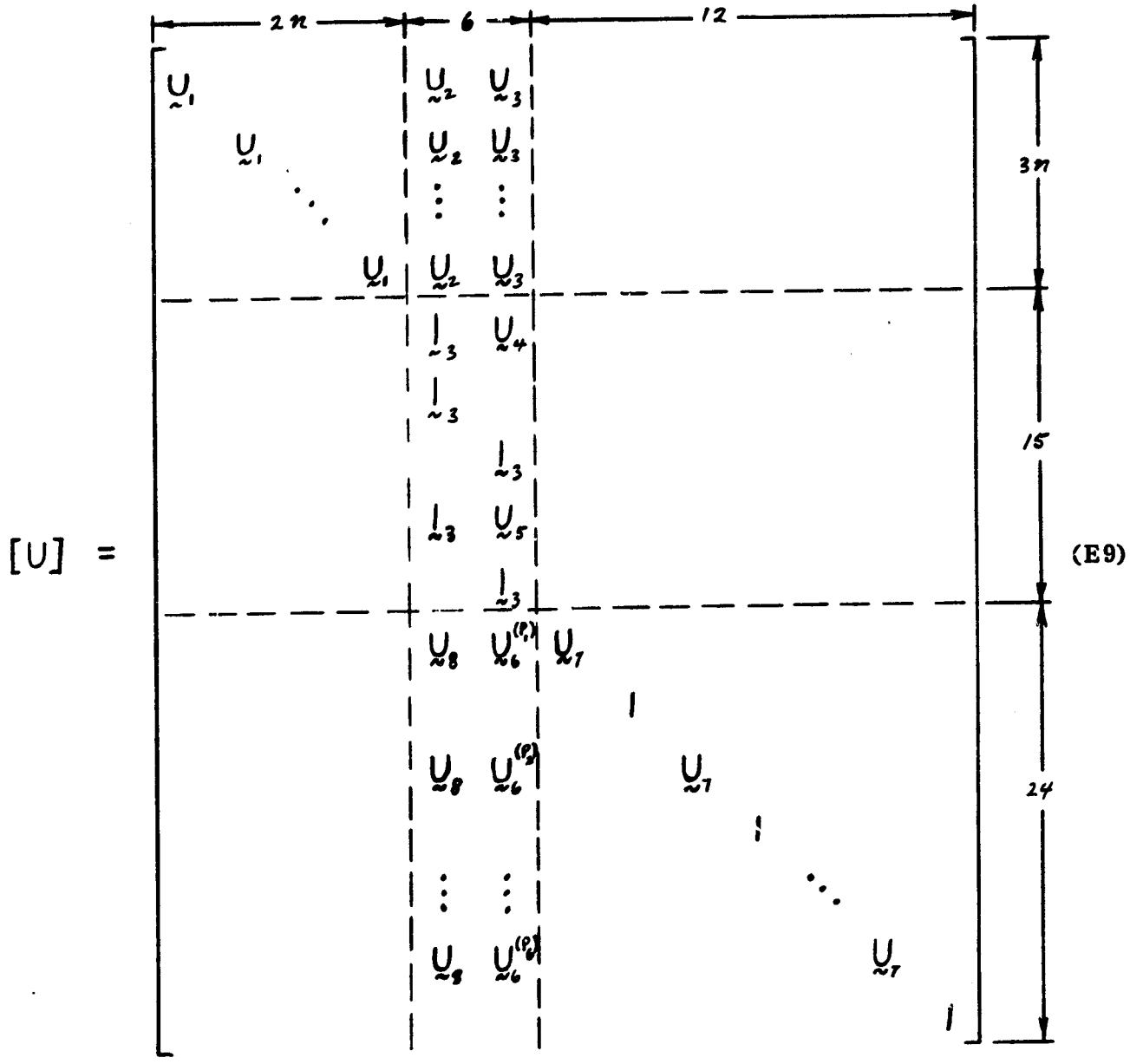

(E9)

and

$$\{Z_F\} = \begin{Bmatrix} \underset{\sim}{q}_1 \\ \underset{\sim}{q}_2 \\ \vdots \\ \underset{\sim}{q}_n \\ \underset{\sim}{u}_{100} \\ \underset{\sim}{\theta}_{100} \\ u_{P_1} \\ \theta_{P_1} \\ u_{P_2} \\ \theta_{P_2} \\ \vdots \\ u_{P_6} \\ \theta_{P_6} \end{Bmatrix}, \qquad \{U_G\} = \ddot{L} \begin{Bmatrix} 0 \\ 0 \\ 1 \\ 0 \\ 0 \\ 1 \\ \vdots \\ 0 \\ 0 \\ 1 \\ \hline 0 \\ 0 \\ \vdots \\ 0 \end{Bmatrix} \quad 3n \tag{E10}$$

where, $u_{p_j} = u_{p_j 1}$, the aft linear displacement of node P_j,

$$\{q_i\} = \begin{Bmatrix} u_{i,1} \\ u_{i,2} \end{Bmatrix} \qquad i = 1, 2, \ldots, n \tag{E11}$$

$$[U_1] = \begin{bmatrix} 1 & 0 \\ 0 & 1 \\ 0 & 0 \end{bmatrix} \tag{E12}$$

$$[U_2] = \begin{bmatrix} 0 & 0 & 0 \\ 0 & 0 & 0 \\ 0 & 0 & 1 \end{bmatrix} \tag{E13}$$

$$[U_3] = \begin{bmatrix} 0 & 0 & 0 \\ 0 & 0 & 0 \\ a_{50,2} & -a_{50,1} & 0 \end{bmatrix} \tag{E14}$$

$$[U_4] = -[\Gamma(a_{50})] \tag{E15}$$

$$[U_5] = -[\Gamma(a_{200})] \tag{E16}$$

$$[U_6^{(P_j)}] = \begin{bmatrix} 0 & 0 & 0 \\ -a_{P_j 3} & 0 & a_{P_j 1} \\ a_{P_j 2} & -a_{P_j 1} & 0 \end{bmatrix} \quad ; \quad j = 1, 2, \ldots, 6 \tag{E17}$$

$$\{U_7\} = \begin{Bmatrix} 1 \\ 0 \\ 0 \end{Bmatrix} \tag{E18}$$

$$[U_8] = \begin{bmatrix} 0 & 0 & 0 \\ 0 & 1 & 0 \\ 0 & 0 & 1 \end{bmatrix} \tag{E19}$$

Equation (E8) is substituted into the equations of motion (2-5), and, in accordance with the procedure of Appendix D, the result is premultiplied by $[U]^T$ yielding

$$[M_{FF}]\{\ddot{Z}_F\} = \{f_F\} - \{g_F\} \tag{E20}$$

where

$$[M_{FF}] = [U]^T [M_{GG}][U] \tag{E21}$$

$$\{f_F\} = [U]^T \{F_G\} \tag{E22}$$

and

$$\{g_F\} = [U]^T [M_{GG}]\{v_G\} \tag{E23}$$

$\{g_F\}$ contains the lower-derivative mass times acceleration terms. Equations (E21) - (E23) must be evaluated every numerical-integration time point. To reduce the computational time required, the matrices were multiplied algebraically by partitions, and the results were programmed. The result, for the reduced mass matrix, is

$$[M_{FF}] = \begin{bmatrix} m_1 I_2 & & & & & & & & & & & \\ & m_2 I_3 & & & & & & & & & & \\ & & \ddots & & & & & & & & & \\ & & & m_n I_2 & & & & & & & & \\ & & & & \underset{\sim}{V}_1 & \underset{\sim}{V}_2 & & & & & & \\ & & & & \underset{\sim}{V}_3 & \underset{\sim}{V}_4 & & & & & & \\ & & & & & & m_{P_1} & & & & & \\ & & & & & & & I_{P_1} & & & & \\ & & & & & & & & m_{P_2} & & & \\ & & & & & & & & & I_{P_2} & & \\ & & & & & & & & & & \ddots & \\ & & & & & & & & & & & m_{P_6} \\ & & & & & & & & & & & & I_{P_6} \end{bmatrix} \tag{E24}$$

where $[I_2]$ is the second-order identity matrix.

To evaluate the matrices $[V_i]$, it is first necessary to compute the following masses. In accordance with Fig. 2.4, the mass assigned to beam node i is

$$\left.\begin{aligned} m_1 &= \tfrac{1}{2}\rho\ell \\ m_2 = m_3 &= \ldots m_n = \rho\ell \end{aligned}\right\} \qquad \text{(E25)}$$

where ρ is an input-data quantity equal to the density of the beam per unit length. The total beam mass is

$$M_B = \sum_{i=1}^{n} m_i \qquad \text{(E26)}$$

If all of the material within the ABB were used to manufacture a beam, its length would be equal to the input-data quantity, L_{max}. Then

$$m_{max} = \rho L_{max} \qquad \text{(E27)}$$

and the variable mass of the ABB is

$$m_{50} = m_{max} - M_B \qquad \text{(E28)}$$

The $[V_i]$'s in (E24) have the following values:

$$[V_1] = \begin{bmatrix} M_R & & \\ & M_p+M_R & \\ & & M \end{bmatrix} \qquad \text{(E29)}$$

where M_R is the mass of the rigid portion of the structure,

$$M_R = m_{50} + m_{100} + m_{200} \qquad \text{(E30)}$$

M_P is the mass of the solar panels

$$M_p = \sum_{i=1}^{6} m_{p_i} \qquad \text{(E31)}$$

and M is the mass of the total structure

$$M = m_{max} + m_{100} + m_{200} + M_p \tag{E32}$$

$$[V_2] = M_B [U_3] + m_{50} [U_4] + [V_2^{(c)}] \tag{E33}$$

where

$$[V_2^{(c)}] = m_{200} [U_5] + \sum_{j=1}^{6} m_{P_j} [U_6^{(P_j)}] \tag{E34}$$

$$[V_3] = [V_2]^T \tag{E35}$$

$$[V_4] = M_B [W_1] + m_{50} [W_2] + [V_4^{(c)}] \tag{E36}$$

where

$$\left.\begin{aligned} [W_1] &= [U_3]^T [U_3] \\ [W_2] &= [U_4]^T [U_4] \end{aligned}\right\} \tag{E37}$$

and

$$[V_4^{(c)}] = m_{200} [U_5]^T [U_5] + \sum_{j=1}^{6} m_{P_j} [U_6^{(P_j)}]^T [U_6^{(P_j)}] + [I_{100}] + [I_{200}] \tag{E38}$$

The $[V_i^{(c)}]$'s are the constant portions of the $[V_i]$'s that are evaluated only once, at t=0.

The reduced load vector, (E22), is

$$\{f_F\} = \begin{Bmatrix} \underset{\sim}{f}_1 \\ \underset{\sim}{f}_2 \\ \vdots \\ \underset{\sim}{f}_n \\ \hline \underset{\sim}{F}_R \\ \underset{\sim}{T}_R \\ \hline f_{P_1} \\ t_{P_1} \\ \hline f_{P_2} \\ t_{P_2} \\ \hline \vdots \\ \hline f_{P_6} \\ t_{P_6} \end{Bmatrix} \tag{E39}$$

where

$$\{f_i\} = \begin{Bmatrix} F_{i1} \\ F_{i2} \end{Bmatrix} \qquad i = 1, 2, \ldots, n \tag{E40}$$

$$\{F_R\} = \sum_{i=1}^{6} \begin{Bmatrix} 0 \\ 0 \\ \\ F_{i3} \end{Bmatrix} + \{F_{50}\} + \{F_{100}\} + \{F_{200}\} + \sum_{j=1}^{\sigma} \begin{Bmatrix} 0 \\ F_{P_j 2} \\ F_{P_j 3} \end{Bmatrix} \quad \text{(E41)}$$

$$\{T_R\} = \left(\sum_{i=1}^{n} F_{i3}\right) \begin{Bmatrix} a_{50,2} \\ -a_{50,1} \\ 0 \end{Bmatrix} + [U_4]^T \{F_{50}\} + [U_5]^T \{F_{200}\}$$

$$+ \sum_{j=1}^{6} [U_6^{(P_j)}]^T \{F_{P_j}\} + \{T_{100}\} + \{T_{200}\} \quad \text{(E42)}$$

Also, $f_{P_j} = F_{P_j 1}$, the fore and aft component of the force on node P_j.

The reduced lower-derivative inertia vector, obtained by carrying out the operations indicated in (E23), is

$$\{g_F\} = M_B \ddot{L} \begin{Bmatrix} 0 \\ 0 \\ \vdots \\ 0 \\ \hline 0 \\ 0 \\ 1 \\ \hline a_{50,2} \\ -a_{50,1} \\ 0 \\ \hline 0 \\ 0 \\ \vdots \\ 0 \end{Bmatrix} \begin{matrix} \\ \\ \\ 2n \\ \\ \\ \\ \\ \\ \\ \\ \\ 12 \\ \\ \end{matrix} \tag{E43}$$

E2. Deletion of Coordinates of Node n

As discussed in Section 2.2 of the main text and Section B5 of Appendix B, when $\ell_n < \ell_c$ the coordinates of node n are eliminated in accordance with (B42). The transformation required for this step is derived from this equation and the result is as follows:

$$\{ Z_F \} = [\bar{G}] \{ \bar{Z}_F \} \tag{E44}$$

where $\{\bar{Z}_F\}$ is identical to $\{Z_F\}$ except that $\{q_n\}$ is omitted; i.e.,

$$\{\bar{Z}_F\} = \begin{Bmatrix} \underset{\sim}{q}_1 \\ \underset{\sim}{q}_2 \\ \vdots \\ \underset{\sim}{q}_{n-1} \\ \underset{\sim}{u}_{100} \\ \underset{\sim}{\theta}_{100} \\ u_{P_1} \\ \theta_{P_1} \\ u_{P_2} \\ \theta_{P_2} \\ \vdots \\ u_{P_6} \\ \theta_{P_6} \end{Bmatrix} \tag{E45}$$

and

$$[\bar{G}] = \begin{array}{c} \overbrace{\qquad 2n-2 \qquad}^{} \overbrace{\quad 6 \quad}^{} \overbrace{\qquad 12 \qquad}^{} \\ \left[\begin{array}{ccccccc} & & & & & & \\ & \underset{\sim}{I}_2 & & & & & \\ & & \underset{\sim}{I}_2 & & & & \\ & & & \ddots & & & \\ & & & & \underset{\sim}{I}_2 & & \\ \underset{\sim}{G}_{n1} & \underset{\sim}{G}_{n2} & \cdots & \underset{\sim}{G}_{n,n-1} & \underset{\sim}{G}_{nu} & \underset{\sim}{G}_{n\theta} & \\ & & & & \underset{\sim}{I}_3 & & \\ & & & & & \underset{\sim}{I}_3 & \\ & & & & & & I \\ & & & & & & \\ & & & & & & \ddots \\ & & & & & & I \end{array}\right] \begin{array}{l} \} 2n-2 \\ \} 2 \\ \} 6 \\ \} 12 \end{array} \end{array} \qquad \text{(E46)}$$

The partitions of $[\bar{G}]$ involving the letter G are obtained by partitioning (B45) (or (B35) when n=1) as follows:

$$[G_n] = [\underset{\sim}{G}_{n1} \quad \underset{\sim}{G}_{n2} \quad \cdots \quad \underset{\sim}{G}_{n,n-1} \quad \underset{\sim}{G}_{nu} \quad \underset{\sim}{G}_{n\theta}] \qquad \text{(E47)}$$

where

$[G_{ni}]$ (i=1, 2, ..., n=1) is a 2 x 2 matrix. These terms are only present when n > 2.

$[G_{nu}]$ is a 2 x 2 matrix

$[G_{n\theta}]$ is a 2 x 3 matrix

and, in (E46),

$$[\bar{G}_{nn}] = [\underset{\sim}{G}_{nn} \quad \underset{\sim}{0}] \tag{E48}$$

where the {0} in (E48) is a 2 x 1 zero vector. When $\ell_n < \ell_c$, (E44) is substituted into (E20) and the result is premultiplied by $[\bar{G}]^T$ in accordance with the procedure of Appendix D. When (E44) is differentiated twice, the derivatives of $[\bar{G}]$ appear. These matrices were found to be small for the ABB problem and are multiplied by small quantities deflections and velocities. Consequently, the effects of the derivatives of $[\bar{G}]$ were neglected.

E3. Equations of Motion

The equations of motion are (E20) when $\ell_n > \ell_c$, or are given by the result of the above procedure when $\ell_n < \ell_c$; i.e., the equations of motion are

$$[M]\{\ddot{z}\} = \{f\} - \{g\} \tag{E49}$$

where

$$[M] = \begin{cases} [M_{FF}] & ; \ \ell_n \geq \ell_c \\ [\bar{G}]^T[M_{FF}][\bar{G}] & ; \ \ell_n < \ell_c \end{cases} \tag{E50}$$

$$\{z\} = \begin{cases} \{z_F\} & ; \ \ell_n \geq \ell_c \\ \{\bar{z}_F\} & ; \ \ell_n < \ell_c \end{cases} \tag{E51}$$

$$\{f\} = \begin{cases} \{f_F\} & ; \ \ell_n \geq \ell_c \\ [\bar{G}]^T\{f_F\} & ; \ \ell_n < \ell_c \end{cases} \tag{E52}$$

and

$$\{g\} = \begin{cases} \{g_F\} & ; \ \ell_n \geq \ell_c \\ [\bar{G}]^T\{g_F\} & ; \ \ell_n < \ell_c \end{cases}$$

In view of (E43) and (E46),

$$\{g\} = \left\{\begin{array}{c} 0 \\ 0 \\ \vdots \\ 0 \\ \hdashline g_{2m+3} \\ g_{2m+4} \\ g_{2m+5} \\ \hdashline 0 \\ 0 \\ \vdots \\ 0 \end{array}\right\} \begin{array}{l} \left.\begin{array}{c} \\ \\ \\ \\ \end{array}\right\updownarrow 2m+2 \\ \\ \\ \\ \left.\begin{array}{c} \\ \\ \\ \\ \end{array}\right\updownarrow 13 \end{array} \qquad m = \begin{cases} n\,; & l_n \geq l_c \\ n-1\,; & l_n \leq l_c \end{cases} \tag{E53}$$

where

$$\left.\begin{aligned} g_{2m+3} &= P_B \\ g_{2m+4} &= P_B\, a_{50,2} \\ g_{2m+5} &= -P_B\, a_{50,1} \end{aligned}\right\} \qquad \text{(E54)}$$

with

$$P_B = M_B \ddot{L} \qquad \text{(E55)}$$

Appendix F

STIFFNESS-PROPORTIONAL DAMPING

To obtain some insight into stiffness-proportional damping, consider the use of this type of damping in a conventional fixed-geometry vibration problem, i.e.,

$$[M]\{\ddot{z}\} + \alpha[K]\{\dot{z}\} + [K]\{z\} = \{f\} \tag{F1}$$

Equation (F1) is reduced to modal coordinates by substituting the following transformation:

$$\{z\} = [\phi]\{\xi\} \tag{F2}$$

The result is premultiplied by $[\phi]^T$, yielding

$$\ddot{\xi}_i + \alpha \omega_i^2 \dot{\xi}_i + \omega_i^2 \xi_i = F_i/\mu_i \tag{F3}$$

where ω_i is the ith undamped natural frequency, μ_i is the ith modal mass, and F_i is the ith modal force. If viscous damping were assumed, then in place of (F3), the equation would be

$$\ddot{\xi}_i + 2\gamma_i \omega_i \dot{\xi}_i + \omega_i^2 \xi_i = F_i/\mu_i \tag{F4}$$

where γ_i is the ratio of the damping coefficient to the critical damping coefficient for the ith mode. By comparing (F3) and (F4),

$$\gamma_i = \frac{1}{2}\omega_i \alpha \tag{F5}$$

It is seen that the damping ratio is proportional to the frequency; consequently higher-frequency contributions to the response are more highly damped than lower-frequency contributions when stiffness-proportional damping is used. In Section 2.7 modal reduction is extended to variable-geometry structures, consequently this conclusion will also be valid for these structures.

Appendix G

MISCELLANEOUS COMPUTATIONS FOR BEAM-FABRICATION PROBLEM

G1. Recovery of Coordinates of Point n When $\ell_n < \ell_c$

Substitution of (E47) into (B42), for the case when $\ell_n < \ell_c$, yields

$$\{q_n\} = \sum_{i=1}^{n-1} [G_{ni}]\{q_i\} + [\bar{G}_{nu}]\{u_{100}\} + [G_{n\theta}]\{\theta_{100}\} \qquad \text{(G1)}$$

Therefore,

$$\{\dot{q}_n\} = \sum_{i=1}^{n-1} [G_{ni}]\{\dot{q}_i\} + [\bar{G}_{nu}]\{\dot{u}_{100}\} + [G_{n\theta}]\{\dot{\theta}_{100}\} \qquad \text{(G2)}$$

$$\{\ddot{q}_n\} = \sum_{i=1}^{n-1} [G_{ni}]\{\ddot{q}_i\} + [\bar{G}_{nu}]\{\ddot{u}_{100}\} + [G_{n\theta}]\{\ddot{\theta}_{100}\} \qquad \text{(G3)}$$

In forming (G2) and (G3), the variation of the partitions of $[G_n]$ with time was neglected. The derivatives of these partitions are multiplied by small displacements; therefore, unless the beam emerges rapidly, the effects of the variation of $[G_n]$ are small. Also, the solution for node n when $\ell_n < \ell_c$ is approximate to begin with; consequently it is felt that the additional effort to compute the derivatives of the partition of $[G_n]$ is unwarranted. Equations (G1) - (G3) are used to compute the motion of node n when $\ell_n < \ell_c$ and $\{q_n\}$ is not an independent variable obtained by the numerical-integration process.

G2. Displacements of Nodes Relative to Coordinates Fixed in the Orbiter

If $\{v$ [illegible] the displacement of node i relative to axes fixed in the orbiter,

$$\{u_i\} = \{v_i\} + \{u_{100}\} + [\Gamma(\theta_{100})]\{a_i\}$$

Since the last product in the above equation represents a cross product

$$[\Gamma(\theta_{100})]\{a_i\} = -[\Gamma(a_i)]\{\theta_{100}\}$$

Therefore,

$$\{v_i\} = \{u_i\} - \{u_{100}\} + [\Gamma(a_i)]\{\theta_{100}\} \qquad \text{(G4)}$$

The pitch deflection angles of the solar-panel nodes relative to the orbiter are

$$\eta_{P_j} = \theta_{P_j} - \theta_{100,2} \; ; \; j = 1, 2, \ldots, 6 \qquad \text{(G5)}$$

G3. Motion of Beam Nodes Before They Emerge From the ABB

In the program output, before the beam node emerges from the ABB, its motion is set equal to the motion of the ABB; i.e.,

$$\{u_{50}\} = \{u_{100}\} - [\Gamma(a_{50})]\{\theta_{100}\} \qquad \text{(G6)}$$

By differentiating (G6),

$$\{\dot{u}_{50}\} = \{\dot{u}_{100}\} - [\Gamma(a_{50})]\{\dot{\theta}_{100}\} \qquad \text{(G7)}$$

Equations (G6), (G7), and (E3) define the motion of any node before it emerges from the ABB.

G4. Internal Torque at Root of Beam on ABB

The torque applied by the beam on the ABB is obtained by summing the torques attributable to the applied and inertia loads on the beam (see Fig. G1). The result is

$$\left.\begin{aligned} \bar{T}_{50,1} &= -\sum_{i=1}^{n} H_i (F_{i2} - m_i \ddot{u}_{i2}) \\ \bar{T}_{50,2} &= \sum_{i=1}^{n} H_i (F_{i1} - m_i \ddot{u}_{i1}) \end{aligned}\right\} \qquad \text{(G8)}$$

G5. Axial Load in Beam

The axial tension load in the beam applied between nodes i and i + 1 is denoted P_i. Its value is obtained by summing the applied and inertia forces on the portion of the beam above and including node i. The result is

$$P_i = \sum_{j=1}^{i} F_{j3} - \left(\sum_{j=1}^{i} m_j\right) \ddot{r}_3 \qquad \text{(G9)}$$

where $\ddot{r}_3$ is the acceleration of the axially rigid beam in the Z_3 direction. Its value is given by (E2) where the subscript i has been dropped since the value is the same for each node.

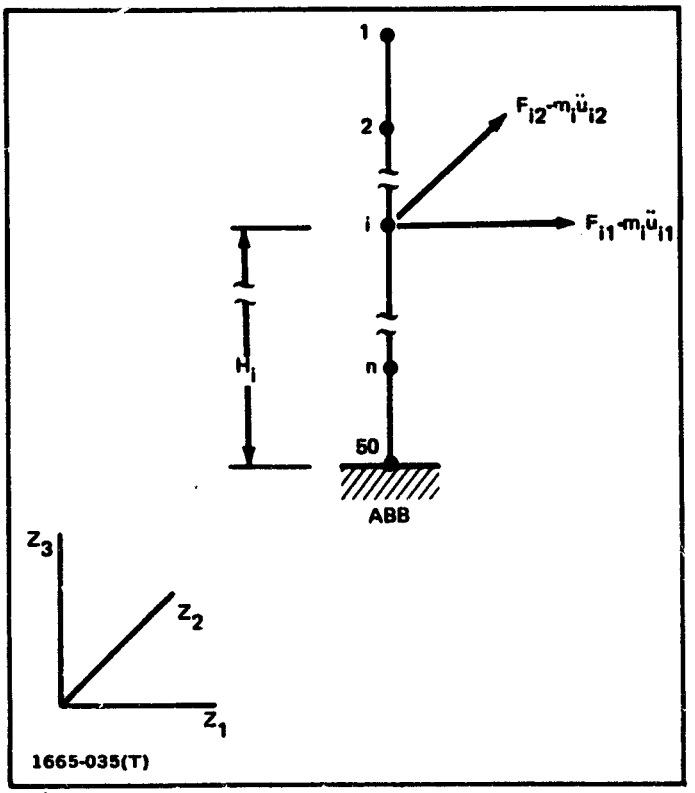

Fig. G1 Diagram Used to Obtain Torque at Root of Beam

Appendix H

APPROXIMATE ORBITER VERNIER CONTROL SYSTEM

H1. Control Law

The basic concepts for the control system are discussed in Section 2.6. Details are presented in this appendix. The switching curves of Fig. 2.7 are based on the angular accelerations induced by the thrusters on a hypothetical rigid structure. For the beam-fabrication problem, this structure consists of the system under consideration prior to beam fabrication. For the beam relocation problem, the hypothetical structure consists of the system under consideration with the beam and RMS (i.e., body B) absent.

The equations for the switching curves are the phase-plane trajectories for constant negative angular acceleration, α_{N_j} for curves A and C and constant positive angular acceleration, α_{P_j}, for curves B and D; thus $\alpha_{N_j} < 0$ and $\alpha_{P_j} > 0$. These curves are used to define the regions in Fig. 2.7. If

$$\left.\begin{array}{lll} \dot{e}_j < 0 & \text{and} & e_j \leq \dfrac{\dot{e}_j^2}{2\alpha_{P_j}} - e_{DB_j} \\ \text{or} & & \\ \dot{e}_j \geq 0 & \text{and} & e_j \leq \dfrac{\dot{e}_j^2}{2\alpha_{N_j}} - e_{DB_j} \end{array}\right\} \quad \text{(H1)}$$

Apply positive torque about axis j

then the angular motion is in Region 1 or 2 and positive torque is applied about axis j. If

$$\left.\begin{aligned} &\dot{e}_j \geq 0 \quad \text{and} \quad e_j \geq \frac{\dot{e}_j^2}{2\alpha_{N_j}} + e_{DB_j} \\ \text{or} \\ &\dot{e}_j < 0 \quad \text{and} \quad e_j \geq \frac{\dot{e}_j^2}{2\alpha_{P_j}} + e_{DB_j} \end{aligned}\right\} \quad \text{(H2)}$$

Apply negative torque about axis j

then the angular motion is in Region 3 or 4 and negative torque is applied about axis j. If neither (H1) nor (H2) is satisfied, then the motion is in the dead band, and no torque is applied about axis j.

In order to determine the value of α_{N_j} and α_{P_j}, the inertial characteristics of the hypothetical structure are first determined. The location of the center of mass of this structure is

$$\{Z_{CM}\} = \frac{1}{M'}\left(m'_{50}\{Z_{50}\} + m_{100}\{Z_{100}\} + m_{200}\{Z_{200}\} + \sum_{j=1}^{6} m_{P_j}\{Z_{P_j}\}\right) \quad \text{(H3)}$$

where the primed symbols have the following meanings:

Symbol	Definition	
	Beam Fabrication	Beam Relocation
M'	M	$\bar{M}$
m'_{50}	m_{max}	m_{50}

The location of each node relative to the center of mass is

$$\{\bar{a}_j\} = \{Z_j\} - \{Z_{CM}\}$$
$$j = 50, 100, 200; P_1, P_2, \ldots, P_6 \quad \text{(H4)}$$

Once the $\{\bar{a}_j\}$'s are computed, the total moment of inertia of the system about the center of mass may be computed by the following equation:

$$[I_T] = [I_{100}] + [I_{200}] - \sum_j m_j [\Gamma(\bar{a}_j)]^2 \qquad \text{(H5)}$$

$$j = 50, 100, 200; P_1, P_2, \ldots, P_6$$

where m_{50} is replaced by m'_{50}

The six thrusters are shown in Fig. H1, and their location and thrust vectors are stated in Table H1. The moment-arm vector from the CM to the i th thruster is

$$\{\bar{a}_{ji}\} = \{Z_{ji}\} - \{Z_{CM}\}; \quad i = 1, 2, \ldots, 6 \qquad \text{(H6)}$$

and the torque that it exerts is

$$\{\bar{T}_{ji}\} = [\Gamma(\bar{a}_{ji})]\{F_{ji}\}; \quad i = 1, 2, \ldots, 6 \qquad \text{(H7)}$$

The contribution of the i th thruster to the angular acceleration of the hypothetical structure is

$$\{\alpha_{Ri}\} = [I_T]^{-1}\{\bar{T}_{ji}\}; \quad i = 1, 2, \ldots, 6 \qquad \text{(H8)}$$

The thruster assignments are shown in Table H2. For example, if e_2 and $\dot{e}_2$ are in Region 1 of Fig. 2.7, a positive torque is required about Axis 2. Then, in accordance with Table H2, Thrusters 1 and 2 have been designated to fire. They cause an angular acceleration of $\alpha_{R1,2} + \alpha_{R2,2}$ of the hypothetical system about Axis 2. Because of cross products of inertia, there will also be some acceleration components about Axes 1 and 3; however, these components will be small. Their effects are left as a disturbance which is automatically

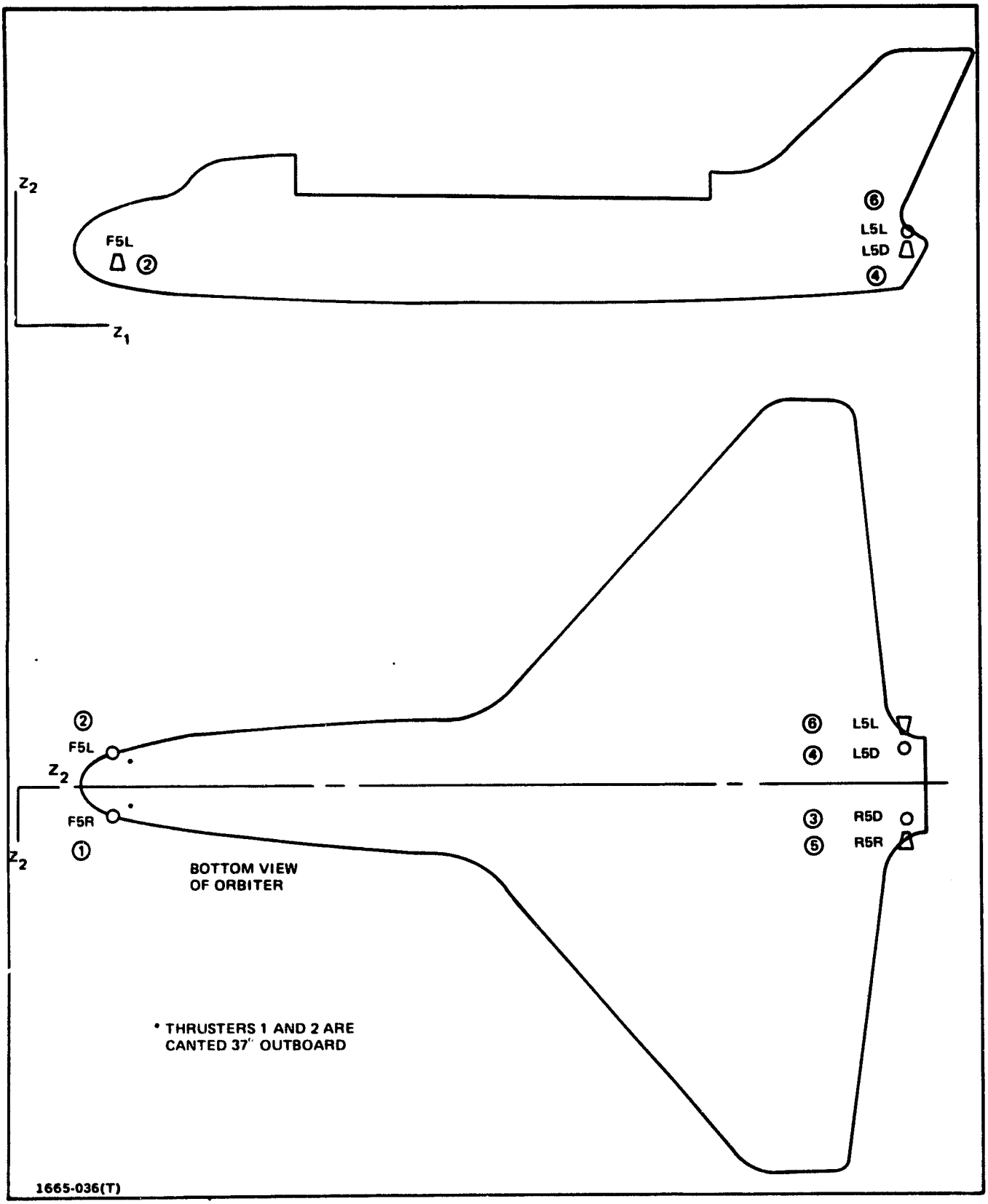

Fig. H1 Vernier RCS Thrusters on Orbiter

TABLE H1 LOCATION OF VERNIER THRUSTERS AND VALUES OF THRUST VECTORS

THRUSTER DESIGNATION		GEOMETRY (in)			THRUST		
THIS STUDY (i)	NASA	Z_{Ji1}	Z_{Ji2}	Z_{Ji3}	F_{Ji1}	F_{Ji2}	F_{Ji3}
1	F5R	324.35	53.33	357.9	0	$-F_J \sin 37°$	$F_j \cos 37°$
2	F5L	324.35	-53.83	357.9	0	$F_j \sin 37°$	$F_J \cos 37°$
3	R5D	1565.0	118.0	455.44	0	0	F_J
4	L5D	1565.0	-118.0	455.44	0	0	F_J
5	R5R	1565.0	143.38	459.0	0	$-F_J$	0
6	L5L	1565.0	-143.38	459.0	0	F_J	0

1665-037(T)

TABLE H2 THRUSTER ASSIGNMENTS AND ANGULAR ACCELERATIONS THAT THEY INDUCE ON HYPOTHETICAL STRUCTURE

TORQUE DIRECTION		THRUSTERS	FRACTION OF TIME PULSED	ANGULAR ACCELERATION WITH BEAM RETRACTED		
AXIS (i)	DESCRIPTION			ROLL	PITCH	YAW
$+Z_1$	COUNTER CLOCKWISE ROLL	3	1.0	$\alpha_{R3,1}$	$\alpha_{R3,2}$	$\alpha_{R3,3}$
		1,2	μ_R	$\mu_R(\alpha_{R1,1}+\alpha_{R2,1})$	$\mu_R(\alpha_{R1,2}+\alpha_{R2,2})$	$\mu_R(\alpha_{R1,3}+\alpha_{R2,3})$
		TOTAL		$\boxed{\approx\alpha_{R3,1}}$	0	$\approx\alpha_{R3,3}$
$-Z_1$	CLOCKWISE ROLL	4	1.0	$\alpha_{R4,1}$	$\alpha_{R4,2}$	$\alpha_{R4,3}$
		1,2	μ_R	$\mu_R(\alpha_{R1,1}+\alpha_{R2,1})$	$\mu_R(\alpha_{R1,2}+\alpha_{R2,2})$	$\mu_R(\alpha_{R1,3}+\alpha_{R2,3})$
		TOTAL		$\boxed{\approx\alpha_{R4,1}}$	0	$\approx\alpha_{R4,3}$
$+Z_2$	PITCH UP	1,2	1.0	$\alpha_{R1,1}+\alpha_{R2,1}$	$\boxed{\alpha_{R1,2}+\alpha_{R2,2}}$	$\alpha_{R1,3}+\alpha_{R2,3}$
$-Z_2$	PITCH DOWN	3,4	1.0	$\alpha_{R3,1}+\alpha_{R4,1}$	$\boxed{\alpha_{R3,2}+\alpha_{R4,2}}$	$\alpha_{R3,3}+\alpha_{R4,3}$
$+Z_3$	YAW LEFT	6	1.0	$\alpha_{R6,1}$	$\alpha_{R6,2}$	$\boxed{\alpha_{R6,3}}$
$-Z_3$	YAW RIGHT	5	1.0	$\alpha_{R5,1}$	$\alpha_{R5,2}$	$\boxed{\alpha_{R5,3}}$

1665-040(T)

corrected by the control system if it becomes sufficiently large. Thus $\alpha_{R1,2} + \alpha_{R2,2}$ is the main angular-acceleration component induced during a pitch-up maneuver while the roll and yaw accelerations are disturbances. The main angular acceleration components are enclosed in a box in the table.

For the case of roll, the induced pitch error would be large; therefore it is assumed that thrusters fire immediately to correct the pitch error. For example, for a positive roll torque, Thruster 3 is fired, and Thrusters 1 and 2 also immediately fire to counteract the induced pitch disturbance. It is assumed that they fire only μ_R times as long as Thruster 3 where μ_R is selected so that there would be no pitch disturbance; i.e.,

$$\mu_R = \frac{-\alpha_{R3,2}}{\alpha_{R1,2} + \alpha_{R2,2}} \tag{H9}$$

The accelerations used to set up the switching curves of Fig. 2.7 are the main accelerations of Table H2. i.e., for Axis 1,

$$\left.\begin{aligned} \alpha_{P_1} &= \alpha_{R3,1} \\ \alpha_{N_1} &= \alpha_{R4,1} \end{aligned}\right\} \tag{H10}$$

For Axis 2,

$$\left.\begin{aligned} \alpha_{P_2} &= \alpha_{R1,2} + \alpha_{R2,2} \\ \alpha_{N_2} &= \alpha_{R3,2} + \alpha_{R4,2} \end{aligned}\right\} \tag{H11}$$

For Axis 3,

$$\left.\begin{aligned} \alpha_{P_3} &= \alpha_{R6,3} \\ \alpha_{N_3} &= \alpha_{R5,3} \end{aligned}\right\} \tag{H12}$$

H2. Control Loads on Orbiter

The moment arm and torque exerted by each of the six thrusters on the orbiter about its center of mass are, respectively,

$$\{a_{Ji}\} = \{z_{Ji}\} - \{z_{100}\} \; ; \quad i = 1, 2, \ldots, 6 \tag{H13}$$

$$\{T_{Ji}\} = [r(a_{Ji})]\{F_{Ji}\} \; ; \quad i = 1, 2, \ldots, 6 \tag{H14}$$

The total control force and torque on the orbiter, about its center of mass, due to a positive torque command about axis i is called $\{F_{Pi}\}$ and $\{T_{Pi}\}$, respectively. For a negative torque axis i, the values are called $\{F_{Ni}\}$ and $\{T_{Ni}\}$. The equations for these quantities are

$$\{F_{P1}\} = \{F_{J3}\} + \mu_R \{F_{P2}\} \tag{H15}$$

$$\{F_{N1}\} = \{F_{J4}\} + \mu_R \{F_{P2}\} \tag{H16}$$

where

$$\{F_{P2}\} = \{F_{J1}\} + \{F_{J2}\} \tag{H17}$$

$$\{F_{N2}\} = \{F_{J3}\} + \{F_{J4}\} \tag{H18}$$

and

$$\{F_{P3}\} = \{F_{J6}\} \tag{H19}$$

$$\{F_{N3}\} = \{F_{J5}\} \tag{H20}$$

$$\{T_{P1}\} = \{T_{J3}\} + \mu_R \{T_{P2}\} \tag{H21}$$

$$\{T_{N1}\} = \{T_{J4}\} + \mu_R \{T_{P2}\} \tag{H22}$$

where

$$\{T_{P2}\} = \{T_{J1}\} + \{T_{J2}\} \tag{H23}$$

$$\{T_{N2}\} = \{T_{J3}\} + \{T_{J4}\} \tag{H24}$$

and

$$\{T_{P3}\} = \{T_{J6}\} \tag{H25}$$

$$\{T_{N3}\} = \{T_{J5}\} \tag{H26}$$

Appendix I

NUMERICAL DATA

The initial structural data was obtained from NASTRAN models that were generated from previous investigations. Models were available for the RMS and the 25 KW power supply. The data for these models was used in the generation of the input data for the NASTRAN and FORTRAN programs of the present study.

I1. Platform Geometry

The platform is composed of the orbiter and the power supply with its solar panels. The node numbering scheme is shown in Figs. 2.1, 2.2, and I1, and the geometry is given in Table I1. Nodes 201, 202, and 206 are used to define the stiffness of the rotational solar-panel drive in the previous NASTRAN model. They were not included in the variable-geometry FORTRAN program. This region is very stiff compared with the solar panels, and it assumed to be rigid. All of the mass in this region was lumped into the rigid portion of the power supply. If mass were assigned to Nodes 202 and 206, low-amplitude high-frequency effects would have to be dealt with in the direct numerical integration.

I2. Beam Fabricated by ABB

The beam fabricated by the ABB is a 1-m deep triangular truss (see Fig. I2). The truss members are .015 in 2024-T3 aluminum. Beams of various lengths have been fabricated with the Grumman ABB ground demonstrator and tested. The overall beam properties are as follows:

density per unit length, ρ	$= 1.843 \times 10^{-4}$ lb-sec^2/in^2
modulus of elasticity, E	$= 10.5 \times 10^6$ lbs/in^2
area moment of inertia, I	$= 95.0$ in^4
bay length	= 59.0551 in (1.5 m)
number of bays between nodes	= 14

The beam is assumed to be axially inextensible. Its allowable bending moment is 13,600 in-lbs which includes a factor of safety of 1.4 (see Ref. I1). This moment was derived from test results.

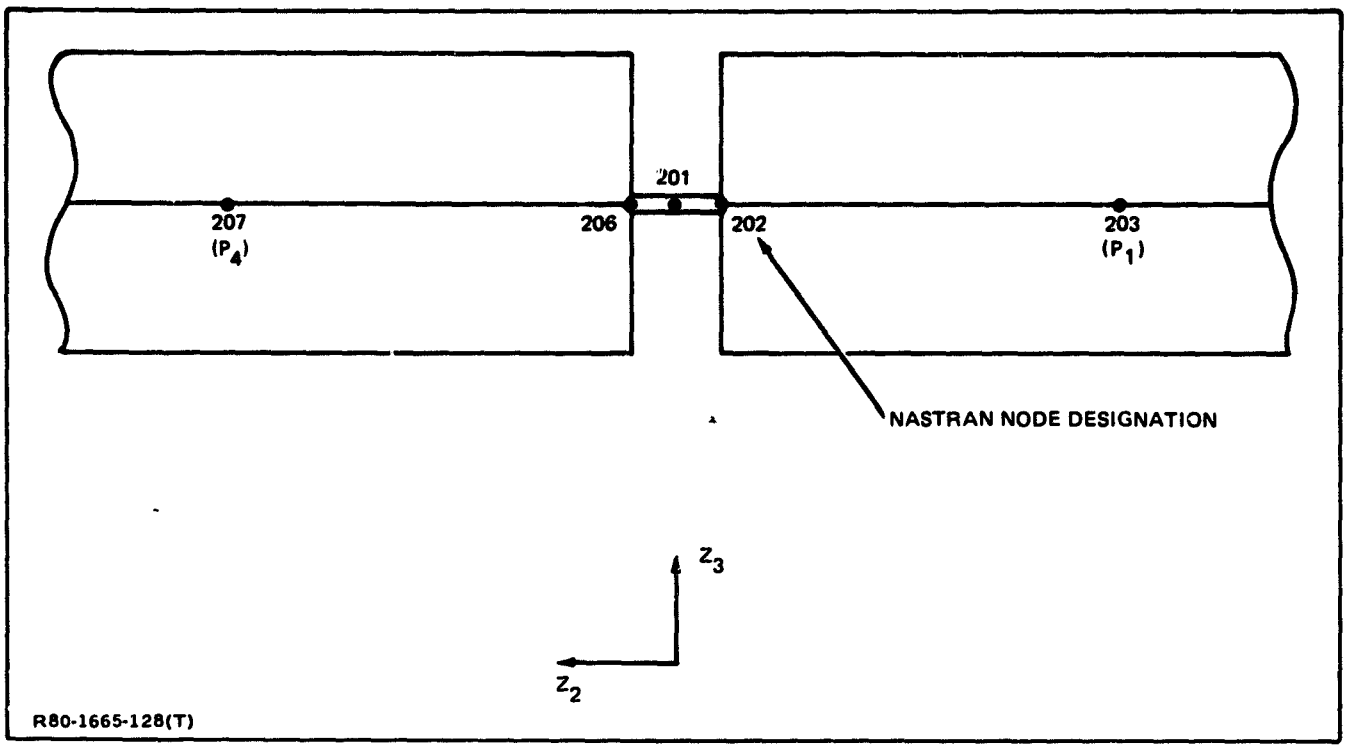

Fig. I1 Front View of Solar Panels

TABLE I1 PLATFORM GEOMETRY

NODE NO.		GEOMETRY		
FORTRAN	NASTRAN	Z_1	Z_2	Z_3
50	50	1053.27	0.0	488.0
100	100	1260.29	0.0	385.1
200	200	430.61	0.0	616.36
*	201	210.0	0.0	599.0
*	202	210.0	-59.04	599.0
P_1	203	210.0	-584.36	599.0
P_2	204	210.0	-1109.7	599.0
P_3	205	210.0	-1635.0	599.0
*	206	210.0	59.04	599.0
P_4	207	210.0	584.36	599.0
P_5	208	210.0	1109.7	599.0
P_6	209	210.0	1635.0	599.0

*POINT IS RIGIDLY CONNECTED TO CENTRAL MASS OF POWER SUPPLY AND IS NOT A NODE IN THE FORTRAN PROGRAM .

R80-1665-143(T)

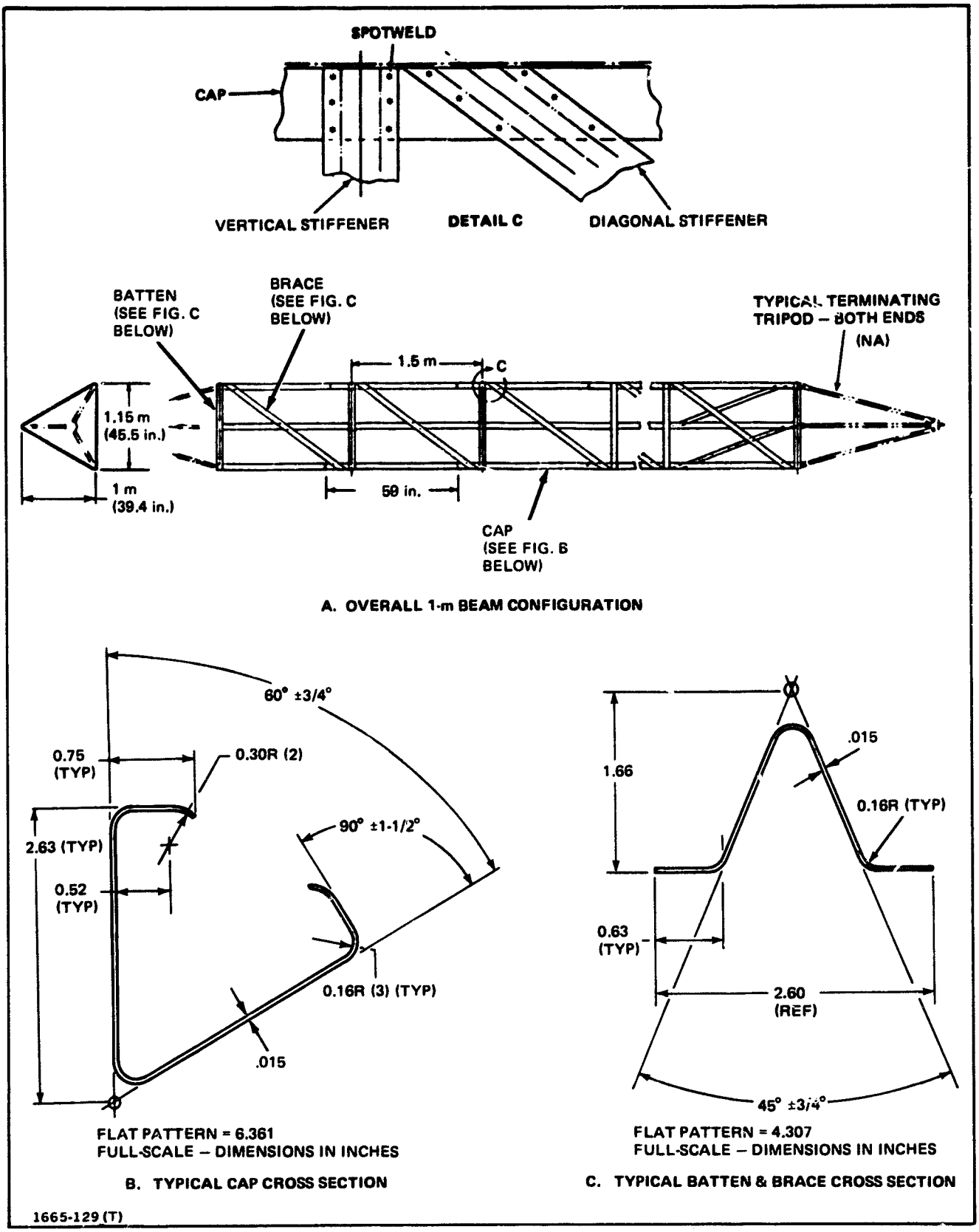

Fig. I2 Beam Fabricated by ABB

I3. Orbiter

The orbiter was idealized as a rigid body. Its mass properties are as follows*:

$$\text{mass} = 530.36 \text{ lb-sec}^2/\text{in}$$

$$I_{11} = 1.097\text{x}10^7 \text{ lb-in-sec}^2$$

$$I_{22} = 7.664\text{x}10^7 \text{ lb-in-sec}^2$$

$$I_{33} = 7.988\text{x}10^7 \text{ lb-in-sec}^2$$

$$I_{12} = 3.6\text{x}10^4 \text{ lb-in-sec}^2$$

$$I_{13} = -3.192\text{x}10^6 \text{ lb-in-sec}^2$$

$$I_{23} = -2.4\text{x}10^4 \text{ lb-in-sec}^2$$

The above values include the fixed-mass portion of the ABB. The variable mass portion initially contains sufficient mass to construct a beam of 199.5 m; i.e., $\ell_{max} = 7854.33$ in (199.5 m).

I4. Power Module

The power module is shown in Fig. I3. The rigid portion has the following mass properties:

$$\text{mass} = 79.5829 \text{ lb-sec}^2/\text{in}$$

$$I_{11} = 21.0\text{x}10^6 \text{ lb-in-sec}^2$$

$$I_{22} = 1.21\text{x}10^6 \text{ lb-in-sec}^2$$

$$I_{33} = 2.63\text{x}10^6 \text{ lb-in-sec}^2$$

The cross products of inertia are zero.

To simplify the model it is assumed that the solar arrays act as beams even though the higher-frequency modes would involve membrane motion. The fundamental mode, solar array bending at .04 Hz, agrees with the mode calculated using a more detailed model. The solar-array beam-model density per unit length is $1.97\text{x}10^3$ lb-sec^2/in^2, and, accordingly, the mass assigned to each interior solar panel node, P_1, P_2, P_4, and P_5 (Fig. 2.1) is 1.03490 lb-sec^2/in. The pitch moment of inertia of each of these nodes is 13040. lb-sec^2-in. The mass of each

---

*The convention for the cross products of inertia is $I_{ij} = \int x_i x_j \, dm$.

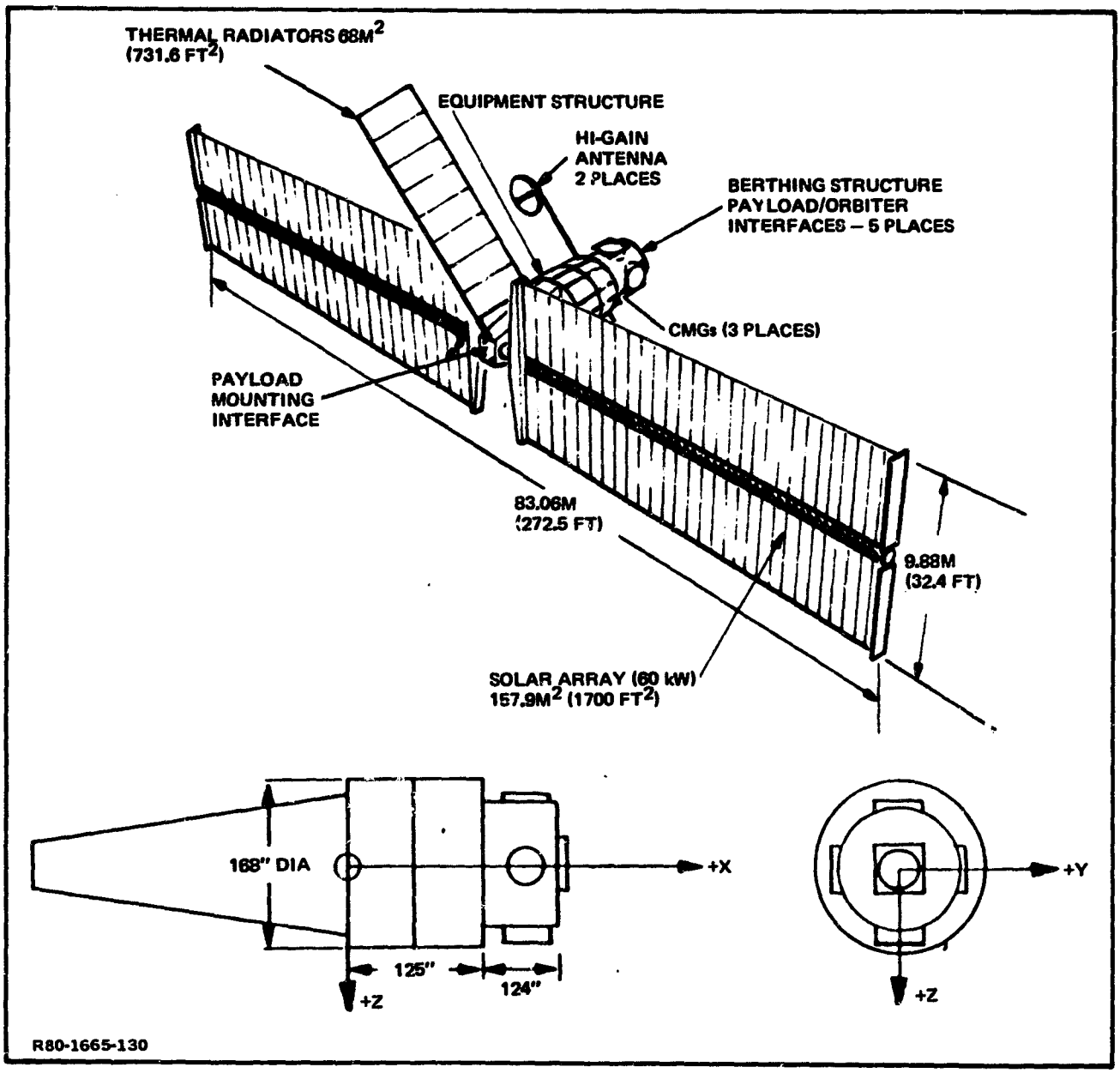

Fig. I3 Power Module Configuration

tip node, P_3 and P_6, is .517450 lb-sec^2/in, and the pitch moment of inertia of each of these nodes is 6520. lb-sec^2-in. The moduli of elasticity in bending and shear are 10.0×10^6 and 4.0×10^6, respectively. The moment of inertia for fore and aft bending is 6.023 in^4 and the torsional moment of inertia is .7455 in^4. The panels are assumed to be rigid for in-plane bending and are assumed to be axially inextensible.

I5. Kinematics of Beam Fabrication

The kinematics data (Fig. 2.5) characteristic of beam fabrication by the Grumman ground-demonstration ABB are as follows:

t_a = 3.5 sec

t_b = 53.0 sec

t_c = 3.5 sec

τ = 187.5 sec

The 59.0051 in (1.5 m) bays are fabricated at rates determined by the above times.

I6. Remote Manipulator System

The RMS with its degrees of freedom is shown in Fig. I4. As indicated in Fig. 2, of the Summary and Introduction, the elbow is straight in this run. The model has been simplified in that the pitch and yaw rotations in the wrist both take place about the same point, the pitch rotation joint in the wrist (see Fig. 3.2). The location of the shoulder joint, Node h, is

Z_1 = 697.5

Z_2 = -108.0

Z_3 = 444.8

Figure I5 shows a schematic representation of the RMS. The properties of each component are listed in Table I2. The 52.6 deg elevation angle and the 19.6 deg offset angle shown in Fig. 2 are not fundamental data; these values can be calculated from the manipulator link lengths in Table I2 and the location of the shoulder joint and the fabricated beam. The values of these angles used in the NASTRAN input data are:

offset angle, α = 19.629°

elevation angle, β = 52.579°

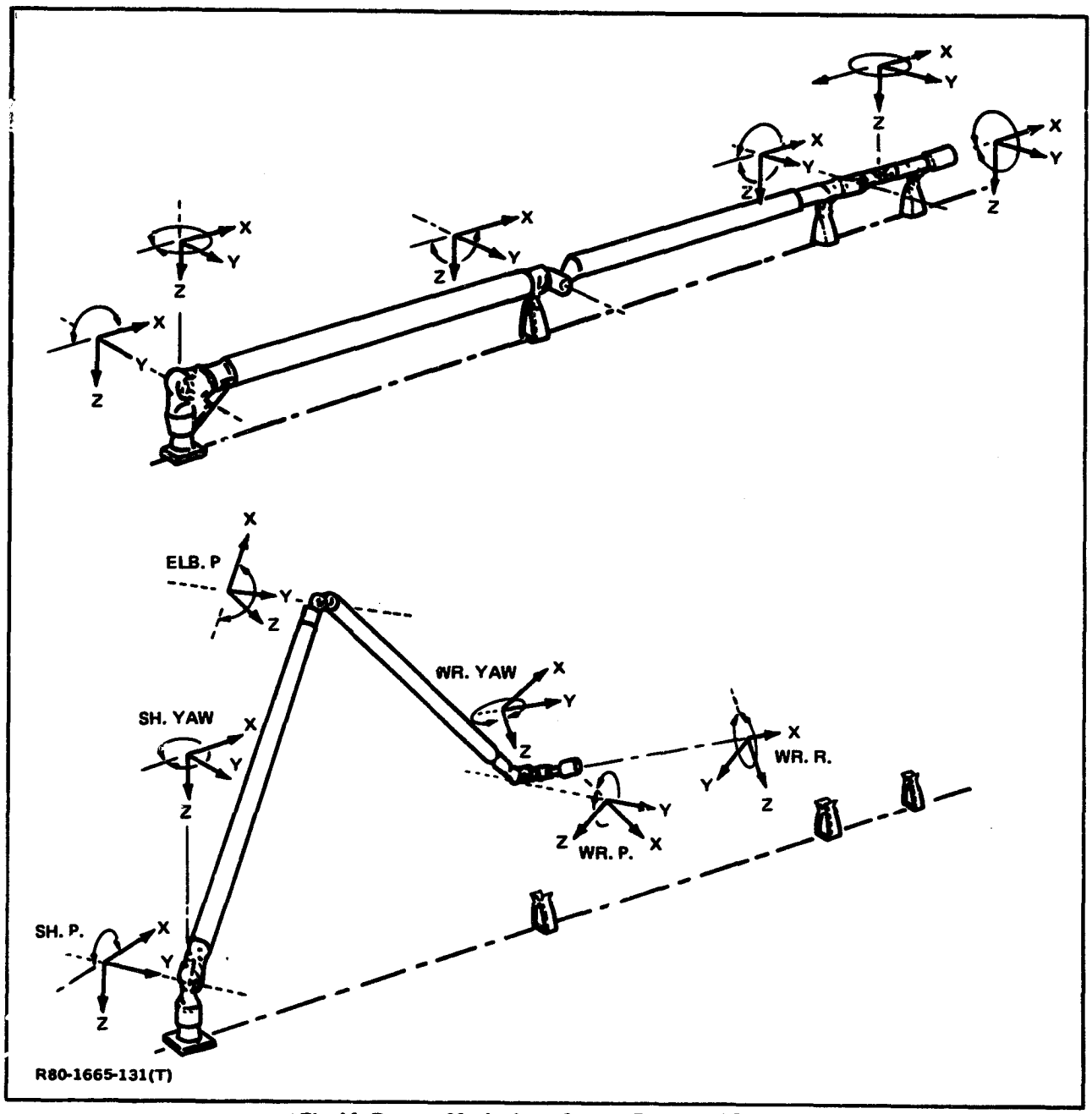

Fig. I4 Remote Manipulator System Degrees of Freedom

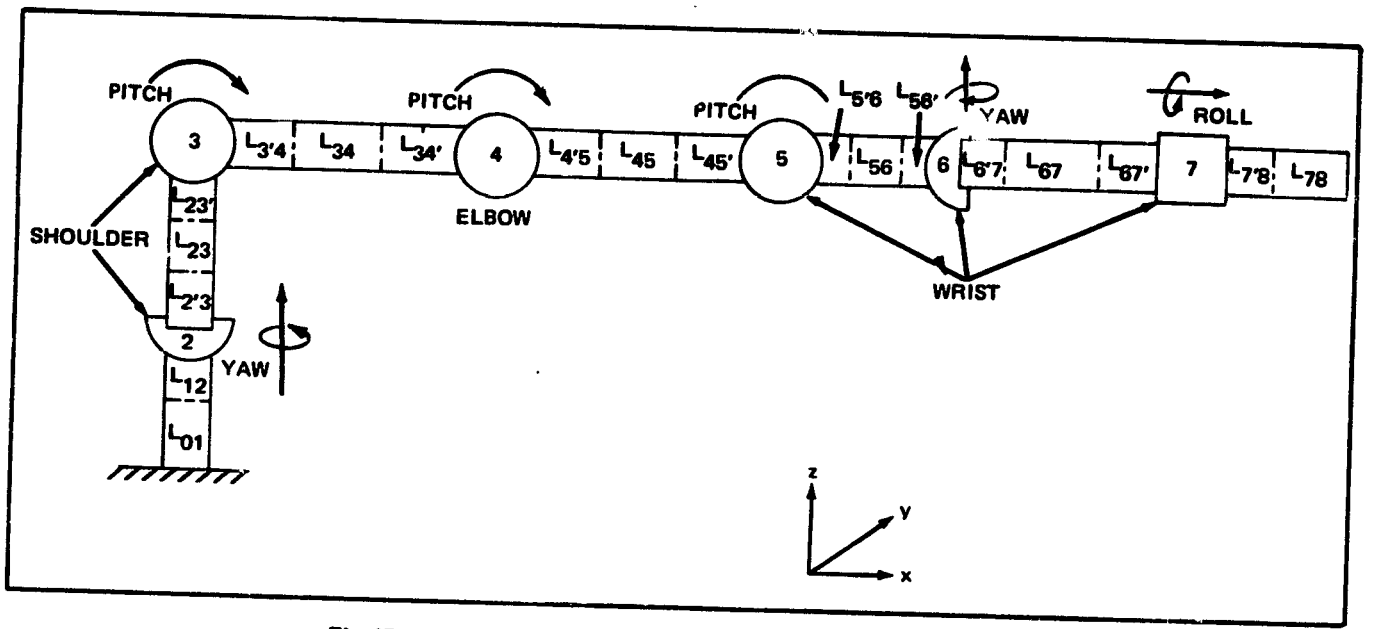

Fig. 15 Schematic Representation of Remote Manipulator System

TABLE 12 REMOTE MANIPULATOR - SYSTEM PROPERTIES

LINK	DESCRIPTION	LENGTH (IN)	WGT (LB)	BENDING STIFF. EI_{XX} or EI_{ZZ} (LB-IN^2)	BENDING STIFF. EI_{YY} (LB-IN^2)	TORS. GJ (LB-IN^2)	AXIAL AE (LB)
L01	MANIP. POSIT. MECH.	13.79	139.14	3.72 + 7*	5.94 + 7	3.63 + 7	2.76 + 7
L12	PED. INTERFACE TRANS.	11.00		3.57 + 8	3.57 + 8	8.80 + 8	1.37 + 8
L2'3	OUTER YAW SLEEVE	1.85	70.19	9.94 + 7	9.94 + 7	1.47 + 9	1.73 + 8
L23	SHOULDER YAW TRANS.	3.5		4.67 + 8	9.47 + 8	6.09 + 8	7.60 + 7
L23'	SHOULDER PITCH CENT. TOROID	6.65		3.42 + 8	5.99 + 9	3.87 + 8	3.25 + 7
L3'4	SHOULDER PITCH TRANS.	28.5	305.13	7.46 + 8	7.76 + 8	5.72 + 8	3.65 + 7
L34	UPPER ARM BOOM	197.084		1.41 + 9	1.41 + 9	7.11 + 8	6.73 + 7
L34'	ELBOW TRANS. SECT	25.5		4.09 + 8	1.01 + 9	5.34 + 8	3.98 + 7
L4'5	INNER TOROID TRAN. SECT	12.5	187.56	2.77 + 8	4.69 + 8	2.77 + 8	3.34 + 7
L45	LOWER ARM BOOM	225.984		9.80 + 8	9.80 + 8	4.94 + 8	4.48 + 7
L45'	WRIST PITCH TRANS	39.5		3.84 + 8	4.78 + 8	3.24 + 8	1.45 + 7
L5'6	WRIST PITCH INNER TOROID	6.0	18.95	5.13 + 7	6.16 + 7	4.24 + 7	3.06 + 7
L56	PITCH TO YAW TRANS	6.0		8.36 + 7	8.36 + 7	6.29 + 7	1.80 + 7
L56'	WRIST YAW INNER TOROID	6.0		8.56 + 7	7.23 + 7	5.94 + 7	3.06 + 7
L6'7	YAW OUTER TOROID	9.966	96.40	2.10 + 8	1.05 + 8	1.18 + 8	7.54 + 6
L67	AFT WRIST ELEC. COMP.	10.14		1.63 + 8	1.63 + 8	1.22 + 8	1.79 + 7
L67'	WRIST ROLL INNER SLEEVE	9.849		1.10 + 8	1.10 + 8	8.27 + 7	4.33 + 7
L7'8	WRIST ROLL OUTER SLEEVE	5.0	90.34	1.32 + 8	1.32 + 8	1.00 + 8	5.10 + 6
L78	END EFFECTOR	18.0		7.21 + 7	7.21 + 7	2.98 + 8	2.55 + 7

JOINT	FUNCTION	$K_{\theta XX}$ (IN-LB/RAD)	$K_{\theta YY}$ (IN-LB/RAD)	$K_{\theta ZZ}$ (IN-LB/RAD)	SLIP TORQUE (MIN) (IN-LB)
2	SHOULDER YAW			1.61 + 7	9260
3	SHOULDER PITCH		2.79 + 7		9260
4	ELBOW PITCH		2.65 + 7		6340
5	WRIST PITCH		1.57 + 7		2770
6	WRIST YAW			1.06 + 7	2770
7	WRIST ROLL	2.98 + 7			2770

*Exponent to the base ten.

R80-1665-144(T)

In order to avoid the appearance of high frequency oscillations in the numerical-integration solution, several stiff members have been idealized as rigid bodies. The post, consisting of all members between the orbiter and Joint 3 (of Fig. I5) is rigid. As described in Appendix K, the structure between Joints 3 and 4 is rigid in the axial direction, and relative motion cannot occur along a straight line between the tip of the end effector (Node q-1) and the elbow (Node q) of Fig. 3.2.

Since the RMS is compact and stiff relative to the beam, all of its mass has been lumped at three points, the tip of the end effector, the elbow, and the shoulder. The first two of these masses are:

mass at tip of end effector, m_{q-1} = .5089

mass at elbow, m_q = .9037

Since the shoulder is rigidly connected to the orbiter, its mass has been included in the orbiter mass properties.

I7. Body B in Beam Relocation Problem

Figure 3.5 shows the idealization for Body B. The RMS properties are given in Section I6. The beam is 105 m. As in the Beam-Fabrication Problem, there are 14 bays between nodes. The geometry and mass data for Body B is presented in Table I3. The coordinates of the nodes are expressed in the $\underset{\sim}{Y}$ axis system.

The motion of the shoulder is based on information in the Shuttle Payload Accommodations Manual. The angular acceleration and deceleration is 8×10^{-5} rad/sec^2 and the cruise angular velocity .0062 rad/sec. Then, by using the formulas for uniformly accelerated motion, the following input-data times were derived.

A) $\Delta\phi > 27.5306$ deg

$$t_a = t_c = 77.5 \text{ sec}$$

$$t_b = \frac{\Delta\phi \text{ (deg)}}{.355234} - 77.5 \text{ sec}$$

TABLE I3 GEOMETRY AND MASS DATA FOR BODY B

NODE j	GEOMETRY IN Y COORDINATES (IN)			MASS (LB SEC^2/IN)
	b_{j1}	b_{j2}	b_{j3}	
1	338.329	-23.836	4177.06	.0761870
2	338.329	-23.836	3350.29	.152374
3	338.329	-23.836	2523.52	.152374
4	338.329	-23.836	1696.74	.152374
5	338.329	-23.836	869.972	.152374
6	338.329	-23.836	43.200	.0761870
7	338.329	-23.836	420.182	.5089
8	152.575	0.0	199.409	.9037

R80-1665-145(T)

B) $\Delta\phi \leq 27.5306$ deg

$$t_a = t_c = \sqrt{\frac{\Delta\phi\ (\text{deg})}{4.58366 \times 10^{-3}}}\ \text{sec}$$

$$t_b = 0$$

In case B above, the RMS never reaches cruise velocity. In all runs, manipulator motion starts 1 sec after the run begins ($t_{11} = 1.0$).

I8. Miscellaneous Data

Beam Fabrication Problem:

Constraint length, ℓ_c = 700 in
Damping coefficient, α = .01
Numerical integration step* = .1 sec (except where indicated)

Beam Relocation Problem:

Damping coefficient, α = .01
Numerical integration step* = .05 sec

Controls data common to both problems:

Thruster geometry is given in Fig. H1 and Table H1
Thrust, F_j = 25. lbs
Deadband, e_{DB} = .1 deg

---

*The numerical integration time step sizes were obtained by running the program for each problem with different step sizes and determining the largest step size that still produced accurate results. For the step sizes used, the computer-generated response curves were overlayed onto response curves obtained with smaller steps, and no difference in the results was detected.

Appendix J
EQUATIONS OF MOTION FOR BEAM-RELOCATION PROBLEM

Figure 3.1 shows the idealization for the beam relocation problem. The notation for the transformation between coordinate systems is shown in Fig. J1. As indicated, [E] transforms vectors with components in $\underset{\sim}{Z}$ coordinates to $\underset{\sim}{Y}$ coordinates, and [D] transforms vectors from the $\underset{\sim}{X}$ to the $\underset{\sim}{Y}$ coordinate system. Since $\{\theta_{100}\}$ is the rotation vector of the orbiter, the transformation from $\underset{\sim}{Z}$ to $\underset{\sim}{X}$ is $[1] - [\Gamma(\theta_{100})]$ where $[\Gamma(\ )]$ is the cross-product matrix defined by (E4). (see Ref. 2, Vol. 1, Appendix B). Thus,

$$[E] = [D]([1] - [\Gamma(\theta_{100})]) \tag{J1}$$

J1. Equations of Motion for Body B

First, the equations of motion will be developed for Body B, taken as a free body (see Fig. J2). The following notation will be used:

m_h is the mass of the portion of the hinge that moves with Body B.

$\{u_h\}$ is the absolute deformation vector of m_h expressed in $\underset{\sim}{Z}$ (i.e., in the $\underset{\sim}{Z}$ coordinate system)

$\underset{\sim}{Y}$ is a fixed coordinate system in m_h and $\underset{\sim}{Y}$ rotates at $\{\omega\}$

$\{v_i\}$ is the relative deformation vector of m_i ($i = 1, 2, \ldots, q$ not including the hinge), expressed in $\underset{\sim}{Y}$

$\{b_i\}$ is the undeformed positon vector of m_i in $\underset{\sim}{Y}$

$\{\omega\}$ is the angular-velocity vector of $\underset{\sim}{Y}$ expressed in $\underset{\sim}{Y}$

Newton's law is written in rotating coordinates for a mass point in Body B.

$$m_i\left(\{\ddot{v}_i\} + 2[\Gamma(\omega)]\{\dot{v}_i\} + [\Gamma(\omega)]^2\{r_i\} - [\Gamma(r_i)]\{\dot{\omega}\} + [E]\{\ddot{u}_h\}\right) = \{f_i\} \tag{J2}$$

$$i = 1, 2, \ldots, q$$

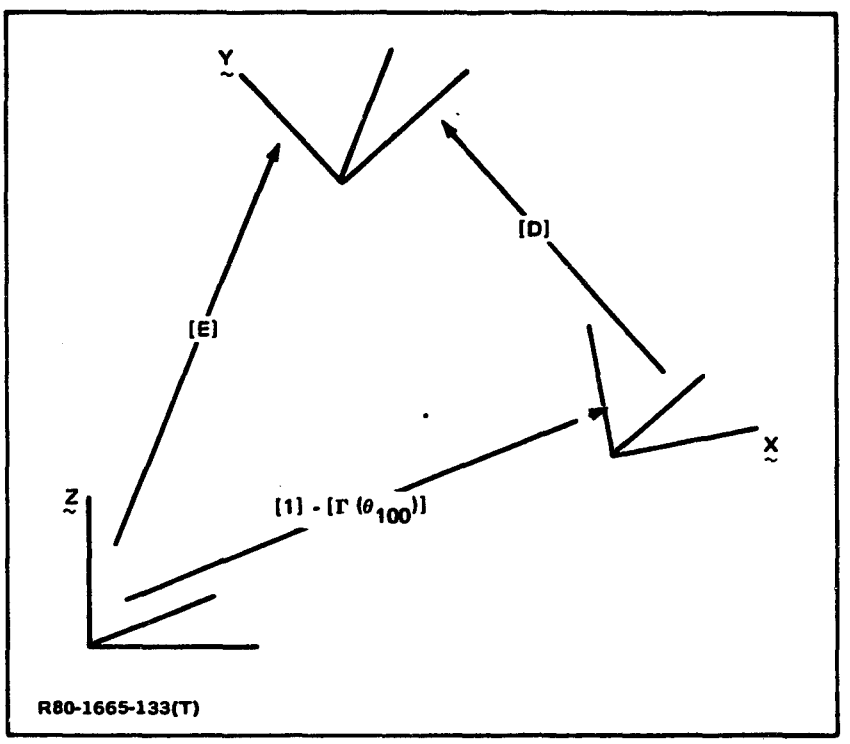

Fig. J1 Transformations Between Coordinate Systems

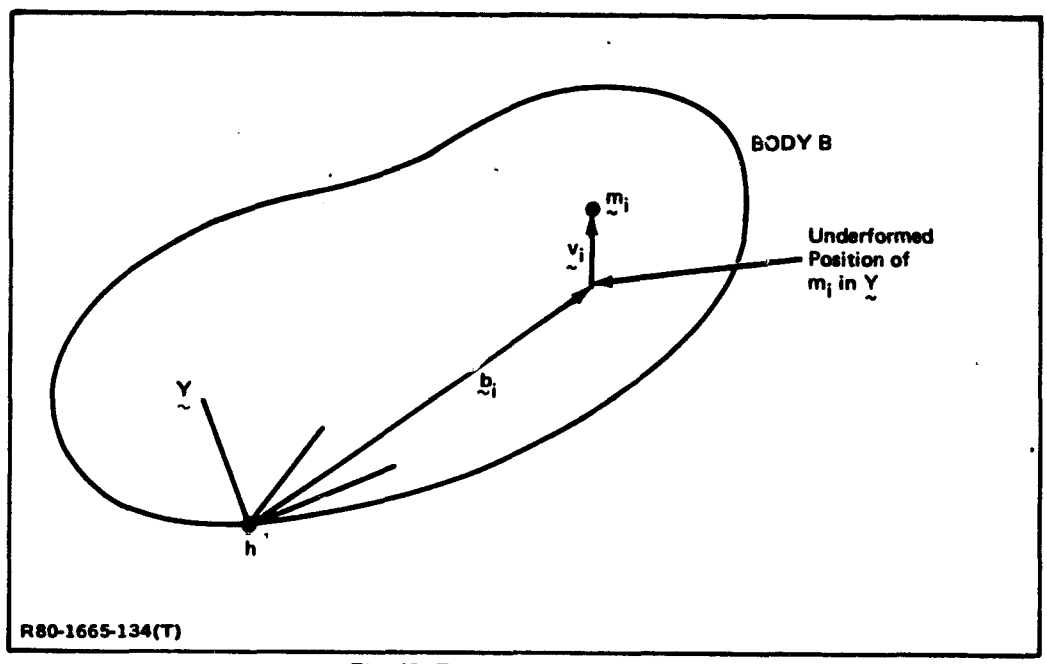

Fig. J2 Free-Body Diagram of Body B

where the $\{f_i\}$'s are expressed in $\underset{\sim}{Y}$ and

$$\{r_i\} = \{v_i\} + \{b_i\} \tag{J3}$$

is the vector locating m_i in Body B.

The center of mass of m_h is assumed to be located at the hinge point. Any offset portion of the hinge mass can be included as a separate mass in one of the equations (J2) and can later be constrained to be rigidly connected to m_h. The equations of motion of m_h are

$$m_h \{\ddot{v}_h\} = \{f_h\} \tag{J4}$$

$$[I_h]\{\dot{\omega}\} + [\Gamma(\omega)][I_h]\{\omega\} = \{t_h\} \tag{J5}$$

where $[I_h]$ is the inertia matrix for m_h, $\{f_h\}$ is expressed in $\underset{\sim}{Z}$, and $\{t_h\}$ is expressed in $\underset{\sim}{Y}$. Equations (J2), (J4), and (J5) are collectively written as follows:

$$\begin{bmatrix} \underset{\sim}{M}_{bb} & \underset{\sim}{M}_{bt} & \underset{\sim}{M}_{br} \\ & \underset{\sim}{M}_h & \\ & & \underset{\sim}{I}_h \end{bmatrix} \begin{Bmatrix} \ddot{\underset{\sim}{v}}_b \\ \ddot{\underset{\sim}{v}}_h \\ \dot{\underset{\sim}{\omega}} \end{Bmatrix} = \begin{Bmatrix} \underset{\sim}{f}_b \\ \underset{\sim}{f}_h \\ \underset{\sim}{t}_h \end{Bmatrix} - \begin{Bmatrix} \underset{\sim}{g}_b \\ \underset{\sim}{0} \\ \underset{\sim}{g}_h \end{Bmatrix} \tag{J6}$$

where

$$[M_{bb}] = \begin{bmatrix} m_1 \underset{\sim}{1}_3 & & & \\ & m_2 \underset{\sim}{1}_3 & & \\ & & \ddots & \\ & & & m_q \underset{\sim}{1}_3 \end{bmatrix} \tag{J7}$$

$$\{v_b\} = \begin{Bmatrix} v_{11} \\ v_{12} \\ v_{13} \\ \hline \vdots \\ \hline v_{q1} \\ v_{q2} \\ v_{q3} \end{Bmatrix} \tag{J8}$$

$$[M_{br}] = \begin{bmatrix} m_1 \underset{\sim}{E} \\ m_2 \underset{\sim}{E} \\ \vdots \\ m_q \underset{\sim}{E} \end{bmatrix} \quad 3q \tag{J9}$$

$$[M_{br}] = -\begin{bmatrix} m_1 \underset{\sim}{\Gamma}(r_1) \\ m_2 \underset{\sim}{\Gamma}(r_2) \\ \vdots \\ m_q \underset{\sim}{\Gamma}(r_q) \end{bmatrix} \tag{J10}$$

$$[M_h] = m_h[I_3] \tag{J11}$$

$$\{f_b\} = \begin{Bmatrix} \underset{\sim}{f}_1 \\ \underset{\sim}{f}_2 \\ \vdots \\ \underset{\sim}{f}_q \end{Bmatrix} \tag{J12}$$

$$\{g_b\} = \begin{Bmatrix} \underset{\sim}{g}_1 \\ \underset{\sim}{g}_2 \\ \vdots \\ \underset{\sim}{g}_q \end{Bmatrix} \tag{J13}$$

where

$$\{g_i\} = m_i\left(2[\Gamma(\omega)]\{\dot{r}_i\} + [\Gamma(\omega)]^2\{r_i\}\right) \tag{J14}$$

and

$$\{g_h\} = [\Gamma(\omega)][I_h]\{\omega\} \tag{J15}$$

J2. Lagrangian Form for Body B

As indicated in Appendix D, the procedure used to delete the constraint forces requires that the equations of motion first be transformed to the Lagrangian, or symmetric, form; i.e., the loads on the right side must be generalized forces corresponding to the coordinates in the sense that

$$\{\delta W\} = \{\bar{f}\}^T \{\delta \pi\} \tag{J16}$$

where $\{\bar{f}\}$ is the generalized force vector to be determined, and

$$\{\delta \pi\} = \begin{Bmatrix} \delta \underset{\sim}{v}_b \\ \delta \underset{\sim}{\omega}_b \\ \delta \underset{\sim}{\pi}_h \end{Bmatrix} \tag{J17}$$

where $\{\pi_h\}$ is defined by the relation $\{d\pi_h\}/dt=\{d\omega\}$. $\{\pi_h\}$ is not an actual coordinate but is a quasi coordinate (Ref. J1); however, this fact does not alter the constraint procedure developed in Appendix D.

To determine $\{\bar{f}\}$, the virtual work of the system will be developed in terms of $\{f\}$, the force vector on the right side of (J6) and $\{\delta\pi\}$. The result will have the following form

$$\delta W = \{f\}^T [Q] \{\delta \pi\} \tag{J18}$$

By comparing (J16) and (J18), it is seen that

$$\{\bar{f}\} = [Q]^T \{f\} \tag{J19}$$

Thus, if the formulation (J6) is multiplied through by $[Q]^T$, the forces on the right will be the generalized forces corresponding to the coordinates in the equation. Consequently, the equations will be in the desired Lagrangian form with a symmetric mass matrix.

The virtual work is obtained by giving each coordinate, in turn, a virtual displacement while holding the other coordinates fixed, and determining the contribution of the work done by the loads. These contributions are summed, and the result is

$$\delta W = \{f_b\}^T\{v_b\} + (\{f_b\}^T[\bar{E}] + \{f_h\}^T)\{\delta u_h\}$$

$$+ (\{f_b\}^T[\Gamma_b]^T + \{t_h\}^T)\{\delta \pi_h\}$$

where

$$[\bar{E}] = \begin{bmatrix} \underset{\sim}{E} \\ \underset{\sim}{E} \\ \vdots \\ \underset{\sim}{E} \end{bmatrix} \quad 3q \tag{J20}$$

and

$$[\Gamma_b] = [\underset{\sim}{\Gamma}(r_1) \quad \underset{\sim}{\Gamma}(r_2) \quad \cdots \quad \underset{\sim}{\Gamma}(r_q)] \tag{J21}$$

The expression for δW is placed into the following form:

$$\delta W = [\underset{\sim}{f}_b^T \quad \underset{\sim}{f}_h^T \quad \underset{\sim}{t}_h^T] \begin{bmatrix} \underset{\sim}{1}_{3q} & \bar{\underset{\sim}{E}} & \underset{\sim}{\Gamma}_b^T \\ & \underset{\sim}{1}_3 & \\ & & \underset{\sim}{1}_3 \end{bmatrix} \begin{Bmatrix} \delta \underset{\sim}{v}_b \\ \delta \underset{\sim}{u}_h \\ \delta \underset{\sim}{\pi}_h \end{Bmatrix} \tag{J22}$$

Comparison of (J22) with (J18) shows that

$$[Q] = \begin{bmatrix} \underset{\sim}{1}_{3q} & \underset{\sim}{E} & \underset{\sim}{\Gamma}_b^T \\ & \underset{\sim}{1}_3 & \\ & & \underset{\sim}{1}_3 \end{bmatrix} \tag{J23}$$

The formulation (J6) is now multiplied through by $[Q]^T$ to obtain the desired Lagrangian form. The result is

$$\begin{bmatrix} \underset{\sim}{M}_{bb} & \underset{\sim}{M}_{bt} & \underset{\sim}{M}_{br} \\ \underset{\sim}{M}_{bt}^T & \underset{\sim}{M}_{tt} & \underset{\sim}{M}_{tr} \\ \underset{\sim}{M}_{br}^T & \underset{\sim}{M}_{tr}^T & \underset{\sim}{M}_{rr} \end{bmatrix} \begin{Bmatrix} \ddot{\underset{\sim}{v}}_b \\ \ddot{\underset{\sim}{u}}_h \\ \dot{\underset{\sim}{\omega}} \end{Bmatrix} = \begin{Bmatrix} \underset{\sim}{h}_b \\ \underset{\sim}{h}_t \\ \underset{\sim}{h}_r \end{Bmatrix} \tag{J24}$$

where $[M_{bb}]$, $[M_{bt}]$, and $[M_{br}]$ are defined by (J7), (J9), and (J10), and

$$[M_{tt}] = M_b [I_3] \tag{J25}$$

with

$$M_b = \sum_{i=1}^{q} m_i + m_h \tag{J26}$$

$$[M_{tr}] = -[E]^T [\Gamma(\sum_{i=1}^{q} m_i r_i)] \tag{J27}$$

$$[M_{rr}] = [I_h] - \sum_{i=1}^{q} m_i [\Gamma(r_i)]^2 \tag{J28}$$

$$\{h_b\} = \{f_b\} - \{g_b\} \tag{J29}$$

$$\{h_t\} = [E]^T \sum_{i=1}^{q} \{f_i\} + \{f_h\} \tag{J30}$$

$$\{h_r\} = \sum_{i=1}^{q} [\Gamma(r_i)](\{f_i\} - \{g_i\}) + \{t_h\} - \{g_h\} \tag{J31}$$

The three matrix equations embodied in (J24) can be identified as Newton's law in $\underset{\sim}{Y}$ axes for each mass, Newton's law in $\underset{\sim}{Z}$ axes for the entire system, and torque equals rate-of-change of angular momentum for the entire system in the $\underset{\sim}{Y}$ axes.

J3. Rigidization Constraints for Body B

In order to delete high-frequency effects from the formulation, thereby facilitating direct numerical integration of the equations of motion, stiff regions of the structure are idealized as rigid regions. The equation expressing these rigidities is

$$\{v_b\} = [R]\{w\} \tag{J32}$$

where {w} contains a reduced set of the coordinates in $\{v_b\}$. The number of coordinates in {w} is ν, so that [R] is a $3q \times \nu$ matrix. The specific form of the rigidization matrix [R] is developed in Appendix K. The relationship between velocities is

$$\begin{Bmatrix} \dot{\underset{\sim}{v}}_b \\ \dot{\underset{\sim}{u}}_h \\ \underset{\sim}{\omega} \end{Bmatrix} = \begin{bmatrix} \underset{\sim}{R} & & \\ & \underset{\sim}{1}_3 & \\ & & \underset{\sim}{1}_3 \end{bmatrix} \begin{Bmatrix} \dot{\underset{\sim}{w}} \\ \dot{\underset{\sim}{u}}_h \\ \underset{\sim}{\omega} \end{Bmatrix} \tag{J33}$$

It can be shown that the constraint procedure of Appendix D is also valid when some or all of the coordinates are quasi coordinates, e.g., when angular velocities, such as $\{\omega\}$ in the current analysis, appear in the equations. The procedure is to substitute (J33) into (J24) and to then premultiply the equations by the transpose of the coefficient matrix in (J33). The result is

$$\begin{bmatrix} \underset{\sim}{M}'_{bb} & \underset{\sim}{M}'_{b\mathcal{I}} & \underset{\sim}{M}'_{br} \\ \underset{\sim}{M}'^{T}_{b\mathcal{I}} & \underset{\sim}{M}'_{\mathcal{I}\mathcal{I}} & \underset{\sim}{M}'_{\mathcal{I}r} \\ \underset{\sim}{M}'^{T}_{br} & \underset{\sim}{M}'^{T}_{\mathcal{I}r} & \underset{\sim}{M}'_{rr} \end{bmatrix} \begin{Bmatrix} \ddot{\underset{\sim}{w}} \\ \ddot{\underset{\sim}{u}}_h \\ \dot{\underset{\sim}{\omega}} \end{Bmatrix} = \begin{Bmatrix} \underset{\sim}{h}'_b \\ \underset{\sim}{h}'_{\mathcal{I}} \\ \underset{\sim}{h}'_r \end{Bmatrix} \tag{J34}$$

where

$$
\left.
\begin{aligned}
[M'_{bb}] &= [R]^T [M_{bb}][R] \\
[M'_{xx}] &= [M_{xx}] \\
[M'_{rr}] &= [M_{rr}] \\
[M'_{bx}] &= [R]^T [M_{bx}] \\
[M'_{br}] &= [R]^T [M_{br}] \\
[M'_{xr}] &= [M_{xr}]
\end{aligned}
\right\} \qquad \text{(J35)}
$$

and, using (J29) - (J31),

$$
\left.
\begin{aligned}
\{h'_b\} &= [R]^T (\{f_b\} - \{g_b\}) \\
\{h'_x\} &= [E]^T \sum_{i=1}^{q} \{f_i\} + \{f_h\} \\
\{h'_r\} &= \sum_{i=1}^{q} [\Gamma(r_i)](\{f_i\} - \{g_i\}) + \{t_h\} - \{g_h\}
\end{aligned}
\right\} \qquad \text{(J36)}
$$

J4. Stiffness Matrix for Body B

The right side of (J34) contains the generalized forces associated with the coordinates {w} and $\{u_h\}$ and the quasi coordinate $\{\pi_h\}$ corresponding to $\{\omega\}$. The portion of these generalized forces due to stiffness is denoted $\{h_b^{(s)}\}$,

$\{h_t^{(s)}\}$, and $\{h_r^{(s)}\}$, respectively. If the system is given a differential displacement, the change in the loads due to stiffness is

$$\begin{Bmatrix} d\underset{\sim}{h}_b^{(s)} \\ d\underset{\sim}{h}_t^{(s)} \\ d\underset{\sim}{h}_r^{(s)} \end{Bmatrix} = - \begin{bmatrix} \underset{\sim}{K}_{bb} & \underset{\sim}{K}_{bt} & \underset{\sim}{K}_{br} \\ \underset{\sim}{K}_{bt}^T & \underset{\sim}{K}_{tt} & \underset{\sim}{K}_{tr} \\ \underset{\sim}{K}_{br}^T & \underset{\sim}{K}_{tr}^T & \underset{\sim}{K}_{rr} \end{bmatrix} \begin{Bmatrix} d\underset{\sim}{w} \\ d\underset{\sim}{u}_h \\ d\underset{\sim}{\pi}_h \end{Bmatrix} \qquad \text{(J37)}$$

Equation (J37) is valid for any differential values of $\{dw\}$, $\{du_h\}$, and $\{d\pi_h\}$. If $\{dw\}$ is set to zero, then the loads cannot change due to any arbitrary motion of the base; i.e., $\{dh_b^{(s)}\} = \{dh_t^{(s)}\} = \{dh_r^{(s)}\} = 0$ for any values of values of $\{du_h\}$ and $\{d\pi_h\}$. Consequently,

$$[K_{bt}] = [K_{br}] = [K_{tt}] = [K_{tr}] = [K_{rr}] = 0$$

Thus,

$$\begin{Bmatrix} \underset{\sim}{h}_b^{(s)} \\ \underset{\sim}{h}_t^{(s)} \\ \underset{\sim}{h}_r^{(s)} \end{Bmatrix} = - \begin{Bmatrix} \underset{\sim}{K}_{bb}\,\underset{\sim}{w} \\ \underset{\sim}{0} \\ \underset{\sim}{0} \end{Bmatrix}$$

These loads are incorporated into (J36), and the result is

$$\left.\begin{aligned} \{h_b'\} &= [R]^T(\{F_b\} - \{q_b\}) - [K_{bb}]\{w\} \\ \{h_t'\} &= [E]^T \sum_{i=1}^{q} \{F_i\} + \{f_h\} \\ \{h_r'\} &= \sum_{i=1}^{q} [\Gamma(r_i)](\{F_i\} - \{q_i\}) + \{t_h\} - \{q_h\} \end{aligned}\right\} \qquad \text{(J38)}$$

where $\{F_b\}$ and $\{F_i\}$ are the values of $\{f_b\}$ and $\{f_i\}$, respectively; however, the capital letters have been used to denote that these load vectors do not include forces due to stiffness. It is seen from (J37) that $[K_{bb}]$ is the stiffness matrix of Body B cantilevered at the hinge point, h.

J5. Body A Taken as a Free Body

The equations for Body A taken as a free body are obtained from the equations for the Beam Fabrication Problem with the beam terms set to zero. The results of Section 2.5 and Appendix E are used, and the matrix equation of motion (2.17) reduces to

$$\begin{bmatrix} \bar{V}_1 & \bar{V}_2 & \\ \bar{V}_3 & \bar{V}_4 & \\ & & M_{PP} \end{bmatrix} \begin{Bmatrix} \ddot{u}_{100} \\ \ddot{\theta}_{100} \\ \ddot{u}_P \end{Bmatrix} + \begin{bmatrix} & K_A & \end{bmatrix} \begin{Bmatrix} u_{100} \\ \theta_{100} \\ u_P \end{Bmatrix} = \begin{Bmatrix} \bar{F}_R \\ \bar{T}_R \\ f_P \end{Bmatrix} \tag{J39}$$

where $[K_A]$ is the stiffness matrix of the platform considered as an unsupported structure, and

$$[\bar{V}_1] = \begin{bmatrix} M_R & & \\ & \bar{M} & \\ & & \bar{M} \end{bmatrix} \tag{J40}$$

with

$$\left.\begin{aligned} M_R &= m_{50} + m_{100} + m_{200} \\ M_P &= \sum_{i=1}^{6} m_{P_i} \\ \bar{M} &= M_R + M_P \end{aligned}\right\} \tag{J41}$$

$$\left.\begin{aligned} [\bar{V}_2] &= m_{50}[U_4] + [V_2^{(c)}] \\ [\bar{V}_3] &= [\bar{V}_2]^T \\ [\bar{V}_4] &= m_{50}[W_2] + [V_4^{(c)}] \end{aligned}\right\} \qquad \text{(J42)}$$

where $[U_4]$, $[V_2^{(c)}]$, $[W_2]$, and $[V_4^{(c)}]$ are given by (E15), (E34), (E37), and (E38), respectively. The other terms in (J39) are

$$[M_{pp}] = \begin{bmatrix} m_{P_1} & & & & & & \\ & I_{P_1} & & & & & \\ & & m_{P_2} & & & & \\ & & & I_{P_2} & & & \\ & & & & \ddots & & \\ & & & & & m_{P_6} & \\ & & & & & & I_{P_6} \end{bmatrix} \qquad \text{(J43)}$$

$$\{u_P\} = \begin{Bmatrix} u_{P_1} \\ \theta_{P_1} \\ \hline v_{P_2} \\ \theta_{P_2} \\ \hline \vdots \\ \hline u_{P_6} \\ \theta_{P_6} \end{Bmatrix}, \qquad \{f_P\} = \begin{Bmatrix} f_{P_1} \\ t_{P_1} \\ \hline f_{P_2} \\ t_{P_2} \\ \hline \vdots \\ \hline f_{P_6} \\ t_{P_6} \end{Bmatrix} \tag{J44}$$

$$\{\bar{F}_R\} = \{F_{50}\} + \{\bar{F}_{100}\} + \{F_{200}\} + \sum_{j=1}^{6} \begin{Bmatrix} 0 \\ F_{P_j,2} \\ F_{P_j,3} \end{Bmatrix} \tag{J45}$$

$$\{\bar{T}_R\} = [U_4]^T\{F_{50}\} + [U_5]^T\{F_{200}\} + \sum_{j=1}^{6} [U_6^{(P_j)}]^T\{F_{P_j}\} + \{\bar{T}_{100}\} + \{T_{200}\} \tag{J46}$$

where $\{\bar{F}_{100}\}$ and $\{\bar{T}_{100}\}$ are total external loads on the orbiter plus the loads applied by the RMS at the hinge. The other terms are defined in Appendix E.

J6. Linking of Body A and Body B - Hinge Constraint

Equations (J34) and (J39) are combined into a single matrix equation. Equation (J38) is used and the result is

$$
\begin{bmatrix}
\underset{\sim}{M}'_{bb} & \underset{\sim}{M}'_{bt} & \underset{\sim}{M}'_{br} & & & & \\
\underset{\sim}{M}'^{T}_{bt} & \underset{\sim}{M}'_{tt} & \underset{\sim}{M}'_{tr} & & & & \\
\underset{\sim}{M}'^{T}_{br} & \underset{\sim}{M}'^{T}_{tr} & \underset{\sim}{M}'_{rr} & & & & \\
\hline
 & & & \underset{\sim}{\bar{V}}_1 & \underset{\sim}{\bar{V}}_2 & & \\
 & & & \underset{\sim}{\bar{V}}_3 & \underset{\sim}{\bar{V}}_4 & & \\
 & & & & & & \underset{\sim}{M}_{PP}
\end{bmatrix}
\begin{Bmatrix}
\ddot{\underset{\sim}{w}} \\ \ddot{\underset{\sim}{u}}_h \\ \dot{\underset{\sim}{\omega}} \\ \ddot{\underset{\sim}{u}}_{100} \\ \ddot{\underset{\sim}{\theta}}_{100} \\ \ddot{\underset{\sim}{u}}_P
\end{Bmatrix}
$$

$$
+
\begin{bmatrix}
\underset{\sim}{K}_{bb} & & & & \\
 & \underset{\sim}{0} & & & \\
 & & \underset{\sim}{0} & & \\
\hline
 & & & \underset{\sim}{K}_A &
\end{bmatrix}
\begin{Bmatrix}
\underset{\sim}{w} \\ \underset{\sim}{0} \\ \underset{\sim}{0} \\ \underset{\sim}{u}_{100} \\ \underset{\sim}{\theta}_{100} \\ \underset{\sim}{u}_P
\end{Bmatrix}
=
\begin{Bmatrix}
\underset{\sim}{\bar{d}}_b \\ \underset{\sim}{\bar{d}}_t \\ \underset{\sim}{\bar{d}}_r \\ \underset{\sim}{\bar{F}}_R \\ \underset{\sim}{\bar{T}}_R \\ \underset{\sim}{f}_P
\end{Bmatrix}
\qquad \text{(J47)}
$$

where

$$
\left.
\begin{aligned}
\{\bar{d}_b\} &= [R]^T(\{F_b\} - \{g_b\}) \\
\{\bar{d}_t\} &= [E]^T \sum_{i=1}^{q} \{F_i\} + \{f_h\} \\
\{\bar{d}_r\} &= \sum_{i=1}^{q} [\Gamma(r_i)](\{F_i\} - \{g_i\}) + \{t_h\} - \{g_h\}
\end{aligned}
\right\} \qquad \text{(J48)}
$$

As indicated in Fig. 3.2, the $\underset{\sim}{Y}$ axes are fixed in the portion of the hinge that moves relative to the orbiter. To rotate the $\underset{\sim}{X}$ axes, that are fixed in the orbiter into the $\underset{\sim}{Y}$ axes, the following two rotations are performed (see Fig. J3):

1. Rotate the $\underset{\sim}{X}$ axes into the $\underset{\sim}{X}'$ axes by rotating about the X_3 axes through a positive angle α (i.e., positive in accordance with the right-hand rule).
2. Rotate the $\underset{\sim}{X}'$ axes into the $\underset{\sim}{Y}$ axes by rotating about the X_2' axis through an angle of $-\phi$.

Thus, α is the offset angle of the manipulator system relative to the orbiter center-line, and ϕ is the RMS rotation angle (see Fig. 3.3). The transformation of vectors expressed in the $\underset{\sim}{X}$ axes into the $\underset{\sim}{X}'$ axes is accomplished by multiplying by the matrix $[C(\alpha)]$ where $[C(\ )]$ is the transformation for a positive rotation about the number 3 axis; i.e.,

$$[C(\alpha)] = \begin{bmatrix} \cos\alpha & \sin\alpha & 0 \\ -\sin\alpha & \cos\alpha & 0 \\ 0 & 0 & 1 \end{bmatrix} \tag{J49}$$

The transformation from $\underset{\sim}{X}'$ axes to $\underset{\sim}{Y}$ axes is $[B(-\phi)]$ where $[B(\ )]$ is the transformation for a positive rotation about the number 2 axis; i.e.,

$$[B(-\phi)] = \begin{bmatrix} \cos\phi & 0 & \sin\phi \\ 0 & 1 & 0 \\ -\sin\phi & 0 & \cos\phi \end{bmatrix} \tag{J50}$$

The derivative of this matrix will be needed. It is

$$[\dot{B}(\phi)] = \begin{bmatrix} -\sin\phi & 0 & \cos\phi \\ 0 & 0 & 0 \\ -\cos\phi & 0 & -\sin\phi \end{bmatrix} \dot{\phi} \tag{J51}$$

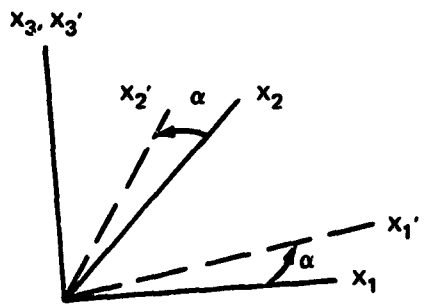

A. FIRST ROTATION

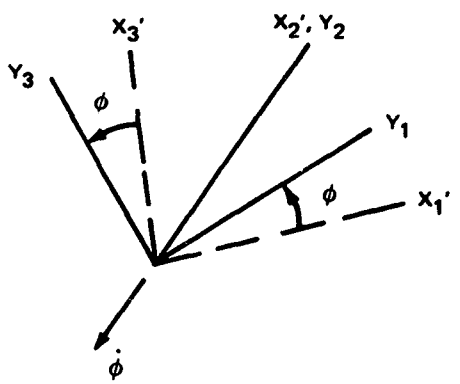

B. SECOND ROTATION

R80-1665-135(T)

Fig. J3 Rotations to Develop Transformations from $\underset{\sim}{X}$ Axes into $\underset{\sim}{Y}$ Axes

Since [D] is the transformation of vectors expressed in the $\underset{\sim}{X}$ axes to the $\underset{\sim}{Y}$ axes,

$$[D] = [B(-\beta)][C(\alpha)] \tag{J52}$$

and

$$[\dot{D}] = [\dot{B}(-\beta)][C(\alpha)] \tag{J53}$$

[D] is used in (J1).

Within linear terms, the angular velocity of the Y axis is

$$\{\omega\} = [D]\{\dot{\theta}_{120}\} - \dot{\phi}\{e_2\} \tag{J54}$$

where

$$\{e_2\} = \begin{Bmatrix} 0 \\ 1 \\ 0 \end{Bmatrix} \tag{J55}$$

By differentiating (J54),

$$\{\dot{\omega}\} = [D]\{\ddot{\theta}_{120}\} + [\dot{D}]\{\dot{\theta}_{120}\} - \ddot{\phi}\{e_2\} \tag{J56}$$

The hinge-point deflection can be related to the orbiter coordinates since the orbiter is rigid. The equation is

$$\{x_h\} = \{x_{120}\} + [U_\gamma]\{\theta_{120}\} \tag{J57}$$

where

$$[U_\gamma] = -[\Gamma(a_h)] \tag{J58}$$

where $\{a_h\}$ is the location of the hinge relative to the orbiter cm (Fig. 3.1), and $[\Gamma(\ )]$ is the cross-product matrix (see (E4)).

In view of (J57) and (J56),

$$\begin{Bmatrix} \ddot{u}_h \\ \dot{\omega} \end{Bmatrix} = \begin{bmatrix} I_3 & U_9 \\ 0 & D \end{bmatrix} \begin{Bmatrix} \ddot{u}_{100} \\ \ddot{\theta}_{100} \end{Bmatrix} + \begin{Bmatrix} 0 \\ \psi \end{Bmatrix} \tag{J59}$$

where

$$\{\psi\} = [\dot{D}]\{\dot{\theta}_{100}\} - \ddot{\phi}(x)\{e_2\} \tag{J60}$$

Thus, the equations required to transform (J47) are

$$\begin{Bmatrix} \ddot{w} \\ \ddot{u}_h \\ \dot{\omega} \\ \ddot{u}_{100} \\ \ddot{\theta}_{100} \\ \ddot{u}_P \end{Bmatrix} = \begin{bmatrix} I_\nu & & & \\ & I_3 & U_9 & \\ & & D & \\ & I_3 & & \\ & & I_3 & \\ & & & I_{12} \end{bmatrix} \begin{Bmatrix} \ddot{w} \\ \ddot{u}_{100} \\ \ddot{\theta}_{100} \\ \ddot{u}_P \end{Bmatrix} + \begin{Bmatrix} 0 \\ 0 \\ \psi \\ 0 \\ 0 \\ 0 \end{Bmatrix} \tag{J61}$$

and

$$\begin{Bmatrix} w \\ 0 \\ 0 \\ u_{100} \\ \theta_{100} \\ u_P \end{Bmatrix} = \begin{bmatrix} I_\nu & & & \\ & I_3 & & \\ & & I_3 & \\ & & & I_{12} \end{bmatrix} \begin{Bmatrix} w \\ u_{100} \\ \theta_{100} \\ u_P \end{Bmatrix} \tag{J62}$$

where each of the two {0} partitions in the left side of (J62) are 3 by 1 vectors. In accordance with the constraint procedure, (J61) and (J62) are substituted into the equations of motion (J47) and the result is premulitplied by the transpose of the acceleration-vector coefficient matrix on the right side of (J61). This pre-multiplication eliminates the forces of constraint at the hinge and reduces the number of equations of motion to the number of independent variables. The result is

$$[\Lambda]\{\ddot{y}\} + [K_T]\{y\} = \{\Delta\} \tag{J63}$$

where

$$\{y\} = \begin{Bmatrix} \underset{\sim}{w} \\ \underset{\sim}{u}_{100} \\ \underset{\sim}{\theta}_{100} \\ \underset{\sim}{u}_{P} \end{Bmatrix} \begin{matrix} \nu \\ 3 \\ 3 \\ 12 \end{matrix} \tag{J64}$$

$$[K_T] = \begin{bmatrix} \underset{\sim}{K}_{bb} & \vdots & \\ \cdots & \cdots & \cdots \\ & \vdots & K_A \end{bmatrix} \begin{matrix} \nu \\ \\ 18 \end{matrix} \tag{J65}$$

The mass and right hand side were mulitplied by partitions to reduce computer time, and (J35) is used. The mass matrix has the following form:

$$[\Lambda] = \begin{bmatrix} \underset{\sim}{\Lambda}_{bb} & \underset{\sim}{\Lambda}_{bt} & \underset{\sim}{\Lambda}_{br} & \\ \underset{\sim}{\Lambda}_{bt}^{T} & \underset{\sim}{\Lambda}_{tt} & \underset{\sim}{\Lambda}_{tr} & \\ \underset{\sim}{\Lambda}_{br}^{T} & \underset{\sim}{\Lambda}_{tr}^{T} & \underset{\sim}{\Lambda}_{rr} & \\ & & & \underset{\sim}{\Lambda}_{pp} \end{bmatrix} \tag{J66}$$

where

$$\left.\begin{aligned}
[\Lambda_{bb}] &= [R]^T [M_{bb}][R] \\
[\Lambda_{bt}] &= [R]^T [M_{bt}] \\
[\Lambda_{br}] &= [R]^T [M_{bt}][U_q] + [R]^T [M_{br}][D] \\
[\Lambda_{tt}] &= [M_{tt}] + [\bar{V}_1] \\
[\Lambda_{tr}] &= [M_{tt}][U_q] + [M_{tr}][D] + [\bar{V}_2] \\
[\Lambda_{rr}] &= [U_q]^T [M_{tt}][U_q] + [U_q]^T [M_{tr}][D] \\
&\quad + [D]^T [M_{tr}]^T [U_q] + [D]^T [M_{rr}][D] + [\bar{V}_3] \\
[\Lambda_{rr}] &= [M_{rr}]
\end{aligned}\right\} \tag{J67}$$

and the right side of (J63) is

$$\{\Delta\} = \begin{Bmatrix} \Delta_b \\ \Delta_{F_R} \\ \Delta_{T_R} \\ \Delta_p \end{Bmatrix} \tag{J68}$$

with

$$\left.\begin{aligned} \{\Delta_b\} &= \{d_b\} - [R]^T[M_{br}]\{\psi\} \\ \{\Delta_{F_R}\} &= \{d_t\} - [M_{tr}]\{\psi\} + \{F_r\} \\ \{\Delta_{T_R}\} &= [U_q]^T\left(\{d_t\} - [M_{tr}]\{\psi\}\right) \\ &\quad + [D]^T\left(\{d_r\} - [M_{rr}]\{\psi\}\right) + \{T_r\} \\ \{\Delta_p\} &= \{f_p\} \end{aligned}\right\} \tag{J69}$$

where the bars have been deleted from $\{d_b\}$, $\{d_t\}$, $\{d_r\}$, $\{F_r\}$, and $\{T_r\}$ to denote that these terms do not include the forces of constraint at the hinge; i.e., from (J45), (J46), and (J48)

$$\{F_R\} = \{F_{50}\} + \{F_{100}\} + \{F_{200}\} + \sum_{j=1}^{b} \begin{Bmatrix} 0 \\ 0 \\ F_{p_j 3} \end{Bmatrix} \tag{J70}$$

$$\{T_R\} = [U_4]^T\{F_{50}\} + [U_5]^T\{F_{200}\} + \sum_{j=1}^{6} [U_6^{(P_j)}]^T\{F_{P_j}\} + \{T_{100}\} + \{T_{200}\} \tag{J71}$$

$$\left.\begin{aligned} \{\alpha_b\} &= [R]^T(\{F_b\} - \{g_b\}) \\ \{\alpha_t\} &= [E]^T \sum_{i=1}^{q} \{F_i\} + \{F_h\} \\ \{\alpha_r\} &= \sum_{i=1}^{q} [\Gamma(r_i)](\{F_i\} - \{g_i\}) + \{T_h\} - \{g_h\} \end{aligned}\right\} \tag{J72}$$

In (J70) and (J71), $\{F_{100}\}$ and $\{T_{100}\}$ are the external force on the orbiter and the torque about its cm, not including the hinge force of constraint, and $\{F_h\}$ and $\{T_h\}$ are the externally applied loads (if any are applied) on the hinge, not including any hinge constraint loads.

Appendix K

RIGIDIZATION CONSTRAINT MATRIX FOR BODY B OF THE BEAM RELOCATION PROBLEM

Figure 3.2 shows the node numbering scheme for Body B. The nodes on the beam are numbered 1, 2, ..., q-2 consecutively down the beam. The grapple point is Node q-1. For the reasons indicated in Appendix I, there is only one other node on the RMS, Node q, and it is located at the elbow.

Since the beam is assumed to be axially inextensible, the axial displacement of each node is set equal to the axial displacement of the grapple point; i.e.,

$$v_{i3} = v_{q-1,3} \; ; \quad i = 1, 2, \ldots, q-2 \tag{K1}$$

The elbow is also assumed to be axially inextensible; i.e., from Fig. K1,

$$v_{q,1} \cos\beta + v_{q3} \sin\beta = 0$$

or

$$v_{q3} = -v_{q,1} \cot\beta \tag{K2}$$

The stiffness matrix was examined and it was found that the system is also very stiff along a line between Nodes q and q-1. To eliminate high-frequency effects, relative motion between these points was neglected; i.e., Nodes q and q-1 were assumed to be rigidly connected. The unit vector from Node q to Node q-1 is

$$\{n\} = \frac{\{b_{q-1}\} - \{b_q\}}{|\{b_{q-1}\} - \{b_q\}|} \tag{K3}$$

The components of {n} are called n_1, n_2, and n_3. Since the motion of Node q-1 relative to Node q is zero in the direction of {n}, the inner product of $\{v_{q-1}\} - \{v_q\}$ with {n} is zero; i.e.,

$$(v_{q-1,1} - v_{q,1})n_1 + (v_{q-1,2} - v_{q,2})n_2 + (v_{q-1,3} - v_{q,3})n_3 = 0$$

Equation (K2) is used to eliminate v_{q3} from the above relation, and the result is solved for $v_{q-1,1}$ yielding,

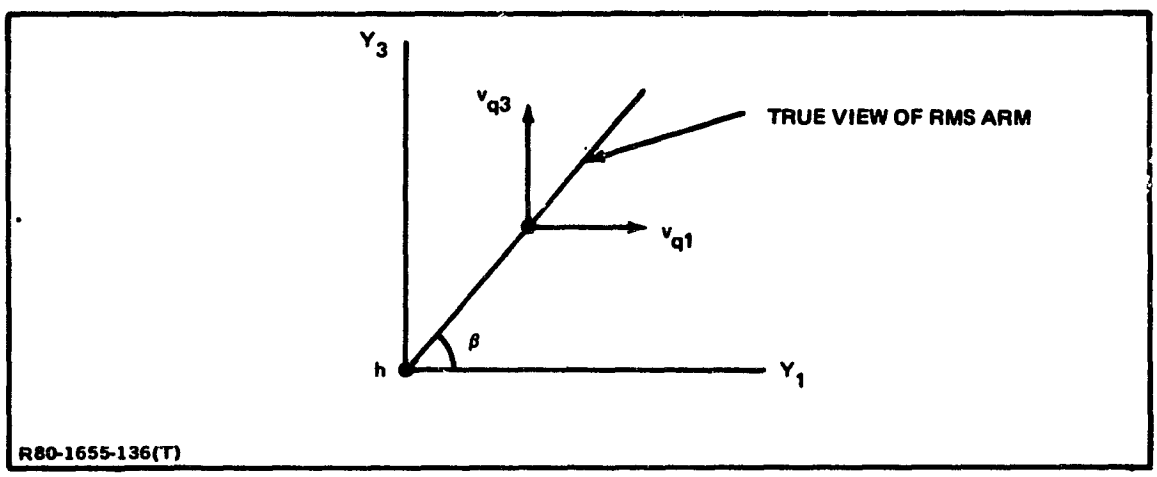

Fig. K1 Horizontal and Vertical Deformation Components of RMS Elbow

$$v_{q-1,1} = \gamma_1 v_{q-1,2} + \gamma_2 v_{q-1,3} + \gamma_3 v_{q1} + \gamma_4 v_{q2} \qquad \text{(K4)}$$

where

$$\left.\begin{aligned} \gamma_1 &= -\frac{n_2}{n_1} \\ \gamma_2 &= -\frac{n_3}{n_1} \\ \gamma_3 &= 1 - \frac{n_3}{n_1}\cot\beta \\ \gamma_4 &= -\gamma_1 \end{aligned}\right\} \qquad \text{(K5)}$$

Equations (K1), (K2), and (K4) are expressed in matrix form as follows:

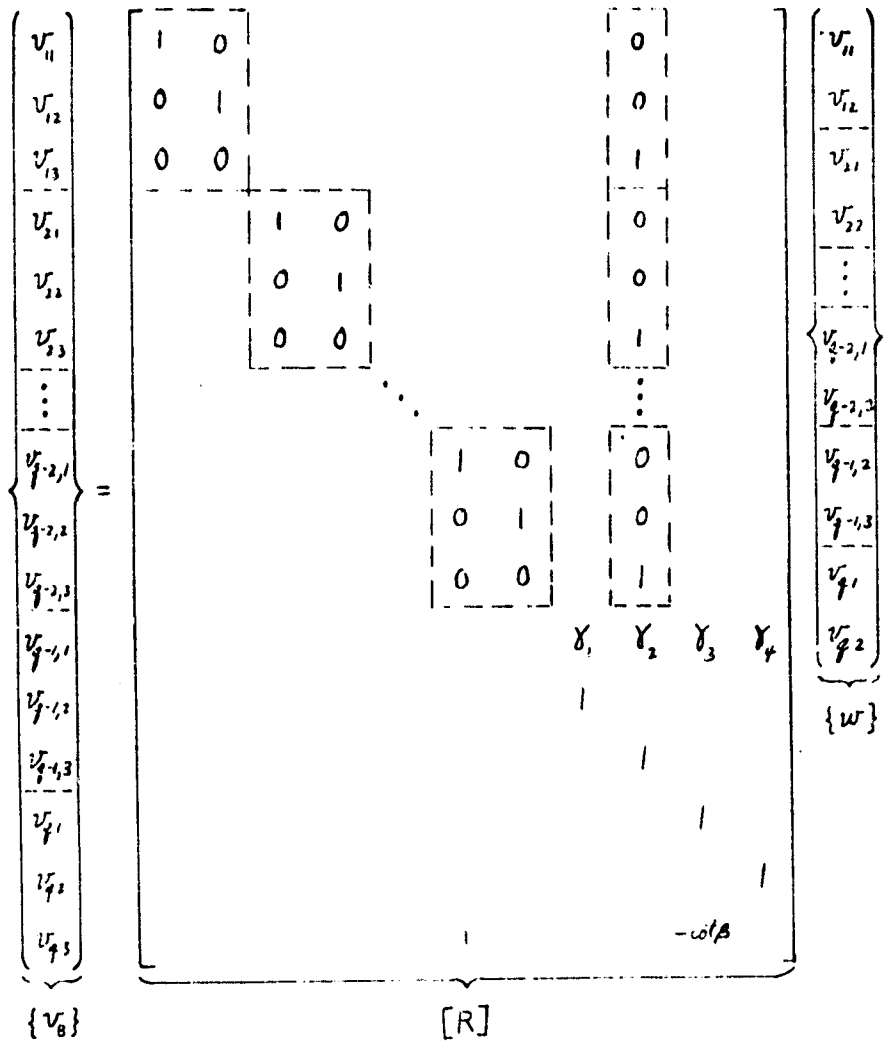

(K6)

This equation defines the terms in (J32). $\{v_B\}$ has already been defined by (J8), and [R] and {w} are the indicated terms in (K6).

Appendix L

LOADS ON RMS AT HINGE (SHOULDER) AND WRIST

The acceleration of m_i on Body B is

$$\{A_i\} = \{\ddot{r}_i\} + 2[\Gamma(\omega)]\{\dot{r}_i\} + [\Gamma(\omega)]^2\{r_i\} - [\Gamma(r_i)]\{\dot{\omega}\} + [E]\{\ddot{u}_h\} \tag{L1}$$

where $\{\ddot{u}_h\}$ is given by (J59).

Figure L1 is helpful in obtaining the internal loads. The force on Body B at the hinge in $\underline{Y}$ axes is

$$\{F_h^*\} = \sum_{i=1}^{q} (m_i\{A_i\} - \{F_i\}) \tag{L2}$$

The torque on Body B at the hinge, or RMS shoulder, is obtained by summing the torques of all of the applied and inertia loads as follows:

$$\{T_h^*\} = \sum_{i=1}^{q} [\Gamma(r_i)](m_i\{A_i\} - \{F_i\}) \tag{L3}$$

where it has been assumed that the moment of inertia of the rotating part of the hinge is negligible. The components of $\{T_h^*\}$ are expressed in the $\underline{Y}$ coordinate system.

The torque that the wrist exerts on the beam in the $\underline{Y}$ coordinate system is obtained similarly. Its value is

$$\{T_{q-1}^*\} = \sum_{i=1}^{q-2} [\Gamma(r_i - r_{q-1})](m_i\{A_i\} - \{F_i\}) \tag{L4}$$

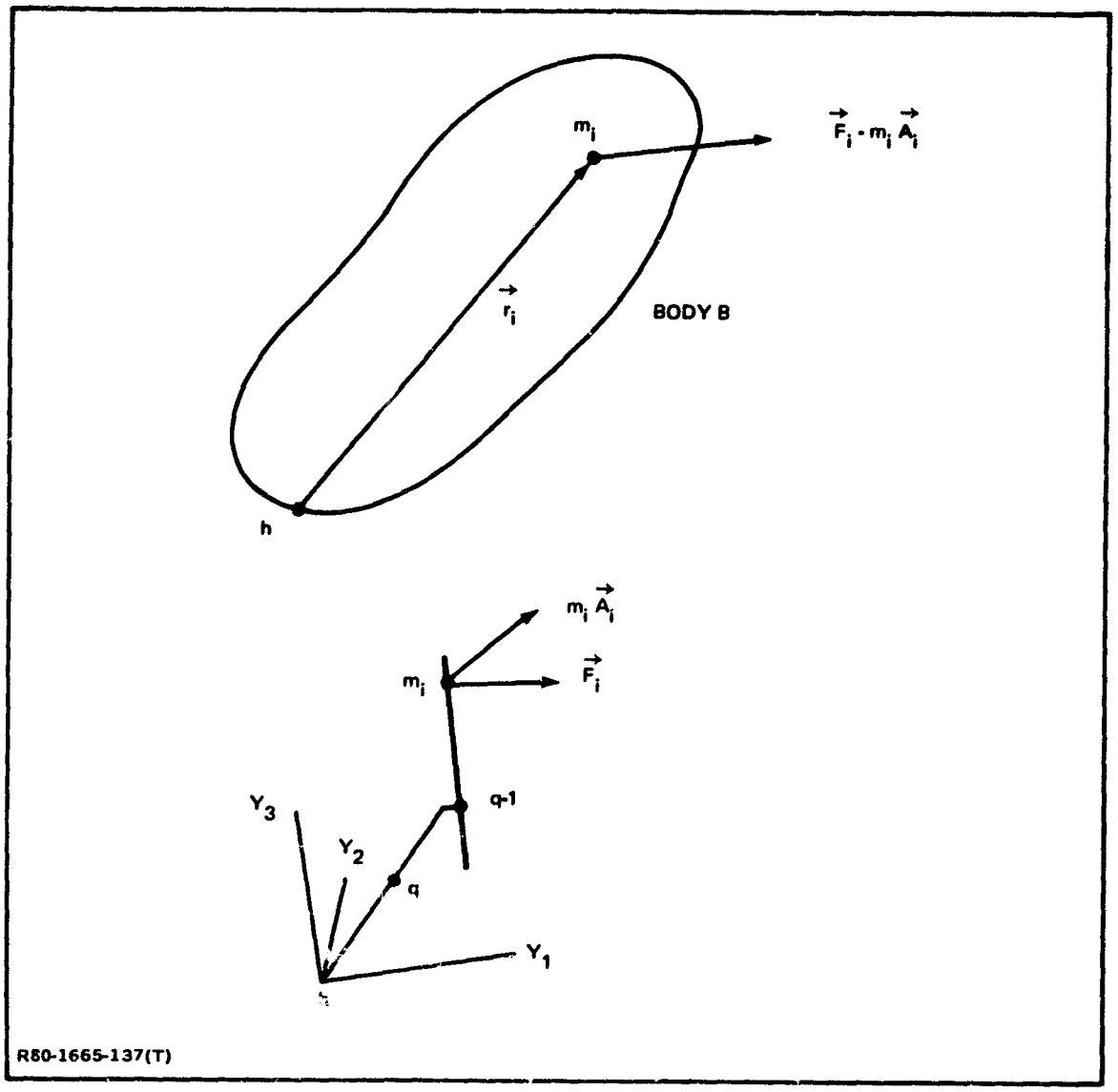

Fig. L1 Diagrams Used to Compute Internal Loads

Appendix M

HINGE CONTROL TORQUE SPECIFIED INSTEAD OF HINGE ANGLE

When the hinge control torque is specified instead of the hinge angle*, an extra degree of freedom, the hinge angle, appears in the formulation. The equations of Appendix J, up to (J58), are useful for this case; however, the equations to link Body B with Body A must be changed.

Instead of (J59)

$$\begin{Bmatrix} \ddot{\underset{\sim}{u}}_h \\ \dot{\underset{\sim}{\omega}} \end{Bmatrix} = \begin{bmatrix} \underset{\sim}{0} & \underset{\sim}{1}_3 & \underset{\sim}{U}_1 \\ -\underset{\sim}{e}_2 & \underset{\sim}{0} & \underset{\sim}{D} \end{bmatrix} \begin{Bmatrix} \ddot{\phi} \\ \ddot{\underset{\sim}{u}}_{100} \\ \ddot{\underset{\sim}{\theta}}_{100} \end{Bmatrix} + \begin{Bmatrix} \underset{\sim}{0} \\ \bar{\psi} \end{Bmatrix} \tag{M1}$$

where

$$\{\bar{\psi}\} = [\dot{D}]\{\dot{\theta}_{100}\} \tag{M2}$$

The transformation equations replacing (J61) and (J62) are

$$\begin{Bmatrix} \ddot{\underset{\sim}{w}} \\ \ddot{\underset{\sim}{u}}_h \\ \dot{\underset{\sim}{\omega}} \\ \ddot{\underset{\sim}{u}}_{100} \\ \ddot{\underset{\sim}{\theta}}_{100} \\ \ddot{\underset{\sim}{u}}_P \end{Bmatrix} = \underbrace{\begin{bmatrix} \underset{\sim}{1}_\nu & & & & \\ & \underset{\sim}{1}_3 & \underset{\sim}{U}_1 & & \\ & -\underset{\sim}{e}_2 & \underset{\sim}{D} & & \\ & \underset{\sim}{1}_3 & & & \\ & & & \underset{\sim}{1}_3 & \\ & & & & \underset{\sim}{1}_{12} \end{bmatrix}}_{[\bar{S}_1]} \begin{Bmatrix} \ddot{\underset{\sim}{w}} \\ \ddot{\phi} \\ \ddot{\underset{\sim}{u}}_{100} \\ \ddot{\underset{\sim}{\theta}}_{100} \\ \ddot{\underset{\sim}{u}}_P \end{Bmatrix} + \begin{Bmatrix} \underset{\sim}{0} \\ \underset{\sim}{0} \\ \bar{\psi} \\ \underset{\sim}{0} \\ \underset{\sim}{0} \\ \underset{\sim}{0} \end{Bmatrix} \tag{M3}$$

---

*A special case is the freewheeling situation where the hinge control torque is specified as zero.

and

$$\begin{Bmatrix} \underset{\sim}{w} \\ \underset{\sim}{0} \\ \underset{\sim}{0} \\ \underset{\sim}{u}_{100} \\ \underset{\sim}{\theta}_{100} \\ \underset{\sim}{u}_{p} \end{Bmatrix} = \begin{bmatrix} \underset{\sim}{I}_{N} & & & \\ & \underset{\sim}{I}_{3} & & \\ & & \underset{\sim}{I}_{3} & \\ & & & \underset{\sim}{I}_{12} \end{bmatrix} \begin{Bmatrix} \underset{\sim}{w} \\ \underset{\sim}{\phi} \\ \underset{\sim}{u}_{100} \\ \underset{\sim}{\theta}_{100} \\ \underset{\sim}{u}_{p} \end{Bmatrix} \tag{M4}$$

The same constraint procedure is used as in the previous case. Equations (M3) and (M4) are substituted into (J47), and the result is premultiplied by $[\bar{S}_1]^T$, where $[\bar{S}_1]$ is the coefficient matrix indicated in (M3). The result is

$$[\bar{\Lambda}]\{\ddot{x}\} + [\bar{K}_T]\{x\} = \{\bar{\Delta}\} \tag{M5}$$

where

$$\{x\} = \begin{Bmatrix} \underset{\sim}{w} \\ \underset{\sim}{\phi} \\ \underset{\sim}{u}_{100} \\ \underset{\sim}{\theta}_{100} \\ \underset{\sim}{u}_{p} \end{Bmatrix} \tag{M6}$$

$$[\bar{\Lambda}] = [\tilde{S}_1]^T [M'] [\bar{S}_1] \tag{M7}$$

[M'] is the acceleration-vector coefficient matrix in (J47),

$$[\bar{K}_T] = \begin{bmatrix} K_{bb} & & \\ & 0 & \\ & & K_A \end{bmatrix} \begin{matrix} \nu \\ 1 \\ 18 \end{matrix} \tag{M8}$$

and

$$\{\bar{A}\} = [\bar{S}_1]^T \{\bar{A}_B\} + \{f_c\} \tag{M9}$$

where

$$\{\bar{A}_B\} = \begin{Bmatrix} \alpha_b \\ \alpha_r \\ \alpha_r \\ F_R \\ T_R \\ f_p \end{Bmatrix} - \begin{Bmatrix} M'_{br}\,\bar{\psi} \\ M_{rr}\,\bar{\psi} \\ M_{rr}\,\bar{\psi} \\ 0 \\ 0 \\ 0 \end{Bmatrix} \tag{M10}$$

All of the hinge loads of constraint (but not the hinge control torque) have been deleted by the constraint-reduction procedure, and they are therefore not present in (M10). The term $\{f_c\}$ in (M9) contains the hinge torque T_ϕ on Body B; i.e.,

$$\{f_c\} = \begin{Bmatrix} 0 \\ T_\phi \\ 0 \end{Bmatrix} \begin{matrix} \nu \\ 1 \\ 18 \end{matrix} \tag{M11}$$

REFERENCES

1. Bodley, C., Devers, A., Park, A., and French, H., "Digital Computer Program for the Dynamic Interaction Simulation of Controls and Structure (DISCOS)," NASA Technical Paper 1219, May 1978.

2. Austin, F., et al., "A Study of the Dynamics of Rotating Space Stations with Elastically Connected Counterweight and Attached Flexible Appendages," Volume I, Theory (NASA CR-112243) and Volume II, Computer Program User's Manual (NASA CR-112244), prepared under Contract NAS1-10973 to the NASA Langley Research Center, March 1973.

3. Austin, F., and Zetkov, G., "Simulation Capability for Dynamics of Rotating Counterweight Space Stations," AIAA Paper No. 73-320, presented at the AIAA Dynamics Specialists Conference, March 1973.

4. DilPare, L., "Transient Nonlinear Deflections of a Cantilever Beam of Uniformly Varying Length by Numerical Methods," AIAA Journal, Vol. 8, No. 12, Dec. 1970, pp. 2293-2295.

5. Wrenn, B. G., Haile, W. B., Jr., and Hedges, J.F. "Structural Dynamics of Flexible Rib Deployable Spacecraft Antennas," The Shock and Vibration Bulletin, V. 42, Part 5, Jan. 1972, pp. 143-154.

6. Hedgepeth, J., "Dynamics of a Large Spin-Stiffened Deployable Paraboloidal Antenna," Journal of Spacecraft and Rockets, V. 7, No. 9, Sept. 1970, pp. 1043-1048.

7. Bainum, P. M., et al., "The Dynamics and Optimal Control of Spinning Spacecraft with Movable Telescoping Appendages," Part C: "Effect of Flexibility During Boom Deployment," Howard University, May 1977.

8. Lang, W. E., "Simulation of Deployment Dynamics of Spinning Spacecraft," NASA-TN-D-4074, August 1967.

9. Williams, C. J. H., Crellin, E. B[illegible] Gotts, S. A., "Mathematical Methods in Flexible Spacecraft Dynamics," British Aircraft Corp., Report No. ESS/SS-766- Vol. 2, Dec. 1976.

10. Winfrey, R. C., "The Finite Element Applied to the Analysis of Mechanisms", Shock and Vibration Digest, Vol. 9, No. 12, Dec. 1977, pp. 27-33.

11. Imam, I., Sandor, G. N., Kramer, S. N., "Deflection and Stress Analysis in High Speed Planer Mechanisms with Elastic Links," Journal of Engineering for Industry, V. 95, No. 2, May 1973.

12. Winfrey, R. C., "Dynamic Analysis of Elastic Link Mechanisms by Reduction of Coordinates," (and accompanying discussion by Imam, I., Erdman, A. G., and Sandor, G. N.) Journal of Engineering for Industry, Trans. of the ASME, May 1972, pp. 577-582.

13. Guyan, R. J., "Reduction of Stiffness and Mass Matrices," AIAA Journal, V. 3, No. 2, Feb. 1965, p. 380.

14. Gallagher, R. H., "Finite Element Analysis Fundamentals," Prentice-Hall, Inc., New Jersey, 1975, Chapt. 3.

15. Shuttle Operational Data Book, Vol. I, Amendment 53, pp. 4.3.2-1 through 4.3.2-9.

16. Hoffman, K. and Kunz, R., "Linear Algebra," Prentice Hall, N.J., 1961, pp. 230 and 231.

17. Mettler, E., "Allgemeine Theorie Der Stabilität Erzwungener Schwingungen Elastischer Körper," Ingenieur-Archiv, V. 17, pp 418-449, 1948.

A1. "Systems Definition Study for Shuttle Demonstration Flights of Large Space Structures (LSS)," Contract NAS8-32390, Grumman Aerospace Corp., Report No. DRD MA-04, June 1978.

A2. "Space Construction Automated Fabrication Experiment Definition Study (SCAFEDS)," Contract NAS9-15310, General Dynamics, Convair Div., Report No. CASD-ASP-77-017, May 1978.

A3. "Systems Definition Study for Shuttle Demonstration of Large Space Structures," Contract NAS8-32390, Grumman Aerospace Corp. April 1979. April 1979.

A4. Kaplan, R., and Schultz, J. L. "Deployable Reflector Structure," U.S. Patent 4030102, assigned to Grumman Aerospace Corp., June 1977.

A5. "Large Space Erectable Structures," Contract NAS9-14914, Boeing Aerospace Co, Report No. D-180-20607-2, April 1977.

A6. "Space Operations Center, A Concept Analysis," Lyndon B. Johnson Space Center, JSC-16277, Volume I, Summary, Nov. 1979.

A7. "Solar Power Satellite System Definition Study," Contract NAS9-15636, Boeing Aerospace Co., Report D180-25037-2, March 1979.

A8. "Solar Power Satellite System Definition Study, Phase 1," Final Report for Boeing Aerospace Co., Contract N520080-9114, Grumman Aerospace Corp., Report No. NSS-SPS-B-RP008, December 1978.

A9. "Satellite Power Systems (SPS), Concept Definition Study," Contract NAS8-32475, Rockwell International, Report No. SSD 79-0010-1, March 1979.

B1. Mason, P., "An Introduction to Automated Structural Analysis Methods " ADR 02-11-65.7, Grumman Aerospace Engineering Corp., June 1965, p. 3-28.

B2. Mason, P. and Balderes, T., "Applications of the Finite-Element Technique in Structural Analysis," ADR 02-11-67.5, Grumman Aerospace Corp., Dec. 1967, p. 225.

I1. "Systems Definition Study for Shuttle Demonstration Flights of Large Space Structures," prepared for NASA by Grumman Aerospace Corporation under Contract NAS8-32390, Vol. 2, p. A-3, July 1979.

J1. Whittaker, E. T., "A Treatise on the Analytical Dynamics of Particles and Rigid Bodies," Cambridge University Press, Fourth Edition, 1937, Reprinted 1964, pp. 41, 42.